Studies of scintillation on earth-space paths

Yu, Ping

Award date:
2003

Awarding institution:
University of Bath

Studies of Scintillation on Earth-Space Paths

Submitted by

Ping Yu

for the degree of

Doctor of Philosophy

The University of Bath, UK

2003

Author's signature 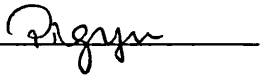 Date June 30, 2003

ProQuest LLC
789 East Eisenhower Parkway
P.O. Box 1346
Ann Arbor, MI 48106-1346

ABSTRACT

This dissertation is concerned with the slant-path scintillation effect induced by the troposphere and observed by Ka- and V- band Earth-station receivers. The emphasis is on the random amplitude fluctuations in the received signals, which may impose significant communication degradation problems for slant-path links. ITALSAT downlink beacon measurements recorded at Sparsholt (51.083N 1.383W), UK, have been used as the principal source of experimental data. High-pass filtering has been used to separate scintillation from slower varieties of signal fading. A thorough analysis of time-series power spectra has been undertaken to ensure an optimum choice of filter cut-off frequency for efficient and effective separation of scintillation and other propagation impairments. The stationary period of scintillation has been carefully addressed. Statistical properties of scintillation log-amplitude and intensity have been drawn from a 19-month database for 18.7, 39.6 and 49.5 GHz measurements under both dry and wet conditions. In addition, scintillation occurring concurrently with rain and cloud are investigated. Three representative models proposed to model long-term scintillation log-amplitude distribution are analysed. A comprehensive set of 15 existing models for scintillation intensity prediction has also been reviewed and compared with the measurements. Various meteorological variables used as climatic dependent predictors for scintillation are assessed. Finally, a path-integrated water vapour estimation technique using the Global Positioning System (GPS) is applied to the prediction of scintillation intensity. New models for long-term scintillation intensity are proposed and tested. The credibility of these techniques is demonstrated and, whilst further validation is required, good evidences are presented for their superior performance when compared to those existing models.

TABLE OF CONTENTS

ACKNOWLEDGMENTS

The author wishes to express her sincere appreciations to Dr Ian A. Glover and Professor Peter A. Watson for their support and guidance during her study and preparation of the thesis. Gratitude is also expressed to Dr Owain T. Davies for his support and assistance in providing the GPS data. He was a member of Telecommunication, Space and Radio Group at the University of Bath.

Special thanks go to Mr Charles Wrench, the division head of Earth-space Services Group, Dr S Ventouras and Ms S. A. Callaghan at the CCLRC Rutherford Appleton Laboratory for providing support and access to the ITALSAT beacon measurement database. The author is grateful to the British Atmospheric Data Centre, which provided with access to the UK Met Office Radiosonde Data and Land Surface Observation Stations Data.

The author thanks her parents and family for their unwavering love and encouragement; her friends for their time and companionship. Peck, for everything.

LIST OF FIGURES

Chapter *Page No.*

Chapter 3

Chapter 4

Chapter 5

Chapter 6

Chapter 7

Chapter 8

LIST OF TABLES

Chapter *Page No.*

Chapter 3

Chapter 4

Chapter 6

Chapter 8

LIST OF ABBREVIATIONS AND ACRONYMS

ACTS	Advanced Communications Technology Satellite
ALC	Adaptive Link Control
APC	Adaptive Power Control
BER	Bit Error Rate
DSD	Drop Size Distribution
DTH	Direct To Home
ESA	European Space Agency
FMT	Fades Mitigation Technique
GEO	Geo-stationary Orbit
GIPSY-OASIS	GPS-inferred Positioning System and Orbit Analysis Simulation
GPS	Global Positioning System
IEEE	Institute of Electrical and Electronic Engineers
IGS	International GPS Service
IPWV	Path-integrated Precipitable Water Vapour
ITU	International Telecommunication Union
ITU-R	International Telecommunication Union-Radiocommunication
JPL	Jet Propulsion Laboratory
LAN	Local Area Network
LEO	Low Earth Orbit
LWC	Cloud Liquid Water Content
NASA	National Aeronautics and Space Administration
OPEX	Olympus Propagation Experiment
RAL	Rutherford Appleton Laboratory
RCRU	Radio Communications Research Unit
RINEX	Receiver Independent EXchange

RMS	Root Mean Square
SCADA	Supervisory Control and Data Acquisition
TDMA	Time Division Multiple Access
TEC	Total Electron Content
ULPC	Up-Link Power Control
UTC	Coordinated Universal Time
VSAT	Very Small Aperture Terminal
WVR	Microwave Radiometer
ZHD	Zenith Hydrostatic Delay
ZTD	Zenith Total Delay
ZWD	Zenith Wet Delay

Introduction

Satellite communications has become an essential part of today's telecommunications industry. Ever since the first communication satellite was launched in 1962, the improvement and advancement in satellite telecommunication technology has been accelerating. With many years of investment in research and development, satellite communications industry has grown into a large business providing a wide range of telecommunications services, generating billions of dollars annually in the sales of products and services. However, the full potential of satellite communication is still waiting to be realised. The next generation high capacity applications require continued research. The origin and effects of scintillation is one of the areas that can be further investigated to improve performance in these next generation systems. Chapter 1 outlines the challenges, justification and objectives of the work reported in this thesis.

1.1 Satellite Communications – An indispensable way to establish a link

Over the last few decades, satellite systems have changed the way in, and speed at, which we communicate and how our economy works. They have introduced new dimensions to television and entertainment. The ultimate aim for this exciting industry of satellite communication is to provide fast and affordable telecommunication services to both urban and rural communities worldwide. With the exponential growth in Internet traffic and the convergence of various information technology (IT) sectors such as broadband services, multimedia, mobile and broadcasting, the telecommunication industry is experiencing rapid growth to become an indispensable component of the global communication infrastructure.

Successfully offering services in today's business environment involves huge challenges from understanding the services market to the component technologies required and its integration. Cost issues, service provisioning, rapid installation, quality concerns and the infrastructure to support new communications environments are all factors to be considered when implementing new services.

Comparison must be made between all the available transmission technologies such as optical fibre, microwave relay, cellular radio and satellite systems. The preferred technology is determined by the application and required service(s) consistent with financial resources and current technology constraints.

Satellite communications have several advantages, for many applications, over terrestrial systems. If positioned in geostationary orbit, a satellite has direct coverage of about 75 percent of the Earth's surface. This puts satellites at an unmatched advantage when providing point-to-multipoint broadcast services and delivering large amounts of information efficiently to a large number of globally distributed users. Satellites can also provide overflow capacity for congested terrestrial network.

New satellite services can be deployed in a relatively short period of time. Once the satellites are operational, any site within the footprint can be equipped quickly and inexpensively. Satellite signals can be transmitted directly to the end user. The alternative of setting up a terrestrial network will typically need lengthy and expensive installation of infrastructure across the entire service coverage area. The versatility of satellite communication systems makes them especially suited for quick deployment, specifically in a situation where high-capacity links are required in a short time.

Satellites links are particularly beneficial when used on low traffic density routes. Transmission prices are relatively insensitive to variations in geographic location within the satellite footprints. Satellite link costs are largely based on user service duration or quantity of data transferred, while optical fibre link costs, for example, increase with the physical diameter of the network. Relative immunity to the danger of physical damage is another obvious advantage of the satellite system over the alternative optical fibre system.

Satellite communication networks are not concerned with the 'last mile' problem, encountered at the end of trans-oceanic optical fibre systems. In this context the 'last mile' problem includes that faced by inland-located countries who incur extra transportation cost to connect the terminal exchange of the fibre (probably located near the coast) to local exchanges close to the centres of population using, for example, terrestrial links. Besides, not all countries are inter-connected via submarine fibre-optic cables. For regions where terrestrial infrastructure is limited or non-existent, satellites give 'equal weight' coverage to all regions.

At present, satellites network are integrated into large hybrid terrestrial infrastructure network providing communications services to both fixed and mobile terminals, with various degrees of transparency. The availability of several types of transmission systems enables service providers to offer the most cost-effective solution possible in many applications. A satellite system can be used, for example, to (i) concentrate data from various low-density traffic sources, the concentrated traffic being transferred to a central location via an optical fibre link; (ii) provide back-up to optical fibres in case of optical fibre outage. Optical fibre links, for example, transport video data from the studio to an earth station for satellite broadcast [1].

Significant research and development efforts have been made to improve a number of aspects of satellite communication system. Ground segments size and

cost have decreased, giving the ability to provide services directly at user premises. The power generation capabilities of satellite have increased. New developments have been achieved in space segment technology such as inter-satellite links, Ku- and Ka-band applications, low earth orbit (LEO) and mid-altitude earth orbit (MEO) constellations, on board processing and switching. It is now possible to use shaped, directional and multi-beam antennas on satellites. Performance of multiple access schemes, modulation and coding techniques have improved. With deregulation across many countries, new dynamic privately owned companies have emerged. There are increased level of cooperation, joint venturing, mergers and acquisitions (upstream, lateral and downstream) as well as new opportunities for niche players. The potential services offered by satellites have thus diversified [2].

1.2 Challenges and Trends in Satellite Communications

Several challenges in satellite communications remain to be overcome. For example there is the inherent delay between two communicating terminals. This problem is especially significant for interactive applications that require handshaking between terminals.

Increasing demand for wider bandwidths to cope with video conferencing and Internet applications has given rise to many requests for use of the 20/30 GHz spectrum allocations made by the International Telecommunication Union (ITU). To allow high data rate transmissions (e.g. several hundred megabits per second), the next generation of satellite frequency allocations will be looking at Ka and V band up to 50 GHz. There is some advantage to these higher frequencies since a reflector antenna smaller than one meter in diameter can be used for dialogue, multicasting and point-to-multipoint services. Furthermore, the bandwidths allocated in the new frequency bands are proportionately larger than the allocations at lower frequencies. The wider bandwidth will be sufficient to

support a number of alternative high capacity telecommunication applications such as broadband interactive multimedia services. Several major companies are hoping to take off with the launch of dedicated systems providing competitive packages of voice, data and digital television services once the new technology enables the extension of current broadband networks.

As operating frequency increases, however, propagation impairments will become increasingly severe. Research into propagation impairments and their impact in these high frequency bands are invited in new measurement campaigns. Higher frequencies also set new challenges for low link margin and low elevation angle systems.

Very small aperture terminals (VSATs), which provide smaller, lower cost terminal equipment, with small margins (usually 1-3 dB), have become an expanding area due to their ability to bypass existing terrestrial infrastructure. Such satellite networks match well with highly asymmetric patterns of traffic use, such as is encountered in broadband Internet access, with subscribers downloading (consuming) much more information than they upload (generate) [3]. Some of the other services that can benefit from small earth terminals include multimedia applications, local area network (LAN) interconnection, supervisory control and data acquisition (SCADA) [4]. The performance of such systems will be affected by atmospheric propagation impairments in a different manner from larger, more complex, and higher margin systems.

The extension of satellite links to lower elevation angles, to extend coverage or to allow for degraded orbits, can also result in systems with lower margin links [5]. The use of low earth orbit (LEO) enables user terminals to operate with reduced size and power by reducing the distance between the satellite and the user and therefore reducing free space path loss.

For systems operating at inclined geo-synchronous orbits or LEOs, the elevation angle varies between its maximum and minimum values. As the elevation angle varies, the length of the radio transmission path and the free space loss also vary.

In addition to confronting new propagation concerns for low link margin, low elevation angle and high frequency satellite systems, conventional satellite communication technology has been subject to increasingly commercial competition. To adapt to the ever-changing market conditions and to remain competitive, satellite systems need to reduce costs and improve quality. Under these pressures, solutions are sought to improve efficiency and cost effectiveness. An estimated 60% of a spacecraft's costs are incurred during its operation [6]. Current trends in the space industry are forcing designers to reassess how spacecrafts are operated.

1.3 Propagation Impairments And General Solutions

1.3.1 Quality-of-Service

Given a certain type of service, ITU-R has recommended quality-of-service (QoS) requirements, judged on the basis of service quality required and the availability of that service. Details are given in [7], [8], [9] and [10]. These guidelines aim to provide information signals of an acceptable quality to the users.

Overall satellite link quality is judged by baseband signal-to-noise ratio (S/N) for analogue satellite system or bit error rate (BER) for a digital system. In both cases, they are proportionally associated with carrier-to-noise ratio (C/N) at the input of earth station terminal by a modulation dependent factor. Link budget designs establish the desired carrier-to-noise ratio, by proper selection of satellite and earth station effective isotropic radiation power (EIRP), antenna gain to

system noise temperature ratio (G/T), interference, and signal loss (e.g. due to the atmosphere).

Availability refers to the percentage of time that the link quality exceeds a specified threshold. The overall availability of service is governed by the propagation dependent link availability and the earth station and satellite availabilities. The link availability is usually assumed to be the overall availability because the earth station and satellite availabilities are always high in comparison (during intended lifetime) [11]. To achieve a high system availability, the fraction of time during which the system is in a down state (i.e. unable to support a connection) should be as low as possible (within the constraints of economic justification) and once a connection has been established, it should have a low probability of being terminated.

The specified link quality is achieved by selection of RF transmit power and antenna size on the downlink and uplink segments, plus consideration of the power margin to allow for propagation impairments such as background gaseous absorption, rain attenuation, scintillation, external noise and pointing error loss [12].

1.3.2 Propagation Impairments

One of the main concerns is the influence of the atmosphere on radio wave propagation. The intervening medium between earth station and satellite – the channel – affects radio wave propagation in several ways, mainly radio noise, ionospheric effects and tropospheric effects. Above 1 GHz, the absorptive constituents of the atmosphere (water vapour, oxygen, hydrometeors) will act as noise sources. The significance of external noise is typically small compared to the impairments of radio wave propagation that occur in the troposphere and the ionosphere. The transmitted signal is modified by the presence of free electrons and the Earth's magnetic field in the ionosphere. The signal is subject to

absorption, phase delay, scintillation and polarisation rotation [13]. Ionosphere effects decrease with increasing frequency. The troposphere may result in rain attenuation (caused by scattering and absorption by the water droplets); depolarisation (caused by large raindrops and by ice crystals) and scintillation (mainly caused by the inhomogeneous refractive index field arising due to turbulence) [14]. These effects result in degraded performance and, ultimately, in reduced availability dependent on link parameters such as operating frequency, antenna elevation angle and polarization, earth station altitude, earth station noise temperature and local meteorology.

1.3.3 Impairment Mitigation

In order to accommodate the effects of degraded signal quality, either compensation methods or avoidance methods may be applied. These methods are known collectively as fade mitigation techniques (FMTs). Adaptive power control (APC) is an example of fade compensation and route diversity (RD) is an example of fade avoidance. FMT schemes take into account operating frequency bands, performance objectives of the system, geometry of the network, meteorology expected close to the earth station and the expected dynamic characteristics of fading events [15].

One of the non-diversity methods is to assign a fixed link margin corresponding to the worst case fading expected for the availability required, in order to compensate the signal loss. When these fading effects become more severe, due to technology limitations, a fixed margin design alone will be impossible to achieve the required quality-of-service cost effectively.

A general objective in the design of satellite system is to minimize the transmitted power because the transmitter cost is significant and the on-orbit power consumption is related to the power requirement. As a result of frequency spectrum congestion, congestion in the geostationary orbit, and the related

widespread use of frequency sharing, interference is an important consideration. The potential to interfere with other radio systems demands transmitted powers be set at the minimum possible level. In addition, there are international, national and regional regulations for the upper limit of power transmissions to ensure satisfactory co-existence between co-frequency services.

Reliable and detailed information about statistical occurrence of impairments and their dynamic behaviour along with datasets to develop impairment detection and prediction schemes are therefore required.

1.3.4 Propagation Experiments and Prediction Modelling

For a given set of link parameters, the most effective technique to identify and measure propagation impairments is to conduct an experiment. Propagation conditions on an Earth-space link are not always highly frequency dependent. With deployment of higher frequencies, the prediction methods for calculating propagation impairments need to be refined. Experiments aiming to minimize the uncertainty of existing models are usually conducted by gathering large amounts of propagation data. A known beacon signal is transmitted from the satellite and received on the ground. The received signal strength can thus be monitored, recorded and analysed offline.

Several such propagation campaigns have been implemented during the last few decades. The multi-national propagation campaign in Europe (OPEX) used Ku- and Ka-band signals transmitted from the Olympus spacecraft [16]. A measurement campaign used the Advanced Communication Technology Satellite (ACTS) took place mainly in the US and Canada from 1991-1996 [17]. The ITALSAT programme was conceived with the aim at assessing the effect of the atmosphere at 18.7, 39.6 and 49.5 GHz.

By collecting experimental data and recording meteorological variables, atmospheric events can be identified and their effect be studied. At the same time, these valuable experimental resources provide a way to develop and validate methods for predicting tropospheric induced propagation events, based on either established physical mechanisms, empirically observed correlations, or some mixture of the two.

Since such experiments are difficult and expensive to set up, a modelling approach with the capability to derive the statistics of propagation effects without needing satellite measurements for a particular site would be extremely useful. This problem has attracted the attention of many researchers from all over the world.

There are generally two types of prediction models being investigated for radio wave propagation: statistical models and deterministic models. Statistical models, like ITU/R recommendations, use a semi-empirical approach and are quite well-suited for systems studies. They are routinely used for planning purposes to estimate the reliability of a system or the level of interference to be expected for a service. They predict path loss exceeded for a given percentage of the time. Statistical models are often based on the underlying physics of the problem. But, because of a shortage, or absence, of the necessary meteorological and other environmental data, and the need for wide applicability and short computation times, these models tend to be semi-empirical; the model parameters being deduced from experimental data. Deterministic models are more complete models, and always based on physical principles so as to provide near real time prediction of performance of the system. Input parameters, however, are not always available for these models, so they are more suited to in-depth case studies.

1.4 Statement of Original Contributions

The work has contributed to the development of three new and robust scintillation prediction models involving skilful manipulation of the path-integrated water vapour content (IPWV) derived from the readily available GPS data. They have demonstrated improved accuracy over the 15 most recent existing models. Important statistics and conclusions were drawn from analysing meteorological, GPS and satellite beacon receiver measurements in order to justify these models. The following is a list of significant findings contributed by the work of "Studies Of Scintillation On Earth-Space Paths":

i. A comprehensive review and evaluation of existing scintillation prediction models.

ii. Detailed investigation of seasonal and diurnal variations of meteorological variables for scintillation prediction has led to the conclusion that IPWV can be an effective scintillation predictor.

iii. Recommendation of an effective 0.01 Hz high-pass filter for extracting scintillation components from other propagation impairments, and 1-minute intervals for calculating scintillation intensity.

iv. Three different scintillation prediction models, in general referred to as the "GPS-informed scintillation model," have been derived and demonstrated prediction accuracy better than 15 existing models. This involved a successful integration of GPS measurements for computing the path-integrated water vapour (IPWV).

v. Comparison and analysis that led to a successful identification of the most suitable probability distribution function for scintillation modelling. This involved looking at Gaussian and Rice-Nakagami for short-term

scintillation log-amplitude distribution and Lognormal and Gamma for long-term scintillation intensity.

vi. Over 300 MatLab routines for pre-processing, validating, analysis and computation for various different types of existing scintillation prediction models and the new model itself.

1.5 Statement of Research Aims and Objectives

The objectives of this work are:

- To assess tropospheric scintillation prediction models in the light of new challenges generated by new services and new satellite networks. Comparisons will be made between predictions and observations.

- To investigate scintillation statistics and dynamic behaviour for systems operating in the Ka and V frequency bands (to be utilized by the next generation satellite communication services)

- To derive useful relationships between scintillation and tropospheric meteorological variables. Attention will be drawn to scintillation during rain and cloudy events.

- To systematically construct a new prediction model for scintillation using a novel predictor that will have improved performance in the UK climate.

1.6 Outline of the Thesis

The thesis is divided into nine chapters including the current introduction, and the remainder is organized as follows:

Chapter 2 reviews the origin of tropospheric scintillation, its dynamic properties and most commonly used descriptors. The impacts of scintillation on satellite communication systems are also examined.

Chapter 3 describes the measurement data used in this work and their sources. The database comprises of GPS measurements, Radiosonde measurements, UK Meteorological Office Synoptic data and ITALSAT beacon receiver measurements.

Chapter 4 presents the theoretical framework of clear-air turbulence with the relevance to radio wave propagation and the characteristics of dry scintillation. A survey of the related work is provided and results from experimental measurements are used to justify these characteristics.

Chapter 5 presents a study of the relationships between scintillation and meteorological variables and is particularly focused on the characteristics of rain induced and cloud related scintillation. This is followed by an analysis to determine a range of suitable scintillation predictors.

Chapter 6 reviews existing and current monthly scintillation prediction models and tests their performance with experimental data. The advantages of each model and their practical applications are discussed.

Chapters 7 and 8 introduce a new scintillation prediction method that uses path-integrated water vapour estimates from the GPS measurements. A justification for the new model in terms of its expected improved scintillation prediction is given. The remaining work in the chapter compares the performance of the new models and existing models with measurements.

Finally, the thesis is concluded and directions for future works are proposed in Chapter 9.

1.7 References:

[1] M. Richharia, *Satellite commuications systems*: The Macmillan Press LTD, 1995.

[2] G. Maral and M. Bousquet, *Satellite communications system - systems, techniques and technology*, third ed: John Wiley & Sons, LTD, 2000.

[3] T. R. Henderson, "Networking over next-generation satellite systems," in *Electrical engineering and computer sciences*: University of California at Berkeley, 1999.

[4] A. Dissanayake, J. Allnutt, and F. Haidara, "A prediction model that combines rain attenuation and other propagation impairments along earth-satellite paths.," *IEEE Trans. Antennas Propagat.*, vol. 45, pp. 1546-1557, 1997.

[5] L. J. Ippolito and T. A. Russell, "Propagation considerations for emerging satellite communications applications," *Proceedings of IEEE*, vol. 81, pp. 923-929, 1993.

[6] W. L. Larson and J. R. Wertz, *Space mission analysis and design*. Torrance, CA: Microcosm, Inc, 1992.

[7] ITU-R, "Allowable noise power in the hypothetical reference circuit for frequency-division multiplex telephony in the fixed-satellite service," S.353-8, 1994.

[8] ITU-R, "Radio-frequency channel arrangement for digital fixed wireless systems operating in the frequency band 406.1-450 MHz," F. 1567, 2002.

[9] ITU-R, "Allowable bit error ratios at the output of the hypothetical reference digital path for systems in the fixed-satellite service using pulse-code modulation for telephony.," S.522-5, 1994.

[10] ITU-R, "Allowable error performance for a hypothetical reference digital path in the fixed-satellite service operating below 15 GHz when forming part of an international connection in an integrated services digital network," S. 614-3, 1994.

[11] B. G. Evans, *Satellite Communicaton Systems*. London: IEE, 1999.

[12] I. E. Otung, "Prediction of troposphereic amplitude scintillation on a satellite link.," *IEEE Trans. Antennas Propagat.*, vol. 44, pp. 1600-1608, 1996.

[13] ITU-R, "Ionospheric propagation data and prediction methods required for the design of satellite services and systems," Rec. P 531-4.

[14] ITU-R, "Propagation data and prediction methods required for the design of Earth-space telecommunications systems," Rec. P 618-7.

[15] L. Castanet, J. Lemorton, and M. Bousquet, "Fade mitigation techniques for new SatCom services at Ku-band and above: a review," COST 255, 1998.

[16] OPEX, "Second workshop of OLYMPUS propagation experiments: Volume 1: Reference book on attenuation measurement and prediction," Noordwijk November 1994.

[17] F. Davarian, D. Rogers, and R. Crane, "Special issue on: Ka-band propagation effects on earth-satellite links," *Proceeding of The IEEE*, vol. 85, pp. 805-1024, 1997.

Chapter 2

SCINTILLATION AND ITS IMPACTS ON COMMUNICATION SYSTEMS

The random property of scintillation is initiated by the randomness in the propagation medium, which causes rapid fading as well as enhancement of the transmitted signal. This chapter describes the origin of scintillation, its dynamic properties and the most commonly used descriptors. The impacts of scintillation on communication systems are also examined.

2.1 Origin of Scintillation Effect

For satellite communications utilizing frequencies above 10 GHz, signal-level variations caused by the troposphere is a significant problem in radio-wave transmission [1]. The impairments to propagation result from several natural factors. Atmospheric water, which will cause considerable variations in the degree of attenuation and depolarisation experienced, depends on the type and intensity of precipitation. Fluctuations in refractive index due to turbulence, depends on temperature, pressure and moisture content variation as a function of position and time. Stratified variation of refractive index with height may cause ray bending and multi-path effects.

The term amplitude scintillation refers to those fluctuations about the mean level of received signal power, which occur continuously to varying degrees. Other amplitude variations, such as slowing-varying gross fades due to rainfall (and characterised by a reduction in mean signal level), and asymmetrical enhancement

and deep fades due to multi-path effects are occasionally also present. Scintillation becomes especially important in system planning for system with low availability, low margin and/or operating at low elevation angles. For example, downlink fade margins proposed for the Next-generation LEO System (NeLS) by the Japanese researchers are 9.6 dB for Ka band and 9.8 dB for V band using antennas of 2.6 m and 1.3 m in diameter respectively [2].

The path between the Earth and a satellite is referred to as an Earth-space slant-path. The elevation angles are obviously higher in general than those for terrestrial paths. The path medium generally has a layered structure, which includes the planetary boundary layer and free atmosphere. Several tropospehric phenomena, such as rain, cloud and turbulence, will disturb the stable layered structure and causes irregularities, resulting in many air parcels with different refractive index (Meteorologists often use the term air parcel when examining to a small volume of air having uniform physical properties). This turbulent medium acts like a multitude of small lenses, focusing and de-focusing the beam and results in a signal that has random phase variation in its wave front. (A signal emitted by a transmitter travelling to a receiver can normally be regarded, in the absence of such effects, as a plane wave.)

The propagating signal experiences refraction, diffraction and (to a lesser extent) absorption effects from these small parcels. The signal amplitude at the receiving antenna can be thought of as the vector sum of many multi-path components. The signal arriving at the receiver via each path will have a different phase (due to different path lengths) and amplitude. Destructive interference will give rise to fading and constructive interference will give rise to enhancement. The wave will therefore exhibit random fluctuations in amplitude and phase both across the receiver aperture (spatial structure) and in time. (The temporal scale of the fluctuation is a few seconds to tens of second and it is this characteristic spectral

band, rather than the physical origin of the variations, that is typically used to define scintillation.) Signal fluctuation originating in the troposphere is referred as tropospheric scintillation.

The irregular air parcels resulting from tropospheric turbulence may have a wide range of dimensions from much smaller than the Fresnel length for the transmitted signal to much larger. When parcel sizes are large enough, geometric optics (GO) theory can be applied. GO describes propagation in media that change gradually with position and the field is represented by signals that travel along ray paths connecting the transmitter and receiver [3]. If parcel sizes are not large with respect to the Fresnel length then diffraction will be significant. These two mechanisms will have different effects on signal, often described in terms of the following three phenomena.

2.1.1 Fast Fluctuation Of Phase

Spatial variation in dielectric constant causes the signal velocity to vary. This will make the phase of an electromagnetic signal varies with time. Phase fluctuations depend primarily on the largest eddies and diffraction effects can be ignored. Geometrical optics provides a good description for the phase fluctuations imposed by random media.

2.1.2 Fast Fluctuation Of Angle-Of-Arrival

Fluctuations of the dielectric constant along the nominal trajectory also cause the ray path to wander. The integrated effect of many small refractive bendings produces angular errors in the tangent vector relative to the nominal ray. It is this effect at optical frequencies that sets the threshold for astronomical seeing with ground-based telescope. It has been found that the angular fluctuations are proportional to lateral gradients of the dielectric variations integrated along the nominal ray path [4]. For horizontal terrestrial links, where receivers are relatively

close to each other, the measured wave-front tilt has been used to quantify angle-of-arrival fluctuations [5], and the angular variance is found to be proportional with the third moment of the refractive index spectrum for plane wave. The aperture smoothing effect of receiving antennas suppresses the contributions of eddies smaller than the receiver. For optical astronomical signals, where the sources are distant and the arriving signal can be described as a plane wave, eddies in the atmosphere that are large relative to the aperture cause quivering of the received image. The angle-of-arrival variance for astronomical sources has been found dependent on the integrated profile of C_n^2 [3].

2.1.3 Fast Fluctuation Of Amplitude

Amplitude scintillation refers to deviations in signal level from the mean value of received power. It is due to the random 'bunching' and 'diverging' of energy-bearing rays, and therefore depend on the smallest eddies for which diffraction effects play a dominant role.

2.2 Descriptors Of Amplitude Scintillation

The medium in which a wave travels can be classified as being either deterministic or random. For many natural media as experienced by slant-path links, they are randomly varying in time and space. Waves passing through such medium will finally inherit this arbitrariness exhibiting varying amplitude and phase. These signals become random variables and must be described in terms of probability densities and statistical averages. The most common descriptor for scintillation is scintillation intensity, which is the variance of the log-amplitude of received signal.

For weak amplitude fluctuations, the Rytov approximation can be used to describe solutions of Maxwell's equations. The waveform can be written as

equation (2.1), its components' amplitude E and phase S are given in equation (2.2) and (2.3):

$$U = \exp(\psi) = U_0 \cdot U_1 = e^{\psi_0 + \psi_1} \quad (2.1)$$

$$U(r) = E(r)\exp(iS(r)) \quad (2.2)$$

$$U_0(r) = E_0(r)\exp(iS_0(r)) \quad (2.3)$$

$$\psi_1 = \chi + iS_1 = \ln(E/E_0) + i(S - S_0) \quad (2.4)$$

The real part of ψ_1 denoted by χ represents the fluctuation of the logarithm of the amplitude and is called log-amplitude fluctuation; the imaginary part denoted by S_1 is the phase fluctuation.

2.2.1 Log-amplitude Of Scintillation χ

The fluctuations in amplitude of the received signal are generally expressed in terms of the variable χ,

$$\chi = \ln\left(1 + \Delta E / \overline{E}\right) \quad (2.5)$$

Where ΔE and $\overline{E}$ are the zero-mean amplitude fluctuations and the mean amplitude respectively (both in Volts); χ is expressed in Nepers (Np). Equation (2.5) implies that χ has to be associated with a period of time, during which the mean amplitude is defined. Scintillation log-amplitude can be calculated by subtracting a moving-averaged (i.e. low-pass filtered) signal from the total signal. More details can be found in [6].

2.2.2 Scintillation Variance σ_χ^2

The scintillation variance σ_χ^2 (measured in dB^2) is the variance of the log-amplitude, χ. The standard deviation σ_χ is often referred as scintillation intensity. σ_χ is given by

$$\sigma_\chi = \sqrt{\frac{1}{N-1}\sum_{i=0}^{N-1}(\chi_i - \overline{\chi})^2} \qquad (2.6)$$

Scintillation intensity is the most commonly used scintillation descriptor, although it is only of indirect interest to the satellite communication system designer. The importance of this quantity has two origins. The first arose from the hypothesis that the signal amplitude fluctuations could be reasonably modelled by a Gaussian distribution based on their similarity on central tendency around a mean level. The Gaussian distribution is completely characterised by a variance and a mean level. (Scintillation was believed to be non-absorption effect at the time). The second relates to the fact that, mathematically, the amplitude variance is equivalent to the spatial auto-correlation of χ in magnitude for a given location. The latter is closely related to the structure function and spectrum density of refractive index, which have been previously developed by well-established theories in the area of wave propagation in random medium [7] and [8].

The suitability/validity of the Gaussian distribution to describe scintillation is investigated in Chapter 4. Nevertheless, σ_χ^2 is a useful quantity that bridges physical process models and system parameters.

σ_χ^2 has been calculated in the literature in two ways. The first is by dividing the time series into many equal intervals, typically several minutes in length [9]; The second is by using a sliding window (again typically several minutes long) in

order to produce one σ_χ^2 sample corresponding to each original time series sample (neglecting samples lost at either end of the time series) and accounting for its possible time-variability [10]. The first method is preferred in the analysis of this project because for samples being separated into intervals, each interval can be considered independent.

It is noted that the long-term mean scintillation intensity/variance (the average of σ_χ^2 over a period of one month or longer) is an important predictor for scintillation. It has been widely used by most statistical prediction of scintillation [11] [12] [13] [14] and [15].

2.2.3 *Log-variance of Scintillation* $\ln(\sigma_\chi^2)$

Probability density function of scintillation variance σ_χ^2 was proposed to be a log-normal distribution [16], [14] and [17]. Referring to these proposals, it is convenient to define log-variance of scintillation as $\ln(\sigma_\chi^2)$, where χ expressed in Nepers (Np).

2.3 Impacts Of Scintillation On Communication Systems

The impact of the tropospheric scintillation on communications system is gaining renewed interest due to the introduction of mobile and fixed digital telecommunications in the K-band (18-27 GHz) based on very small aperture terminals (VSAT), clusters of low-elevation orbit (LEO) satellites and wireless multipoint distribution services (MDS) with low link margins for high availability [18].

Amplitude scintillation causes enhancement of the received amplitude as well as fading to occur on a time scale of a few seconds to several tens of seconds. The amplitude fluctuations are especially large for system operating at low elevations,

where the peak-to-peak amplitudes variations exceeding 2 dB are found. It is therefore necessary for the system designer to allow for the effect of scintillation in link planning. Amplitude scintillation affects the performance of a satellite communication link in a number of ways as described in the following sections.

2.3.1 Reduction Of System Margin

Signal fading causes a net reduction of the signal for a given percentage of time, which affects performance, link availability and resistance to interference. For links with modest fade margins, this contributes more to degraded performance than to link unavailability. For low margin systems, this effect on link outage can be more severe.

Large enhancement can also affect system performance since the operating point of the receiver is selected to avoid saturation. Signal enhancement would consequently reduce the dynamic range available for fading compensation. Increased signal amplitude may also introduce extra inter-modulation interference.

2.3.2 Impacts on Uplink Power Control Systems

The rate at which fluctuations occur is as important as the magnitudes of fluctuations [19]. The rapidity with which scintillation fades occur will have an impact on uplink power control (UPPC) systems, depending on the length of time constant used in the particular system. In order to be compensated for scintillation by power control, the control system must have a sufficiently fast response.

2.3.3 Antenna Tracking Systems

Temporal variations in bending can cause apparent signal attenuation in systems using antennas without auto-pointing capability. If the signal fluctuation rate

exceeds the inverse of the time constant of the tracking system, it is not possible to complete a search for a stable peak signal level. In a step-track system, continual searching can harm tracking mechanisms [20]. These system degradations would be particularly significant for receivers operating at low elevation angels and under unfavourable climatic conditions; and would be more severe for scintillation events occurring in association with moderate attenuation due to thick clouds and rain [21] and [14]. Assuming if the angle-of-arrival fluctuation contributing to scintillation occurs principally at the lower frequency of the scintillation spectrum, then antenna tracking of these fluctuation should be possible at least in principle.

2.3.4 Effects of Scintillation Fade Duration

For many types of service it is necessary to know not only the total fade time but also the distribution of the durations of the individual fades. Scintillation fades duration is useful, therefore, for predicting link quality performance measures such as the percentage of degraded minutes and error-free seconds [22] and [23]. The distribution of scintillation fade duration and inter-fade intervals are also required in the design of countermeasures using digital signal processing schemes [24].

Most importantly, knowledge of probability density function (PDF) of the scintillation amplitude together with considerations for other propagation impairments is essential to obtain the overall satellite link availability. The scintillation fade depth for a given time percentage is therefore a common goal of scintillation prediction models [11]. The following chapters are centrally concerned about the statistical features and related aspects of scintillation with a view to the design of an improved prediction model.

2.4 References:

[1] P. A. Watson and Y. F. Hu, "Prediction of attenuation on satellite-earth links for systems operating with low fade margins.," *IEE Proc. Microwave Antenas and Propgation.*, vol. 141, pp. 467-472, 1994.

[2] R. Suzuki, K. Sakurai, I. Nishiyama, and Y. Yasuda, "Key technology developments for Next-generation LEO systems," presented at 4th European workshop on mobile/personal satcoms (EMPS2000), 2000.

[3] A. D. Wheelon, *Electromagnetic scintillation - 1. Geometrical optics*: Cambridge university press, 2001.

[4] S. Chandrasekhar, "A statistical basis for the theory of stellar scintillation," *Monthly notices of the royal astronomical society*, vol. 112, pp. 475-483, 1952.

[5] C. B. Hogge and R. R. Butts, "Frequency spectra for the geometric representation of wave-front distortions due to atmospheric turbulence," *IEEE Trans. Antennas Propagat.*, vol. AP-24, pp. 144-145, 1976.

[6] Y. Karasawa, K. Yasukawa, and M. Yamada, "Tropospheric scintillation in the 14/11 GHz bands on earth-space paths with low elevation angles," *IEEE Trans. Antennas Propagat.*, vol. 36, pp. 563-569, 1988.

[7] V. I. Tatarskii, *Wave propagation in a turbulent medium.* New York: McGraw-hill, 1961.

[8] A. Ishimaru, *Wave propagation and scattering in random media.* New York: Academic, 1978.

[9] I. E. Otung, M. O. Al-Nuaimi, and B. G. Evans, "Extracting scintillation from satellite beacon propagation data," *Letters, IEEE Trans. Antennas Propagat.*, vol. 46, pp. 1580-1581, 1998.

[10] OPEX, "Second workshop of OLYMPUS propagation experiments: Volume 1: Reference book on attenuation measurement and prediction," Noordwijk November 1994.

[11] ITU-R, "Propagation data and prediction methods required for the design of Earth-space telecommunications systems," Rec. P 618-7, 2001.

[12] Y. Karasawa, M. Yamada, and J. Allnutt, "A new prediction method for tropospheric scintillation on earth-space paths.," *IEEE Trans. Antennas Propagat.*, vol. 36, pp. 1608-1614, 1988.

[13] I. E. Otung, "Prediction of tropospheric amplitude scintillation on a satellite link.," *IEEE Trans. Antennas Propagat.*, vol. 44, pp. 1600-1608, 1996.

[14] T. J. Moulsley and E. Vilar, "Experimental and theoretical statistics of microwave amplitude scintillations on satellite down-links," *IEEE Trans. Antennas Propagat.*, vol. 30, pp. 1099-1106, 1982.

[15] H. Vasseur, "Prediction of tropospheric scintillation on satellite links from radiosonde data.," *IEEE Trans. Antennas Propagat.*, vol. 47, pp. 293-301, 1999.

[16] T. J. Moulsley, J. Haddon, P. Lo, and E. Vilar, "Measurement and modelling of the probability density function of amplitude scintillations on an X-band satellite down-link.," *Electron. Lett.*, vol. 17, pp. 625-626, 1981.

[17] G. Ortgies, "Probability density function of amplitude scintillations," *Electron. Lett.*, vol. 21, pp. 141-142, 1985.

[18] F. S. Marzano and G. d'Auria, "Model-based prediction of amplitude scintillation variance due to clear-air tropospheric turbulence on Earth-Satellite microwave links.," *IEEE Trans. Antennas Propagat.*, vol. 46, pp. 1506-1518, 1998.

[19] O. P. Banjo and E. Vilar, "Measurement and modeling of amplitude scintillations on low-elevation earth-space paths and impact on communication systems.," *IEEE Trans. Antennas Propagat.*, vol. COM 34, pp. 774-780, 1986.

[20] D. V. Rogers, L. J. Ippolito, and F. Davarian, "System requirements for Ka-band Earth-Satellite propagation data.," *Proceeding of The IEEE*, vol. 85, pp. 810-820, 1997.

[21] D. C. Cox, H. W. Arnold, and H. H. Hoffman, "Observations of cloud-produced amplitude scintillation on 19 and 28 GHz earth-space paths.," presented at 2nd Int. Conf on Anten & Propag, 1981.

[22] ITU-R, "Allowable error performance for a hypothetical reference digital path in the fixed-satellite service operating below 15 GHz when forming part of an international connection in an integrated services digital network," S. 614-3, 1994.

[23] R. W. Mclintock and B. N. Kearsey, "Error performance objectives for digital networks," *Brit Telecommun. Eng.*, vol. 3, pp. 92-98, 1984.

[24] I. E. Otung, "Scintillation fade and enhancement duration on a 20GHz satellite downlink," *Electron. Lett.*, vol. 32, pp. 1319-1321, 1996.

Chapter 3

MEASUREMENT DATA

The measurement databases that have been used for this scintillation study are recorded from four different sites. They are the receiver measurement database of ITALSAT satellite beacon for scintillation analysis; the GPS measurement database for path-integrated water vapour estimation; the radiosonde measurement database and the ground hourly report database of weather conditions. Although the ideal case would be for all the measurement sites to be co-located, there are some practical constraints that have to be considered. The choice of radiosonde and weather report sites is ccarefully made in order to achieve minimum distance from both GPS and ITALSAT sites among all the available meteorological stations to which we were granted access.

3.1 Geographic Summary of Measurement Sites

Figure 3. 1 Map of measurements sites

The locations of measurement sites are summarized in Figure 3. 1 with Sparsholt, Chilbolton and Middle-wallop observatory position in Hampshire while Larkhill observatory positions in Wiltshire, southern England. Sparsholt observatory is where the beacon receivers are located. Sparsholt is 8 km away from Chilbolton, where the GPS receiver is located. Middle-wallop, where hourly weather reports are available, is 15 km from Sparsholt. Larkhill, where radiosondes are launched up to four times daily, is 31 km from Sparsholt. Their accurate locations together with observatory altitude are given in Table 3. 1.

Site Name	Latitude (°)	Longitude (°)	Altitude (m)
Sparsholt	51.083 N	1.383 W	118.5
Chilbolton	51.168 N	1.438 W	84
Middle-wallop	51.150 N	1.567 W	90
Larkhill	51.20 N	1.80 W	132

Table 3. 1 Summary of sites location

3.2 GPS Measurements

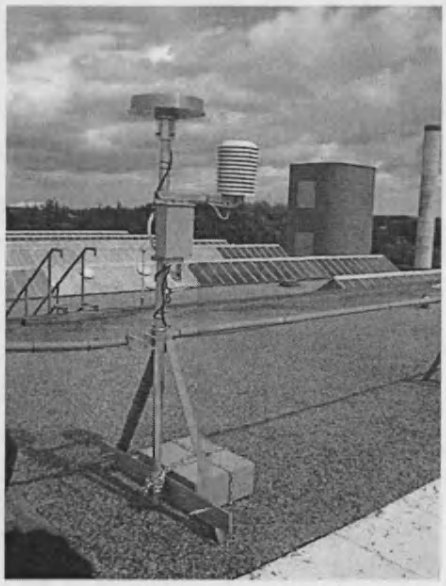

Figure 3. 2 GPS receiver and attached meteorological sensors

A picture of a GPS receiver and attached meteorological sensors is shown in Figure 3. 2. The same type of equipment has been set up by the University of Bath at Chilbolton observatory, RAL, providing us with measurements available for use over the period from July 1999 to Jan 2001.

Ashtech Continuous Geodetic Reference Station (CGRS) and choke ring antenna are used in the design of our GPS receiver. Choke ring antennas have been chosen because of their advantage in minimizing the multi-path problem by inclusion of GPS data as low as 5 degree in elevation.

Vaisala PTU200 measures atmospheric pressure, temperature and relative humidity and is connected directly to Ashtech CGRS. CGRS requests and logs meteorological data every 30 seconds – pressure accuracy is +/- 0.2 hPa (ZHD +/- 0.2 mm), temperature accuracy is +/- 0.3°C (IPWV +/- ~0.03 mm)

3.3 Radiosonde Measurements

Radiosonde measurements at Larkhill station for period 1999-2001 are available from UK Met Office or the British Atmospheric Data Centre website at http://www.badc.nerc.ac.uk.

The RS80 radiosonde, manufactured by the Finnish company Vaisala, has been used by the UK Met Office to take the measurements used in this work. The schematic diagram of RS80 has been shown in Figure 3. 3. Radiosonde measurements data comprise of vertical profiles of temperature, dew-point temperature, wind speed and wind direction at standard and significant pressure levels and apparatus are required for radiosonde ascents.

The standard pressure levels are 1000, 925, 850, 700, 500, 400, 300, 250, 200, 150, 100, 70, 50, 30, 20 and 10 mb. Significant pressure levels are calculated according to the Met Office criteria and constitute levels at which significant events occur in

the profile, for example, turning points. The apparatus rises through the atmosphere at approximately 5 m/s. The instrument takes measurements at approximately 1.3 seconds intervals during the ascent and up to the height of 20 to 30 km. Standard practice states that all measurements in the profile are attributed to the nominal hour of the ascent, up to four times daily at the synoptic hours of 00, 06, 12, 18 GMT.

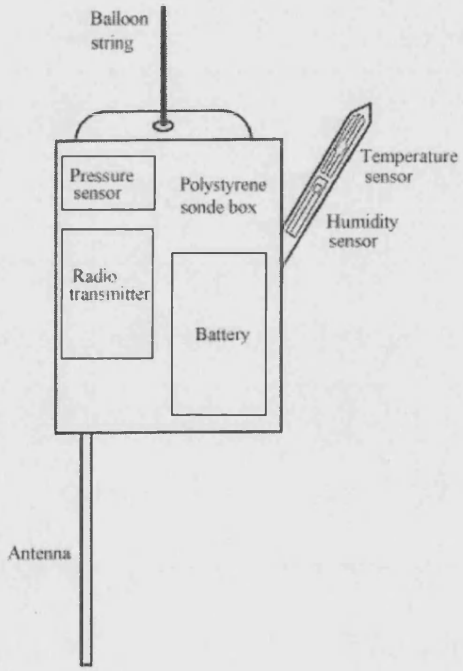

Figure 3. 3 Schematic diagram of the RS80

It takes approximately an hour for the sonde balloon to reach 100 mb. The flight pathway of the instrument varies according to the strength of the wind and thus may not ascend strictly vertically. When analysing weather systems on the synoptic scale, the profiles can be assumed to be vertical without significant error [1].

3.4 Synoptic Report Data

The concurrent synoptic reports of year 1999-2001 are also readily available from UK Met Office's land surface observation database. Middle-wallop station has been identified as the closest station from Sparsholt and Chilbolton. The distance between Middle-wallop and Sparsholt is about 15 km. The synoptic measurements include hourly-measured wind speed, wind direction, temperature, pressure, relative humidity, cloud type and cloud coverage.

Measurements of total cloud amount, low/medium/high level cloud type and amount are reported. Cloud amount has been measured in okta, which means eighth of sky is covered by cloud. Most of the observations of cloud amount and type are through manual observations; some measurements of cloud amount and height at different layers are with the help of Laser Cloud Base Recorder (LCBR). A complete description of cloud type can be found in Appendix B. Amount and occurrence of various cloud type can be obtained though statistical process for a certain period of time.

Comparison has been made between two months in winter and summer, January 2000 and June 2000. Big difference in the total cloud coverage amount has not been found between these two months. Much attention has been given to the type and amount of lower level cloud, such as stratocumulus, stratus, stratocumulus, cumulus and cumulonimbus. This is mainly because these types of cloud normally appear at about 2000 meter above the earth's surface, with temperature likely to be found at base level range from +15 to –5 °C, in which water exists in the form of water vapour and small droplets. Clouds that have great vertical development, such as cumulus and cumulonimbus have apparently bigger coverage amount in June, 2000 than in January, 2000; These clouds are normally believed to be associated with unstable air. On the other hand, increase in the amount of stratocumulus cloud has been found in January than in June;

however, no significant difference has been found in stratocumulus and stratus for the compared months.

3.5 ITALSAT Measurements

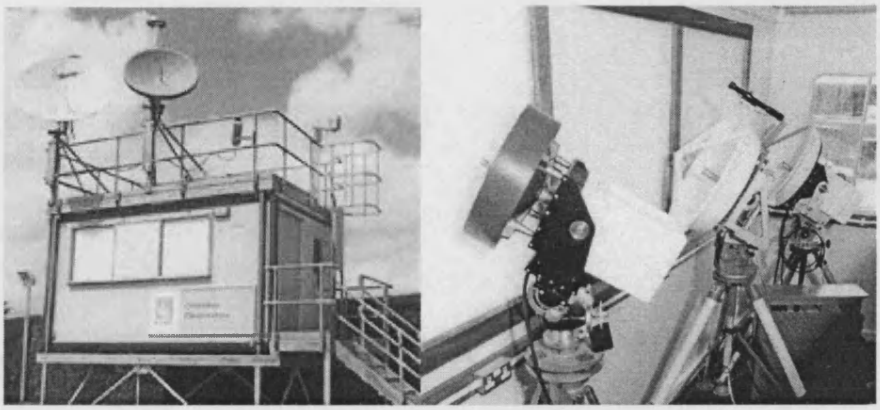

Figure 3. 4 Beacon measurement receivers

The Radio Communications Research Unit (RCRU) of the CLRC Rutherford Appleton Laboratory operates a receiving ground station to monitor and record ITALSAT F1 beacon signals at Sparsholt in Hampshire. Figure 3. 4 displays the set-up of the satellite ground station. The picture on the left shows the 20 GHz beacon receiver equipped on top of the main measurement room, combined with meteorological sensors measuring surface air temperature, pressure and humidity. The picture on the right shows equipments operating in a laboratory environment with dishes viewing the satellite signal through a polystyrene window. From left to right they are: 51 GHz radiometer; 39.1, 39.6 & 40.1 GHz beacon receiver and 49.5 GHz beacon receiver.

3.5.1 Original Measurements

The original experimental source used for this study of amplitude scintillations is mainly from the propagation beacon of ITALSAT F1 received at Sparsholt earth station in Hampshire UK. ITALSAT F1 has been placed at 13.2° east in geo-

stationary orbit in January 1991 by the Italian Space Agency, who was carrying a propagation payload with 3 beacon transmitters operating at 18.7, 39.6 and 49.5 GHz. The elevation angle from Sparsholt looking at ITALSAT F1 is 29.9°, and azimuth angle of the receiver is about 162°. Details of the experiment system design and operation can be found in paper [2] and [3], the configuration of the experiments is indicated in Table 3. 2.

Frequency	Ant Diameter	Rx Beamwidth	Ant. Efficiency	Polarisation
18.7GHz	122 cm	0.9 degree	70 %	V
39.6GHz	61 cm	E=1.1, H=0.86	70 %	C (RHCP)
49.5GHz	61 cm	E=1.2, H =1.1	70 %	V

Table 3. 2 Receiving antenna parameters

Sparsholt station started collecting measurements of the Ka and V-Band beacons of ITALSAT F1 in April 1994. In August 1999, the 18.7 GHz receiver was switched to monitor the beacon on ITALSAT F2. The azimuth angle of the receiver for F2 is about 158°. At the end of January 2001, the ITALSAT experiment concluded when the satellite was de-commissioned.

It is noted that, due to a number of operation years after its first launch, the control of F1 and F2 satellite station keeping has been reduced in order to preserve fuel supplies. Operation of station keeping is to perform orbit correction and relevant spacecraft attitude control. Throughout the period of our observations (1999-2001) north-south tracking of the satellite with the beacon receivers has maintained about 20 dB of dynamic range. The lack of station keeping will cause problems such as large background diurnal variations of received amplitude. However, this is not deemed to be important in the context of scintillation study because the variations are relatively slow compared with scintillation fluctuations and can be removed with careful circumspections.

As is shown in Figure 3. 4, the green-coloured 20 GHz receiver is situated at the top of the measurement unit roof. The 40 & 50 GHz receivers locate in a laboratory environment, with dishes viewing the satellite signal through a polystyrene window. There is about a 3 meter vertical distance between the two horizontal planes, where the centre of 20 GHz antenna and 40 & 50 GHz antenna lie. The indoor environment design for higher frequency receivers is attempted to achieve an improved performance with respect to stability and to avoid corruption of genuine propagation effects through raindrops on the windows.

580 days of data are recorded between July 1999 and Jan 2001 (19 months). The recorded data is sampled at 1-second interval period, together with concurrent and co-located ground-based measurements of ancillary meteorological variables including temperature, pressure and relative humidity. Meteorological measurements are also sampled at 1 Hz.

3.5.2 Data Pre-processing

Pre-processing of the data includes separation of valid measurements from invalid recording due to satellite movements, loss-of-lock of satellite antennas and other system failure. These factors usually cause error data during a small portion of time within a day or occasionally cause missing data of few days. Slow system drifts were removed by subtracting from the original data by applying a 24-hour running average, which is equivalent to applying a 12×10^{-6} Hz high pass filter.

To get rid of the invalid recordings due to loss-of-lock and other system failure, the following two-stage processing is used to realize the pre-processing of the data. (A receiver loss-of-lock flag was presented in the data and data was discarded when this flag was set. Loss-of-lock occasionally occurs when this flag was either absent or not set. Thus requiring loss-of-lock detection algorithm to be

implemented.) At the first stage, by visual inspection through the total 580 days, gaps and specious samples are identified as well as typical features of these spurious data. Three main types of spurious data are distinguished and analysed. At the second stage, based on the identified spurious features, Matlab routines have been specially designed to automatically detect faulty data, discard them and save the valid data as a new database. Judgements of the effectiveness of these routines were made on the basis that the routine-sorted data should have comparable degree of accuracy as visually inspected data. At the same time, detection routines should try to minimise any statistical biases. At the end of running the inspection programme, valid new database is ready to use for separation scintillation from other propagation impairments such as rain attenuation.

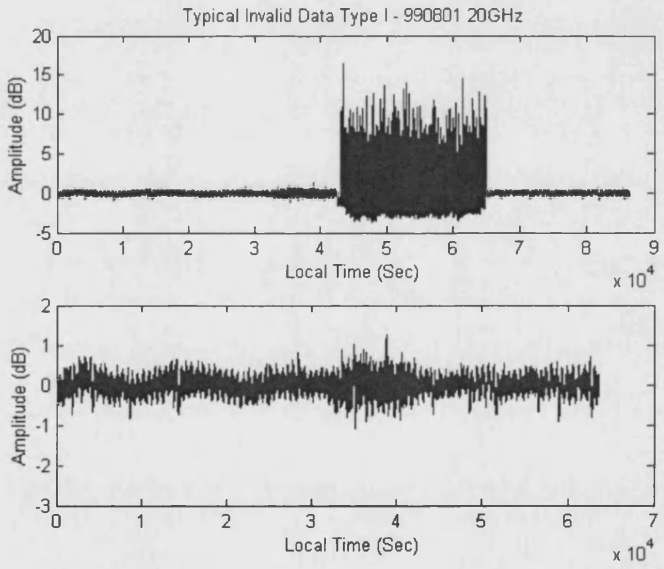

Figure 3. 5 Typical invalid data type I and after pre-processing

Three types of typical invalid data – defined as type I, type II and type III, are shown in Figure 3. 5, Figure 3. 6 and Figure 3. 7 respectively, compared with corrected/selected data after the pre-processing routines. The listed types of

invalid data or their combinations nearly contributed 95 percent of the total invalid data that has been found during the considered period. All of the listed types of invalid data have effects on measured RMS fluctuation of the signal and therefore need to be removed. The displayed output results from inspection routines suggest that the pre-processing can be considered as highly effective.

The above process leads to the confidence that the observed scintillation dynamic and statistics properties from the pre-processed database are real indications of scintillation characteristics.

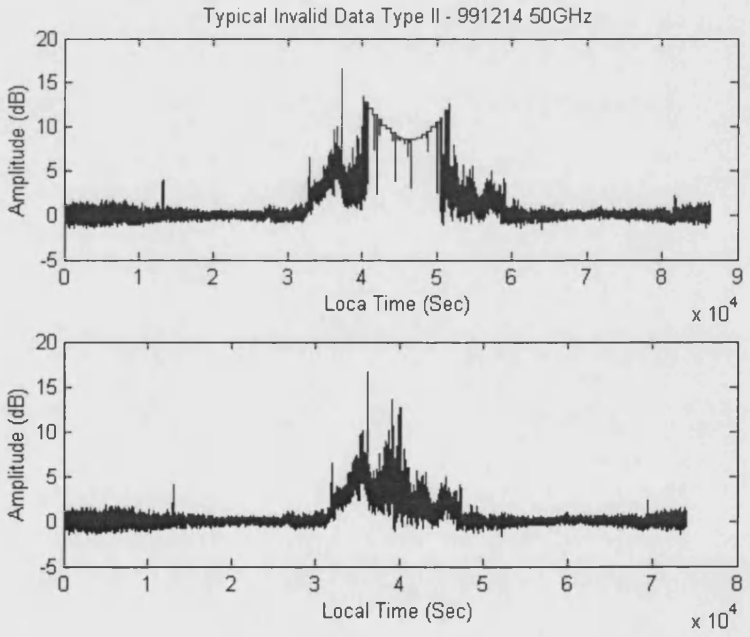

Figure 3. 6 Typical invalid data type II and after pre-processing

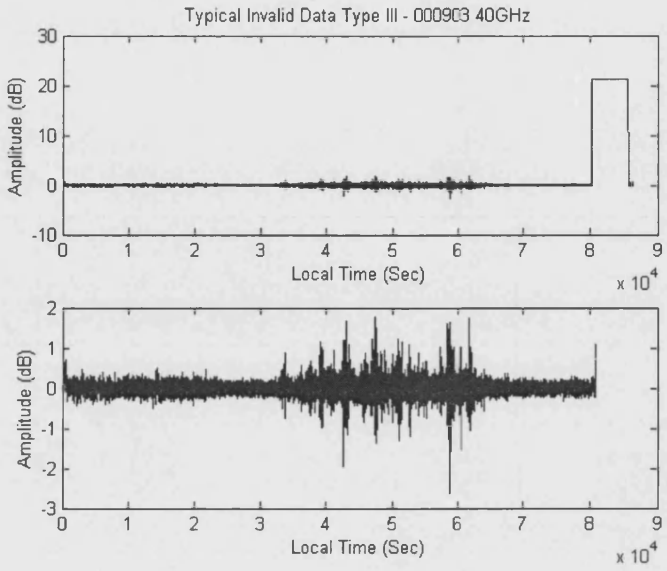

Figure 3. 7 Typical invalid data type III and after pre-processing

The pre-processed ITALSAT dataset has been further divided into two subsets: subset 1 (July 99 – Dec99) and subset 2 (Jan 00 – Jan 01) for the development and validation of new models presented in later chapters.

3.5.3 Validation of Meteorological Measurements

Meteorological sensors that used for temperature, pressure and relative humidity measurements are exposed in an outdoor environment, and subject to local interference. Concurrent recordings of these variables available from Sparsholt, Chilbolton and Middle-wallop provide useful information to validate these measurements.

All of these sources are providing ground recording of temperature, pressure and relative humidity. Recordings from meteorological sensors attached to the Sparsholt satellite station is referred to as Sparsholt (ITALSAT). Recordings of hourly weather reports from UK Met Office middle-wallop station, are referred to as Middle-wallop (SYNOP). Measurements of meteorological sensors

attachment to Sparsholt GPS receiver operated by University of Bath, are referred to as Sparsholt (GPS). And measurements of meteorological sensors attachment to Chilbolton GPS receiver operated by University of Bath, are referred to as Chilbolton (GPS). Their measurements periods are summarized in Table 3.3:

Data	Location	Measurement	Available
Sparsholt (ITALSAT)	Sparsholt	ITALSAT beacon	Jul99-Jan01
Sparsholt (GPS)	Sparsholt	GPS	Jun00-Jul00
Chilbolton (GPS)	Chilbolton	GPS	Jul99-Jan01
Middle-wallop (SYNOP)	Middle-wallop	SYNOP report	1999-2001

Table 3. 3 Summary of data used for meteorological measurements validation

The temperature sensor attached to the Sparsholt satellite station was reported to have outrage measurements during June 15 2000 - July 16 2000. Cautions upon measurements of co-located pressure and humidity sensors for the duration of the same period have also been taken. Comparisons have been made between variables at Sparsholt (ITALSAT) and available data from other locations. The results are presented in the following subsections:

3.5.3.1 Temperature

The three experiment sites have nearly equal altitudes above the mean sea level. The maximum distance between them is 15 km, which is from Middle-wallop to Sparsholt. This separation distances are short enough that the measurements sites should have identical climate over duration of a week or a month, and reasonably similar weather variation over duration of a day or a couple of days. Therefore, the measured meteorological variables are expected to have reasonably close and highly correlated values.

The monthly averaged values of temperature from Sparsholt (ITALSAT), Chilbolton (GPS) and Middle-wallop (SYNOP) are compared in Figure 3. 8.

Differences of up to 4 Celsius degrees between Sparsholt (ITALSAT) and temperature measurements at other locations were found for both June and July 2000.

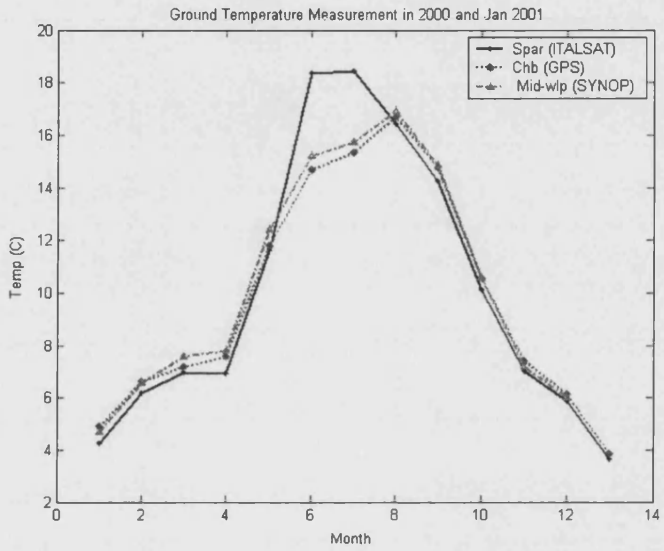

Figure 3. 8 Comparison of monthly averaged temperature at Sparsholt (ITALSAT), Chilbolton (GPS) and Middle-wallop (SYNOP) for year 2000

The temperature differences less than 1 Celsius degree or nearly identical measurements can be found for the rest of months in 2000. The big departure of measurement for June and July do no agree with the annual observed trend of temperature distribution among the three sites. Factors biased the monthly mean temperature of Sparsholt (ITALSAT) could be either because of small number of odd measurements with great deviation from the normal due to environmental incidence (certain undesired interference or human activity) within the month, or because of several continuous odd measurements due to equipment degrading performance. Further comparison of averaged values over shorter period is made for the above-mentioned two months. Scatter plot of daily averaged temperature

values from Sparsholt (ITALSAT) and Chilbolton (GPS) for June and July are shown in Figure 3. 9 and Figure 3. 10.

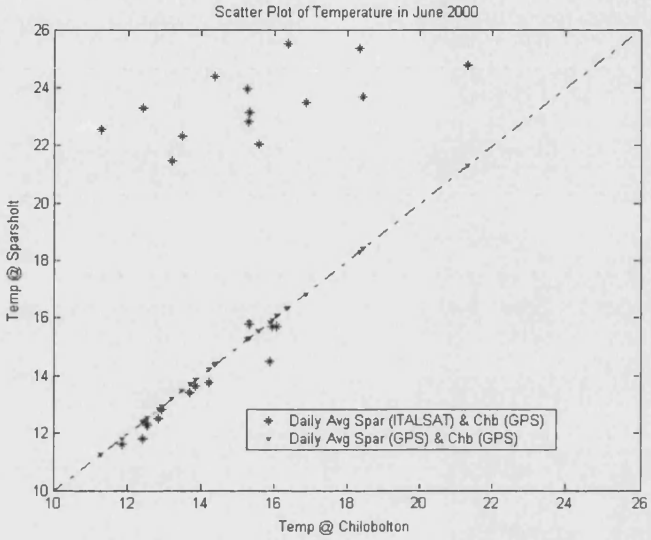

Figure 3. 9 Comparison of daily averaged temperature measurements at Sparsholt (ITALSAT) and Chilbolton (GPS) for June 2000

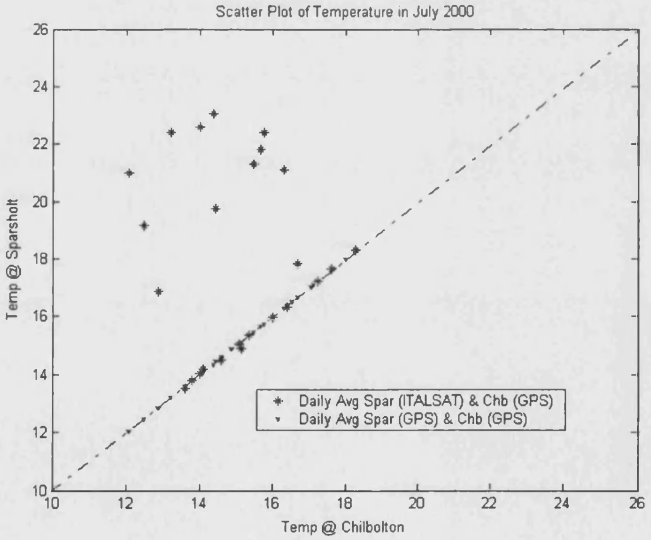

Figure 3. 10 Comparison of daily averaged temperature measurements at Sparsholt (ITALSAT) and Chilbolton (GPS) for July 2000

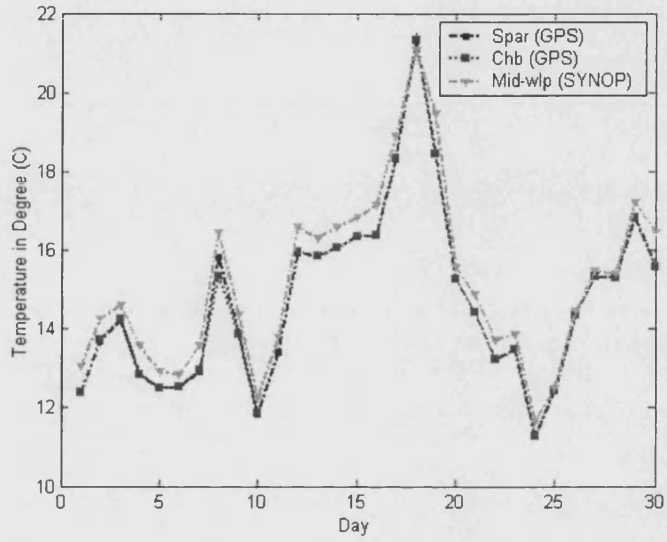

Figure 3. 11 Comparison of daily averaged temperature measurement at Sparsholt (GPS), Chilbolton (GPS) and Middle-wallop (SYNOP) for June 2000

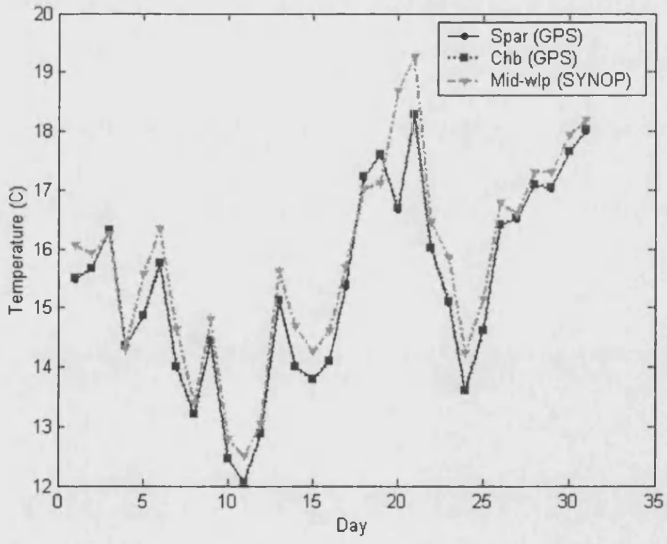

Figure 3. 12 Comparison of daily averaged temperature measurement at Sparsholt (GPS), Chilbolton (GPS) and Middle-wallop (SYNOP) for July 2000

To replace the invalid measurements with valid ones and reflect the real weather conditions as much as possible, solutions are sought by substituting the bad measurements with valid data obtained from available sources. For both of the problematic months, temperature measurements from Sparsholt (GPS) are available, which is the nearest alternative location from Sparsholt (ITALSAT). Daily averaged temperature has been compared and shown in Figure 3.11 and Figure 3.12.

If data points fall onto the straight dash-dotted line, two sites are giving equal measurements, when data points depart from the straight line, it suggests a difference between these measurements exist. Measurement deviation is directly related to the departure from the straight line. Considering the geographical separation of the two sites, a number of randomly distributed points centred around the straight line would be expected for valid measurements. Daily averaged temperature difference bigger than 8 degree celsius are not plausible, however. Such temperature differences are observed in several cases, and abnormal temperature measurements can thus be confirmed. Results suggest temperature measurements from Sparsholt (GPS) are valid substitute for Sparsholt (ITALSAT) for the two problematic months in 2000.

3.5.3.2 Relative Humidity

Parallel analyses have been performed on relative humidity measurements from Sparsholt (ITALSAT), as shown in Figure 3. 13 and Figure 3. 14. As humidity is a highly variable parameter both horizontally and vertically, some degree of difference may exist even on monthly averaged values; for daily scatter comparison, more loose points that deviate from the straight line are expected. Result shows fairly balanced symmetrical distributions on both side of the line are found for both months, with only one or two points of up to 20 units difference

from two sites, hence the relative humidity measurements at Sparsholt (ITALSAT) can be considered as valid.

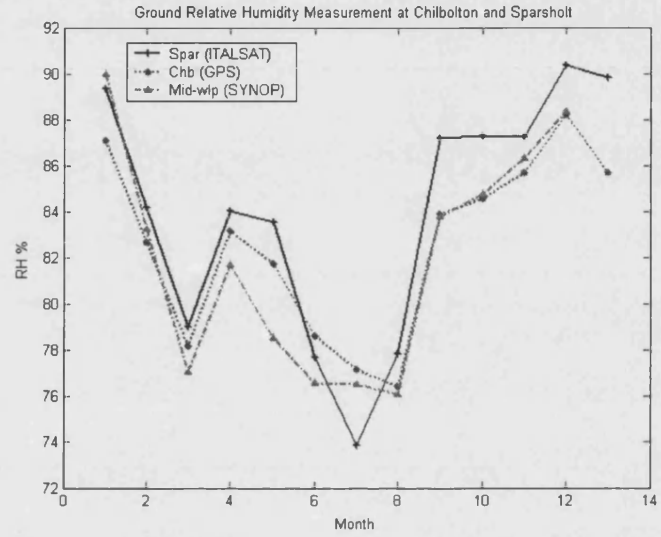

Figure 3. 13 Comparison of monthly averaged RH measurements at Sparsholt (ITALSAT), Chilbolton (GPS) and Middle Wallop (SYNOP) for year 2000

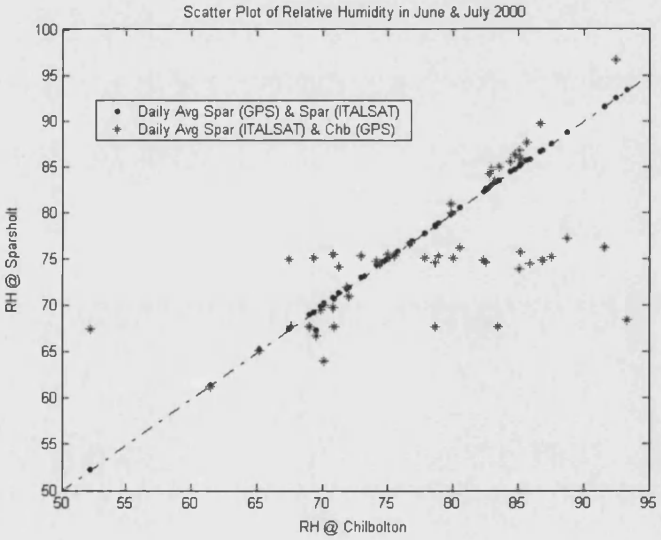

Figure 3. 14 Comparison of daily averaged RH measurements at Sparsholt (ITALSAT) and Chilboton (GPS) for June and July 2000

3.5.3.3 Pressure

Similar testing approaches have found very good agreement of monthly averaged pressure for Sparsholt (ITALSAT) and Chilbolton (GPS), suggesting Sparsholt (ITALSAT) pressure measurements are valid as shown in Figure 3. 15.

3.5.4 Temperature Measurements After Correction

After substituting the temperature measurements at Sparsholt (ITLASAT) by Sparsholt (GPS) for June and July 2000, the monthly average of newly corrected values are compared in Figure 3. 16.

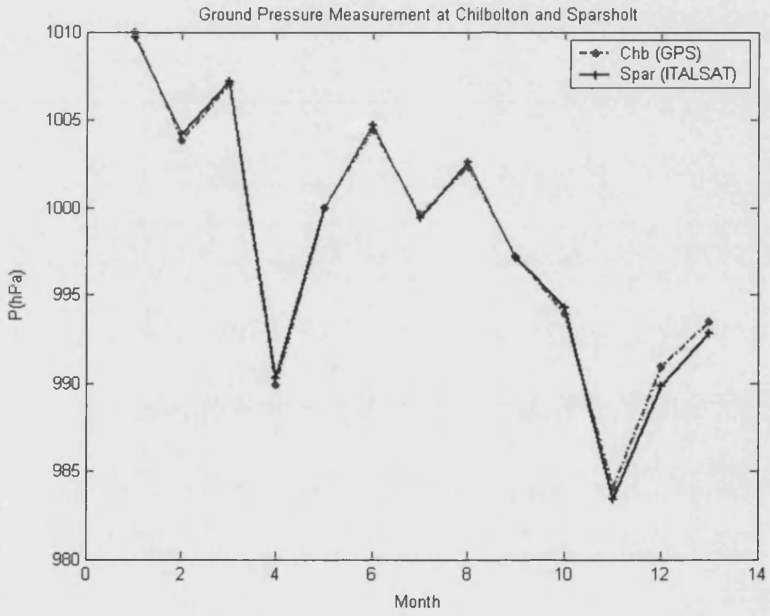

Figure 3. 15 Comparison of monthly averaged pressure measurements at Sparsholt (ITALSAT) and Chilbolton (GPS) for year 2000

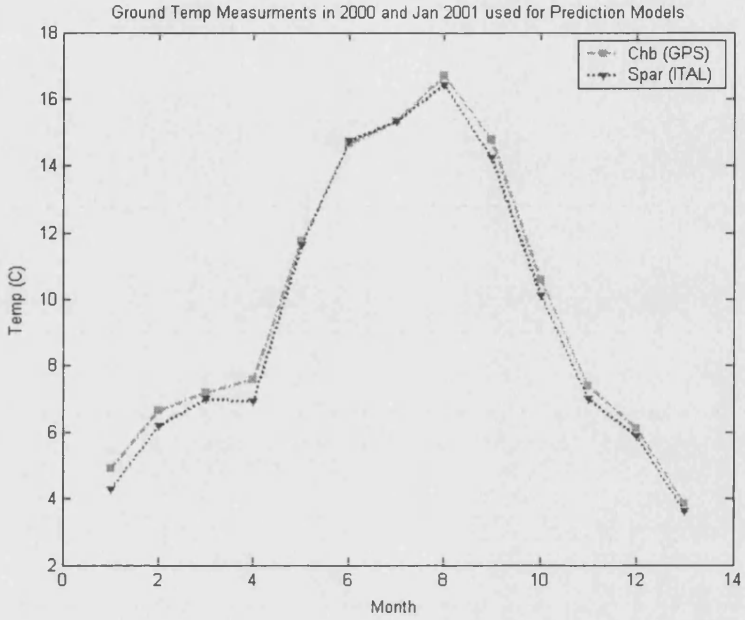

Figure 3. 16 Comparison of monthly averaged temperature measurements at Sparsholt (ITALSAT) after correction and Chilbolton (GPS) for year 2000

3.6 Summary

The surface measured pressure and relative humidity from Sparsholt (ITALSAT) for year 2000 have been validated using meteorological sensor recording from Chilbolton (GPS) and Middle-wallop (SYNOP). Temperature measurements of Sparsholt (ITALSAT) for June and July have been found untrue and these are replaced with measurements of Sparsholt (GPS) for the two months. The corrected temperature database can be used for further study of the relationship between scintillation and meteorological variables.

3.7 References:

[1] BADC Help File, "Radiosonde Data."

[2] J. M. Woodroffe, P. G. Davies, and J. R. Norbury, "Combined Olympus and ITALSAT propagation experiment in the UK," presented at Olympus Utilisation Conference, Seville, Spain, 1993.

[3] S. Ventouras, C. L. Wrench, and P. G. Davies, "Propagation measurements using ITALSAT beacons together with associated measurements of radar reflectivity from rain and clouds at 3 GHz and 35 GHz," presented at 10th Int. Conf. on Antennas and Propag., Edinburgh, U.K., 1997.

Chapter 4

MECHANISMS, CHARACTERISTICS AND EXTRACTION OF SCINTILLATION

It is desired to formulate a new scintillation prediction model as the goal of this work. For the design of such a model, considerations of system parameters and path geometry will be included in order to have wide applicability for different systems. In this chapter the most important few characteristics of tropospheric scintillation regarding to the above two aspects will be examined. Investigation will be made through both the physical theory of wave propagation in clear-air turbulence and experimental results, in the context of scintillation power spectra, probability distribution function and frequency dependence. The fundamental understanding of these dynamics and causes will also help to find solutions, such as FMTs, to counteract and minimize scintillation disadvantages.

4.1 Theoretical Explanation of Scintillation

There are two categories of random medium appearing in the troposphere that will affect propagation of radio wave, namely random scatterers and random continuum. Both media have refractive index that varies randomly in time and space, apart from the fact that the dielectric constant of random continuum is a continuous function of position and time; while that of random scatterers is discretely distributed. A common example of the first category is raindrops, whilst tropospheric turbulence belongs to the second category [1].

Scintillation has been observed to occur both during periods of rain [2] and dry weather [3], referred as wet scintillation and dry scintillation respectively. The utilization of 'dry scintillation' is supported here rather than 'clear-air scintillation'. Clear-air often implies that the effects of condensed water, such as rain and clouds, are ignored [4]. However, as far as scintillation is concerned, the presence of cloud will not be appropriately excluded, since some clouds are heavily involved in the production and manifestation of turbulence activities in the troposphere. Turbulence in clouds has been demonstrated linked with most of the significant scintillation events as observed by Cox, Arnold and Hoffman on satellite links [5].

In the absence of rain, fluctuations of the refractive index are principally responsible for the received amplitude fluctuations. In the presence of rain, various mechanisms are involved in the production of amplitude fluctuations, such as scattering of the wave by the raindrops and variation of rain rate and drop size distribution due to wind gusts. This is in addition to the turbulent mixing of air masses of various characteristics. Hence, scintillation characteristics will be discussed for dry scintillation and wet scintillation separately.

4.1.1 Dry Scintillation

In order to correctly evaluate dry scintillation, it is very essential to have the best characterisation of the propagation medium under this criterion. Under this category, a propagation medium that affects the radio link can be regarded solely as a random continuum when the radio refractive index of the troposphere is a randomly but continuously distributed variable over time and space.

Under the influence of incident electromagnetic field, electrons inside the atoms will react with this field and the atoms will act as small oscillators. The oscillating charges in the medium generate a second field to counteract the incident electric field, depending on the strength of the wave from the source and quantum

mechanical molecular resonance of the atoms. As a consequence, the newly generated field will contribute to the total field strength.

As a whole, the modifications of the incident electromagnetic field due to the propagation medium can be described by the refractive index of the medium. The real part of refractive index determines the effective propagation velocity of the radio wave, therefore determines the phase delay in traversing the material. Considering the oscillators may have a damping rate in a natural environment, the damping force will cause friction and absorbing of the energy of the wave resulting in the imaginary part of refractive index. This causes a decrease in the magnitudes of the field and represents absorption of the wave.

4.1.1.1 Refractive Index Expressions

In the troposphere (height < 17 km) under dry conditions, the index of refraction n is due to the molecular constituents of the air, principally nitrogen, oxygen, carbon dioxide and water vapour. The value of n deviates from unity because of the polarization ability of these molecules. The index of refraction has been found to be dependent of temperature, pressure and relative humidity [6] and is given as:

$$n = 1 + \frac{77.6}{T}(P + 4810e/T) \times 10^{-6} \tag{4.1}$$

where T is the absolute temperature in Kelvin, P is the total pressure in millibars, and e the water vapour pressure in millibars. This expression is considered valid for frequencies ranging from 1 MHz up to 72 GHz.

When n in the atmosphere is greater than 1, the effective propagation velocity of the radio wave is slowed. The incremental optical path length compared to the propagation path in vacuum ($\Delta\rho$) can be determined by integrating these parameters over the total path length in the troposphere. Approximation

proposed by Smith-Weintraub is given as Equation (4.2), which is claimed to be accurate to 0.5% [7].

$$\Delta\rho = 7.76\cdot 10^{-5}\cdot\int_0^{top}\frac{P}{T}\cdot dx + 3.73\cdot 10^{-1}\cdot\int_0^{top}\frac{e}{T^2}\cdot dx \tag{4.2}$$

where e is related to the relative humidity H and temperature T by Equation (4.3):

$$e = \frac{H}{100}\cdot\exp(-37.2465 + 0.213166\cdot T - 0.000256908\cdot T^2) \tag{4.3}$$

The first term of Equation (4.2) is referred as hydrostatic term, which can be relatively well-determined using surface measurements. The evaluation of the second term, however, would be complicated due to high spatial and temporal variability of the relative humidity, especially in the atmospheric boundary layer (the first 1.5 km) or in layer of clouds.

4.1.1.2 Clear-Air Turbulence (CAT)

In the literature, theory of scintillation due to clear-air turbulence has been established for many years. It has been developed using both classical experiments and mathematical calculations, of which a short summary is presented below.

Classic experiments have shown that when the Richardson number is smaller than 0.25, dynamic (shearing) instability will generally lead to turbulence [8]. The Richardson number is a dimensionless parameter denoted as Ri. It is the ratio of the local static stability to the local shears and can be used to determine whether or not the flow will become turbulent due to the dynamic (shearing) instability. Full expression of Ri can be found in Appendix A. It can be seen that an increase in vertical shear or a decrease in potential temperature with height, or

both, would be needed to lower the Richardson number and induce frequent turbulence.

Turbulent transfer in the atmosphere is the main mechanism by which heat, moisture and momentum are exchanged between air surroundings and the earth's surface. In the earth's atmosphere, turbulence varies in size. There are two general cases: 1) turbulence occurring near the ground, which is strongly dependent on height above the surface, called 'boundary layer' turbulence. The boundary layer is defined as the part of the troposphere that is directly influenced by the presence of the earth surface, and responds to surface forces with a time of about an hour or less; 2) turbulence occurring above the boundary layer, called turbulence in free atmosphere.

According to Kolmogorov [9], well-developed homogeneous turbulence can be modelled by identifying two extreme scales of turbulence, the outer L_0 and the inner scale l_0. The former is the scale at which energy enters into the turbulence, ranging from a few tens of meters to a kilometre. When kinetic energy is introduced, and the Reynolds number is larger than a critical value, turbulent flow results. When eddy size > L_0 (input range), energy is introduced into the turbulence due to wind shear and temperature gradient. In general, turbulence is anisotropic in this range and the spectrum depends on how the turbulence is created. At this large scale, the dissipation is negligible and the energy is transferred successively into eddies of decreasing size. Kinetic energy may be continuously transferred to eddies of smaller size and the dissipation increases until the smallest size of eddies are reached. When the kinetic energy is of the same order as the energy dissipation, turbulence reaches the smallest size, l_0, all the energy is dissipated as heat and practically no energy is left for eddies of size smaller than l_0, which is of the order of a millimetre.

Since the structure function of refractive irregularities D_n is defined as:

$$D_n(r_1, r_2) = \left\langle [\delta n(r_1, t) - \delta n(r_2, t)]^2 \right\rangle \tag{4. 4}$$

and the spatial covariance function can be calculated from the ensemble-averaged product of fluctuations at two locations r_1 and r_2:

$$B_n(r_1, r_2) = \langle \delta n(r_1, t) \delta n(r_2, t) \rangle \tag{4. 5}$$

the structure function of refractive irregularities can then be expressed as a function of spatial covariance, and thus can be associated with Fourier wave number integrals of the turbulence spectrum. Experimental data often suggests, within the inertial sub-range, the $2/3$ scaling law of refractive-index structure function is frequently observed over a wide range of separation [10], which will correspond to a $-11/3$ slope of the spectrum.

By using the classical Kolmogorov refractive index spectrum ϕ_n [9], the variance and temporal spectral density for point receiver can be derived, as been proposed by [1] and [11]. Assuming the medium is transported by the wind without changing its detailed variation, (the frozen-in hypothesis), results are given as below:

$$\sigma_\chi^{\,2} = 0.31 C_n^2 \cdot k^{7/6} \cdot L^{11/6} \qquad \left(L_0 >> \sqrt{\lambda L} >> l_0\right) \tag{4. 6}$$

$$W_\chi^{\,0}(\omega) \to 2.765 \frac{\sigma_\chi^{\,2}}{\omega_t} \qquad (\text{as } \omega << \omega_t\,,\ \ \omega \to 0) \tag{4. 7}$$

$$W_\chi^{\,\infty}(\omega) \to 7.13 \frac{\sigma_\chi^{\,2}}{\omega_t} \left(\frac{\omega}{\omega_t}\right)^{-8/3} \quad (\text{as } \omega >> \omega_t, \omega \to \infty) \tag{4. 8}$$

Where $\sigma_\chi^{\,2}$ is the variance of the log-amplitude fluctuation, C_n^2 is the structure constant of refractive index, which is a measure of the intensity of the refraction

index variations, k is the wave number of the signal and L is the effective turbulent path (the path length in turbulence). ω_t is known as Fresnel frequency and given as $\omega_t = v_t(k/L)^{1/2}$, and v_t is the wind velocity component transverse to the propagation path. C_n^2 is reported to be of the order of $10^{-7}\,\mathrm{m}^{-1/3}$ for strong turbulence and $10^{-9}\ \mathrm{m}^{-1/3}$ for weak turbulence [1].

It is understood that under Taylor's frozen-in hypothesis, the connection between space and time can be made, relating the temporal covariance function with the spatial correlation function of refractive index variations. A random medium can be considered frozen only if the evolution time of an eddy is much greater than the crossing time it takes for the eddy to pass the measurement point [11]. This condition is generally satisfied both in the inertial and in the dissipation ranges of the turbulence spectrum.

The atmosphere generally exhibits a layered structure, and a slant path passes through regions of more or less intense turbulence. Within each region of turbulence, the atmosphere can be considered homogeneous. There are two limiting simplified models for the atmosphere used in the analysis of turbulence effects. They are the uniform atmosphere model, describing the layer extending between the surface $z_1 = 0$ and $z_2 = L$, and thin layer turbulence model, $z_2 = z_1 + \Delta z$, where z_1 and z_2 are the starting and ending altitude of the turbulence layer, and $\Delta z << z_1$.

Thin layers of air can work as a spatial filter function and introduces a cut-off effect on the transmitting wave [12]. The two asymptotes of refractive spectrum as described in Equation (4.7) and (4.8) intersect at a corner frequency ω_c, which is dependent upon the transverse wind speed. Calculations of corner frequency can be made for the two above simplified atmosphere models, with $\omega_c = 1.43\omega_t$ for the uniform model and $\omega_c = 1.04\omega_t$ for the thin layer model [1].

Furthermore, three points need to be noted in the above derivation. First of all, one of the assumptions used by Kolmogorov model is that the refractive index fluctuation is presumed to be both isotropic and homogeneous in the inertial range. This has enabled some simplification in the development of spatial covariance and structure function of refractive index. Secondly, from Equation (4.6), it is reasonable to assume that for microwave frequencies and short distances ($L \leq l_0^2 / \lambda$), the amplitude fluctuation does not vary much due to turbulence. As the distance increases, the amplitude fluctuation rises and eventually reaches strong fluctuation region where the average (coherent) field is negligible and the field is almost totally incoherent. Thirdly, the classic Kolmogorov model admits that in the energy input region, large eddies (energy) may exist but their influence on refractive index irregularities is not known. This effectively places a lower boundary on the wave numbers to which the spectrum applies [10].

4.1.2 Wet Scintillation

Scintillation occurring during rain may also become a problem for wave propagation in a mixture of the two types of random media. Falling raindrops intersecting the Fresnel ellipsoid of a microwave link cause field amplitude variations by both absorption and scattering. Therefore, during event of rain, the turbulence-induced amplitude fluctuations are superimposed on slow signal fluctuations due to the absorption mechanism and fast signal fluctuation caused by incoherent scattering by the falling raindrops. As precipitation evolves along the wave propagation path, the consequent change in the received signal strength can be regarded as a net fading effect with fast amplitude fluctuations superimposed on the former faded signal component [13]. Further investigation of simultaneous rain effects on scintillation is addressed in more details in chapter 5.

4.2 Extraction Of Amplitude Scintillation

For systems operating at frequency ranges within our consideration (20 - 50GHz), the received beacon signal will suffer from a number of propagation impairments and system performance degradations [14]. Among them, several causes will contribute to the enhancement and fade of the received signal amplitude. These are: 1) underlying trend of attenuation due to gaseous absorption and precipitation conditions on the slant path, 2) fluctuations of attenuation assumed to be due to the variable spatial distribution of atmospheric liquid water content in cloud, and 3) fluctuations due to the focusing/defocusing effect of the turbulent refractive index field. Since the remaining study of scintillation characteristics and the validation of proposed prediction models will both rely on the raw satellite beacon measurement, signal power affected by scintillation needs to be properly extracted from the received beacon signals, in order to exclude contributions to the amplitude fluctuation from other propagation impairments.

Attenuation by atmospheric gases is entirely caused by absorption. At a given frequency, the oxygen contribution to atmospheric absorption is relatively constant compared to that due to water vapour. In the case of rain events, the rate at which signal attenuation may change (rain fade slope) is affected by a few factors. It will depend on the rain attenuation level and the raindrop size distribution, and hence depend on the type of rain. The wind velocity perpendicular to the path is another meteorological parameter of influence. In general, when slight attenuation exists due to light rain (with relatively small fade typically < 3 dB), the dominant time scale of fading variations is typically greater than 5 min [15]. Scintillation, however, results in amplitude variations containing frequency components up to several hertz. A study on the spectral contributions of various tropospheric impairments has identified scintillation due to turbulence

with the more rapid components of the spectrum, and the more slowly changing regions of the spectrum being mainly due to rain fading [16].

To isolate scintillation from the other atmospheric effect, a method based on their different and characteristic frequency components is required.

4.2.1 De-raining Process

Several methods to separate scintillation fluctuations from low frequency fading components have been utilized in the literature. They are: 1) subtraction of a reference signal level calculated from a moving average window in the time domain, or 2) by applying a high-pass filter to exclude the low frequencies, or 3) by using wavelet techniques. Among these methods, the time-domain moving average method is not an instantaneous operation and largely does smoothing and redistributing scintillation effects across the time-series [17]. The method of using high-pass filter is alternatively the most traditional and favoured technique employed by researchers.

A suitable cut-off frequency of the high-pass filter needs to be carefully chosen in a way that it is desired to be high enough to exclude the non-scintillation effects but low enough to preserve the scintillation effects as much as possible [18]. Since a large part of scintillation energy will be distributed over a short frequency intervals around the theoretical corner frequency of spectrum asymptotes, the value of the desired cut-off frequency is thus expected to be in the close neighbourhood of the corner frequency, which has been predicted dependent on the transverse wind speed and carrier frequency for a given link geometry.

Table 4. 1 summarizes various values of cut-off frequency that have been proposed in the past, compared together with information of the path geometry and operating beacon frequencies.

Cut-off Frequency	System Parameters
0.01Hz	12GHz beacon at 30° elevation angle [19]
0.00441Hz	20 GHz beacon at 30° elevation angle [20]
0.01Hz	12.5, 20 and 30 GHz beacon at 30° elevation angle [21]
0.02Hz	20, 40 and 50 GHz beacon at 38° elevation angle [22]
5min moving-avg	12.5 and 30 GHz beacon at 28° elevation angle [23]
60s moving-avg	12 GHz beacon at 6.5° elevation angle [15]

Table 4. 1 Summary of proposed cut-off frequency

The power spectrum density (PSD) function provides a measure for the distribution of the power of the sampled signal in the frequency domain. The processing of long sequences of random process data for the purpose of spectral analysis is conventionally performed by dividing the data into short sections, either overlapping or non-overlapping. Samples of each section are usually multiplied by an appropriate windowing function in the time domain or equivalently, the Discrete Fourier Transform (DFT) of the data is convolved with the corresponding spectral window in the frequency domain, before computing the periodograms. This window function is applied to the data section to control the spectral leakage, which will in turn cause biases in the estimate. It also reduces the frequency resolution however due to the increased width of the main lobe of the spectral window. The modified periodograms are averaged to obtain the resulting spectral estimate. By using overlapped sections of time-series, a reduction in estimation variance can be obtained, although the transforms are correlated.

The above process is referred to as the Welch method [24] and it is valid as long as the sampled data can be considered from a zero-mean wide-sense stationary random process. Therefore, the estimation of PSD of our time-series is computed on a block of 4096 samples (equivalent to 68 min) by breaking the block into seven half-overlapping segments of 1024 samples (equivalent to 17

min), and removing the mean from each segment before multiplying by a Hanning window. For the Hanning window, a 50% overlap will result in an Overlap Processing Gain (OPG) of about 1.8 [24], Finally, the periodograms of each modified segment are averaged. A moving average filter of five points is applied in the frequency domain if necessary, to smooth the spectrum for the purpose of visual convenience.

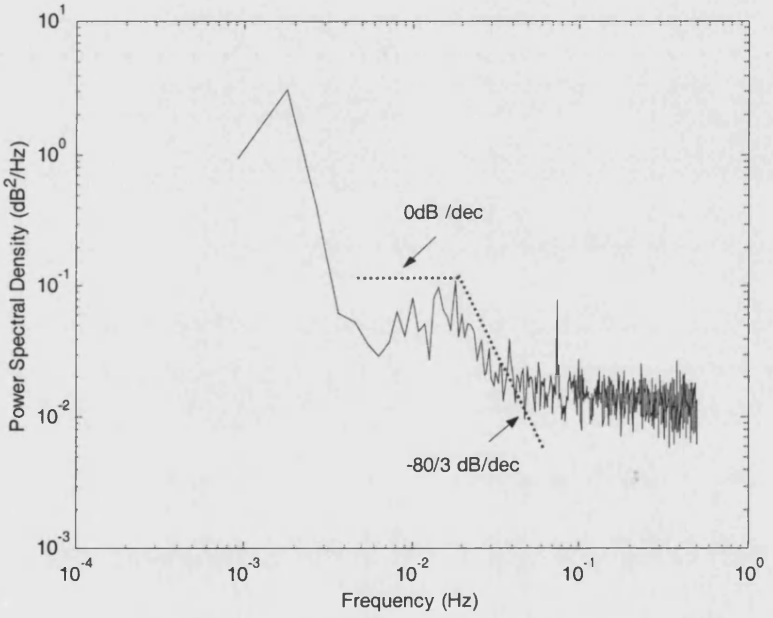

Figure 4. 1 Averaged power spectrum of 21600 min data during dry condition

Figure 4. 1 displays the averaged power spectrum of 21600 minutes of dry beacon measurement data samples. The theoretical prediction of scintillation −80/3 dB/decade slope is clearly identifiable following an approximately flat part of spectrum. For frequency components below 0.003 Hz, power attenuation appears to be caused by atmospheric variations occurring on a time scale longer than about 10 min. These may be clear-sky gases absorption and slow attenuation caused by cloud. The power spectral density of the signal level variation due to scintillation tends to be strongly biased toward the region of 0.01 to 0.3 Hz.

The 21,600 min of data chosen by visual inspection to exclude rainy conditions were used to calculate PSD. The measurements are distributed randomly over four seasons and they are free from loss-of-lock or saturations of the receiver and other artefacts or interferences that might cause the signal level to deviate from normal behaviour. The observation is considered to be representative and the separation of fluctuations from the background overall fading therefore can be realized by using a high pass filter with a cut-off frequency of 0.01 Hz. By applying the high-pass filtering, the low frequency variations such as diurnal amplitude variations due to satellite station-keeping are also removed.

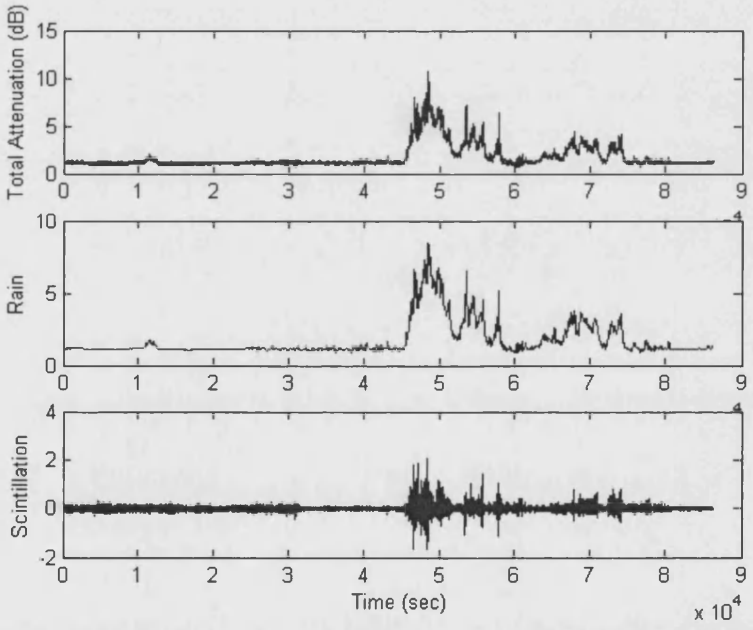

Figure 4. 2 Time-series of total attenuation, rain fading and extracted scintillation

For rainy events, the spectral power density due to rain effects will be superimposed onto the scintillation spectrum. Under certain conditions, rain scattering may produce fast fluctuations in the amplitude of the received signal, although most of its power lies at the lowest frequencies. The rain power may extend beyond where the flat slope of dry scintillation appears and contributes to

the fast fluctuations. A complete separation in the frequency domain of fluctuations due to rain and turbulence is therefore practically impossible. By referring rain scattering induced fluctuation faster than 0.01 Hz as wet scintillation, the extraction process of scintillation from raw satellite measurement is believed to be satisfactory, which is referred to as de-raining. A typical rain event has been analysed using the above de-raining process, and the time-series of rain attenuation and scintillation are shown in Figure 4. 2. The high-pass filtered data is referred to as scintillation and the low-pass filtered data is referred to as rain.

4.2.2 Calculation of Scintillation Intensity

Standard deviations of scintillation log-amplitudes need to be calculated for each time interval of filtered data. These intervals are required to be sufficiently long so that the contained data is statistically representative, yet sufficiently short to reflect any variations resulting from changes in the underlying trend of attenuation. A period of 1-minute, in our case, has been chosen to be representing a stationary period for each scintillation event. It has provided us with a reasonable number of statistical samples and further justification for this choice will be presented shortly. Long-term scintillation intensity is calculated by averaging individual 1-min intensities over a period of a month or year.

4.3 Dry Scintillation Characteristics

After a signal has propagated through a turbulent medium, it can be regarded as a random variable, best described by its probability density function (PDF) and power spectrum. Due to the random property of the propagation fading processes, the channel capacity also has a random variability, which imposes performance degradation on the system that utilizes the channel [25]. Therefore, knowledge of the probability density function (PDF) or cumulative distribution function (CDF) of the fading process should help the system designer with the

selection of potentially suitable modulation/coding techniques to optimise the channel utilization. In order to make corresponding comparisons with the results of scintillation characteristics reported in the literature, only dry scintillation characteristics will be presented in this chapter.

4.3.1 Temporal Frequency Spectrum Of Scintillation

Adopting the estimation method described earlier, a typical PSD of dry scintillation is calculated and shown in Figure 4. 4. It corresponds to the 1 hour time-series of scintillation amplitude, shown in Figure 4. 3. The length of the period is chosen for display purposes and it is longer than the period normally taken as to be stationary.

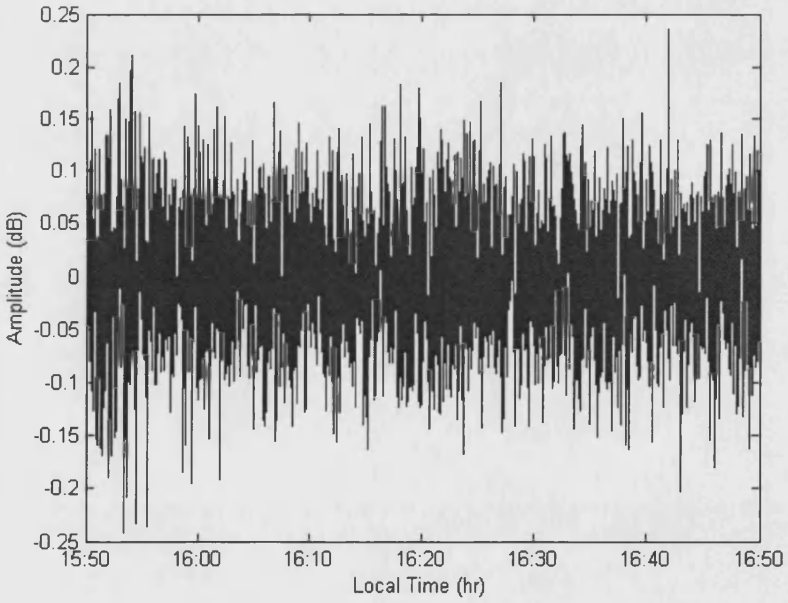

Figure 4. 3 Example of scintillation time-series

The characteristic roll-off of the scintillation process from a corner frequency around 0.02 Hz is clearly visible. The upper frequency limit of the spectrum is imposed by the sampling and integration time of the data-logging process, in our

case frequency components of up to 0.5 Hz can be analysed. The resolution (low frequency limit) is determined by the windowing length, which is desired to be long but within the constraints of scintillation stationary period.

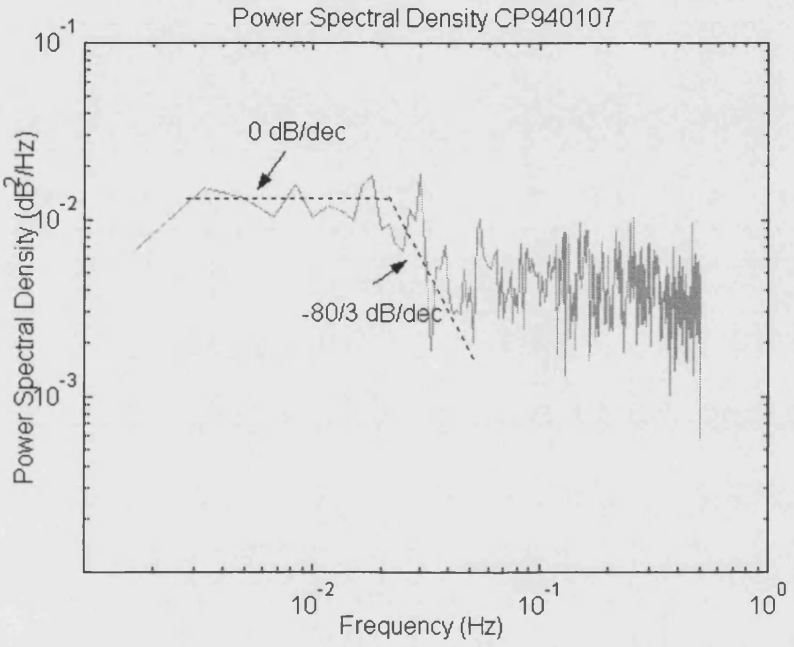

Figure 4. 4 Power spectral density of scintillation

For the calculation of Equation (4.6) and (4.7), classic Kolmogorov spectrum requires $\frac{2\pi}{L_0} < \kappa < \frac{2\pi}{l_0}$, thus the $-80/3$ dB/decade slope of spectrum and the two asymptotes are valid in the range of $\frac{\sqrt{\lambda L}}{L_0} < \frac{f}{f_t} < \frac{\sqrt{\lambda L}}{l_0}$.

4.3.2 Probability Distribution Of Scintillation (PDF)

Scintillation causes random fluctuations of amplitude, phase and angle-of-arrival of the received signal, thus it is natural to use statistical methods to describe the structure of such fluctuating random variables. When studying the probability

distribution of scintillation, the period within which scintillation can be regarded as a stationary random process is very important.

A random function is called stationary if its mean value does not depend on the time and if its correlation function for two given instances depends only on the difference of the time interval between the two instances. Not all the actual random processes can be described with sufficient accuracy by using stationary random functions. For those, the random processes cannot be regarded as stationary, if the difference of the random function at two instances can be modelled by a stationary random function of time and if durations of time intervals between the two instances are not too large, the original function is called a random function with stationary first increments, or simply a random function with stationary increments.

One of the assumptions for Equation (4.6) to lie above is, that the random medium should be locally homogeneous and isotropic in the transverse direction of the propagation path. It is a rough approximation to regard actual meteorological fields as homogeneous and isotropic, since atmospheric turbulence may always contains large-scale components, usually destroying the homogeneity and isotropy of the fields of the meteorological variables whose variation affects the observed scintillation intensity. Statistically, the turbulence causes the meteorological fields to be non-stationary.

However, a random field can be considered locally homogeneous in the region when the distribution functions of the random variable are invariant with respect to shifts of the pair of points, as long as these points are located in the same region. This is implying a close relationship among the stationarity, homogeneity and isotropy of a field. Therefore, scintillation can be modelled by a stationary process with sufficient accuracy as long as the field of refractive index can be

regarded as locally homogeneous and isotropic. This is equally to say that the Equation (4.6), (4.7) and (4.8) only hold for the scintillation stationary period.

The determination of the stationary period is not always a straightforward process in practice, because inhomogeneity and anisotropy of turbulence field are nearly impossible to measure. From the definition of stationarity, scintillation fluctuations should have zero mean within the period, which suggest that only shorter time intervals can be qualified; conversely, in practice, the time interval should be long enough to obtain a statistically reliable estimate of σ_χ^2. Table 4. 2 summarizes periods that have been assumed stationary for scintillation in the literature.

Stationary Period	System Parameters
10 min	12 GHz beacon at 3 Hz sampling rate [26]
1 min	20, 40 and 50 GHz beacon at 1 Hz sampling rate [22]
1 min	12 GHz beacon at 13.9 Hz sampling rate [27]
1 min	12.5, 20 and 30 GHz beacon at 1 Hz sampling rate [28]
34.13 min	12.5 and 30 GHz beacon [29]
~1 hour	97 GHz urban-link at 30 Hz sampling rate [30]
1 min (sliding)	12.5 and 30 GHz beacon at 1Hz sampling rate [23]

Table 4. 2 Summary of proposed stationary period

4.3.2.1 Amplitude Scintillation Statistics during Stationary Period (Short-term)

During a stationary period, the predicted probability distribution function of scintillation amplitude depends on the model suggested for the random medium. If it is assumed that the receiver is located in a turbulent region composed of a large number of independent slabs oriented perpendicularly to the direction of propagation and the scattering volume is long and narrow, the received field is a result of multiple scattering, by applying the central limit theorem. Thus the log-

amplitude χ of weak fluctuation should follow a normal distribution with zero mean and constant variance [31], described in Equation (4.9):

$$P(\chi \mid \sigma_\chi) = \frac{1}{\sqrt{2\pi}\sigma_\chi} \exp\left(-\frac{\chi^2}{2{\sigma_\chi}^2}\right) \tag{4.9}$$

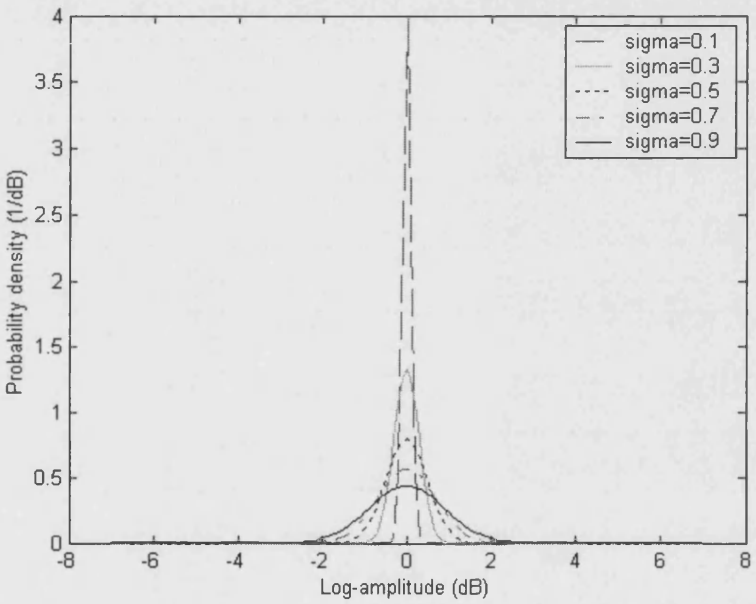

Figure 4. 5 Probability density distribution of log-amplitude for different values of σ_χ

If it is assumed that the turbulence is confined to a thin slab located far from the receiver (such as turbulent cloud layer), the received field is the sum of a large number of waves scattered from different regions in the slab, the dielectric constants in the physically different regions are uncorrelated. The amplitude at the receiving point obeys a Rice-Nakagami distribution, as proposed by [31] and [32]. Distribution of the log-amplitude can be described by Equation (4.10):

$$P(\chi \mid \xi) = \frac{\ln 10}{20} \cdot \frac{10^{2\chi/20}}{\xi^2} e^{-\left(10^{2\chi/20}+1\right)/2\xi^2} I_0\left(\frac{10^{\chi/20}}{\xi^2}\right) \tag{4.10}$$

where $\xi = \sigma_\chi / E_1$ and E_1 is the amplitude of the direct wave. Figure 4. 6 is an illustration of how $P(\chi|\xi)$ varies with ξ. When $\xi \to \infty$, Equation (4.10) reduces to a Rayleigh distribution; when $\xi \to 0$, it reduces to a Gaussian distribution.

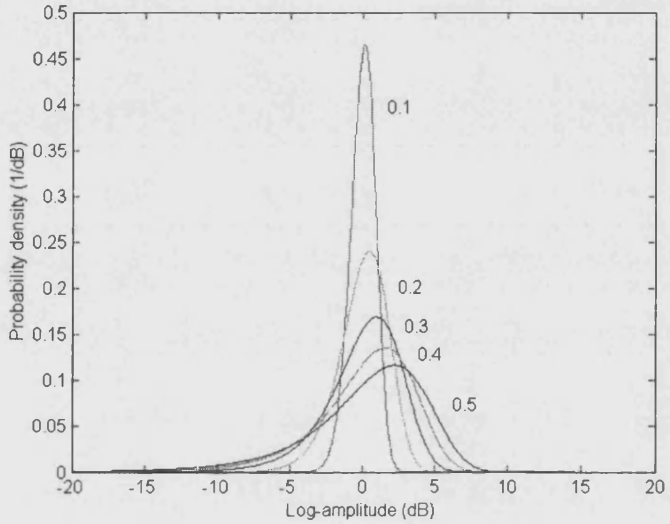

Figure 4. 6 Probability density distribution of log-amplitude for different values of ξ.

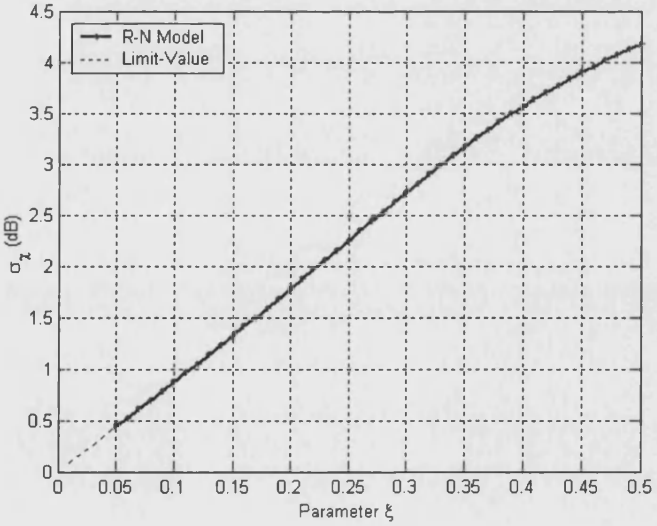

Figure 4. 7 Standard deviation of scintillation log-amplitude in dB with relevant parameter ξ

Figure 4. 7 further illustrates how scintillation intensity varies with the parameter ξ as given by the Rice-Nakagami distribution. It is noted that for values of ξ less than 0.05, the output of modified Bessel function in Equation (4.10) will increase dramatically to the extent that most numerical programmes cannot handle, resulting in infinite values. The limits of these values of $P(\chi|\xi)$ are shown by dotted line. From our measurements, scintillation intensity under dry conditions over a short period (few minutes) is very unlikely to exceed 0.5 dB and the Rice-Nakagami model needs only very small ξ (less than 0.05) in this case. Hence, there is practically not much difference in using the Rice-Nakagami model or the normal distribution for the modelling of weak scintillation in a stationary period.

The PDF of 1-min χ was observed and compared to a Gaussian distribution with $\mu = 0$ and $\sigma = 0.0962$ as shown in Figure 4. 8. Figure 4. 9 displays the normal probability plot of scintillation amplitude probability distribution function during the same period. If the data does come from a normal distribution, the scattergram will appear as a straight line, other probability density functions will introduce curvature in the plot. For the range of (-0.2 0.2), the scattergram agrees well with the theoretical dotted line.

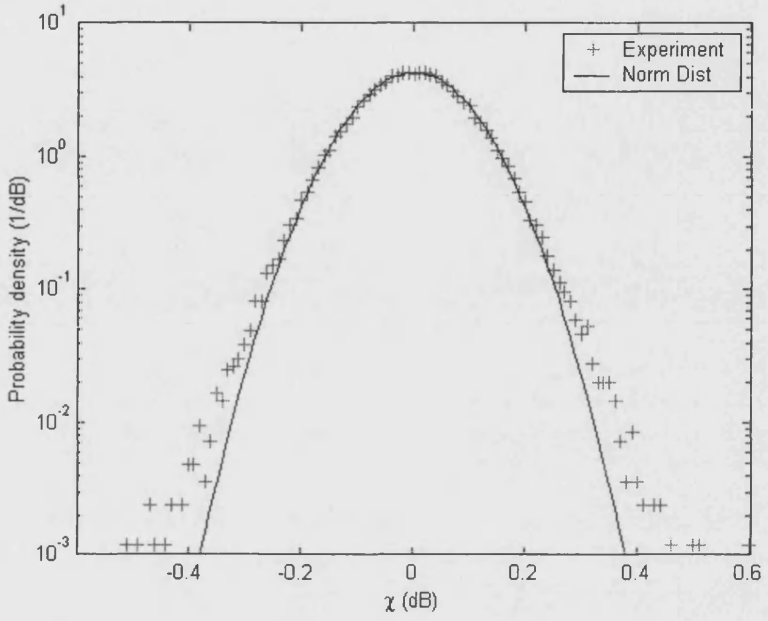

Figure 4. 8 Scintillation amplitude probability density function for a sample period at 20 GHz compared with Gaussian distribution function

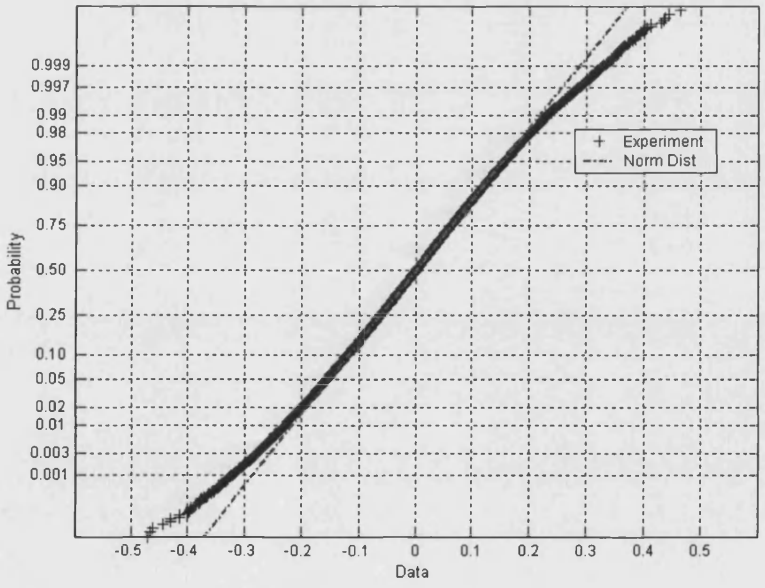

Figure 4. 9 Normal probability plot of a sample period of scintillation log-amplitude at 20 GHz

Example of histogram plots of n-minute scintillation amplitude, as shown in Figure 4. 10, appears to suggest that as the measurement interval increases, the normality of the data decreases.

A more quantitative experiment has been carried out to test the proposed stationary period of our beacon measurements under dry conditions. The scintillation data within a day is divided into several blocks of different length. Jarque-Bera test for goodness-of-fit to a normal distribution has been employed to test whether these blocks would pass the normality test or not [33]. The percentage of blocks passing the test against block length is recorded and shown in Figure 4. 11. It can be seen that as the time interval increases, the normality of χ decreases.

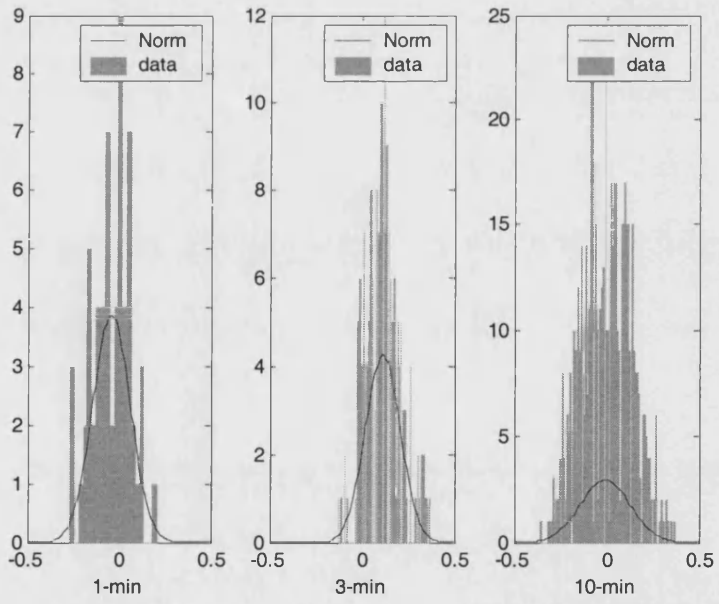

Figure 4. 10 Example of histogram of measured ITALSAT data against normal distribution probability functions

with the same mean and standard deviation for 1-min, 3-min and 10-min, 2000/04/06

The intervals of 1 min appear to have the highest percentage of passed tests among intervals having been considered. This is desired in the respect of normality within a stationary period.

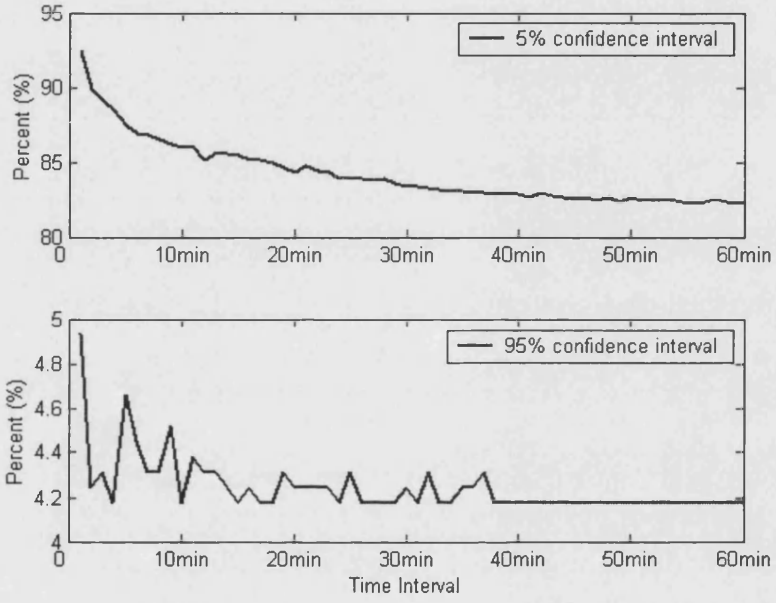

Figure 4. 11 Percentage passed the Jarque-Bera test for goodness-of-fit to a normal distribution at different time intervals of 2000/04/06

Concerning the fact that the sampling rate of our recorded digital beacon measurements is 1 Hz, there will be 60 samples in a minute. Further verification of whether this amount of samples is enough to provide stable estimation of scintillation statistics will be addressed in a later subsection. It has been found that as the time interval increases, the observed long-term mean scintillation intensity increases, as shown in Figure 4. 12.

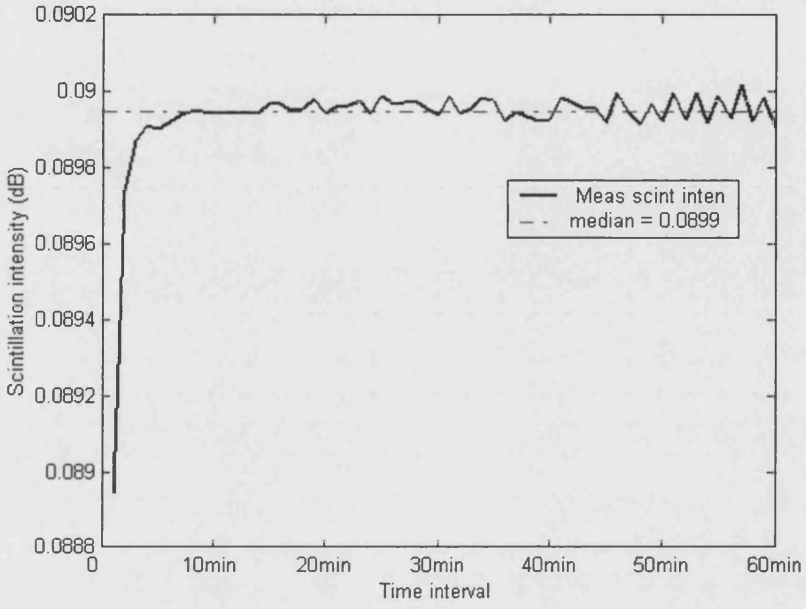

Figure 4. 12 Mean scintillation intensity variation with calculation time intervals

4.3.2.2 Amplitude Scintillation Statistics during Non-stationary Period (Long-term)

Variances in meteorological conditions along the path affect scintillation intensity. For short time periods, these meteorological conditions can be regarded as constant and scintillation log-amplitude can be well modelled by a stationary process that follows a Gaussian distribution. For duration longer than a stationary period, varying turbulent conditions and various atmospheric events along the propagation path are likely to result in scintillation intensity changes. Observations have established that under these conditions, scintillation departs significantly from a log-normal distribution, especially when scintillation amplitude is large [26], [34], [19], [27] and [22].

Several well-known statistical distributions have been considered for modelling of the long-term log-amplitude scintillation distribution. However, there appears to be no distributions in the literature with the necessary property to describe the apparent central tendency with a relative wide spread (outlier-prone) in the range

of higher values compared to a Gaussian distribution in both positive and negative directions.

A modelling approach of deriving scintillation amplitude distribution $P(\chi)$ indirectly from measured scintillation intensity (σ) distribution has been proposed [26]. The model is based on a modified form of normal distribution in which its standard deviation is also a random variable, i.e. if the probability density of scintillation intensity denoted by $P(\sigma_\chi)$ can be measured through experiment, the probability density of scintillation amplitude $P(\chi)$ will be expressed as Equation (4.11), in which $P(\chi \mid \sigma_\chi)$ is weighted by the probability of occurrence of a given value of σ_χ:

$$P(\chi) = \int_0^\infty P(\sigma_\chi) P(\chi \mid \sigma_\chi) d\sigma_\chi \tag{4.11}$$

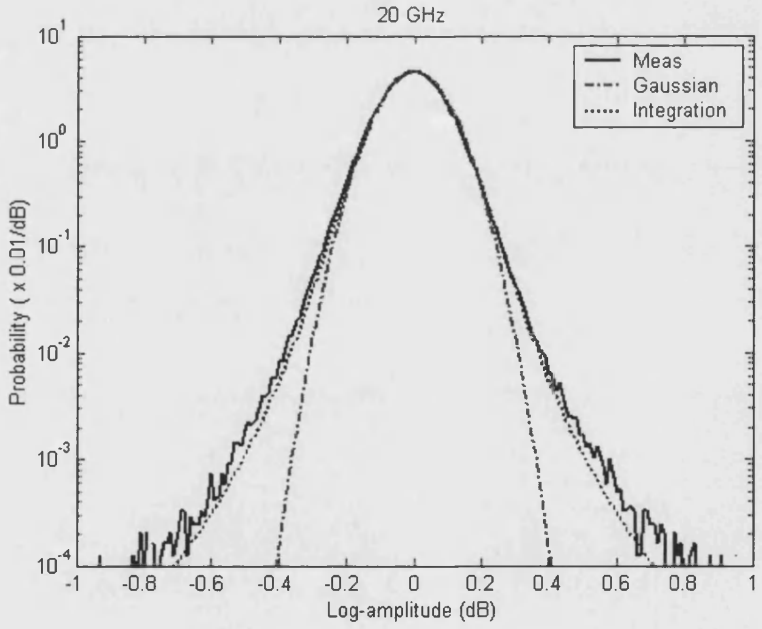

Figure 4. 13 Long-term scintillation log-amplitude distribution for 20 GHz compared with Gaussian prediction and prediction using integration method

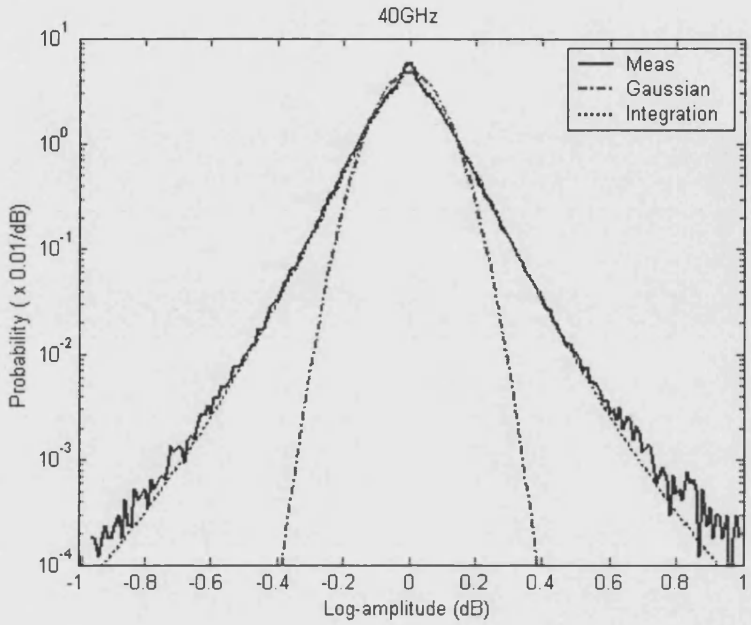

Figure 4. 14 Long-term scintillation log-amplitude distribution for 40 GHz compared with Gaussian prediction and prediction using integration method

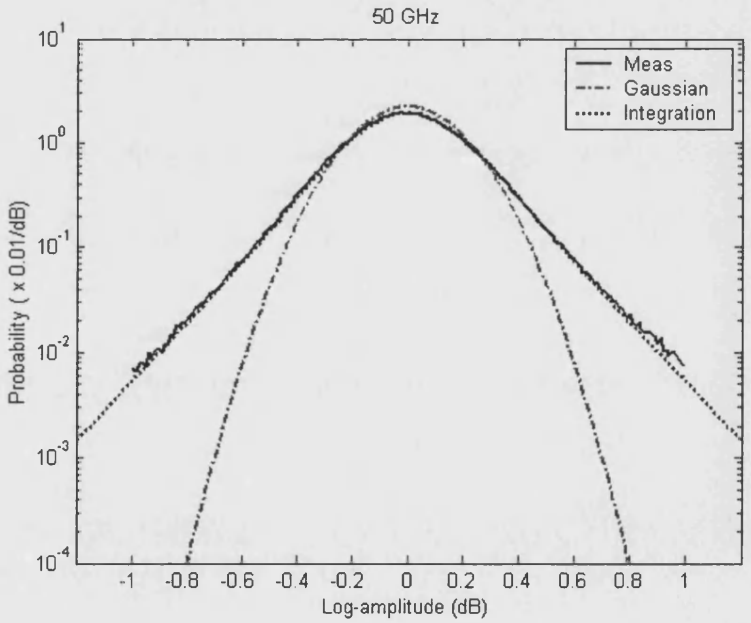

Figure 4. 15 Long-term scintillation log-amplitude distribution for 50 GHz compared with Gaussian prediction and prediction using integration method

The results of applying this method to three frequencies are shown in Figure 4. 13, Figure 4. 14 and Figure 4. 15. The measured long-term distribution of scintillation log-amplitude departs considerably from the Gaussian distribution as log-amplitude magnitude increase, where the former appears to have a wider spread than the latter. The difference between the measured distribution and the Gaussian distribution for a given log-amplitude level increases with increasing beacon frequency. The proposed method in Equation (4.11) gives good estimation of the measured distribution up to 0.1 percentage for 20 GHz, 40 GHz and 50 GHz.

Equation (4.11) relates the distribution of χ to that of σ_χ, and thus links it to the physical mechanism of σ_χ. This modelling approach avoids direct measurements and recording of χ and has the advantage of considerable data reduction compared to recording individual samples [27]. Besides, the approach provides a possibility of indirect modelling of $P(\chi)$ through $P(\sigma_\chi)$. Several researchers have developed models to realize the prediction of $P(\chi)$ by using well-known existing distribution models to describe $P(\sigma_\chi)$ based on straightforward measurements of meteorological variables. Performance of these models will be assessed in the chapter 6.

4.3.2.3 Discussions on Scintillation Stationary Period

The performance of the above approach to model the distribution of scintillation log-amplitude is grounded on the stationarity of the scintillation process within each time interval where scintillation log-amplitude follows the central-limit theorem and can be accurately modelled by a Gaussian distribution. The agreement between measurements and such predictions has been found very good on our data, which also serves as an evidence for short-term scintillation log-amplitude to be modelled by a Gaussian distribution.

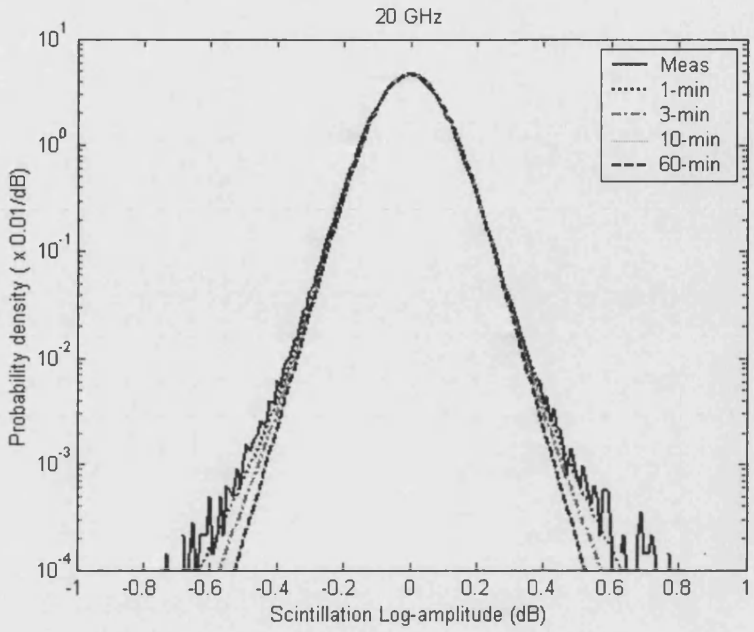

Figure 4. 16 Long-term scintillation log-amplitude distribution for 20 GHz compared with prediction using integration method for different chosen stationary periods

It is reasonable to expect an increased difference between measurement distributions and method predictions when the time intervals used to calculate σ_χ increase, and the stationarity of scintillation for that period tend to decrease until they disappear, because the Taylor's hypothesis will no longer hold.

The performance of prediction methods using various time intervals proposed in Table 4. 2, has been compared for 20 GHz data in Figure 4. 16 and Figure 4. 17. It is noted that when the interval is longer than 10 minutes, there is virtually no difference among their predictions. This is consistent with the interpretation from Figure 4. 11. The 1-min intervals produce stable prediction through entire log-amplitude range, and thus it can be concluded from our measurements, 1-min intervals are long enough to have sufficient samples for stable results when used for calculation of σ_χ, but also short enough to preserve stationarity so as to

produce truthful estimates of scintillation statistics. 1-min has therefore been adopted as the stationary period in the subsequent processing.

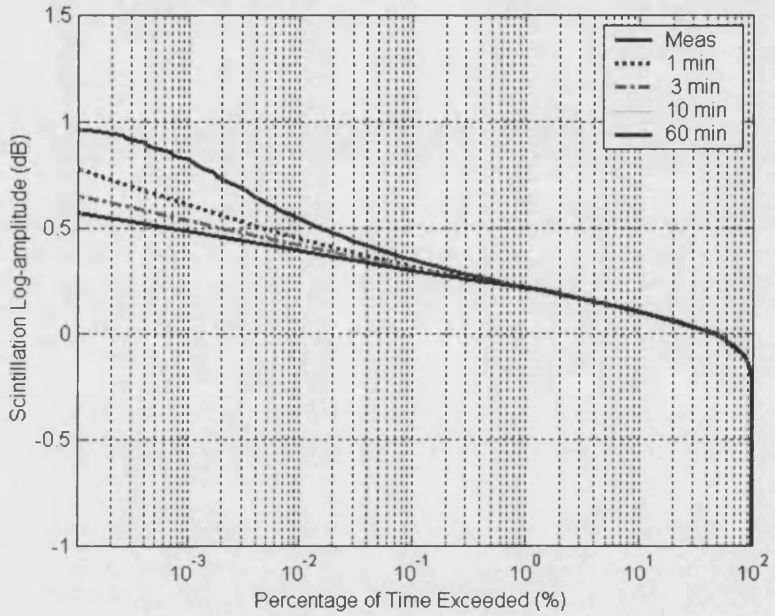

Figure 4. 17 Long-term cumulative distribution of scintillation log-amplitude for 20 GHz compared with prediction using integration method for different chosen stationary periods

4.3.2.4 Asymmetry of Scintillation Log-amplitude Distribution

In the past, scintillation has been traditionally treated due to pure forward scattering by atmospheric turbulence and the observed enhancement and fading appears equally likely. An investigation of the symmetry of scintillation log-amplitude distribution will hopefully provide useful information in interpreting the physical process producing scintillation.

Skewness is a measure of the asymmetry of the data around the sample mean. If skewness is negative, the data spread more to the left of the mean than to the right, and if skewness is positive, the data spread out more to the right. The

skewness of the normal distribution (or any perfectly symmetric distribution) is zero.

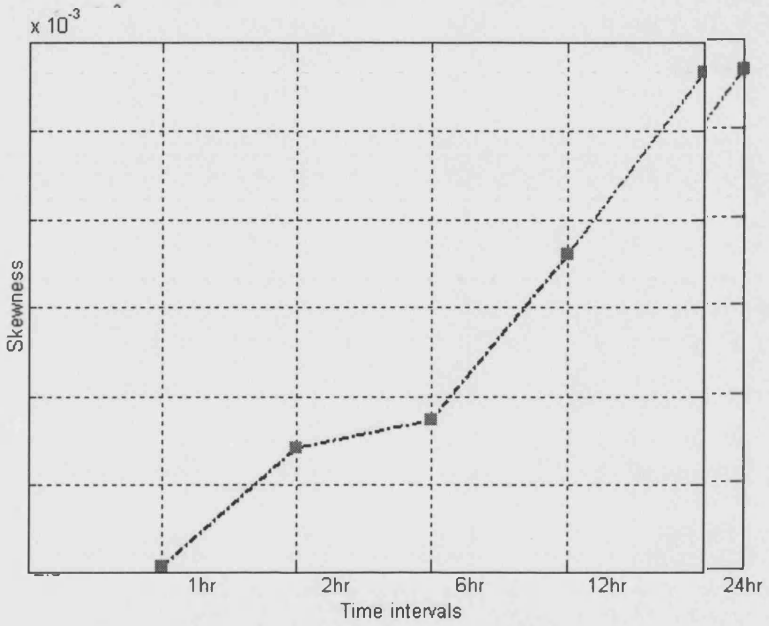

Figure 4. 18 Variation of skewness with time intervals for 20 Ghz

Figure 4. 18 shows the variation of averaged skewness calculated using different time intervals ranging from 1 hour to 1 day. All the experimental values of mean skewness are positive, describing data spread toward fade rather than enhancement. Skewness increasing with increased calculation interval, is consistent with the expectation that more outlier values of amplitude will appear within longer measurement periods. Figure 4.18 demonstrates that the skewness is small but non-zero and increasingly positive with increasing length of the time intervals. Figure 4. 19 shows the variation of values of skewness conditional for different σ_χ. In the calculation programme, the range of σ_χ has been divided into small bins with width of 0.015 dB and ten bins in total are used. Each data segment of 1-min length has been grouped into its relevant bin according to its measured intensity. The skewness of each bin group is then estimated after all the

measurements are examined. All values of skewnesses are found positive and smaller values exist when σ_χ is between 0.075 and 0.120. Since there are no rain events involved in the selected measurement periods, the asymmetry is not a consequence of un-removed rain attenuation. Reasons may be due to the fluctuations in the angle-of-arrival of the main signal, causing fast fluctuating fading (not enhancement) of the signal in the case of a very narrow antenna beam. Another contributing factor would be cloud activities, which is going to be inspected in the chapter 5. Besides, for the range of $\sigma_\chi < 0.075$, the accumulated samples could occupy only a relatively small portion of the total data amount, bias in the estimation of skewness may exist.

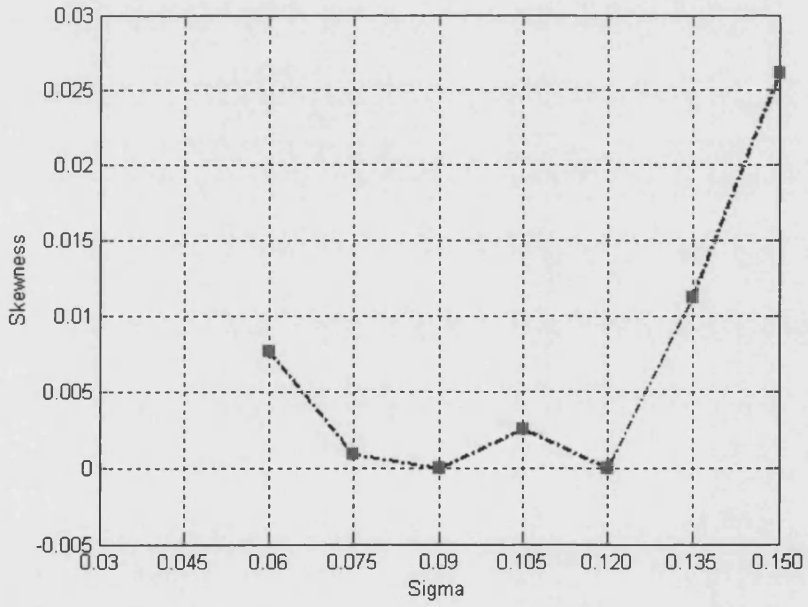

Figure 4. 19 Variation of skewness with scintillation intensity σ_χ for 20 GHz

All values of observed skewness are positive and in the order of 10^{-2}, which means there is a slightly greater probability of scintillation fading than enhancement. However, the asymmetry of the distribution is not severe.

Nevertheless, the proposed symmetrical models for long-term scintillation log-amplitude distribution generally reflect the experimentally observed nature of the distribution. Amplitude scintillations display signal enhancements as well as signal fades, which occur with nearly equal probability.

4.3.2.5 Scintillation Intensity Statistics during Non-stationary Period (Long-term)

When scintillation process is assumed to be stationary, the scintillation intensity is considered constant. Conversely, during non-stationary periods scintillation intensity varies due to changes in atmospheric conditions. Two distributions have been proposed to model the long-term distribution of scintillation intensity, namely the Gamma distribution and the Log-normal distribution.

The lognormal distribution has certain similarities to the normal distribution. A random variable is log-normally distributed if the logarithm of the random variable is normally distributed. The general formula for the probability distribution function of a Log-normal distribution is given in Equation (4.12):

$$f(x)=\frac{e^{-\left(\ln((x-\theta)/m)^2/(2\varsigma^2)\right)}}{(x-\theta)\sigma\sqrt{2\pi}} \quad x\geq 0,\sigma>0 \tag{4.12}$$

where σ is the shape parameter of the distribution, θ is the location parameter and m is the scale parameter. The distribution is unimodal and skewed to the right. The general formula for the probability density function of the gamma distribution is:

$$f(x)=\frac{\left(\frac{x-\mu}{\beta}\right)^{\gamma-1}\exp\left(-\frac{x-\mu}{\beta}\right)}{\beta\cdot\Gamma(\gamma)} \quad x\geq\mu,\gamma,\beta>0 \tag{4.13}$$

where γ is the shape parameter, μ is the location parameter and β is the scale parameter and $\Gamma(\cdot)$ is the gamma function which has the formula:

$$\Gamma(a)=\int_0^{\infty} t^{\alpha-1}e^{-1}dt \qquad (4.14)$$

By varying the parameter of γ, the distribution will have a rich variety of shapes. The Gamma distribution function does not have a simple and closed representation and a working precision need to be determined when doing numerical calculation.

Karasawa found that the long-term PDF of σ_χ follows a Gamma distribution [35]; Mouslesy-Vilar found that $\sigma_\chi{}^2$ is log-normally distributed [19]. The best-fit log-normal and gamma distribution for our long-term measurement of σ_χ in terms of PDF have been compared in Figure 4. 20. Both proposed distributions show comparably good fit for all three frequencies, although there are slight overestimates of the probability density for regions of small value of σ_χ. The difference between these two models can be better observed using the time cumulated distribution exceedence curves as shown in Figure 4. 21 where log-normal distributions appear to have better fit than gamma distributions. For 20 GHz beacons for example, the mean scintillation amplitude is 0.091 dB with a minimum value of 0.05 dB (attributed to receiver noise). For 1% of the total time, the scintillation intensity exceeds 0.147 dB.

In order to facilitate more accurate estimation of scintillation statistics, a detailed investigation of correlation with meteorological variables is needed, along with investigation of seasonal and diurnal variations. These aspects are addressed in Chapter 5.

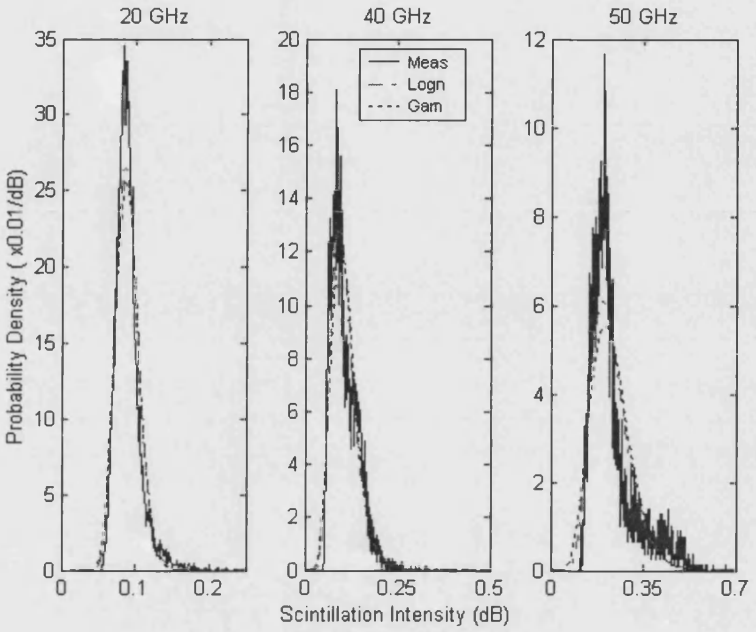

Figure 4. 20 Long-term scintillation intensity distribution at 20 GHz, 40 GHz and 50 GHz compared with best-fit log-normal distribution and gamma distribution

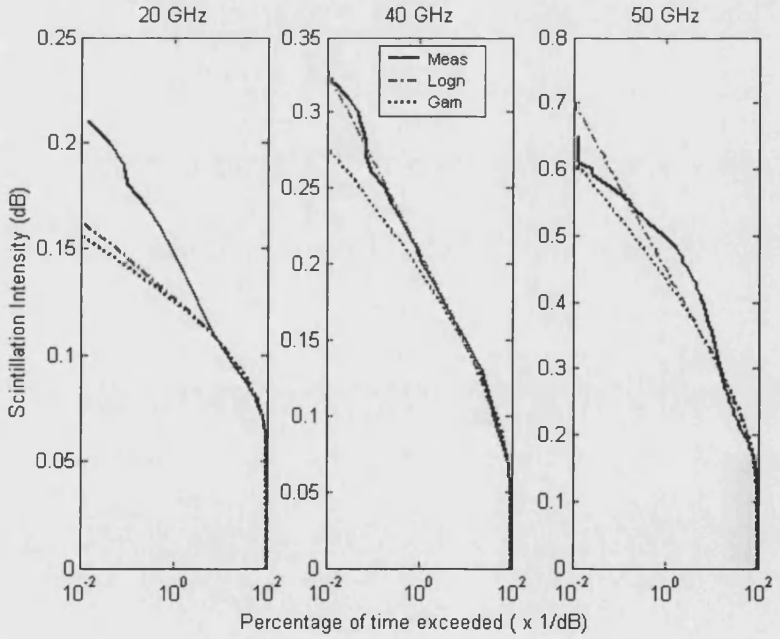

Figure 4. 21 Comparison of scintillation intensity cumulative distributions at 20GHz, 40 GHz and 50 GHz with best-fit lognormal distribution and gamma distribution

4.3.3 Antenna Aperture Averaging Effect

The variance and temporal spectral density of Equation (4.6), (4.7) and (4.8) are originally derived for point receivers only. For an antenna of finite effective diameter D (D is the diameter of an axi-symmetric paraboloid having the same effective area as the antenna being used), some corrections need to be made, as antenna diameter increases the incident wave front fluctuations may become less correlated across the aperture.

The antenna output is the spatial average of the random fluctuations across the wave front. If the transverse correlation length of the scintillation is smaller than the antenna diameter, the antenna acts as a low-pass filter and the observed fluctuations are smaller than those expected for a point antenna. If the scattered components corresponding to wave numbers are smaller than about $1/D$, i.e. D is less than the correlation length, the fluctuations across the wave front are well correlated and the antenna acts as a point receiver. Haddon and Vilar found the following expression for the normalization to a point receiver, using a rectangular (cylindrical) pedestal, an Airy function and an approximation of the Bessel function [36], for slope of the spectrum assumed to be $n = -11/3$, it is given:

$$g(x) = \frac{\sigma_g^2(D)}{\sigma_g^2(0)} = 3.8637\left(x^2+1\right)^{11/12} \cdot \sin\left[\frac{11}{6}\arctan\left(\frac{1}{x}\right)\right] - 7.0835x^{5/6} \qquad (4.15)$$
$$\approx 1 - 7.0835x^{5/6} \qquad (x \ll 1)$$

where $x = 0.0584kD^2/L$ is a measure of the ratio between the effective antenna diameter and the size of the first Fresnel-zone size (L is the effective path length through the turbulence).

The temporal spectrum of a finite aperture antenna can be solved using the same approach as above:

$$\frac{W_\chi^0(\omega,D)}{W_\chi^\infty(\omega,0)} = \frac{14}{3}x^{4/3} - 2(1+x^2)^{7/6} \cdot \sin\left[\frac{7}{3}\tan^{-1}\left(\frac{1}{x}\right)\right], \quad \omega \ll \omega_t \quad l_0 < D < L_0 \tag{4.16}$$

$$\frac{W_\chi^\infty(\omega,D)}{W_\chi^\infty(\omega,0)} = 1.053\left(\frac{\omega_s}{\omega}\right) \cdot \exp\left(-\omega^2/{\omega_s}^2\right) \quad \omega \gg \omega_s \quad \omega \gg \omega_t \tag{4.17}$$

where $\omega_s = 2v_t/bD = 4.0391v_t/D$ can be interpreted as the Fourier component above which the spectrum becomes dominated by aperture smoothing effects and rolls off at a faster rate.

From Equation (4.15), the effect of antenna aperture averaging depends on the ratio between the antenna diameter and the diameter of first Fresnel zone. Major earth stations use large receiving antennas, attempting to smooth the fluctuations and minimize scintillation. At low elevations, however, the signal experiences a longer effective turbulence path and the antenna size required to be comparable to the first Fresnel zone increases quickly especially when elevation angles are below 4 or 5 degrees. In this case increasing receiver antenna size becomes impractical, and scintillation intensity remains high and virtually equal to that of a point antenna.

In addition to the closed form of antenna averaging as described in Equation (4.15), Equation (4.16) and Equation (4.17), Crane and Blood also proposed a piecewise linear approximation for antenna averaging factor [37] given by:

$$\begin{aligned} G(D) &= 1.0 - 1.4\left(\frac{D}{2\sqrt{\lambda L}}\right), && 0 \le \frac{D}{2\sqrt{\lambda L}} \le 0.5 \\ &= 0.5 - 0.4\left(\frac{D}{2\sqrt{\lambda L}}\right), && 0.5 < \frac{D}{2\sqrt{\lambda L}} \le 1.0 \\ &= 0.1 && 1.0 < \frac{D}{2\sqrt{\lambda L}} \end{aligned} \tag{4.18}$$

The Crane-Blood model stated that when effective antenna diameter is equal or larger than the first Fresnel zone size, $G(D)$ ceases to decrease when the antenna diameter increases. The two antenna averaging factor models are compared in Figure 4. 22.

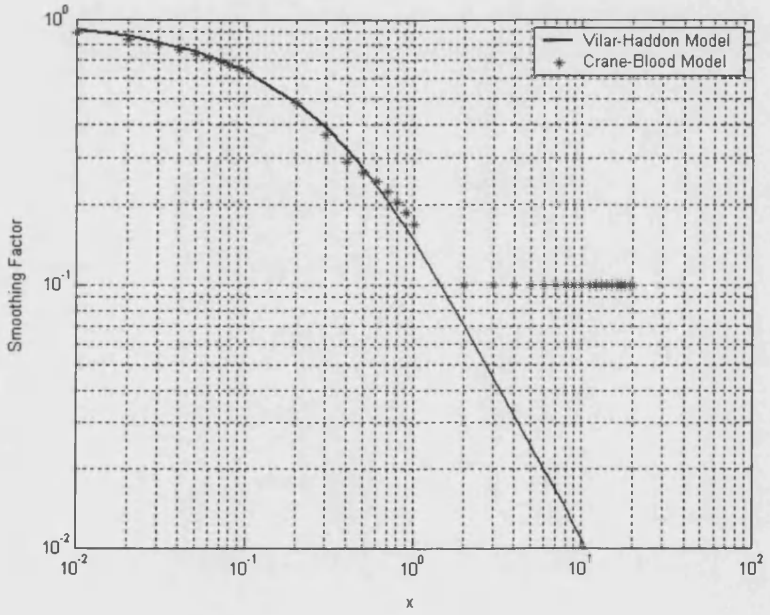

Figure 4. 22 Antenna aperture smoothing factor comparison

It can be seen that, for $x <= 0.2$, the difference between model estimates is small. For $0.2 < x < 1.02$, they remains close to each other, but for $x >= 1.02$, $G(D)$ stays constant while $g(x)$ continues to decrease.

Frequency	$g(x)$ (Haddon)	$G(D)$ (Crane)	Difference
20 GHz	0.9508	0.9200	3.2%
40 GHz	0.9687	0.9418	2.8%
50 GHz	0.9633	0.9349	2.9%

Table 4. 3 Comparison of antenna aperture smoothing factor calculated by Haddon-Vilar model and Crane-Blood model

Smoothing factors of our ITALSAT receivers have been calculated using the two models by assuming the turbulence height to be 1000 m as suggested by the ITU, and results are compared in Table 4. 3. The provided values of averaging factors are particularly close to each other. Since the Haddon-Vilar model also has a closed form, it will be employed in our design for a new scintillation prediction model. The effective path length is calculated according to the turbulence height. For the Haddon-Vilar model, variations of antenna averaging factor with turbulence height are shown in Figure 4. 22.

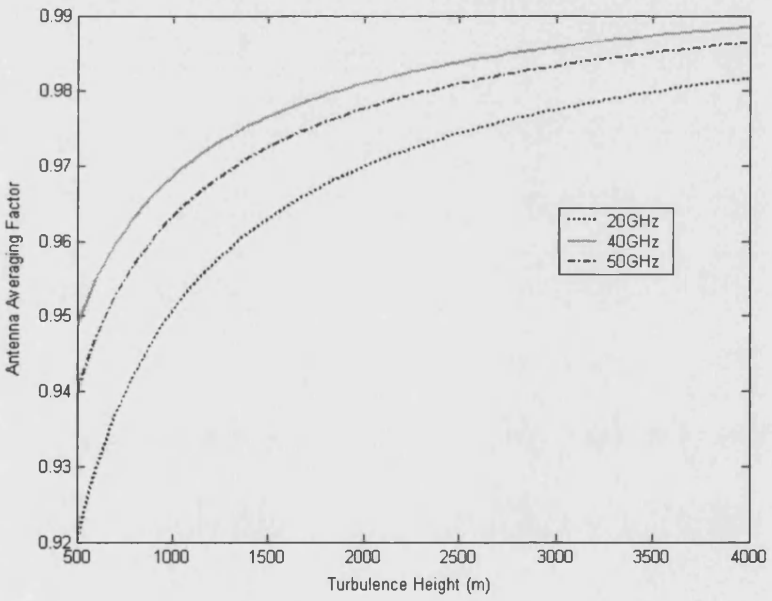

Figure 4. 23 Turbulence height and antenna averaging factor using Haddon-Vilar model

Strong antenna averaging effects have been found when turbulence appearing at low altitude compared with turbulence appearing at high altitude. As the height of turbulence increases, the transverse correlation length of the scintillation increases and eventually oversize the antenna diameter. The smoothing effect of antenna thus reduces with the averaging factor approaching to 1.

Significant turbulence is believed to happen mostly contained in the boundary layer, which is up to about 1500 m above the surface. The estimated value given by the ITU-R is 1000 m. It has been shown above, even for extreme cases when turbulence height vary from 500 to 4000 m, the resultant variation of antenna aperture averaging factor bears difference of 7%, 5% and 4% for 20 GHz, 40 GHz and 50 GHz beacons. Hence, the variations of turbulence height do not have considerable effect on the measured scintillation from our receivers.

4.3.4 Frequency Scaling Factor

When studying for scintillation frequency scaling factor, fair comparisons between scintillation intensity data at different frequencies gathered using individual receivers have to be made. The smoothing effect of an individual antenna needs to be excluded, and the received scintillation variance is to be scaled to a reference value corresponding to a hypothetical point receiver using the aperture averaging function proposed by Haddon and Vilar. The height of turbulence h is assumed to be 1000 m. Both the variability of the instantaneous scaling observed on a short-term basis (stationary period) and scaling of mean averaged variance over a longer term will be studied.

4.3.4.1 Short-term Frequency Scaling Factor

The instantaneous frequency scaling index α of amplitude scintillation is defined as the ratio of the variance of normalized amplitude scintillation (to exclude the effect of antenna aperture smoothing and elevation dependence) $\sigma_n^2(f_1)$ and $\sigma_n^2(f_2)$, concurrently experienced on a given satellite path by a pair of beacon frequencies f_1 and f_2, given as:

$$\frac{\sigma_n^2(f_1)}{\sigma_n^2(f_2)} = \left(\frac{f_1}{f_2}\right)^{\alpha} \tag{4. 19}$$

For the design of ULPC systems that can compensate for amplitude scintillation fading, the short-term frequency-scaling factor is needed. The amount of extra power needed to compensate for the fading experienced on the uplink is obtained from measurement of the attenuation at the downlink frequency, which is generally lower than the up-link frequency, by applying a frequency scaling algorithm.

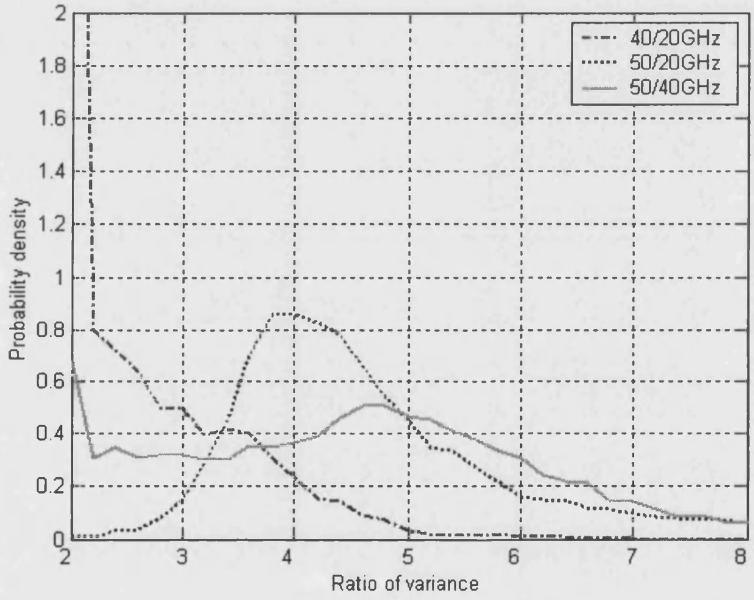

Figure 4. 24 PDF of ratio of variance for three frequency pairs

Under the assumption made by Equation (4.6), when the diameter of the first Fresnel zone is between the inner and outer scale of the turbulence, theoretically predicted α will be $7/6$ if the slope of fluctuation spectrum n is given as $-11/3$. Experiment has found that n is a random variable [12] and is directly related to the shape of the turbulence spectrum. When the diameter of Fresnel zone is larger than the outer scale, α will be 2, which has been observed by experiment over a 4.1 km path on a dual link at frequency of 36 GHz and 110 GHz [38].

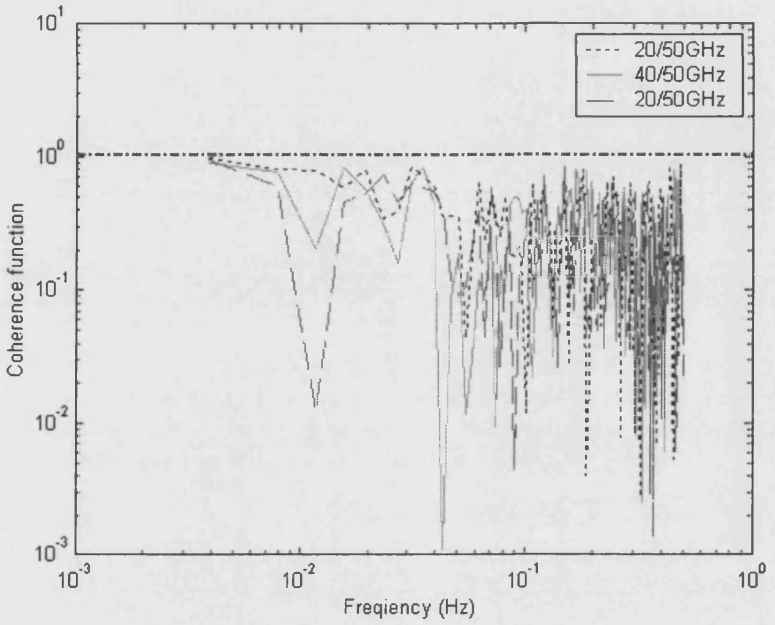

Figure 4. 25 Coherence function of scintillation variance measured on beacon signals of 08/21/1999

The measured simultaneous ratios of variance between three pairs of beacon frequencies are highly variable as demonstrated by the PDF shown in Figure 4. 24. Their mean and median values are listed in Table 4. 4. The 'measured' α has been calculated using the median value.

Frequency Pair	Mean Ratio	Median Ratio	Meas. α
40/20	1.393	1.364	0.896
50/20	2.276	2.305	1.823
50/40	2.084	1.967	6.064

Table 4. 4 Measured instantaneous variance ratio and frequency scaling index α

Coherent function of scintillation variance measured on three pairs of frequencies on 08/21/1999 is shown in Figure 4. 25. The coherence function is defined as the ratio of the square of the cross spectral density function of amplitude scintillation experienced by two radio waves with different carrier frequencies and

the products of the corresponding PSD function. Measurements for the degree of correlation between amplitude scintillation measured on two beacon signals operating on different carrier frequencies are the value of the coherence function in the low frequency region and the coherence bandwidth, which is the bandwidth when the coherence function is flat. For a perfect correlation, the coherence function should be equal to 1 for all spectral components. Results show that scintillations experienced by two radio waves operating at different carrier frequencies and propagating along the same path simultaneously have various degree of correlation.

4.3.4.2 Long-term Frequency Scaling Factor

Karasawa investigated scintillation on an 11/14 GHz 6.5°-elevation link, and based on a one year databases [13], from which wet data (mean fades>3 dB) were excluded, the reported α = 0.9, which is below the theoretical value of 7/6 (=1.17). The theoretical frequency dependence of scintillation has been tested using ITALSAT measurements and the results are summarized in Table 4. 5.

Frequency Pair	Ratio	Meas. α
40/20 GHz	1.317	0.795
50/20 GHz	2.312	2.418
50/40 GHz	2.031	6.350

Table 4. 5 Measured mean variance ratio and frequency-scaling factor α

Results of Table 4.4 and 4.5 are derived from the dry database that rainy periods have been excluded. Since the same propagation path is used, the elevation angle dependence does not have impact on the measured scintillation variance ratio. The frequency scaling factor has been observed to be smaller than the theoretically predicted value for 40/20 GHz pair and larger for the 50/40 pair for both instantaneous and long-term comparisons. Turbulence attenuation induced scintillation and angle-of arrival fluctuations due to turbulence have been

reported to have greater exponent of the power than clear-air induced scintillation [39], [40] and [41].

4.4 References:

[1] A. Ishimaru, *Wave propagation and scattering in random media.* New York: Academic, 1978.

[2] E. Matricciani, M. Mauri, and C. Riva, "Relationship between scintillation and rain attenuation at 19.77 GHz," *Radio Sci*, vol. 31, pp. 273-279, 1996.

[3] D. C. Cox, H. W. Arnold, and H. H. Hoffman, "Observations of cloud-produced amplitude scintillation on 19 and 28 GHz earth-space paths.," presented at 2nd Int. Conf on Anten & Propag, 1981.

[4] M. P. M. Hall, L. W. Barclay, and M. T. Hewitt, *Propagation of radiowaves.* London: The Institution of Electrical Engineers, 1996.

[5] D. C. Cox, H. W. Arnold, and H. H. Hoffman, "Observation of cloud-produced scintillation on 19 and 28 GHz earth-space paths," *Radio Sci*, vol. 16, pp. 885-907, 1981.

[6] B. R. Bean and E. J. Dutton, "Radio meteorology," US National Bureau of Standards, monograph 92, chap. 1, 1966.

[7] E. K. Smith and S. Weintraub, "The constants in the equation for atmospheric refractive index at radio frequencies.," *Proceeding of the I.R.E*, vol. 41, pp. 1035-1037, 1953.

[8] J. T. Houghton, *The physics of atmospheres*: Cambridge University Press 1997, 1986, 1997.

[9] A. N. Kolmogorov, "The local structure of turbulence in incompressible viscous fluid for very large Reynolds' numbers," *Comptes Rendus (Doklady) de l'Academie des Sciences de l'URSS*, vol. 30, pp. 301-305, 1941.

[10] A. D. Wheelon, *Electromagnetic scintillation - 1. Geometrical optics*: Cambridge university press, 2001.

[11] V. I. Tatarskii, *Wave propagation in a turbulent medium.* New York: McGraw-hill, 1961.

[12] E. Vilar and J. Haddon, "Measurement and modelling of scintillation intensity to estimate turbulence parameters in an earth-space path," *IEEE Trans. Antennas Propagat.*, vol. AP-32, pp. 340-346, 1984.

[13] Y. Karasawa and T. Matsudo, "Characteristics of fading on low-elevation angle earth-space paths with concurrent rain attenuation and scintillation," *IEEE Trans. Antennas Propagat.*, vol. 39, pp. 657-661, 1991.

[14] I. E. Otung, "Prediction of tropospheric amplitude scintillation on a satellite link.," *IEEE Trans. Antennas Propagat.*, vol. 44, pp. 1600-1608, 1996.

[15] Y. Karasawa, K. Yasukawa, and M. Yamada, "Tropospheric scintillation in the 14/11 GHz bands on earth-space paths with low elevation angles," *IEEE Trans. Antennas Propagat.*, vol. 36, pp. 563-569, 1988.

[16] D. Vanhoenacker and A. V. Vorst, "Atmospheric fluctuation spectra and radio system implications," presented at 4th ICAP, 1985.

[17] R. Ross and M. Kharadly, "An improved method for fade-slope calculation," presented at AP2000, Davos, 2000.

[18] I. E. Otung, M. O. Al-Nuaimi, and B. G. Evans, "Extracting scintillation from satellite beacon propagation data," *Letters, IEEE Trans. Antennas Propagat.*, vol. 46, pp. 1580-1581, 1998.

[19] T. J. Moulsley and E. Vilar, "Experimental and theoretical statistics of microwave amplitude scintillations on satellite down-links," *IEEE Trans. Antennas Propagat.*, vol. 30, pp. 1099-1106, 1982.

[20] I. E. Otung and B. G. Evans, "Tropospheric scintillation and the influence of wave polarisation.," *Electron. Lett.*, vol. 32, pp. 307-308, 1996.

[21] G. Ortgies, "Slant-path frequency scaling of amplitude scintillation during clear-sky conditions and rain.," *Archivfur Elecktronik and Ubertragungstechnik*, vol. 47, pp. 203-208, 1993.

[22] M. M. J. L. v. d. Kamp, "Experimental verification of asymmetrical short-term scintillation distribution model," *Electron. Lett.*, vol. 36, pp. 663-664, 2000.

[23] H. Vasseur, "Prediction of tropospheric scintillation on satellite links from radiosonde data.," *IEEE Trans. Antennas Propagat.*, vol. 47, pp. 293-301, 1999.

[24] D. J. DeFatta, J. G. Lucas, and W. S. Hodgkiss, "Digital Signal Processing - A system design approach," John Willey & Sons, 1988.

[25] M. Filip and E. Vilar, "Optimum utilization of the channel capacity of a satellite link in the presence of amplitude scintillations and rain attenuation.," *IEEE Trans. Commun.*, vol. 38, pp. 1958-1965, 1990.

[26] T. J. Moulsley, J. Haddon, P. Lo, and E. Vilar, "Measurement and modelling of the probability density function of amplitude scintillations on an X-band satellite down-link.," *Electron. Lett.*, vol. 17, pp. 625-626, 1981.

[27] G. Ortgies, "Probability density function of amplitude scintillations," *Electron. Lett.*, vol. 21, pp. 141-142, 1985.

[28] D. Mertens and D. Vanhoenacker-Janvier, "Instantaneous frequency scaling ratio statistics for scintillation during rain," *Electron. Lett.*, vol. 36, pp. 1424-1425, 2000.

[29] I. E. Otung and B. G. Evans, "Short-term distribution of amplitude scintillation on a satellite link," *Electron. Lett.*, vol. 31, pp. 1328-1329, 1995.

[30] S. A. Khan, A. N. Tawfik, and C. J. Gibbins, "Short-term amplitude scintillation at 97 GHz on 6.5 urban link," *Electron. Lett.*, vol. 36, pp. 1654-1656, 2000.

[31] J. W. Strohbehn, T. Wang, and J. P. Speck, "On the probability distribution of line-of-sight fluctuation of optical signals," *Radio Sci*, vol. 10, pp. 59-70, 1975.

[32] M. M. J. L. v. d. Kamp, "Asymmetric signal level distribution due to tropospheric scintillation," *Electron. Lett.*, vol. 34, pp. 1145-1146, 1998.

[33] Matlab, *statistics toolbox manual: jbtest.*

[34] OPEX, "Second workshop of OLYMPUS propagation experiments: Volume 1: Reference book on attenuation measurement and prediction," Noordwijk November 1994.

[35] Y. Karasawa, M. Yamada, and J. Allnutt, "A new prediction method for tropospheric scintillation on earth-space paths.," *IEEE Trans. Antennas Propagat.*, vol. 36, pp. 1608-1614, 1988.

[36] J. Haddon and E. Vilar, "Scattering induced microwave scintillations from clear air and rain on earth space paths and the influence of antenna aperture.," *IEEE Trans. Antennas Propagat.*, vol. 34, pp. 646-657, 1986.

[37] R. K. Crane and D. W. Blood, "Handbook for estimation of microwave propagation effects - link calculations for earth-space paths," Greenbelt June 1979.

[38] R. S. Cole, K. L. Ho, and N. D. Mavrokoukoulakis, "The effect of the outer scale of turbulence and wavelength on scintillation fading at millimetre wavelengths.," *IEEE Trans. Antennas Propagat.*, vol. 26, pp. 712-715, 1978.

[39] S. M. R. Jones, I. A. Glover, P. A. Watson, and R. G. Howell, "Evidence for the presence of turbulent attenuation on low-elevation angle Earth-space paths - part2: frequency scaling of scintillation intensity on a 10 degree path," *IEEE Trans. Antennas Propagat.*, vol. 45, pp. 85-92, 1997.

[40] E. Vilar, P. Lo, C. Weaver, and M. Smith, "An offsetting technique to study scintillation in direction of arrival in Earth-space paths," presented at URSI Comm. F Symp., Louvain-la-Neuve, Belgium, 1983.

[41] M. M. J. L. v. d. Kamp, C. Riva, J. K. Tervonen, and E. T. Salonen, "Frequency dependence of amplitude scintillation," *IEEE Trans. Antennas Propagat.*, vol. 47, pp. 77-85, 1999.

Chapter 5

TROPOSPHERIC SCINTILLATION AND METEOROLOGICAL VARIABLES

The atmosphere is full of naturally occurring events. In this chapter, the effects of meteorological variables on scintillation are investigated. The focus is on two main areas: quasi-periodic patterns such as diurnal and seasonal variations, and the connection of these patterns of scintillation with weather related variables such as air temperature, pressure, humidity, clouds and precipitation.

5.1 Scintillation and Meteorological Variables

Scintillation effect is due to wave propagation in a natural varying environment. Some noticeable atmospheric events are signs and consequences of this variation. A study of the physics mechanism causing scintillation in dry conditions (chapter 4) has associated scintillation with parameters describing atmospheric turbulence. A remaining area of interest is thus concerned with how these turbulence characterising parameters are correlated with easily measured meteorological variables and weather-related events.

5.1.1 Vertical Distribution Of Meteorological Variables

To establish the properties of turbulent irregularities in the lower atmosphere, some direct measurements have to be relied upon. Temperature, pressure, humidity have been measured near the surface for many years and by different approaches. In the troposphere, their values vary with height. For example, in an

atmosphere at rest without any heat sources, the pressure can be found to decrease exponentially with height, dropping to a fraction $1/e$ of its surface value at a height of approximately 8 km. In unsaturated air, the temperature roughly falls in a linear relationship with height at about 6.5 K per 1 km [1]. The behaviour of water-vapour pressure is more complicated. Ignoring the effect of condensation, it would fall exponentially at the same rate as the pressure. As saturation vapour pressure decreases with temperature and condensation occurs above a certain height, the amount of water vapour content in the air will be reduced dramatically. Water vapour pressure thus decreases more rapidly with height than pressure.

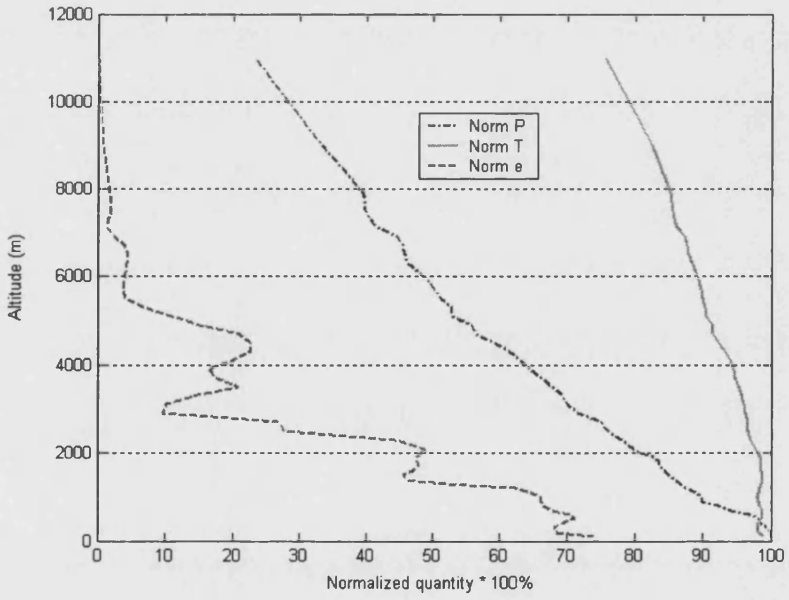

Figure 5. 1 Example of meteorological variables vertical profile from radiosonde measurements of 06hr launch on 02/07/1999

An example of vertical profiles of pressure (P), temperature (T) and water vapour pressure (e) is shown in Figure 5. 1, where the value of variable have

been normalized to 100 percent by their values at surface for presentation convenience. Temperature and pressure appear to follow a linear relationship with height very well. Water vapour pressure profile, however, cannot be modelled accurately by a simple linear function of altitude.

5.1.2 Seasonal and Diurnal Variation Of Meteorological Variables

Figure 3.1 has presented a geographical summary of measurement locations.

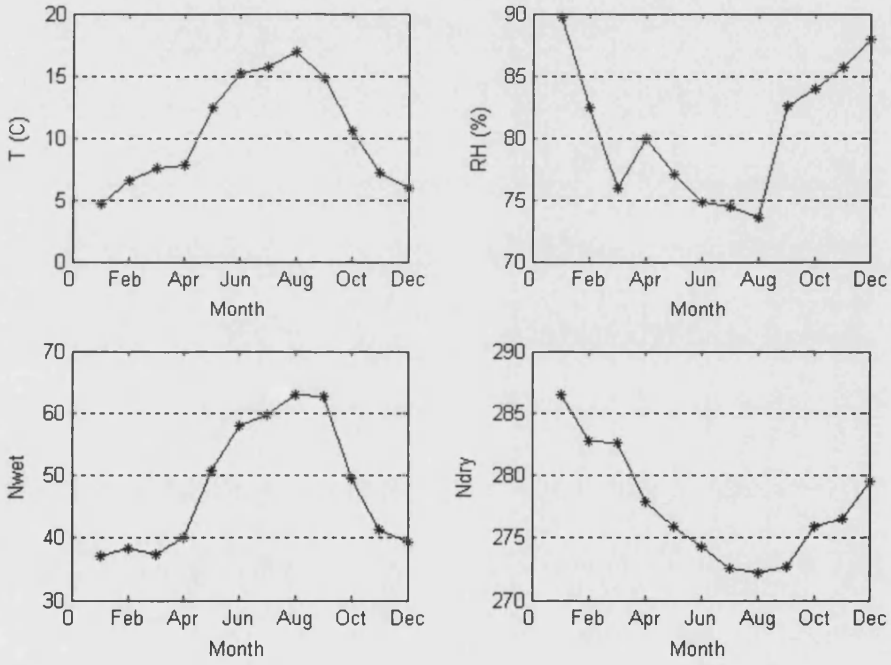

Figure 5. 2 Seasonal variation of temperature (°C), relative humidity (%), wet term of refractivity (Nwet) and dry term of refractivity (Ndry) of the year 2000.

Since all the sites are positioned in the humid oceanic climate zone as classified originally by Koppen [2], the four marked seasons can be referred, in relation to the calendar months as follows: spring (March - May), summer (June - August), autumn (September - November) and winter (January, February and December).

Monthly mean values of surface measured meteorological variables are summarized in Figure 5. 2.

Temperature and relative humidity have been measured directly using meteorological sensors at the surface, while wet and dry terms of refractivity are calculated using formulas given by the ITU-R [3]. Mean values of these variables as a function of the hour of the day is shown in Figure 5.3.

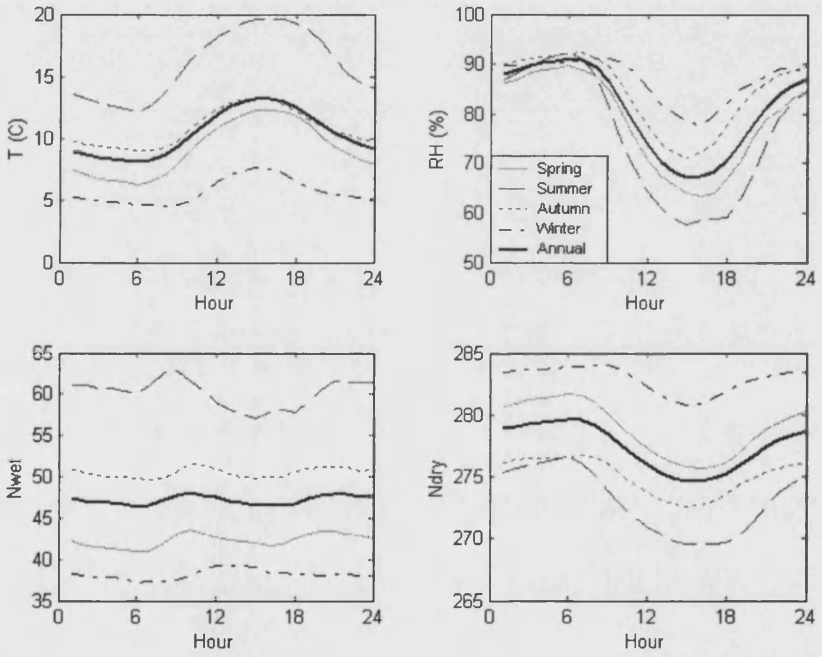

Figure 5. 3 Diurnal variation of temperature (°C), relative humidity (%), wet term of refractivity (Nwet) and dry term of refractivity (Ndry) of the year 2000: Spring (solid line), Summer (dash line), Autumn (dotted line), Winter (dash dotted line) and annual (bold line)

The local solar noon in Middle-wallop occurs at about 12 GMT, whose occurrence can be found generally early in winter and late in summer by a few minutes difference. Due to the warming effect of solar radiation during the day, the air temperature reaches its maximum normally two to four hours after noon as we observed. Highest relative humidity has been found occurring in the early

morning during the coolest part of the day, while lowest humidity is found during the warmest part of the afternoon. The lag between the time of maximum solar heating and the time of maximum air temperature several meters above the surface depend on a shallow layer of air in contact with the ground. It has been reported that cloudiness or haze can cause the temperature maximum to occur earlier [4].

Variations of meteorological variables will result in the instability of the air, which is directly related to the environmental lapse rate (rate of air temperature decreasing with height). The atmosphere is stable when air aloft warms or when surface air cools. The atmosphere may become unstable when either air aloft cools or surface air warms. A layer of air may also be made less stable by turbulent mixing, caused by convection or wind-induced turbulent eddies. The stability of the air changes during the course of a day. In clear calm weather around sunrise, surface air is normally colder than the air above it due to radiation cooling of the surface during the night and the air close to the ground is consequently quite stable. As the day progresses, solar radiation warms the ground and the temperature near the ground increases, the lower atmosphere thus gradually becoming less stable. Maximum instability usually occurs during the hottest hours of the day. It is therefore expected that the variations of meteorological variables will have effect on scintillation and result in similar variations with seasons and time of the day, which can be observed on the received signal fluctuation intensity.

5.1.3 Seasonal and Diurnal Variation Of Scintillation

The monthly mean scintillation intensity has been calculated from measurements at three frequencies for the year 2000 and is shown in Figure 5. 4. There are 12 months of valid data recorded for the 20 GHz beacons, 8 months for 40 GHz and 7 months for 50 GHz. Comparison of these measurement can be viewed

both vertically and horizontally. In the horizontal direction, for the 20 GHz measurement, maximum scintillation intensity has been found in August with the minimum occuring in January, which agrees very well with those of the monthly mean surface temperature and wet term of refractivity. Although valid data are limited for higher frequencies, a similar trend of variation throughout the year has been revealed. In the vertical direction, beacons operating at higher frequencies were found to have experienced more intense scintillation. Scintillation intensity increases more quickly from 40 GHz to 50 GHz than from 20 GHz to 40 GHz. Among the months that beacons were recorded at all the three frequencies, the variation range of scintillation intensity has also been shown to increase with carrier frequency, e.g. between August and April, are found increasing with frequency, 0.0173 dB for 20 GHz, 0.0371 dB for 40 GHz and 0.0416 dB for 50 GHz. The observed values of scintillation intensity have been consistent with published results in [5] and [6].

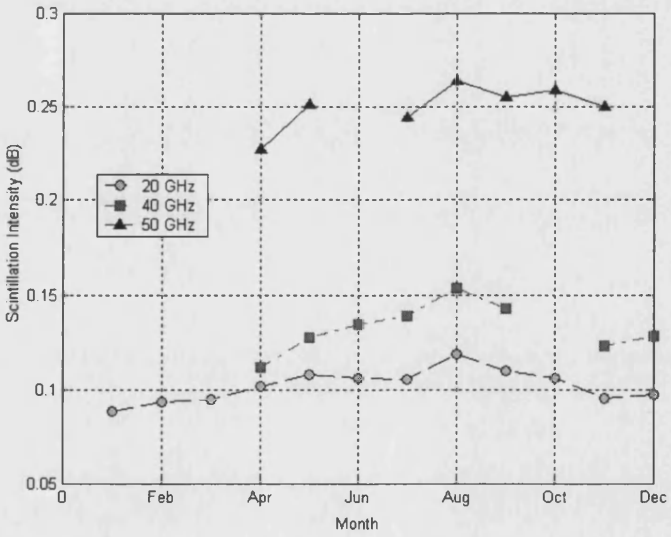

Figure 5. 4 Seasonal variation of scintillation intensity for the year 2000

Diurnal variations of scintillation could be taken advantage of in the design and use of slant path communications system if the variation were repeatable [7]. This can be explained, for example, by its potential importance for commercial transmissions in the context of statistics conditioned on working hours, differential tariffs for day and night etc. [8]. However, this issue has yet to be addressed by the ITU-R.

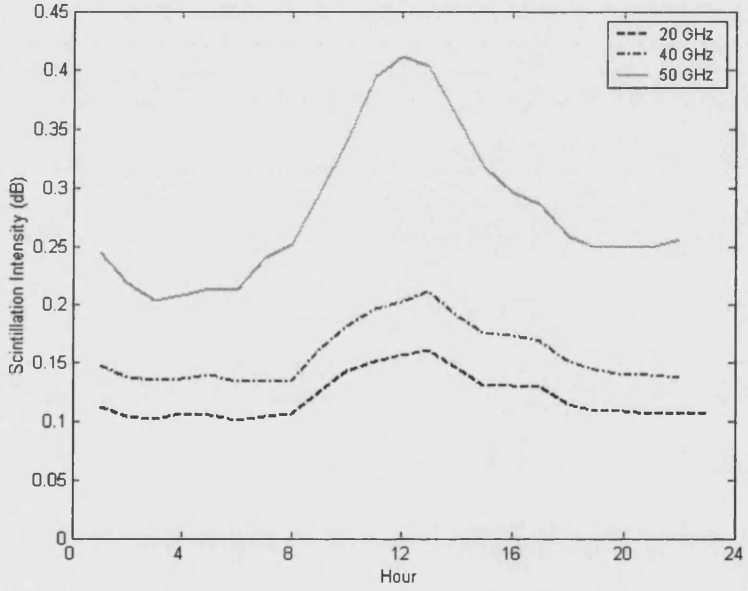

Figure 5. 5 Diurnal variation of scintillation for August 2000

Mean scintillation intensity as a function of the hour of the day calculated for August 2000 is shown in Figure 5. 5. Diurnal varying patterns of scintillation intensity have been observed repeatedly through the month. A strong peak existing between 12.00 and 13.00 hours can be identified for all three frequencies. A second peak, relatively rather weak can be seen close to midnight, which has been consistent with previous observations reported in the literature [9]. Differences between maximum and minimum values of the hourly averaged scintillation intensity appear to increase as operating frequency rises, up to 0.2 dB

for 50 GHz beacons. The second peak of the intensity also gets more intense as frequency increase, especially at 50 GHz. It can be expected that spread of diurnal variation for different time intervals (e.g. every 2 hours or longer time averaging) is expected to decrease as time slot width increases.

5.2 Scintillation And Simultaneous Rain Events

Hydrometeors comprise particles such as fog, rain, hail and snow, formed by the condensation of atmospheric water vapour. Among them, rainfall occurs most often in the climate region in which our measurement sites are located. For satellite communication system designed with low power margins, statistical relationship between concurrent rain attenuation and scintillation are needed to efficiently utilize a given system capacity as in very small aperture terminals (VSAT) at 20-30 GHz [10]. The knowledge of such relationship can also improve the instantaneous frequency scaling of attenuation by separating rain effects from turbulence effects [11]. In the literature, the statistical relationship between rain and scintillation is controversial [10], [11] and [12]. To carry out this investigation, we have used our experimental beacon data together with the rain gauge measurements at Chilbolton.

5.2.1 Rain Measurements at Chilbolton

Drop size, shape and orientation distributions of rain particles are important quantities in the study of rain effects on radiowave propagation. Rainfall is a natural, time-varying phenomenon. Distribution of raindrops can vary both within and between individual rain events. The diameter of a typical raindrop is 2 mm compared to 20 μm for a cloud droplet [4]. Smallest drops may be equivalent to those found in clouds and largest drops will reach 4 mm in radius. (Drops with radii > 4 mm are hydro-dynamically unstable and break up [13].) Observations show that on average, the drop size distribution is a relatively stable function of rain-rate. Measurements carried out with fast-response rain gauges have indicated

that rainfall of high intensity tends to be constrained to short periods of time, typically a few minutes. Consequently, experimental cumulative distributions of rainfall intensity depend on the integration time employed.

As a rain cell moves across a rain gauge, the measured rain rate varies with time due to both the advection of the spatial pattern of rain and changes that occur within that pattern during the time required for the cell to pass over the rain gauge [14]. Rain rate measurements of year 2000 at Chilbolton are shown in Figure 5. 6, in the form of annual and seasonal cumulative distributions. The distance between Sparholt and Chilbolton is 8 km. This is greater than the 'diameter' of a typical rain-cell, so the two sites are unlikely to simultaneously experience the same rain intensity. The distance between them is short enough, however, to provide accurate annual and seasonal rain statistics for Sparsholt.

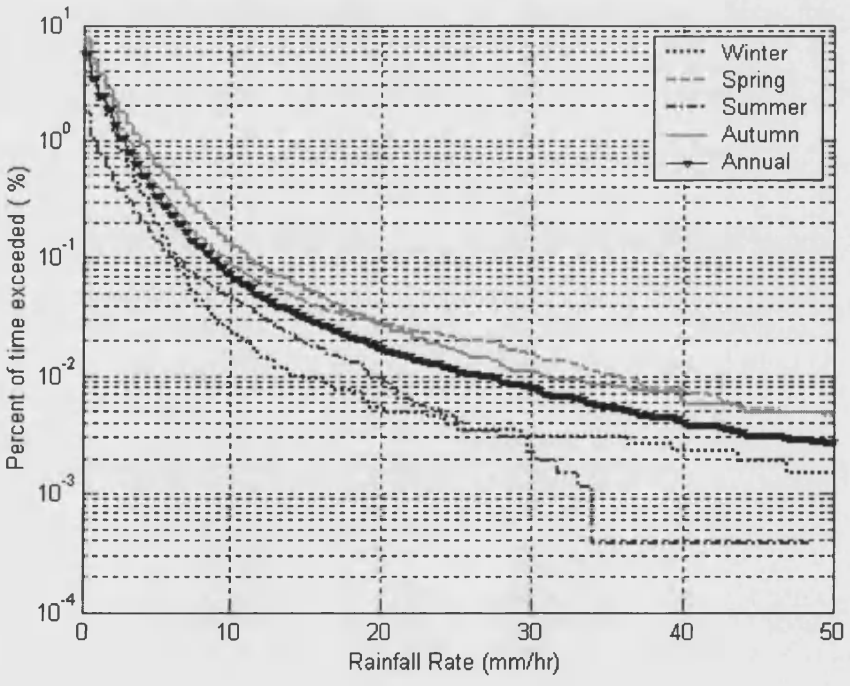

Figure 5. 6 Annual rain rate cumulative distribution for the year 2000

From Figure 5. 6, for a given percentage of time, rain appears to be more intense in spring and autumn and less intense in summer and winter. The integration time of rain-rate measurement is 30 s. It can be seen that on an annual basis, rain events recorded at our measurement site using these rain gauges (located at the surface) occur up to only 6% of total time. Results have shown that over a long-term period, the rain event demonstrates a seasonal and diurnal dependence. In the year 2000, January, March, June, July and August had the smallest amount of rain and rain tended to occur in the day-time, especially around 15:00 hr to 21:00 hr. For the remaining 94% of the total time either no rain occurred or rain occurred only aloft along the path – the rain-drops evaporating before reaching the surface or encountering rapidly rising air. The latter situation may have as much consequence to the transmitted signals as observed rain events, but are not registered at the rain gauge.

5.2.2 Frequency Dependence of Rain Attenuation

A typical example of rain attenuation from ITALSAT beacon measured at Spino D'Adda, 07/01/1994 at three frequencies is shown in Figure 5. 7. Stronger attenuation effects are observed at higher frequencies but significant correlation exists between all three frequency-pairs. The attenuation correlation coefficients are 0.9790 between 20 and 40 GHz measurements, 0.9696 between 20 and 50 GHz measurements and 0.9939 between 40 and 50 GHz measurements.

The instantaneous ratios of rain attenuation between the three frequency pairs are shown in Figure 5. 8. There are three noticeable peaks in the first two plots, which correspond to similar peaks of attenuation in Figure 5. 7. The third plot, however, does not display a similar trend and even suggests an opposite trend. Mean values of the ratio are marked beside the legend of each subplot.

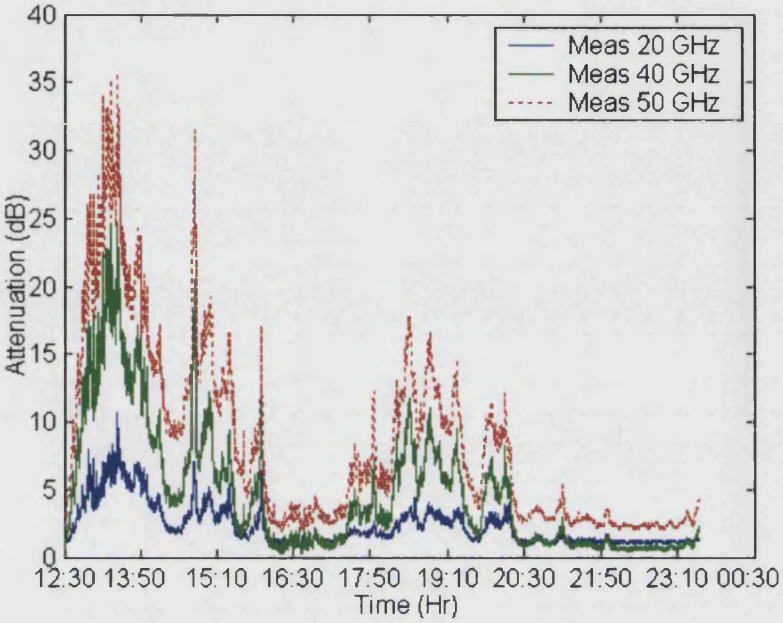

Figure 5. 7 Measured rain attenuation at three frequencies

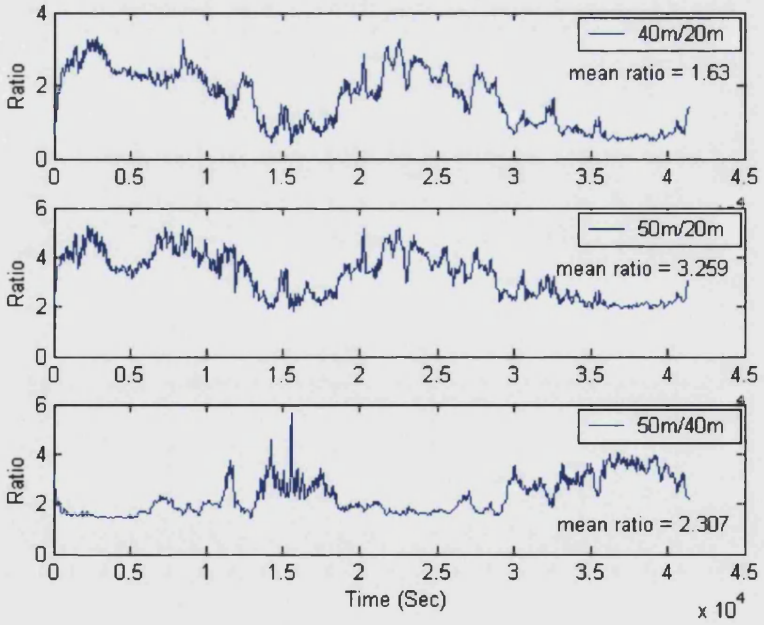

Figure 5. 8 Ratio between measure rain attenuation (data denoted as m) for three frequency pairs

For long-term rain attenuation statistics, the ITU-R recommends an equi-probable frequency scaling law [15]. Given A_1 and A_2 are the equi-probable values of rain attenuation at frequencies f_1 and f_2, frequency scaling on the same path in the frequency ranges 7 to 55 GHz is given by:

$$A_2 = A_1(\varphi_2 / \varphi_1)^{1-H(\varphi_1,\varphi_2,A_1)} \tag{5. 1}$$

$$\varphi(f) = \frac{f^2}{1+10^{-4f^2}} \tag{5. 2}$$

$$H(\varphi_1,\varphi_2,A_1) = 1.12\times10^{-3}(\varphi_2/\varphi_1)^{0.5}(\varphi_1 A_1)^{0.55} \tag{5. 3}$$

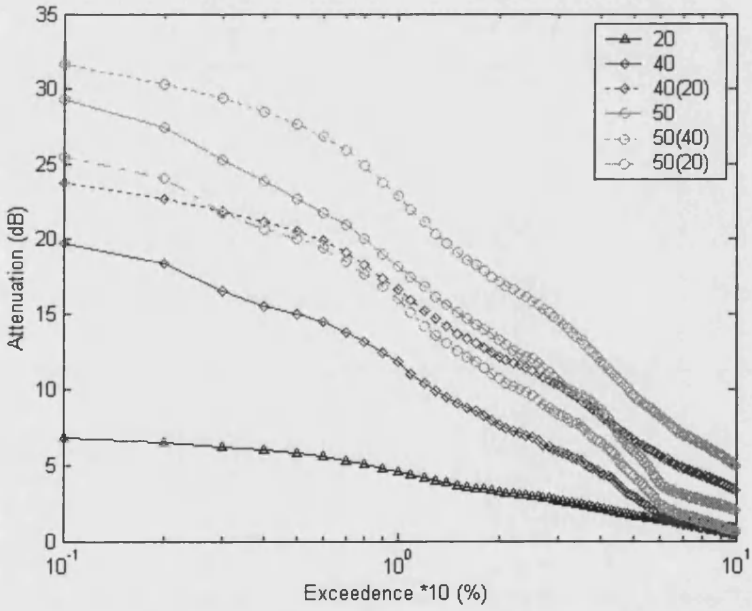

Figure 5. 9 Example of rain attenuation frequency scaling using ITU-R model

Results of frequency dependence of rain attenuation using ITU-R model are shown in Figure 5. 9. Solid lines are measurements at three frequencies, dotted lines are predictions using 20 GHz data as the known signal (marked with 20 in bracket) and dash-dot lines are predictions using 40 GHz data (market with 40 in bracket).

5.2.3 Power Spectrum of Measured Time-series during Rain Events

Vanhoenacker has observed that during rainy conditions, three different regions can be identified within the frequency spectrum: a low-frequency region decreasing with frequency, a flat region and finally a high-frequency region exhibiting the -80/3 dB/decade slope [16]. The three regions are separated by two corner frequencies. By applying the synthetic storm concept, Matricciani predicts the power spectrum of rain attenuation has a slope of –20 dB/decade up to a higher frequency when turbulence effects dominate. The bandwidth of the rain attenuation spectrum depends on the storm translation speed along the path [17]. Ortgies has illustrated that the -80/3 dB/decade slope of scintillation spectrum is observed for wet scintillation which is similar to that for dry scintillation [18].

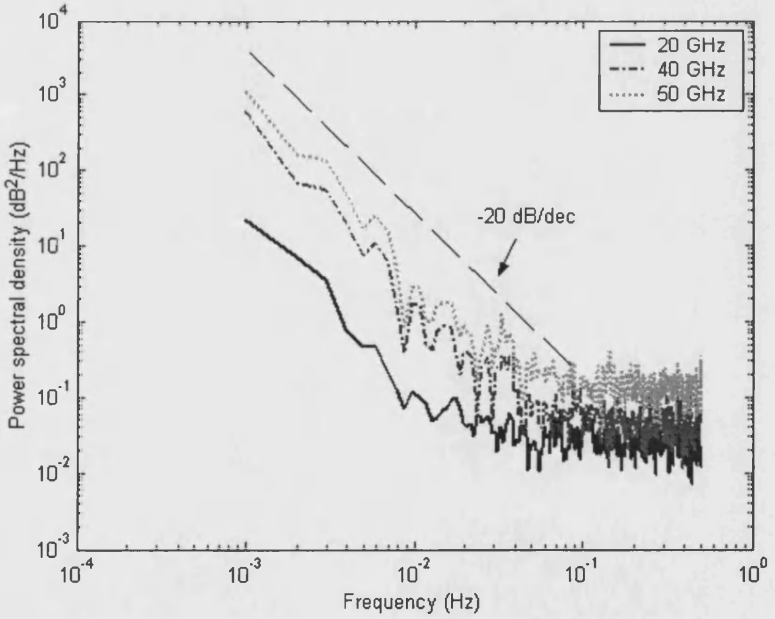

Figure 5. 10 Power spectrum of a rain event on 04/26/2000

Figure 5. 10 shows power spectrum measured during a rain event at three frequencies. The spectra have similarities. The –20 dB/decade slope predicted for

rain agrees well with the measurements and is dominant compared to other attenuating effects over the lower frequencies. For frequencies greater than about 0.01 Hz, the averaged spectrum shows a marked deviation from the –20 dB /decade slope, and we regard this to as indicating the start of scintillation. More results suggest that the two phenomena of rain and scintillation are usually separated for frequency. The spectrum of rain-induced amplitude fluctuations may extend beyond the frequency where scintillation becomes significant, however, only under certain conditions as shown in Figure 5. 11.

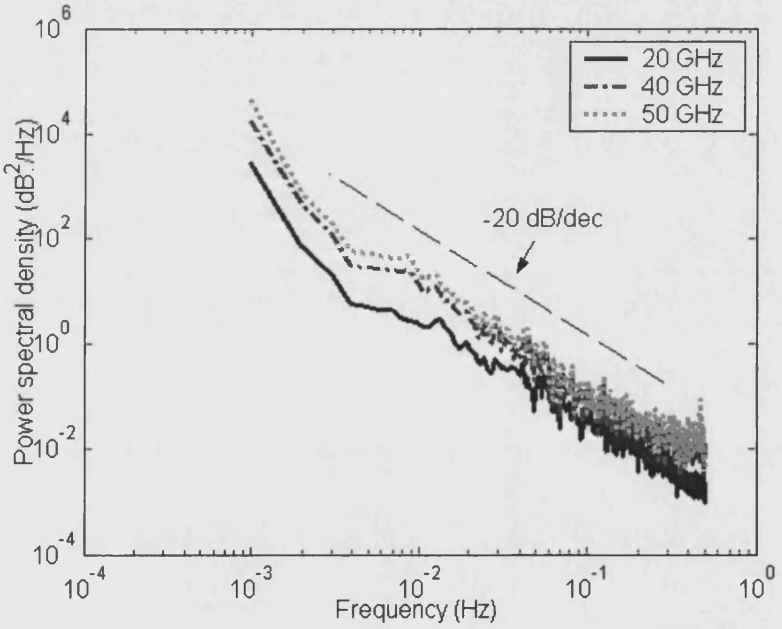

Figure 5. 11 Power spectrum of a rain event of CP940107.DAT

By reviewing the results of Chapter 4, under dry conditions the frequency spectrum above 0.01 Hz has the characters predicted by clear-air (turbulence-induced) scintillation. From our observation here, under certain rain conditions, the rain-induced spectrum may extend outside 0.01 Hz overlapping with the scintillation spectrum. In such cases, the attempt to find a cut-off frequency to separate the two effects completely will be futile. The conventional de-raining

process (based on filtering) retains significant utility, however, since it has the ability to exclude the bulk of the power in the frequency spectrum due to rain.

5.2.4 Relationship Between Wet Scintillation Intensity and Concurrent Rain Attenuation

Traditionally, scintillation has been analysed using data excluding rain periods. This is due to one, more or all of the following reasons: i) There was the early notion that rain and scintillation occurred at mutually exclusive time. ii) It was found difficult to discriminate scintillation from signal level variation caused by rain [19]. iii) Rainy periods only account for a small fraction of the time and will not be statistically important for scintillation. iv) Within the duration of rain event, signal fading due to rain is typically much worse than other atmospheric impairments for system operating at frequencies above 10 GHz [20] and thus scintillation during these periods deemed to be an insignificant problem. For a system requiring high availability using a fixed link margin, knowledge of the statistical dependence of scintillation on rain attenuation is important in designing a strategy of efficient channel utilization [10], since the two mechanisms represent significant fading effects on satellite links at 20/50 GHz band [21].

Rain attenuation and dry scintillation are normally treated separately, because the occurrence mechanisms of these effects are entirely different. It is now usually accepted, however, that both effects occur concurrently. Scintillation during simultaneous rain fading is often referred to as wet scintillation. There have been different points of view regarding the dependence between rain attenuation and scintillation in the literature. Filip and Vilar assumed that the two effects are statistically independent in the development of their global fading statistical model [10]; Karasawa found that the magnitude of scintillation increases slightly during light rain but proposed that the effects of rain attenuation and scintillation could be treated independently [12]; Matricciani suggested that during rain the relationship between scintillation and rain attenuation can be described by a

power law, expressed as Equation (5.4), derivable from a turbulent-thin layer model and based on beacon measurements at 12.5, 19.77 and 49.5 GHz [11], [22], and [23].

$$\sigma_\chi = CA^{5/12} \tag{5.4}$$

Where σ_χ in Equation (5.4) is the scintillating signal standard deviation in dB, A is the rain attenuation in dB and C is a constant. Under the thin layer model assumption that thin turbulent layer simulate cloud turbulence in rain conditions. Mertens and Vanhoenacker have found that the long-term magnitude of tropospheric scintillation steadily increases with worsening rain attenuation [24].

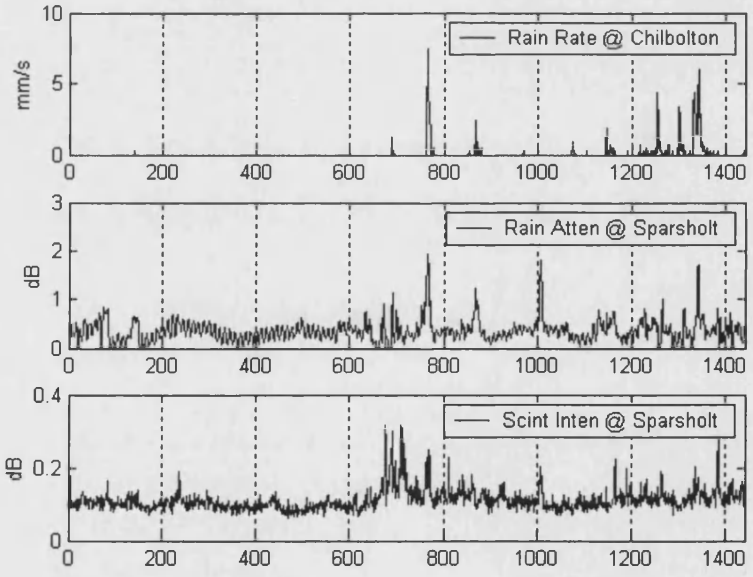

Figure 5. 12 Rain attenuation and scintillation intensity 20GHz time-series from beacon measurement at Sparsholt compared with measured rain rate at Chilbolton on 05/17/2000

Figure 5. 12 shows rain attenuation and scintillation intensity time-series on 05/17/2000 from 20 GHz beacon measurements at Sparsholt compared with rain rate measurements from Chilbolton. Scintillation intensity has large values when rain emerges, and this value appears to increase with increased rain attenuation during light rain.

To further assess whether, and to what extent, the two phenomena are statistically correlated, rain attenuation has been divided into 0.2 dB wide bins and the averaged scintillation intensity corresponding to the points in each bin are plotted as a scattergram, Figure 5. 13. The coefficient of Equation (5.4) is given as $C = 0.075$ (for $A \in [1,3]dB$) and $C = 0.056$ (for $A \in [3,10]dB$) by Matricciani for 49.5 GHz measurement. The value obtained for our experiment is $C = 0.190$. In general, scintillation is more intense during rainy than dry conditions. At this point, our observation supports that scintillation is associated with thin turbulence layer.

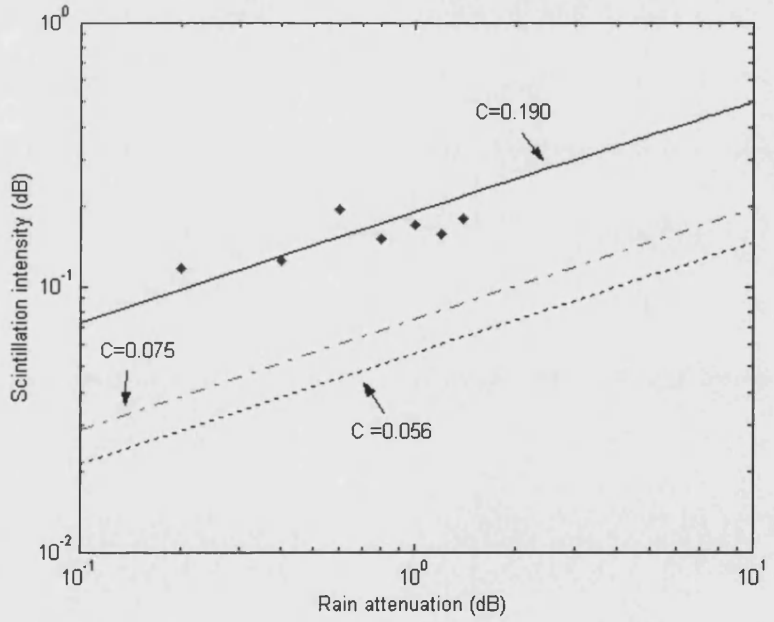

Figure 5. 13 Experimental averaged scintillation intensity and corresponding rain attenuation for 20GHz beacon measurements for 34 rain events

There is another kind of rain that can exist on the path but is absent from surface scalar rain measuring equipment such as the rain gauge. It is produced by clouds in the same way as normal rain. The raindrops break into small liquid droplets and evaporate before reaching the ground, however, either due to strong updrafts or due to under-saturation in some region between the cloud and the ground. Since this type of rain is correlated with the presence of cloud, its effects may sometimes have been ascribed to cloud directly. In the next part of Chapter 5, an investigation of scintillation related to cloud is reported.

5.3 Scintillation And Simultaneous Cloud Events

Additional to rain, clouds represent a second type of atmospheric moisture, which contain various forms of water. They reflect (or scatter) solar radiation and absorb the Earth's infrared energy and play an important role in regulating the Earth's energy balance. On average, clouds cover nearly 50% of the Earth's surface [25]. They are closely associated with rainfall, of course, since without it, there would be no precipitation. In contrast to clear air turbulence, clouds provide visual indication of the physical processes taking place in the atmosphere and make the current movement visible.

The appearance of a cloud depends, to a great extent, on the nature of its constituent particles and also on the concentration of water present, both of which are largely controlled by the temperature. Ten detailed categories of cloud are reported. These are divided into high altitude clouds types: cirrus (CI), cirricumulus (CC), cirrostratus (CS); middle altitude clouds: altocumulus (AC), altostratus (AS); and low altitude clouds: nimbostratus (NS), stratocumulus (SC), stratus (ST), cumulus (CU) and cumulonimbus (CB). Further details of these cloud types and their unique characters are explained in Appendix B.

Long-term observation by weather forecasters and meteorologist indicates that CU and CB are clouds that contain higher density of moister. Large amounts of

energy are released by condensation of water vapour within a CU/CB cloud and result in the development of violent up and down drifts. Therefore, these two types of clouds normally have vertical development and large convection currents are often found beneath them. It was also suggested that heavy dense clouds containing large amount of liquid water and water vapour have refractive index values significantly different from the surrounding clear air [26]. These facts seem to indicate the occurrence of CU/CB clouds and their liquid water density may be closely related to scintillation effect.

5.3.1 Cloud Observations

The UK Met Office surface weather records at Middle-wallop include observations of the above clouds coverage (amount). The time resolution of these reports is 1 hour. For each observation time, the amounts of CU and CB indicate the portion of sky being covered by these clouds, and the unit is hence referred to as Oktas. Monthly mean coverage of CU and CB in 2000 is plotted in Figure 5. 14. The mean coverage is calculated by averaging the observed amount over a month expressed in percent.

Cumulus occurs more often than cumulonimbus during the period of observation. In general, significant seasonal variations in their distribution can be identified for both cloud types, with the least cloud coverage can be found during coldest months (December and January).

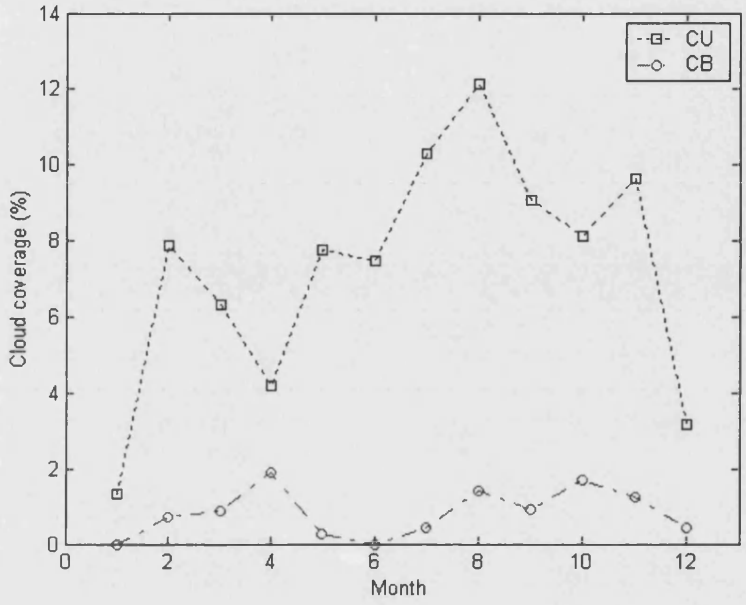

Figure 5. 14 Monthly mean Cumulus and Cumulonimbus cloud amount for the year 2000

Figure 5. 15 presents the hourly mean Cumulus and Cumulonimbus cloud coverage within the year. Unlike hourly temperature and relative humidity measurements, graphs of cloud are not quite smooth, which can be attributed to the cluster and masses nature of cloud and the methods used to record them. Mean Cumulus amount starts to increase after 09.00 hr and arrives at its maximum around 1500 hr before decreasing again until about 20.00 hr when it drops back to its low level. Cumulonimbus appears to have a later and slower increase than Cumulus, whose amount is relatively large between 11.00 hr and 18.00 hr. It is noted that solar noon of middle-wallop is about 12 GMT (but may occur earlier in winter with a few minutes difference from January to December). Concerning the fact that clouds are developed gradually for most of the time, diurnal variations of cloud amount are expected to be smooth compared with monthly mean, which has been consistent with our observation in the graph.

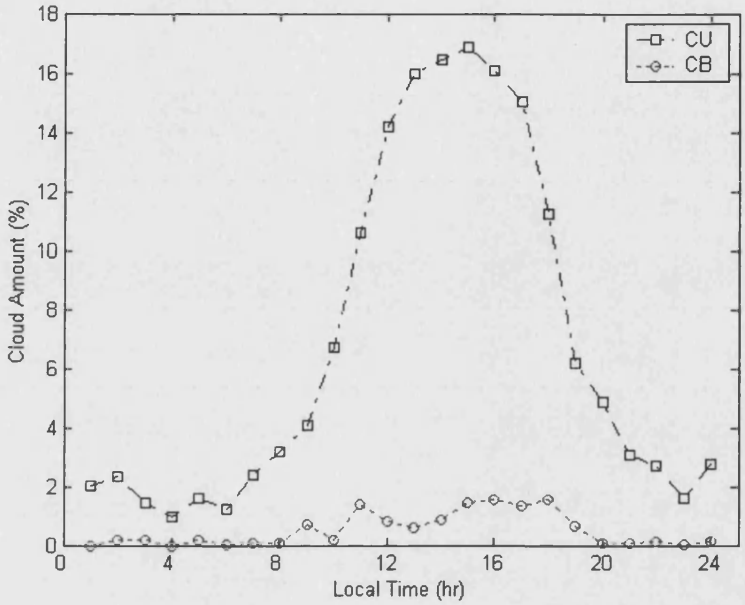

Figure 5. 15 Hourly mean Cumulus and Cumulonimbus cloud amount for the year 2000

5.3.2 Cloud Liquid Water Content and Salonen Model

When considering the effects of cloud on scintillation, the measurement of cloud liquid water path (LWP) is often used, which is defined as the path-integrated liquid water content within each cloud layer. It has been found that LWP has a natural variability especially on a short timescale, and the measured values may depend on the measurement techniques being employed [27]. Since cloud radar and simultaneous lidar data, which are ideally required to measure cloud occurrence or coverage do not normally offer cloud liquid water as a direct observation, a numeric model using height profiles of pressure, temperature and humidity has been proposed by Salonen and Uppala [28] to estimate the occurrence, height and the thickness of clouds, as well as their water content as a function of height. The Salonen-Uppala model involves two steps: they are the detection of cloud using a critical humidity function and the determination of liquid water content using temperature and pressure profile.

The critical humidity function is given as:

$$U_c = 1 - \alpha \cdot \sigma(1-\sigma) \cdot [1 + \beta(\sigma - 0.5)] \quad (5.5)$$

where α = 1.0 and $\beta = \sqrt{3}$, σ is the ratio of pressure at the height in question and pressure at the surface. If the measured humidity is higher than the value of U_c at the same height then cloud is assumed to be present at that height.

An example of cloud inference using the Salonen-Uppala model is demonstrated in Figure 5. 16, based on vertical profile of relative humidity and pressure obtained from UK Met Office Larkhill Radiosonde measurement at 10.00 hr, 10/10/2000. According to the Salonen-Uppala model, a single cloud layer is expected to exist between 825 m and 2430 m above the surface.

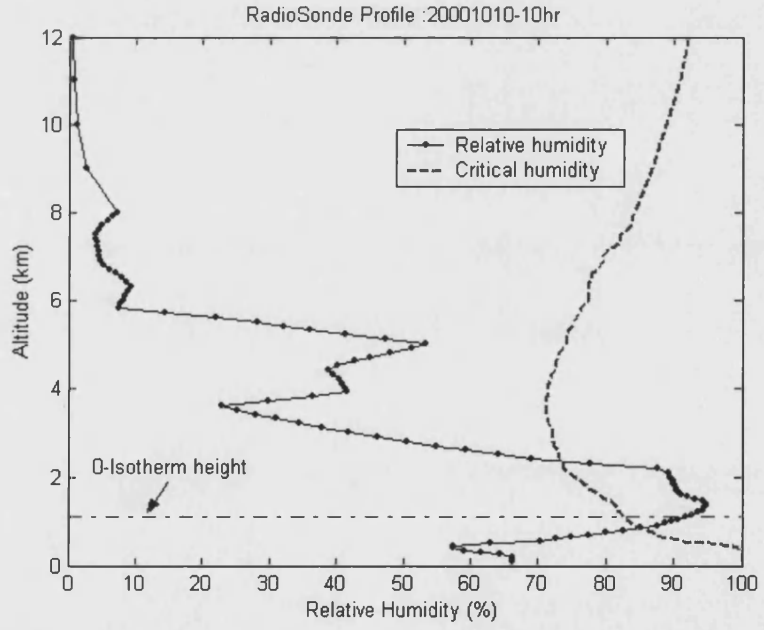

Figure 5. 16 Example of cloud inference using Salonen model

Within the layer of cloud, liquid water content denoted as w (g/m^3), is a function of temperature t (°C) and the given height from the cloud base h_c (m). It can be calculated using:

$$w = w_0(1 + c \cdot t) \cdot \left(\frac{h_c}{h_r}\right)^a p_w(t) \tag{5. 6}$$

where a = 1.4, c = 0.041 /°C and w_0 = 0.14 g/m^3 is the liquid water content, if h_c = h_r = 1500 m at 0°C. Liquid water fraction $P_w(t)$ is approximated by the following function:

$$p_w = \begin{cases} 1 & 0°C < t \\ 1 + \dfrac{t}{20} & -20°C < t < 0°C \\ 0 & t < -20°C \end{cases} \tag{5. 7}$$

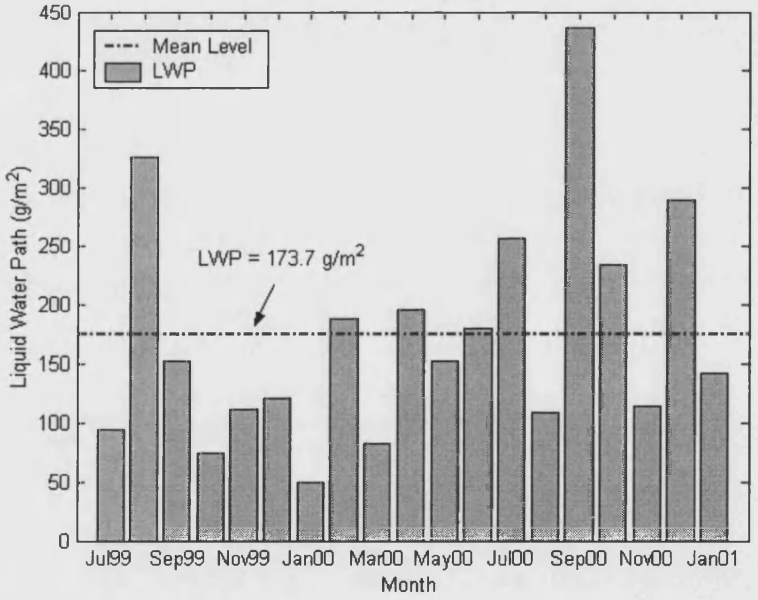

Figure 5. 17 Monthly mean LWP for July 99 – January 01 (19 month)

Figure 5. 17 presents the monthly mean LWP for the whole measurement period (July 1999 – January 2001) with a mean level of 173.7 g/m^2. In general, cold months have lower values of LWP and hot months have higher values of LWP. The two greatest months are August 99 and Sept 00, which are within the anticipation that autumn is habitually a rainy season in southern England and more thicker and heavier clouds are expected. One exception existed in Dec 00, where had the third greatest LWP rising 114 unit above the mean level.

It has been found that there were 17 valid warm-time launchings (between 10.00 hr and 15.00 hr) in Dec 99, counting for 47 % of the total launches, compared with 33 in Nov 99 counting for 56 % and 19 in Jan 01 counting for 44%. Hence, the uneven distribution of radiosonde launch time seems not to be the reason to produce high value of LWP in Dec 99.

5.3.3 Relationship between Scintillation and Cloud

Among the common cloud compositions, water vapour and liquid water content are expected to have possible significant effects on the transmitted signal, as scattering of ice crystals is diminutive for Ka and V band frequencies. It was claimed by Cox, Arnold and Hoffman that clouds are visibly turbulent, and it seemed reasonable to anticipate a clear-air turbulence theory applicable to cloud-produced scintillation events [26]. Marzano and Riva further suggested that cloud liquid water effects on amplitude scintillation in the millimetre wave band are expected to be due to the superposition of an absorption and scattering fluctuation mechanisms [29]. As diameters of cloud droplet (typically 20 μm) are normally very small compared to raindrops (typically 2 mm), and as water droplet scattering effect increases considerably with its agglomerated size, it can be expected that scattering fluctuations produced by cloud liquid water are small compared to that of rain events, and only clouds of high density of liquid water content are likely to have significant effect on received signal fluctuation.

An investigation has been carried out to study each dense cloud event predicted by the Salonen-Uppala model and simultaneous observation of scintillation intensity. Mean cloud liquid water density (g/m^3) is defined as the ratio between total liquid water content (LWP in g/m^2) and total cloud thickness (m). Only clouds of high liquid water density are taken into consideration, which are categorized as clouds of mean density higher than 0.0324 g/m^3. The threshold value of 0.0324 g/m^3 is the annual mean cloud liquid water density of the year 2000. Scatter plot of scintillation intensity (dB) and concurrent cloud mean liquid water density results at 11.00 hr for the year 2000 are shown in Figure 5. 18.

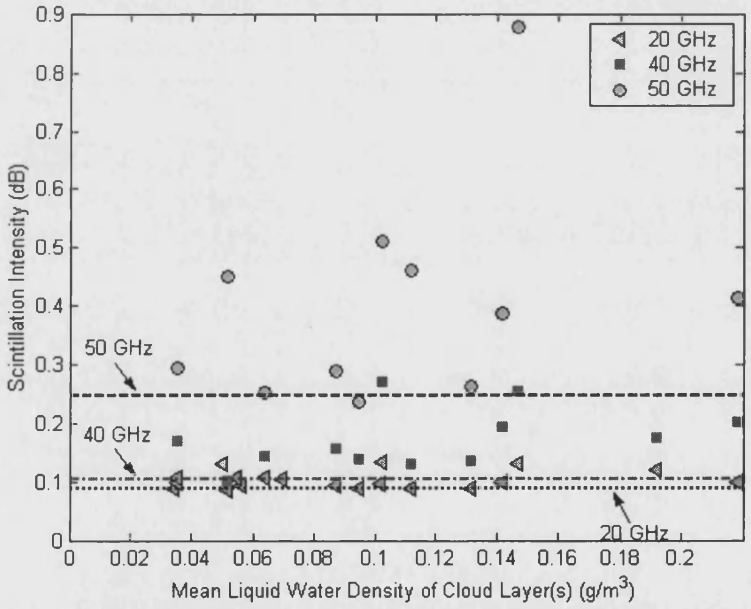

Figure 5. 18 Scatter plot of scintillation intensity (dB) and concurrent cloud mean liquid water density (g/m^3) at 11.00 hr for the year 2000

Scintillation intensities are calculated from beacon recording time series measured within a one-hour period, which is centred at the time of radiosonde ascent. Since scintillation intensity displays significant diurnal variation, fair comparison of the intensity need to be made for a specific measurement time. Observations at 20

GHz, 40 GHz and 50 GHz are marked as triangle, square and circle correspondingly, where x-axis reveals the estimated mean cloud liquid water density in accordance with Salonen-Uppala model and y-axis reveals the averaged scintillation intensity. Straight lines marked using dotted, dash-dot and dash styles are the mean scintillation level for non-cloud events at 11.00 hr for the year 2000.

It can be seen that as frequencies increase the observed scintillation intensity rises, however, for the chosen time of measurement scintillation occurring with high-density cloud appears to have higher intensity compared with scintillation without dense cloud for all the frequencies. Higher cloud liquid density seems to have stronger effect on scintillation for higher frequencies. Correlation coefficients between measured scintillation intensity and measured liquid water content are found to be 0.1589 for 20 GHz, 0.3976 for 40 GHz and 0.3345 for 50 GHz. As values of the correlation are generally low especially for 20 GHz, where our beacon measurement are more reliable, the direction correlation or relationship between scintillation intensity and cloud liquid water density cannot be confirmed from our observation of individual sounding profiles.

5.3.4 Variations of 0 °C-isotherm Height

The available radio sounding profiles have also made it possible to evaluate the height of 0°-isotherm. Isotherms are lines of constant temperature and 0°-isotherm separates above-freezing and below-freezing temperatures. The 0°-isotherm usually locates midway throughout the cloud and moves primarily by thermal advection as has been shown in Figure 5. 16. The 0°C-isotherm heights have apparent variations appear both on a profile-to-profile basis and over a longer period of time such as a month or a season.

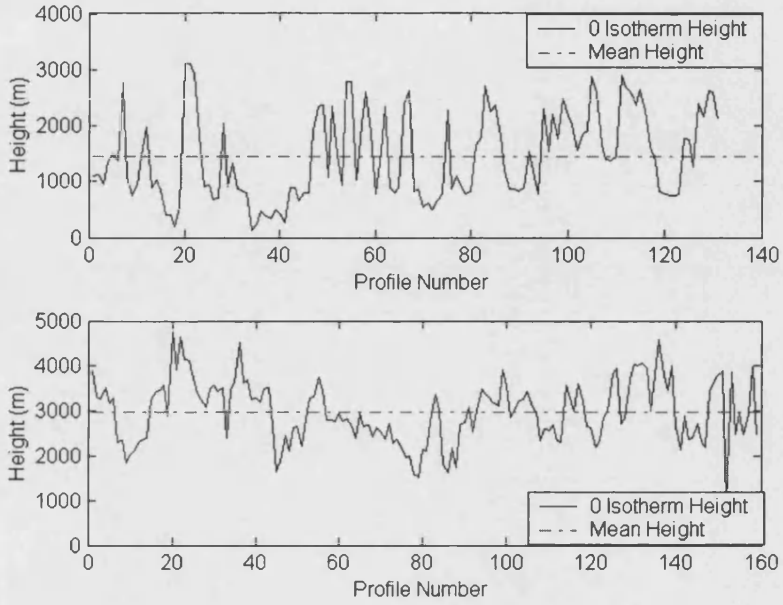

Figure 5. 19 0-Isotherm height in winter and summer of the year 2000

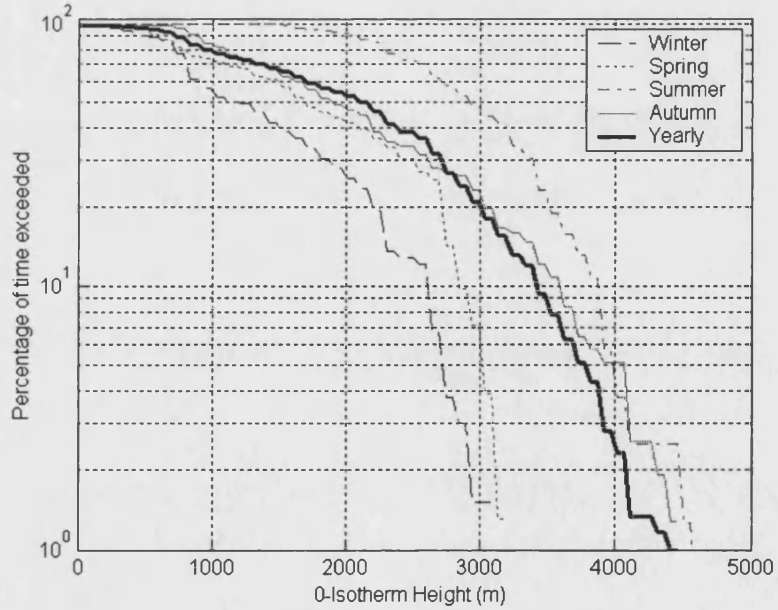

Figure 5. 20 Annual 0-isotherm height exceedence of the year 2000

Figure 5. 19 shows results from sounding profiles of the year 2000 for summer and winter respectively. Despite the fact that radiosonde measurements are taken, at best, four times daily (and sometime only twice daily), the graph indicates a diurnal variation of 0°C-isotherm heights as we expect from diurnal variations of surface temperature. Annual exceedance for the year 2000 shown in Figure 5. 20 reveals clearer variation of 0°C-isotherm heights distribution among four seasons. The corresponding error-bar plot of monthly averaged 0°C-isotherm heights are shown in Figure 5. 21. In general, the 0°C-isotherm heights are lower in winter and higher in summer.

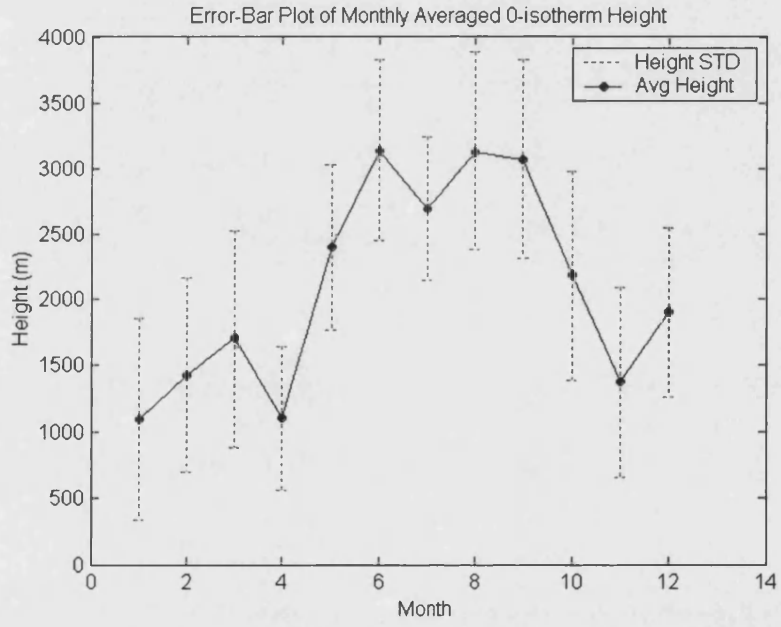

Figure 5. 21 Error-bar plot of monthly averaged 0-isotherm height for the year 2000

5.4 References:

[1] D. H. McIntosh and A. S. Thom, *Essentials of meteorology*: Wykeham publications (London) Ltd, 1969.

[2] R. C. Sutcliffe, *Weather and climate*: Weidenfeld and Nicolson, 1966.

[3] ITU-R, "The radio refractive index: its formular and refractivity data," P. 453-7.

[4] C. D. Ahrens, *Meteorology today - an introduction to weather, climate, and the environment*: West publishing company, 1994.

[5] F. S. Marzano and G. d'Auria, "Model-based prediction of amplitude scintillation variance due to clear-air tropospheric turbulence on Earth-Satellite microwave links.," *IEEE Trans. Antennas Propagat.*, vol. 46, pp. 1506-1518, 1998.

[6] V. d. Kamp, "Climatic radiowave propagation models for the design of satellite communication systems," Technische Universiteit Eindhoven, 1999.

[7] S. Ventouras, C. L. Wrench, and S. A. Callaghan, "Propagation performance of satellite systems derived from measurements in the sough of England," 2000.

[8] A. Paraboni, "Summary of preparation for fixed propagation modelling," *COST 255 Documents*, 1996.

[9] E. Vilar and J. Haddon, "Measurement and modelling of scintillation intensity to estimate turbulence parameters in an earth-space path," *IEEE Trans. Antennas Propagat.*, vol. AP-32, pp. 340-346, 1984.

[10] M. Filip and E. Vilar, "Optimum utilization of the channel capacity of a satellite link in the presence of amplitude scintillations and rain attenuation.," *IEEE Trans. Commun.*, vol. 38, pp. 1958-1965, 1990.

[11] E. Matricciani, M. Mauri, and C. Riva, "Relationship between scintillation and rain attenuation at 19.77 GHz," *Radio Sci*, vol. 31, pp. 273-279, 1996.

[12] Y. Karasawa and T. Matsudo, "Characteristics of fading on low-elevation angle earth-space paths with concurrent rain attenuation and scintillation," *IEEE Trans. Antennas Propagat.*, vol. 39, pp. 657-661, 1991.

[13] T. Oguchi, "Electromagnetic wave propagation and scattering in rain and other hydrometeors," *Proc. of IEEE*, vol. 71, pp. 1029-1078, 1983.

[14] G. Drufuca, "Rain attenuation statistics for frequencies above 10 GHz from raingauge observations.," *J. Rech. Atmos.*, vol. 1, pp. 399-411, 1974.

[15] ITU-R, "Propagation data and prediction methods required for the design of Earth-space telecommunications systems," Rec. P 618-7, 2001.

[16] OPEX, "Second workshop of OLYMPUS propagation experiments: Volume 1: Reference book on attenuation measurement and prediction," Noordwijk November 1994.

[17] E. Matricciani, "Physical-mathematical model of the dynamics of rain attenuation with application to power spectrum.," *Electron. Lett.*, vol. 30, pp. 522-524, 1994.

[18] G. Ortgies, "Slant-path frequency scaling of amplitude scintillation during clear-sky conditions and rain.," *Archivfur Elecktronik and Ubertragungstechnik*, vol. 47, pp. 203-208, 1993.

[19] Y. Karasawa and M. Yamada, "Prediction on statistics for tropospheric scintillations on earth-space paths," presented at 23rd URSI-GA, Prague, Czechoslovakia, 1990.

[20] P. A. Watson and Y. F. Hu, "Prediction of attenuation on satellite-earth links for systems operating with low fade margins.," *IEE Proc. Microwave Antenas and Propgation.*, vol. 141, pp. 467-472, 1994.

[21] E. Vilar, "The dynamic aspects of cm and mm wave propagation and impact on satellite communications above 18 GHz.," presented at IEE Colloquium on Satellite Communications Above 18 GHz, London, 1987.

[22] E. Matricciani, M. Mauri, and C. Riva, "Scintillation and simultaneous rain attenuation at 12.5 GHz to satellite Olympus," *Radio Sci*, vol. 32, pp. 1861-1866, 1997.

[23] E. Matricciani, M. Mauri, and C. Riva, "Scintillation and simultaneous rain attenuation at 49.5 GHz," presented at International Conference on Antenna and Propagation, 1995.

[24] D. Mertens and D. Vanhoenacker-Janvier, "Rain fade dependence model of long-term scintillation amplitude distribution at 12.5 GHz," *Electron. Lett.*, vol. 37, pp. 657-658, 2001.

[25] J. T. Houghton, *The physics of atmospheres*: Cambridge University Press 1997, 1986, 1997.

[26] D. C. Cox, H. W. Arnold, and H. H. Hoffman, "Observation of cloud-produced scintillation on 19 and 28 GHz earth-space paths," *Radio Sci*, vol. 16, pp. 885-907, 1981.

[27] C. L. Wrench, P. M. Simpson, A. J. Gibson, and O. T. Davies, "Statistics of liquid water path in cloud, and slant path propagation loss in cloud at V-band, based on measurement at Chilbolton," presented at 12th International Conference on Antenna and Propagation, Exeter, UK, 2003.

[28] E. T. Salonen and S. Uppala, "New prediction method of cloud attenuation," *Electron. Lett.*, vol. 27, pp. 1106-1108, 1991.

[29] F. S. Marzano and C. Riva, "Analysis of cloud liquid effects on amplitude scintillation along microwave and millimetre-wave links," presented at URSI Commission F meeting on climatic parameters in radiowave propagation prediction, 2001.

Chapter 6

LONG-TERM SCINTILLATION PREDICTION MODELS

This chapter reports on the most commonly used statistical models for long-term scintillation log-amplitude distribution prediction as well as 'empirical' and 'model-based' prediction models for scintillation variance/intensity. For the prediction of scintillation variance, in particular, this chapter represents a comprehensive review comprising 15 models. After the review of each model their performances are compared. Error analysis subsequently leads to an innovative approach to develop a new prediction model for long-term averaged scintillation intensity.

6.1 Long-term Statistics Prediction Model for Amplitude Scintillation

The short-term distribution of scintillation log-amplitude is well-modelled by a Gaussian distribution, whilst the long-term distribution has been found to deviate from the Gaussian distribution significantly. As observation time accumulates, the distribution demonstrates heavier tail on both side of the mean value than Gaussian with slight skew towards signal fading. So far, no distribution model has been proposed, which is suitable to describe the probability behaviour of the signal completely satisfactory.

Alternatively, indirect approaches have been proposed to model the distribution of scintillation log-amplitude conditional on scintillation variance/intensity [1]. Several proposed methods will be presented in this category. A common assumption shared by them is that the short-term scintillation log-amplitude

follows a Gaussian distribution within some stationary period, whilst the long-term log-amplitude scintillation can be considered to have a modified Gaussian distribution with varying standard deviation affected by the variations in the meteorological conditions. Conditional probability is explained in Equation (6.1),

$$P(\chi)=\int_0^\infty P(\sigma_\chi)P(\chi\,|\,\sigma_\chi)d\sigma_\chi \tag{6. 1}$$

Two distributions that model long-term scintillation intensity have been reviewed and investigated in Chapter 4. The PDF and CDF of measured scintillation intensity for the 20 GHz beacon are compared with the best-fit Lognormal and Gamma distribution, plotted using maximum likelihood parameters, in Figure 6. 1 and Figure 6. 2.

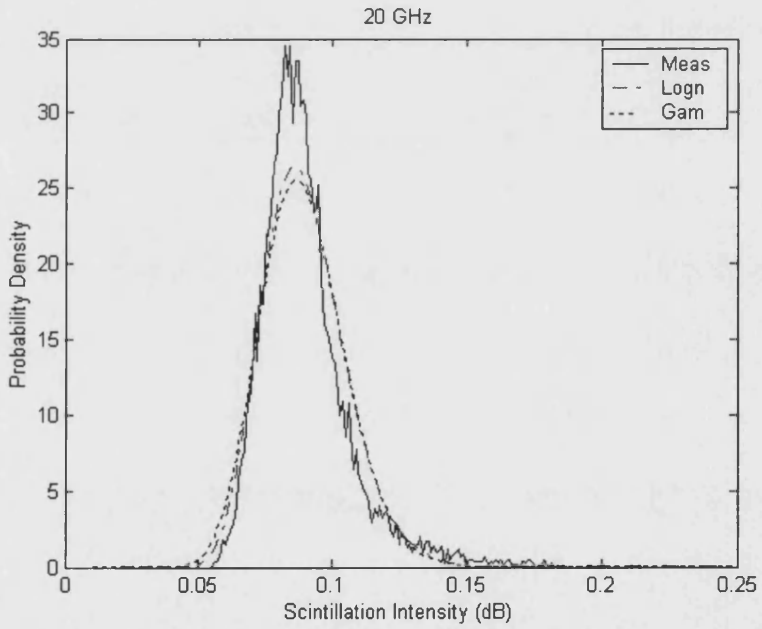

Figure 6. 1 Long-term scintillation intensity distribution compared with best-fit Lognormal distribution and Gamma distribution for 20 GHz

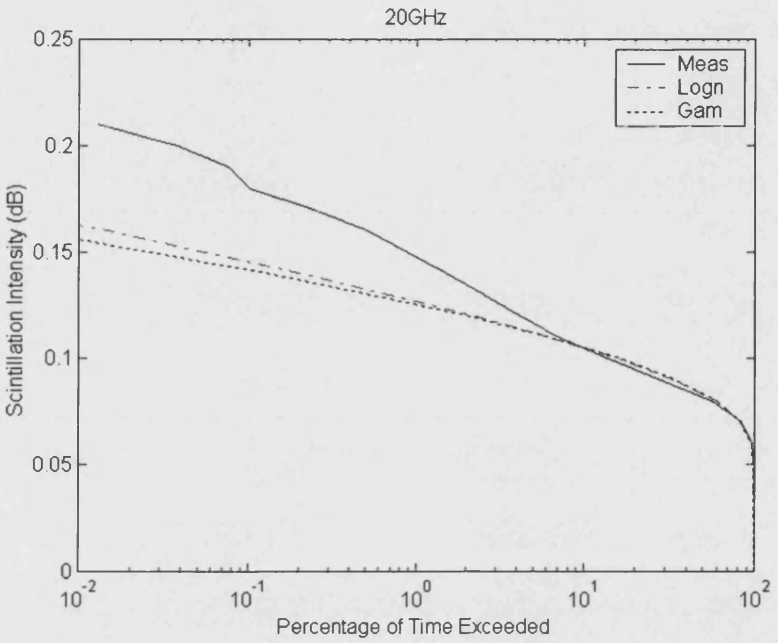

Figure 6. 2 Comparison of scintillation intensity cumulative distributions at 20GHz with best-fit Lognormal distribution and Gamma distribution

For the range of our measured scintillation intensity (0, 0.5), both Lognormal and Gamma distributions have similar shapes with larger tails toward the higher values of data (only values up to 0.21 dB are shown in Figure 6.2). Both are deemed suitable to describe the distribution of scintillation intensity. The two distributions appear to provide accurate estimation for up to 97 % of the time. For higher percentage of time, both models appear to under-estimate the scintillation intensity, the under-estimation increasing with increasing percentage. For example, for 99.9% of time, the under-estimation of intensity exceedence is less than 0.035 dB for the Lognormal distribution and less than 0.038 dB for Gamma distribution.

The disagreement between measured and modelled distributions for scintillation intensity will limit the prediction accuracy of statistical models for scintillation log-amplitude, which employs Lognormal or Gamma distribution in the above conditional probability equation.

By applying either Lognormal or Gamma distribution to model scintillation intensity, three models are selected as representatives for the prediction of long-term log-amplitude scintillation statistics as summarized below. The treatment of these models, presented in chronological order of publication is focused on their mathematical background.

6.1.1 Moulsley-Vilar Model (1982)

Mousley and Vilar proposed a model for long-term scintillation log-amplitude using a modified form of the Gaussian distribution in which the standard deviation is also a random variable. In this model, the physical nature of the scintillation process is taken into account by assuming σ_χ as a band-limited variable with its maximum rate of change depending on the prevailing meteorological conditions [1]. Observation of σ_χ is obtained over a chosen time interval (10 minutes). If scintillation variance σ_χ^2 is assumed to be lognormally distributed as given in Equation (6.2):

$$p(\sigma_\chi)=\frac{1}{\sigma_\chi \sigma_\sigma}\sqrt{\frac{2}{\pi}}\exp\left[-\left(\frac{\ln^2\left(\sigma_\chi^2/\sigma_m^2\right)}{2\sigma_\sigma^2}\right)\right] \tag{6.2}$$

where $\ln(\sigma_m^2)$ is the mean of $\ln(\sigma_\chi^2)$ and σ_σ is the standard deviation of $\ln(\sigma_\chi^2)$. And following the assumption that $p(\chi|\sigma_\chi)$ is normally distributed,

$$p(\chi|\sigma_\chi)=\frac{1}{\sigma_\chi\sqrt{2\pi}}\exp\left[-\left(\frac{\chi^2}{2\sigma_\chi^2}\right)\right] \tag{6.3}$$

The combined distribution using Equation (6.1) will result in the long-term pdf of χ as:

$$\langle p(\chi) \rangle = \frac{1}{2\sigma_\sigma \sigma_m \pi} \int_{-\infty}^{\infty} \exp\left[-\left(\frac{A^2}{2{\sigma_\sigma}^2} + \frac{\chi^2}{2{\sigma_m}^2} e^{-A} + \frac{A}{2} \right) \right] \cdot dA \tag{6. 4}$$

where $A = \ln\left({\sigma_\chi}^2 / {\sigma_m}^2\right)$.

It is noted that the only input required in the Mously-Vilar model for the prediction of $\langle p(x) \rangle$ is ${\sigma_m}^2$ and ${\sigma_\sigma}^2$, which are obtained from the measurements or modelling of scintillation variance. Throughout the approach Moulsley and Vilar adopted, scintillation log-amplitude distribution was deemed to be symmetrically distributed for both signal log-amplitude fading and enhancement.

6.1.2 Karasawa Model (1988)

Karasawa and others have found that scintillation intensity is statistically stationary over periods up to one month with a probability density that approximates a Gamma distribution of mean m and standard deviation σ_{σ_χ}, which vary with transition of the season [2]. The model for scintillation log-amplitude uses a Gamma distribution to approximate the distribution of the scintillation intensity. The principal equations of the Karasawa model are [3]:

$$p(\sigma_\chi) = \frac{\beta^\alpha}{\Gamma(\alpha)} {\sigma_\chi}^{\alpha-1} \exp(-\beta\sigma_\chi) \tag{6. 5}$$

$$p(\chi \mid \sigma_\chi) = \frac{1}{\sqrt{2\pi}\sigma_\chi} \exp\left[-\frac{\chi^2}{2{\sigma_\chi}^2} \right] \tag{6. 6}$$

where $\beta = m / {\sigma_{\sigma_\chi}}^2$, $\alpha = m^2 / {\sigma_{\sigma_\chi}}^2$ and $\Gamma(\cdot)$ is a Gamma function. A linear relationship has been found, experimentally, between the mean variance m and the standard deviation of σ_χ by $m^2 = 10{\sigma_{\sigma_\chi}}^2$. Thus, the Gamma function can be defined by the single parameter m.

Equation (6.5) and (6.6) are combined by Equation (6.1) to give $p(\chi)$. An analytic approximation is provided by Karasawa, however [3]. The signal level X for p % in the cumulative time distribution can therefore be calculated by:

$$X(p) = \eta(p) \cdot m \tag{6.7}$$

As the long-term distribution of χ has been found asymmetrical, $\eta(p)$ for enhancement ($_+$) and fade ($_-$) are found by regression and are given, respectively by:

$$\eta_+(p) = -0.0597[\log(100-p)]^3 - 0.0835[\log(100-p)]^2 - 1.258 \cdot \log(100-p) + 2.672 \quad (for\ 50 < p \le 99.99) \tag{6.8}$$

$$\eta_-(p) = -0.061[\log(p)]^3 + 0.072[\log(p)]^2 - 1.71 \cdot \log(p) + 3.0 \quad (for\ 0.01 \le p \le 50) \tag{6.9}$$

The coefficients of Karasawa model were originally developed using INTELSAT-V satellite beacon received in Japan. It has been found from this measurement database that the Karasawa model distribution of σ_χ fits annual data less well than monthly data. The Karasawa model has been subsequently validated using data from US and UK locations. In 1991, ITU-R has adopted this method for its recommendation of prediction for signal fade depth corresponding to p percentage of time in ITU-R 618-6 [4].

6.1.3 Otung Model (1996)

The Otung model has been derived using experimental scintillation data obtained at Sparsholt (UK) using one-year Olympus satellite beacon measurements. Dependence on time percentage is obtained by detailed regression analysis and both annual distribution and worst-month distribution of scintillation log-amplitude are given [5].

The worst month concept defined by ITU-R is a useful way of presenting statistics [6]. It is designed to enable performance criteria to have reference relevant to an unambiguous period for a radio-communication system. The worst month of a year for a given pre-selected threshold (for any performance degrading mechanism) is defined as the month in a period of twelve consecutive calendar months, during which the threshold is exceeded for the longest time. The worst month is not necessarily the same month for all threshold levels. The worst month distribution is a synthetic peak envelope of monthly cumulative distribution obtained by selecting at each time percentage the maximum value of the parameter exceeded in 12 months.

Otung has also evaluated the model using Olympus satellite beacon data recorded in Germany. The annual distributions are given in Equation (6.10) and (6.11), and worst-month distributions are given in Equation (6.12) and (6.13).

$$X(p)_{-a} = m \cdot 3.619 \exp\left[-\frac{9.50142\times10^{-4}}{p} - (0.40454 + 0.00285p)\ln(p)\right] \quad 0.01 \le p \le 50 \tag{6.10}$$

$$X(p)_{+a} = m \cdot 3.1782 \exp[-0.0359654p - (0.272113 - 0.00438p)\ln(p)] \quad 0.01 \le p \le 50 \tag{6.11}$$

$$X(p)_{-w} = m \cdot 6.8224 \exp\left[-10^{-4}\left(\frac{913.12}{p} + 1.8264p^2\right)\right] \cdot \exp\left[-\left(\frac{0.023027}{p} + 0.51664\right)\ln(p)\right] \quad 0.03 \le p \le 50 \tag{6.12}$$

$$X(p)_{+w} = m \cdot 5.5499 \exp\left[-10^{-4}\left(946.849p + 4.4974p^2\right)\right] \cdot \exp[(0.023573p - 0.261135)\ln(p)] \quad 0.01 \le p \le 50 \tag{6.13}$$

Alternatively, the average annual time fraction of excess can be converted to the average annual worst-month time fraction of excess using model described in ITU-R Rec. 841-2 [7].

Predictions using the three proposed models above are compared with our ITALSAT measurements in Figure 6. 3 and Figure 6. 4 for scintillation amplitude enhancement and fading respectively.

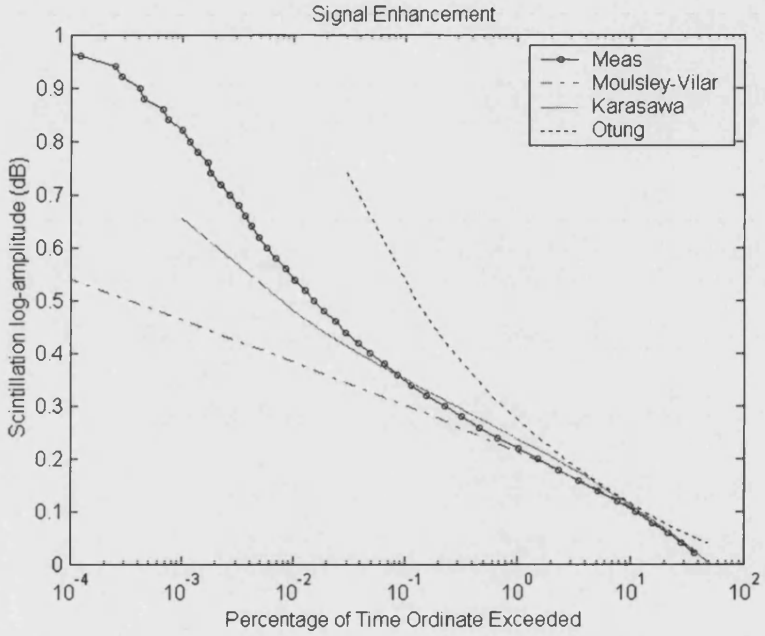

Figure 6. 3 Comparison of scintillation enhancement cumulative distributions measured at 20 GHz with prediction using proposed methods

Figure 6. 3 shows the annual distribution of scintillation amplitude giving the percentage of time in the year that scintillation enhancement exceeds abscissa value. All the models give good prediction for $p > 6\%$. The Karasawa model gives the best prediction among the three models and the figure reveals that weak fluctuation ($\chi > -0.2\,dB$) occurring nearly 99 percent of the fading time.

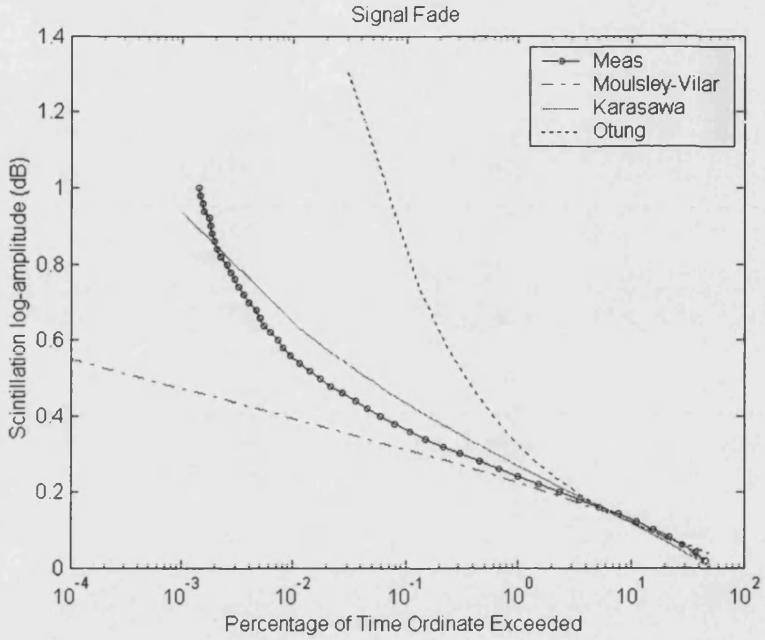

Figure 6. 4 Comparison of scintillation fade cumulative distributions measured at 20 GHz with prediction using proposed methods

Figure 6. 4 shows the annual distribution of scintillation amplitude giving the percentage of time that scintillation fade exceeds the abscissa value. All the models give good prediction for percentage values up to 4 %. The Karasawa model gives the best prediction among the three models, although it under-estimates fading for $p < 4\%$. It reveals that weak fluctuation ($\chi < 0.2dB$) occurring nearly 98 percent of the time, which suggests that strong scintillation fades occur more frequently than enhancements of the same magnitude.

6.2 Prediction Models for Mean Amplitude Scintillation Variance

Until 2000, several models have been proposed to help the system engineer predict monthly mean scintillation intensity values.

Prediction Model	**Year**	**Database Descriptions**
Karasawa Model	1988	14/11 GHz propagation experiment at Yamaguchi, Japan for one year, at elevation angle of 6.5 °, antenna diameter 7.6 m [3]
ITU-R Model	1992	DBSG5 database [4]
Marzano – MPSP & DPSP, STH2 & STN2, STHV2 & STNV2	1998	ITALSAT downlink 18.7, 39.6 and 49.5 GHz beacon acquired in Milan, Italy, elevation angle of 30.6 ° for one year [8]
Otung	1996	Olympus 19.8 beacon received at Sparsholt, UK, at a elevation of 28.74 ° for one year [5]
Tervonen-Kamp-Salonen Model	1998	Olympus 19.8 and 29.7 GHz beacon received at an elevation of 12.7 ° at Helsinki, Finland for a year. All diameters of antenna is 1.8m [9]
Van-de-Kamp Model	1999	Olympus 19.8 and 29.7 GHz beacon received at Helsinki, Finland for a year [10]
Vasseur Model	1999	12.5 and 30 GHz link at elevation angle of 27.6 ° received in Louvain-la-Neuve, Belgium from 1990- 1993 [11]
Ortgies-N Model Ortgies-T Model	1993	Olympus beacon 12.5, 20 30 GHz received by antennas with diameters of 0.6, 1.8 and 3.7m, at Darmstadt in Germany [12]

Table 6. 1 Summary of scintillation intensity prediction models and the used experiment databases

Existing models can be generally grouped into two categories, scintillation intensity/variance prediction models and scintillation log-variance prediction models. Scintillation log-variance prediction models have the underlying assumption that scintillation intensity follows a Lognormal distribution, and the models are formulated as such. Examples of scintillation intensity/variance models are the Tartaskii model [13], the Karasawa model [3], the ITU-R model [4], the Otung model [5], the Tervonen, Van de Kamp and Salonen model [9], the Van de Kamp model [14] and the Vasseur Model. Examples of the scintillation log-variance models are the Marzano models, the Ortgies-T model and the Ortgies-N model [12].

Alternatively, these models may also be classified as 'model-based' and 'empirical'. Although both of these model types use regression analysis to build a scintillation predictor, those that are 'model-based' introduce an atmospheric propagation model to derive the regression coefficients from meteorological measurements such as from radiometer and radiosonde, while those that are 'empirical' are primarily based on the monthly mean surface meteorological measurements.

These models are reviewed in brief below. The original measurements dataset(s) used to derive or assess each model are summarized, where applicable, in Table 6. 1.

6.2.1 Tartaskii Model

The theoretical work of Tartaskii on propagation through turbulent media provides the framework for a predictive model of scintillation variance in terms of refractive index structure function constant. The model assumes that the first Fresnel zone size lies between the inner and outer scale size of the turbulence, and the refractive index structure has a Kolmogorow spectrum. Details of the model have been explained in Chapter 4. In order to calculate σ_χ^2, the structure

constant C_n^2 of refractive index and the effective turbulence path length L would be needed based on instrumental measurements. However, for most practical cases, these parameters are difficult or impossible to measure directly.

An absence of knowledge of these meteorological parameters along the propagation path length has led to the development of semi-empirical models representing the magnitudes and other characteristics of scintillations [15]. The mathematical complexity of the problem of turbulent scattering and the randomness of its occurrence also necessitate a strong dependence on satellite beacon measurements to develop empirical models for scintillation prediction.

Two different approaches to the development of scintillation intensity prediction models can be identified among the more recently proposed models. They are formulated either by taking empirical or semi-empirical relationships between scintillation intensity or variance and local meteorological measurements, or through intensive modelling and approximation of atmospheric process in order to allow the application of the theoretical Tartaskii model. In the latter approach, vertical profiles of basic meteorological parameters provided by radiosonde are needed as input.

6.2.2 Karasawa Model

Karasawa, Yamada and Allnutt have presented a method for calculating mean standard deviation of signal fluctuations due to scintillation starting with Equation (6.14) [3].

$$\sigma_{pre} = 0.0228\sigma_n \cdot f^{0.45} \cdot \sqrt{G(D_a)} / (\sin\theta)^{1.3} \quad , (\theta \geq 5^\circ) \tag{6.14}$$

where $G(D_a)$ is the antenna averaging factor given by Equation (4.18). An empirical estimation of the intensity of fluctuations, equivalent to a C_n^2 profile in

the Tartaskii model, is represented by the normalised prediction σ_n, which is a function of wet term of ground-based refractivity N_{wet}.

$$\sigma_n = 0.15 + 5.2\times10^{-3} N_{wet} \tag{6. 15}$$

The wet term of refractivity is calculated using surface measured temperature and relative humidity as in Equation (6.16)

$$N_{wet} = \frac{22790H \cdot \exp(19.7t/(t+273))}{(t+273)^2} \tag{6. 16}$$

where H is the relative humidity in percent, and t is the temperature in degrees Celsius. For the calculation of $G(D_a)$, Karasawa et al. suggest 2000 m as the turbulence height.

6.2.3 ITU-R Model

ITU-R Recommendation PN 618-3 [4] adopts the basic formulation technique used in the Karasawa model. The recommended prediction formula is:

$$\sigma_{pre} = \frac{\sigma_n \cdot f^{7/12} \cdot g(x)}{\sin\varepsilon^{1.2}} \tag{6. 17}$$

where $g(x)$ is the aperture averaging function of the receiver, given in Equation (4.15) and a turbulent height of 1000 m is suggested. The given normalized intensity has a similar linear relationship with N_{wet} to that in the Karasawa model, but with different coefficients, i.e.:

$$\sigma_n = 3.6\times10^{-3} + 10^{-4} N_{wet} \tag{6. 18}$$

N_{wet} is calculated using Equation (6.19)

$$N_{wet} = 3.732\times10^5 \cdot \frac{e}{T^2} \tag{6. 19}$$

The partial pressure of water vapour e, is given in terms of the saturated partial pressure e_s in hPa, and relative humidity H in percent by:

$$e = \frac{He_s}{100} \tag{6.20}$$

Between -20°C and 50°C the saturated vapour pressure over (liquid) water is given (to the accuracy of ± 0.2%) by Equation (6.21),

$$e_s = 6.1121 \exp\left(\frac{17.502t}{t+240.97}\right) \tag{6.21}$$

It is noted that for a dry environment, where e equals zero and N_{wet} is negligible, the ITU-R model gives a constant value for σ_{ref}, this suggest that ITU-R model does not take variations of dry term of refractivity (N_{dry}) into account or assumes variations of N_{dry} do not affect the intensity of scintillation.

The coefficients in Equation (6.18), 3.6×10^{-3} and 10^{-4} are obtained by the ITU-R through experimental regression using beacon receiver data at Ka band and concurrent meteorological measurements. They represent the weighted contributions of N_{dry} and N_{wet} to scintillation intensity. From the meteorological measurement database, a typical value of N_{dry} is nearly 5 times that of N_{wet}, a typical value of N_{wet} being 50 units. The ratio, therefore, between the given contributions in the ITU-R model is much higher than the ratio between the actual values of the two components of refractivity. Physically, ITU-R model underlines the importance of wet component of refractivity and suggests the variation of N_{wet} is the main cause of the variation of scintillation intensity. This is consistent with the statement that water vapour works as a disclosure agent of the variations of refractive index. Furthermore, in the ITU-R model, the effects of meteorological variables on scintillation is included only through the wet term

of refractivity N_{wet}, which has a fixed relationship of water vapour partial pressure e and temperature t.

The ITU-R model has been developed based on Tatarskii theory for weak turbulence and measurements in frequency range 7-14 GHz. The measurement campaign of OLYMPUS has extended the frequency range of the model up to 30 GHz. The model has been assessed using inputs from various locations in Western Europe and North America [16] and has been widely validated. It provides general good performance when compared against actual data but has following limitations: 1) it is based on mean values calculated over one month or more, and does not give indications on the variability of the parameters for a single event; 2) some parameters used in the model are not directly accessible (e.g. turbulence height); 3) the scintillation superimposed on rain attenuation has not been given sufficient consideration.

6.2.4 Otung Model

A theoretical value for elevation angle (θ) dependence as suggested by Tatarskii model is utilized in Otung model as given in Equation (6.22) [5]:

$$\sigma_{pre} = \frac{\sigma_{ref} f^{7/12} g(x)}{(\sin\theta)^{11/12}} \tag{6.22}$$

It is claimed that a form based on a theoretical dependence on path elevation gives better prediction [17].

Marzano has proposed three pairs of models for monthly scintillation variance prediction using extensive regression analysis. The first letter of their names indicates whether the method is based on a direct correlation of the variables (name starts with 'D') or the method has been partly based on physical modelling (name start with 'M').

6.2.5 Marzano MPSP and DPSP Model

The Direct Physical Statistical Prediction (DPSP) and the Modelled Physical Statistical Prediction (MPSP) models both predict the monthly mean value of the scintillation variance from ground meteorological measurements. The physical model behind these models is the Tatarskii model [13], intermittent turbulence hypothesis developed by d'Auria and Marzano [18] and [19].

DPSP model is based on the direct correlation between the monthly averaged $\ln(\sigma_{pre}^2)$ and the monthly mean surface temperature $\langle T \rangle$, given as Equation (6.10) [8]:

$$\left\langle \ln(\sigma_{pre}^2) \right\rangle = \ln\left[g^2(x)k^{1.166}(\sin\varepsilon)^{-2.4}\right] + \left[-16.95 + 0.1235\langle T \rangle\right] \quad (6.23)$$

MPSP model assumed a thin-layer of homogeneous turbulent atmosphere and scintillation variance has been related to the layer parameters. Direct correlations between the monthly averaged value of the logarithm of the structure constant $\ln(C_n^2)$ and the monthly mean ground temperature $\langle T \rangle$ are developed, given as Equation (6.24) [20]:

$$\left\langle \ln(\sigma_{pre}^2) \right\rangle = \ln\left[g^2(x)k^{7/6}(\sin\varepsilon)^{-11/6}\right] + \ln(h^{11/6}) + \ln(C_n^2) \quad (6.24)$$

where $\ln(C_n^2) = -24.905 + 0.0684\langle T \rangle$ and $h = 2058 + 94.05\langle T \rangle$ estimates the height of turbulence. The model has been tested valid, using ITALSAT data at 18, 40 and 50 GHz for a one-year period in Italy [8] [21] and [20].

6.2.6 Marzano STH2 and STN2 Model

Both of the log normalized-variances in the models have quadratic forms. They are based either on surface temperature $\langle T \rangle$ and relative humidity $\langle H \rangle$ for STH2

model or on surface temperature $\langle T \rangle$ and wet refractivity $\langle N_{wet} \rangle$ for STN2 model. Equations and coefficients are given as below:

$$\left\langle \ln\left(\sigma_{pre}^{\ 2}\right) \right\rangle = \ln\left[g^2(x) \cdot k^{1.166} (\sin\varepsilon)^{-1.833}\right] + \left\langle \ln\left(\sigma_{\chi n}^{\ 2}\right) \right\rangle \tag{6. 25}$$

$$\left\langle \ln\left(\sigma_{\chi n}^{\ 2}\right) \right\rangle = -14.9504 + 0.1546\langle T \rangle + 0.0747\langle H \rangle - 0.0011\langle T \rangle^2 - 0.0005\langle H \rangle^2 \tag{6. 26}$$

$$\left\langle \ln\left(\sigma_{\chi n}^{\ 2}\right) \right\rangle = -12.3889 + 0.1300\langle T \rangle + 0.0151\langle N_{wet} \rangle - 0.0016\langle T \rangle^2 \tag{6. 27}$$

6.2.7 Marzano STHV2 and STNV2 Model

An extension of the STH2 and STN2 models has been investigated and further developed into the STHV2 and STNV2 models as expressed in Equation (6.28) and (6.29).

$$\begin{aligned} \left\langle \ln\left(\sigma_{\chi n}^{\ 2}\right) \right\rangle = & -15.0762 + 0.1473\langle T \rangle + +0.0772\langle H \rangle + 0.0133\langle IWV \rangle \\ & -0.0006\langle T \rangle^2 - 0.0005\langle H \rangle^2 - 0.0007\langle IWV \rangle^2 \end{aligned} \tag{6. 28}$$

$$\begin{aligned} \left\langle \ln\left(\sigma_{\chi n}^{\ 2}\right) \right\rangle = & -12.4255 + 0.1226\langle T \rangle + 0.0076\langle N_{wet} \rangle + 0.0427\langle IWV \rangle \\ & -0.0013\langle T \rangle^2 + 0.0001\langle N_{wet} \rangle^2 - 0.0014\langle IWV \rangle^2 \end{aligned} \tag{6. 29}$$

The relationships have been derived by applying the multivariate statistical regression method, where $\langle IWV \rangle$ is the monthly averaged vertically integrated water vapour content $\langle IWV \rangle$ (kg/m^2 or mm). Both need Equation (6.25) in order to calculate the estimated log-variance.

6.2.8 Tervonen, Van de Kamp and Salonen Model

The Tervonen-Kamp-Salonen model predicts diurnal variations of scintillation intensity.

$$\sigma_{pre} = g(x) \cdot f^{0.45} / \sin^{1.3} \cdot \left(7.74\times10^{-5} + 1.34\times10^{-4}\overline{N_{wet}} + 9.13\times10^{-5}\overline{P_{hc}}\right) \tag{6. 30}$$

where $\overline{P_{hc}}$ (%), derived from observations of cumulus cover, is the probability of cumulus cloud intersecting the satellite link. Both $\overline{N_{wet}}$ and $\overline{P_{hc}}$ are averaged over the diurnal circle using a long-term measurement database. It has been stated that a significant improvement of the diurnal and seasonal correlation, and prediction accuracy is obtained when cloud information is included in the prediction model.

6.2.9 Van de Kamp Models

Van de Kamp has found that the water content $\overline{W_{hc}}$ (kg/m^2) of heavy clouds ($\overline{W_{hc}}$ > 0.70kg/m^2) provides an additional indictor of scintillation, presumably due to cloudy turbulence. A new scintillation prediction model using both $\overline{N_{wet}}$ and $\overline{W_{hc}}$ has been proposed, referred to here as the Kamp I model [10]:

$$\sigma_\chi = g(x)\cdot f^{0.45}/\sin^{1.3}\cdot 0.98\times 10^{-4}\left(N_{wet}+\left(-39.2+56\langle W_{hc}\rangle\right)\right) \quad (6.31)$$

As an alternatives to $\langle W_{hc}\rangle$, the probability of heavy clouds $\langle P_{hc}\rangle$ (%) or the cumulus cloud cover $\langle Cu\rangle$ (%) may also be used to predict of scintillation intensity. Equation (6.32) and (6.33) are referred to as Kamp II and III models respectively [10]:

$$\sigma_\chi = g(x)\cdot f^{0.45}/\sin^{1.3}\cdot 1.09\times 10^{-4}\left(N_{wet}+\left(1.85+2.3\langle P_{hc}\rangle\right)\right) \quad (6.32)$$

$$\sigma_\chi = g(x)\cdot f^{0.45}/\sin^{1.3}\cdot 1.12\times 10^{-4}\left(N_{wet}+\left(6.68+0.78\langle Cu\rangle\right)\right) \quad (6.33)$$

The Van de Kamp models are based on the observation that scintillation is at least partly associated with turbulence in heavy clouds.

6.2.10 Vasseur Model

A scintillation prediction model that does not rely on empirical relationships has been proposed by Vasseur [11]. The development of the model is exclusively

based on radiosonde ascents and statistical features of tropospheric turbulence. The kernel of the model can be represented as a three-step process as shown in Figure 6. 5

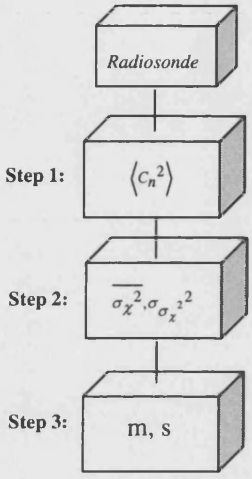

Figure 6. 5 Vasseur model diagram

In order to derive the theoretical process into mathematical formulas that can be solved directly by numerical calculation, a probabilistic approach has to be used in the Vasseur model to estimate the mean structure parameter. Step 1 is the extraction of the radio frequency refractive index structure parameter $\langle C_n^2 \rangle$ profile from the analysis of many radiosonde measurements using Equation (6.34).

$$\langle C_n^2(z) \rangle = 2.8 M_0(z)^2 \langle R(z) \rangle \int_0^\infty L_0^{4/3} P_{L_0} \int_0^\infty P_S \cdot \int_{-\infty}^{S^2 R_w} \langle N^2 \rangle P_{N^2} dN^2 dS dL_0 \qquad (6.34)$$

The detailed calculation of the parameter $M_0(z)$, $R(z)$, L_0, S and N^2 is described in Appendix A. Figure 6. 6 shows the $\langle C_n^2 \rangle$ profile so obtained for September 1999 compared with the median and standard deviation profiles. It can be seen that strong turbulence occurs in the lower troposphere (below 2000

m) and the mean values of refractive index structure function are consistent with what had been obtained experimentally,(in the range of 0.5×10^{-12} to 4×10^{-14} $m^{-2/3}$ [22]).

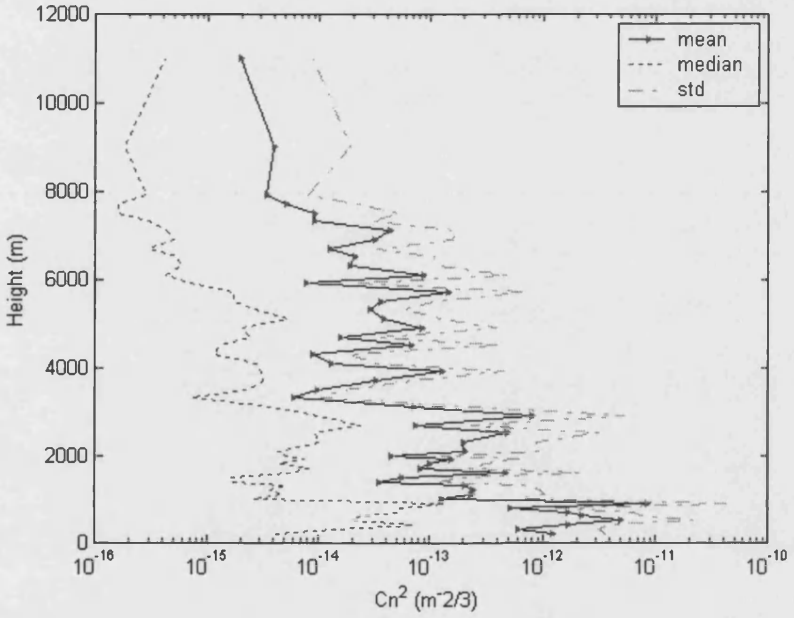

Figure 6. 6 Monthly mean refractive index structure constant inferred from radiosonde measurements for Sept 1999: mean (solid line), median (dotted line) and standard deviation (dashes line)

Step 2 estimates the mean scintillation variance m_{σ^2} and the variance of scintillation variance ${\sigma_{\sigma_\chi}}^2$ from extracted $\left\langle {C_n}^2 \right\rangle$ profile using Equation (6.35) and (6.36):

$$m_{\sigma^2} = 42.48 \frac{k^{7/6}}{(\sin\theta)^{11/6}} \sum_z \overline{\left\langle {C_n}^2(z) \right\rangle} z^{5/6} \Delta z \tag{6. 35}$$

$${\sigma_{\sigma_\chi}}^2 = \left(\sum_z \sum_{z'} \left[42.48 \frac{k^{7/6}}{(\sin\theta)^{11/6}} \right]^2 \cdot \Gamma_{{C_n}^2}(z, z', 0) z^{5/6} z'^{5/6} \Delta z \Delta z' \right) - {m_{\sigma^2}}^2 \tag{6. 36}$$

where $\Gamma_{C_n^2}(z,z',0)$ is the two dimensional cross-correlation function of the refractive index structure parameter, an expression for which can be also found in Appendix A.

Step 3 computes two key parameters (m and s) defining the long-term scintillation variance distribution:

$$m = \frac{{m_{\sigma^2}}^2}{\sqrt{{\sigma_{\sigma^2}}^2 + {m_{\sigma^2}}^2}} \tag{6. 37}$$

$$s = \sqrt{\ln\left(1 + \frac{{\sigma_{\sigma^2}}^2}{{m_{\sigma^2}}^2}\right)} \tag{6. 38}$$

where m is the median value of the scintillation variance distribution and s is the standard deviation of $\ln(\sigma_\chi^2)$. The above results wil be used in the computation of the scintillation log-amplitude distribution based on the premise that this quantity is Gaussianly distributed with Log-normally distributed variance.

$$p_{long-term}(\chi) = \int p_{short-term}(\chi \mid \sigma_\chi^2) p(\sigma_\chi^2) d\sigma_\chi^2 \tag{6. 39}$$

$$p_{short-term}(\chi \mid \sigma_\chi^2) = \frac{1}{\sqrt{2\pi\sigma_\chi^2}} \exp\left(-\frac{\chi^2}{2\sigma_\chi^2}\right) \tag{6. 40}$$

$$p(\sigma_\chi^2) = \frac{1}{\sqrt{2\pi}\sigma_\chi^2 s} \exp\left(-\frac{\left[\ln(\sigma_\chi^2/m)\right]^2}{2s^2}\right) \tag{6. 41}$$

The lower and upper limits of turbulence outer scale are assumed to be 3 m and 100 m respectively. The model is designed to predict scintillation on a long-term basis (longer than a month) so the extracted statistical characteristics from radiosondes reflect the tropospheric features over that period. Note that

Equation (6.35) is for a point receiver; for a receiving antenna of finite size, aperture smoothing must be taken into account.

Use of the Vasseur modle requires radiosonde data. Furthermore, the vertical resolution of individual radiosonde data is required to be of the order of 1 m or so in order to detect the fine structure of the random turbulent troposphere. Even if the radiosonde data is available this resolution is not always easy to realize, as the measurement equipment carried will have a reaction time of, typically a few seconds. This results in the height resolution of balloon-borne soundings being limited to several tens of meters for a large percentage of time, especially at the higher altitude. The fine structure of turbulence is therefore normally obscured by the necessary interpolation.

6.2.11 Ortgies Models

Two models are proposed by Ortgies based on direct linear relationships between mean surface measurement and monthly mean normalized log-variance of scintillation $\langle \ln(\sigma_\chi^2) \rangle$. The first method uses the monthly surface temperature $\langle T \rangle$ as a predictor and is referred to as the Ortgies-T model, Equation (6.42):

$$\langle \ln(\sigma_{pre}^2) \rangle = \ln\left[g^2(x) \cdot k^{1.21} (\sin\varepsilon)^{-2.4}\right] + e_{01} + e_{11}\langle T \rangle \qquad (6.42)$$

The second method relates the monthly log-variance to the monthly surface wet refractivity $\langle N_{wet} \rangle$ and referred to as Ortgies-N model, Equation (6.43):

$$\langle \ln(\sigma_{pre}^2) \rangle = \ln\left[g^2(x) \cdot k^{1.21} (\sin\varepsilon)^{-2.4}\right] + e_{02} + e_{12}\langle N_{wet} \rangle \qquad (6.43)$$

where coefficients $e_{01} = -12.5$, $e_{12} = 0.0865$, $e_{02} = -13.45$ and $e_{12} = 0.0462$.

6.3 Assessing Performance Of the Models

All the model predictions have been converted into monthly averaged scintillation intensity. A comparison of experimental and predicted values by the entire set of models is shown in Figure 6.7.

All the models follow the same general trend predicting that scintillation is more intense in the summer months and less intense in the winter months. Those models using measured/estimated meteorological variable as predictors appear to show smooth variation over the seasons. This contrasts with models using threshold-chosen variables (e.g. Kamp I and Kamp II models), which result in predictions that have large fluctuations especially during summer. All the proposed models seem to under-estimate scintillation intensity during the winter months, the ITU-R model appearing best (or least worst) in this respect. July and August are the months with the largest prediction errors. The pair of liner models from Marzano (Marzano DPSP and Marzano MPSP) suffer from the greatest over-estimation of intensity during the summer months, with predicted intensity increasing in the opposite direction as the measured scintillation intensity on both occasions from July to August. Furthermore, the model-based Vasseur prediction using radiosonde data give comparably good prediction for summer months.

The assessment of performance of an individual model needs a quantitative analysis of its prediction error.

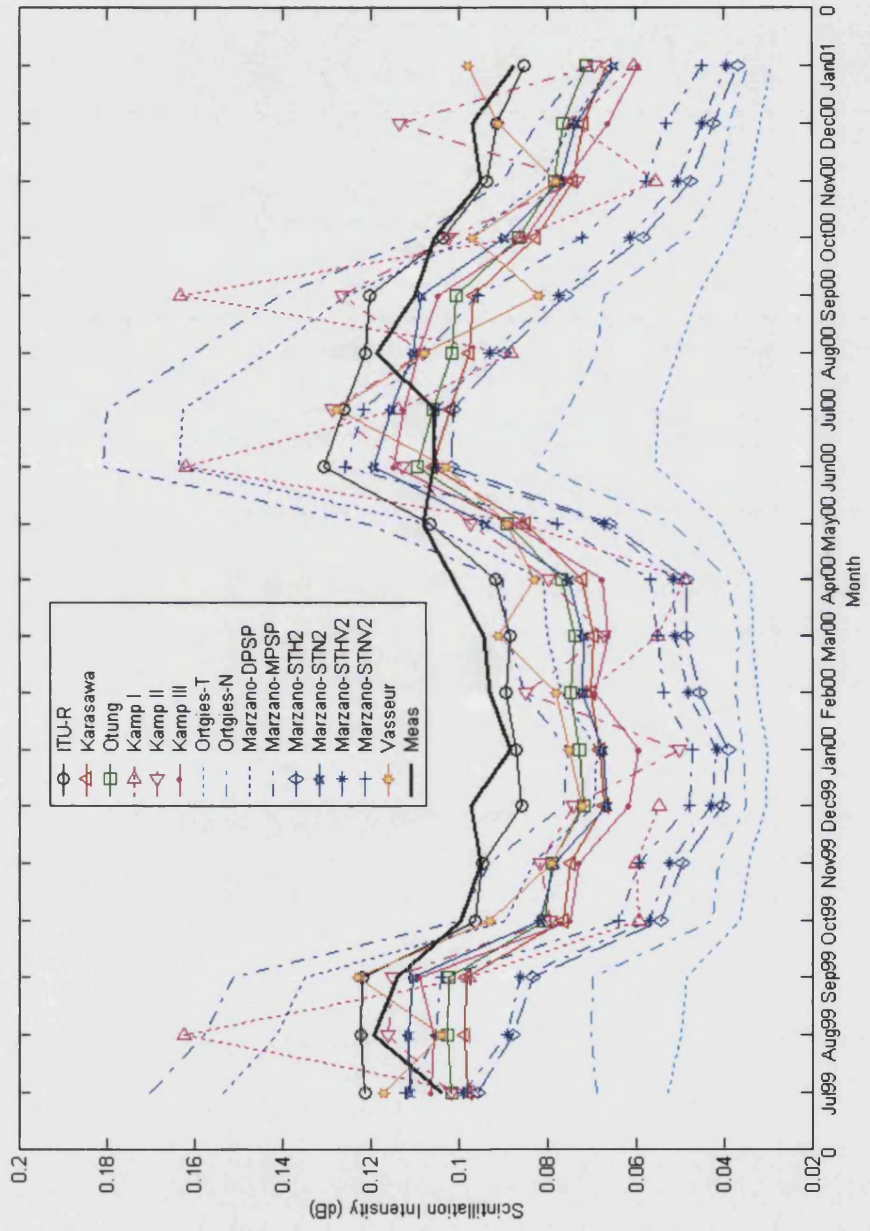

Figure 6. 7 Prediction comparison using existing models using originally published coefficients

6.3.1 Error Comparison

The RMS error is often used as a measure of general reliability of estimates calculated from regression equations, which is defined as:

$$RMS\ error = \sqrt{\frac{1}{n}\sum_{j=1}^{n}\left(x_{estj} - x_{measj}\right)^2} \tag{6. 44}$$

It is obviously desirable for a prediction model to have small RMS error and high correlation with experimental measurements. These quality indicators are compared for the models examined above in Table 6. 2.

Model	RMS Error	Correlation Coefficient
ITU-R	0.0099	0.8294
Karasawa	0.0209	0.8294
Otung	0.0170	0.8294
Kamp I	0.0354	0.6719
Kamp II	0.0180	0.7776
Kamp III	0.0221	0.8403
Ortgies-T	0.0624	0.7904
Ortgies-N	0.0515	0.7990
Marzano-DPSP	0.0276	0.7772
Marzano-MPSP	0.0345	0.7870
Marzano-STH2	0.0417	0.7830
Marzano-STN2	0.0178	0.8419
Marzano-STHV2	0.0394	0.7706
Marzano-STNV2	0.0328	0.7863
Vasseur	0.0154	0.5669

Table 6. 2 RMS errors and correlation coefficient coefficients between estimated and measured scintillation intensity at 20 GHz on a monthly basis

It can be seen from Table 6. 2 that the models using different predictors have different errors and correlation coefficients with the measured intensity. Those models with identical correlation coefficients depend on Nwet in an identical way and therefore give rise to identical curves in Figure 6.2. Kamp III model using N_{wet} and cumulus cloud amount $\langle Cu \rangle$ as predictors for normalized scintillation intensity and Marzano STN2 model using wet refractivity (N_{wet}) and temperature as predictors for normalized scintillation log-variance provide highest correlation with measurements, but with big RMS errors. Relatively, the ITU-R model has the lowest RMS error and second greatest correlation coefficients. As small RMS errors and high correlation coefficients suggest good reliability, it follows that the reliability of scintillation intensity predicted using the ITU-R model is better than that predicted using other models. The RMS errors are themselves small and the difference between RMS errors even smaller. These small values relate to monthly mean scintillation intensity however, and their impacts for scintillation intensity exceeded for a small fraction of time is significant.

The percentage fractional errors ε_f of an estimate:

$$\varepsilon_f = \frac{x_{meas} - x_{est}}{x_{meas}} \times 100\% \tag{6. 45}$$

is also a useful measure of model performance [23]. In the author's comparison, following Marzano [20], the fractional error performance is summarised by its mean value (fractional bias error), its root mean square value (fractional RMS error) and its skewness factor as defined below:

$$Fractional\ Bias\ error = \frac{1}{n}\sum_{j=1}^{n} \varepsilon_{f\,j} \tag{6. 46}$$

$$Fractional\ RMS\ error = \sqrt{\frac{1}{n} \cdot \sum_{j=1}^{n} \varepsilon_{f_j}{}^2} \tag{6. 47}$$

$$\textit{Fractional Skewnes of error} = \frac{1}{N}\sum_{j=1}^{N}\left[\frac{\varepsilon_{f_j} - \mu_{\varepsilon_f}}{\sigma_{\varepsilon_f}}\right]^3 \quad (6.48)$$

where μ_{ε_f} is the mean of $\{\varepsilon_f\}$ and σ_{ε_f} is the standard deviation of $\{\varepsilon_f\}$. The percentage fractional errors of the above models are compared in Table 6. 3.

Model	Bias (F)	RMS error (F)	Skewness (F)
ITU-R	-1.5837	9.4806	-0.9821
Karasawa	19.25	21.0093	-0.9174
Otung	15.0808	17.0484	-0.9733
Kamp I	15.4205	34.5623	-1.1095
Kamp II	9.0708	18.7795	-0.0834
Kamp III	18.0493	22.8299	-0.4973
Ortgies-T	61.1017	61.4370	-0.9887
Ortgies-N	50.0741	51.5850	-0.7861
Marzano-DPSP	-1.4926	26.6830	-0.8516
Marzano-MPSP	-12.8679	32.2724	-0.7900
Marzano-STH2	38.6812	42.5867	-0.7747
Marzano-STN2	13.2356	18.4038	-0.6197
Marzano-STHV2	36.0036	40.2083	-0.8465
Marzano-STNV2	26.0489	33.9751	-0.7713
Vasseur	7.9117	15.0655	-0.7150

Table 6. 3 Bias,RMS error, skewness of the percentage fractional error together with the correlation coefficient between estimated and measured scintillation intensity at 20 GHz on a monthly basis

The ITU-R prediction again presents the least fractional errors. The skewnesses of the fractional errors are all negative suggesting that all the models have prediction errors with more left-spread values than right-spread values with respect to the mean.

As the fractional errors are relative percentages of the predicted values, it is possible to make a parallel comparison with results of modelling predictions using beacon measurement at different locations in a different climate region. We make such a comparison, therefore, using Table 6. 4 extracted from the literature, which relates to the 18.7 GHz ITALSAT beacon received at Spino d'Adda (elevation angle 37.8°) Italy, - a continental region [20].

Method	Bias (F)	RMS error (F)	Skewness (F)	CorrCoef (F)
DPSP	-3.2	6.58	21.87	0.942
MPSP	-1.64	5.78	20.30	0.938
STH2	0.72	5.92	2.87	0.932
STN2	-4.53	6.64	-19.23	0.952
STHV2	-1.22	6.07	3.57	0.937
STNV2	-6.66	8.91	-14.76	0.959
Karasawa	35.32	50.58	93.92	0.851
ITU-R	63.98	79.14	76.42	0.851
Ortgies-T	10.48	10.66	-20.56	0.943
Ortgies-N	6.16	12.94	11.07	0.871

Table 6. 4 Bias, RMS error, skewness of the percentage fractional error together with the correlation coefficient between estimated and measured scintillation intensity at 20 GHz on a monthly basis obtained by Marzano, 1999

The performance of prediction models when tested with the data from Italy is very different to that observed using our measurement database. Differences between the two climate patterns are believed to have played a key role, the coefficients of the Marzano and Ortiges models have being derived from continental databases, (Italy and Germany respectively).

6.4 Summary

The distribution of long-term scintillation variance can be reasonably modelled by a Lognormal or Gamma distribution. Karasawa's model, based upon a Gamma distribution, appears to give the best prediction of scintillation log-amplitude distribution (fade and enhancement).

The review of scintillation intensity prediction models has considered most of the well-known models that have been published until 2000. Statistical results in terms of RMS error, correlation, bias percentage error, RMS percentage error and skewness of the percentage error have been used to compare existing published scintillation intensity prediction models. In the context of our measurement database, the ITU-R appears to have the best performance. Models using surface measured N_{wet} and temperature T give high correlation with measurement. These models will be used as benchmarks to access the performance of the author newly developed models described in the following two chapters.

6.5 References:

[1] T. J. Moulsley and E. Vilar, "Experimental and theoretical statistics of microwave amplitude scintillations on satellite down-links," *IEEE Trans. Antennas Propagat.*, vol. 30, pp. 1099-1106, 1982.

[2] Y. Karasawa, K. Yasukawa, and M. Yamada, "Tropospheric scintillation in the 14/11 GHz bands on earth-space paths with low elevation angles," *IEEE Trans. Antennas Propagat.*, vol. 36, pp. 563-569, 1988.

[3] Y. Karasawa, M. Yamada, and J. Allnutt, "A new prediction method for tropospheric scintillation on earth-space paths.," *IEEE Trans. Antennas Propagat.*, vol. 36, pp. 1608-1614, 1988.

[4] ITU-R, "Propagation data and prediction methods required for the design of Earth-space telecommunications systems," Rec. P 618-7, 2001.

[5] I. E. Otung, "Prediction of tropospheric amplitude scintillation on a satellite link.," *IEEE Trans. Antennas Propagat.*, vol. 44, pp. 1600-1608, 1996.

[6] ITU-R, "The concept of 'worst month'," Rec. 581-2, 1990.

[7] ITU-R, "Conversion of annual statistics to worst-month statistics," Rec. 841-2, 2001.

[8] F. S. Marzano and G. d'Auria, "Model-based prediction of amplitude scintillation variance due to clear-air tropospheric turbulence on Earth-Satellite microwave links.," *IEEE Trans. Antennas Propagat.*, vol. 46, pp. 1506-1518, 1998.

[9] J. K. Tervonen, M. M. J. L. v. d. Kamp, and E. T. Salonen, "Prediction model for the diurnal behaviour of the tropospheric scintillation variance.," *IEEE Trans. Antennas Propagat.*, vol. 46, pp. 1372-1378, 1998.

[10] V. d. Kamp, "Climatic radiowave propagation models for the design of satellite communication systems," Technische Universiteit Eindhoven, 1999.

[11] H. Vasseur, "Prediction of tropospheric scintillation on satellite links from radiosonde data.," *IEEE Trans. Antennas Propagat.*, vol. 47, pp. 293-301, 1999.

[12] G. Ortgies, "Prediction of slant-path amplitude scintillation from meteorological parameters.," *Proc. Int. Symp. Radio Propagat. Beijing, China.*, pp. 218-221, 1993.

[13] V. I. Tatarskii, *Wave propagation in a turbulent medium.* New York: McGraw-hill, 1961.

[14] M. M. J. L. v. d. Kamp, J. K. Tervonen, E. T. Salonen, and J. P. V. P. Baptista, "Improved models for long-term prediction of tropospheric scintillation on slant paths.," *IEEE Trans. Antennas Propagat.*, vol. 47, pp. 249-260, 1999.

[15] C. E. Mayer, B. E. Jaeger, R. K. Crane, and X. H. Wang, "Ka-band scintillations: measurements and model predictions," *IEEE Trans. Antennas Propagat.*, vol. 85, pp. 936-945, 1997.

[16] OPEX, "Second workshop of OLYMPUS propagation experiments: Volume 1: Reference book on attenuation measurement and prediction," Noordwijk November 1994.

[17] F. Haidara, C. W. Bostian, and T. Pratt, "Measurements of tropospheric scintillation on a 14 path at 12, 20 and 30 GHz," *Amer. Inst. Aeronaut. Astronaut.*, pp. 921-931, 1994.

[18] G. d'Auria, F. S. Marzano, and U. Merlo, "Model of the refractive-index structure constant in intermittent clear-air turbulence.," *Appl. Opt.*, vol. 32, pp. 2673-2680, 1993.

[19] F. S. Marzano and G. d'Auria, "Estimation of intermittent scintillation on microwave links from meteorological data," *Alta Frequenza*, vol. 6, pp. 94-97, 1994.

[20] F. S. Marzano, C. Riva, A. Banich, and F. Clivio, "Assessment of model-based scintillation variance prediction on long-term basis using Italsat satellite measurements.," *Int. J. Satell. Commun.*, vol. 17, pp. 17-36, 1999.

[21] F. S. Marzano and C. Riva, "Evidence of long-term correlation between clear-air attenuation and scintillation in microwave and millimetre-wave satellite links.," *IEEE Trans. Antennas Propagat.*, vol. 47, pp. 1749-1757, 1999.

[22] R. S. Cole, K. L. Ho, and N. D. Mavrokoukoulakis, "The effect of the outer scale of turbulence and wavelength on scintillation fading at millimetre wavelengths.," *IEEE Trans. Antennas Propagat.*, vol. 26, pp. 712-715, 1978.

[23] J. S. Bendat and A. G. Piersol, *Random Data: Analysis and Measurement Procedure.* New York: Wiley, 1971.

Chapter 7

GPS-INFORMED MODEL – PART I

A new approach for the prediction of scintillation intensity is reported in two parts. Chapter 7 (Part I) concerns the derivation of an integrated path informed parameter - the integrated precipitable water vapour (IPWV) - from the Global Positioning System (GPS) measurement. Chapter 8 (Part II) focuses on the development of new models using the IPWV as a principal parameter. In Chapter 7, the background and methodology of GPS water vapour estimation is presented. The estimated IPWV is shown to have excellent agreement with measurements from radiosonde assents.

7.1 Measuring Water Vapour Using GPS

The random component of the refractive index of the atmosphere causes random temporal and spatial variations of the amplitude, phase, polarisation and angle of arrival of radio waves travelling through it. This phenomenon affects all satellite-based systems: telecommunication satellites, GPS, SAR etc, but the level and significance of the effects depend on the system parameters and path geometry. By taking measurements of the received signal level for a particular system, and given appropriate data about the relevant environmental parameters, information about the refractive index variations and/or atmospheric components that caused the variations can be retrieved. The fundamental physics of GPS meteorology lies in the pressure, temperature and humidity dependence of microwave refractivity in the neutral atmosphere.

7.1.1 Principle of the GPS System

The Global Positioning Systems (GPS) has three segments: the space segment, the user segment, and the control segment. The space segment operates twenty-four satellites at an altitude of 20,000 km in six orbital planes inclined at 55° with respect to the equatorial plane. The GPS constellation is illustrated in Figure 7. 1. Each satellite has an orbital period of 12 hours and repeats the same ground track every 24 hours. GPS satellites radiate L-band microwave signals whose frequency and phase are tightly controlled.

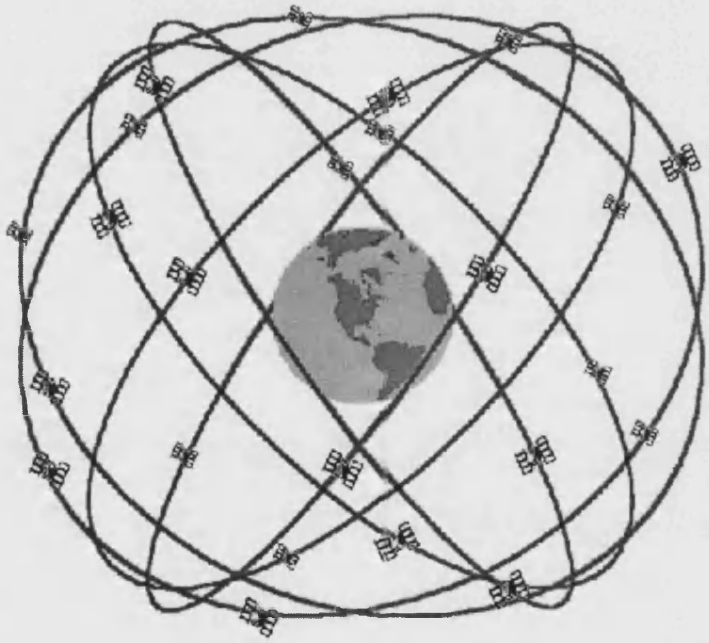

Figure 7. 1 GPS system constellation map

The development of precise, ultra-stable clocks and stable space platforms in predictable orbits are the two key enabling technologies for GPS. The constellation provides the user with visibility to between five and eight satellites from any point on the Earth's surface. Four GPS satellite signals are needed to compute the positions of receiver and the time offset in the receiver clock.

The provision of precise estimates of position, velocity and time are the original and principal function of GPS, which was developed for military applications by the USA. GPS is used widely, however, in the civilian sector, with applications ranging from large-scale commercial services to personal consumer products. The civil applications have grown rapidly, many being realized in combination with other technologies, especially communication systems and geographic databases. The civil applications of GPS may be divided into four broad categories: high-precision (millimetre-to-centimetre level) positioning; specialized applications such as aviation and space; land transportation and maritime uses and consumer products [1].

Originally the timing of the GPS satellites' atomic clocks were degraded using a secret code to prevent adversaries of the USA from using GPS to determine locations precisely. This technique was referred to as 'selective availability' (SA). SA was soon circumvented, however, by comparing received pseudo-ranges with known location ranges, thus making corrections to achieve maximum precision. A similar approach has later been developed as 'deferential GPS'. With the discontinuation of SA since May 1 2000, a GPS poisoning unit can achieve location accuracy to within 10 m in good conditions. Further plans for improving the accuracy of GPS are currently being pursued, including the launch of additional satellites and utilization of new signals [2].

As the cost and weight of GPS receivers have decreased, a number of meteorological applications have emerged. In particular GPS can be used to remotely sense several properties of the Earth's atmosphere, for example water vapour content. Such remote sensing applications typically involve data collection by dual-frequency GPS receivers at fixed locations on the ground.

7.1.2 Theory of Atmospheric Delay

Microwave radio signals transmitted by GPS satellites are delayed by the atmosphere as they propagate to Earth-based GPS receivers. The delay incurred due to the presence of water vapour is approximately proportional to the amount of water vapour present along the signal path. This can be quantified as the integrated precipitable water vapour content (IPWV).

The fundamental variable measured by GPS receivers is the total signal delay. Each GPS satellite transmits L-band signals at two frequencies $f_1 = 1.57542$ GHz and $f_2 = 1.2276$ GHz. These signals are refracted and delayed by the gas/plasma composing the atmosphere as they propagate through it.

The atmosphere affects the signals in two distinct ways. First, the signal's propagation path bends in response to gradients in the refractive index of the atmosphere, the energy travelling a curved trajectory rather than a straight-line that would be travelled in a region of constant refractivity. The difference between the lengths of these two paths is known as the geometrical delay. Second, the wave travel slower than it would be in vacuum. The increase in time required to cover a given distance, known as the optical delay, can also be expressed in terms of excess path length. The total delay, then, is the sum of these two components which can be written as [3]:

$$\Delta L = \int_L [n(s)-1]ds + (S-G) = 10^{-6}\int_L N(s)\cdot ds + (S-G) \tag{7.1}$$

where $n(s)$ is the refractive index as a function of position s along the curved path L, S is the curved path length along L, G is the straight-line path length through the atmosphere and $N(s)$ is the refractivity along the path. The first term on the right hand side of Equation (7.1) is due to slowing effect, and the second term is due to bending. For paths with elevations greater than about 15°, the

bending term is small, about 1 cm or less [4]; For zenith rays the bending term vanishes.

In a neutral atmosphere, the air is composed of a mixture of gases, each gas contributing separately to the total delay, which is the sum of that caused by water vapour (ΔL_w) and that caused by other atmospheric constituents (ΔL_d), mainly oxygen (referred to as the hydrostatic, or dry delay), in Equation (7.2).

$$\Delta L = \Delta L_d + \Delta L_w \tag{7.2}$$

Dry, clean air has a stable composition and measurements have shown that this composition changes very little with height [5].

The atmosphere closely satisfies the ideal gas law Equation (7.3), where R is the molar gas constant, M_w is the molar mass of water, M_d is the molar mass of dry air, e is water vapour partial pressure (in millibars) and T is the temperature (in Kelvin).

$$\rho = \rho_d + \rho_w = \frac{M_d}{R}\left[\frac{p}{T} - \left(1 - \frac{M_w}{M_d}\right)\frac{e}{T}\right] \tag{7.3}$$

The atmosphere also satisfies the hydrostatic equation:

$$\frac{dp}{dz} = -\rho g \tag{7.4}$$

The effect of zenith hydrostatic delay is well modelled as Equation (7.5) where p_s is surface pressure (in hPa) and $f(\lambda, h)$ describes the variation of the acceleration due to gravity with latitude λ and height h by [6]:

$$\Delta L_d = \frac{0.0022768 \cdot p_s}{f(\lambda, h)} \tag{7.5}$$

The remaining delay can then be assumed to be due to water vapour caused by the water vapour molecule's permanent electric dipole moment. The moment, which exists because of the molecule's asymmetric distribution of charge, retards the propagation of electromagnetic radiation [7].

Using Equation (7.3) and (7.4), the wet delay can be expressed as Equation (7.6), where k_2' and k_3 are constants and T_m is the mean temperature of the water vapour, defined in Equation (7.7).

$$\Delta L_w = 10^{-6} \cdot \left(k_2' + k_3 / T_m\right) \cdot \int_H^\infty \frac{e}{T} dz \tag{7.6}$$

$$T_m = \frac{\int_H^\infty \frac{e}{T} dz}{\int_H^\infty \frac{e}{T^2} dz} \tag{7.7}$$

It is noted that T_m depends on surface temperature, the tropospheric temperature profile and the vertical distribution of water vapour [8].

7.1.3 Calculation of Precipitable Water Vapour from Wet Delay

A useful variable that has been much used by meteorologist is the integrated precipitable water vapour (IPWV), defined by Equation (7.8)

$$IPWV = \frac{1}{\rho_1} \int_H^\infty \rho_w dz = \frac{1}{\rho_1 R_w} \int_H^\infty \frac{e}{T} dz \tag{7.8}$$

ρ_1 is the liquid water density 1000 kg/m^3, ρ_w is the water vapour density of the air at height z. $R_w = R / M_w$ where R is the molar gas constant (8.314 J/mol/K) and M_w is the molar mass of water (18.0152 g/mol). Comparing Equation (7.8) with Equation (7.6), ΔL_w and $IPWV$ can be related by:

$$IPWV = \Delta L_w \cdot \left[\frac{10^6}{\rho (R / M_w) \left[(k_3 / T_m) + k_2' \right]} \right] \tag{7.9}$$

There are two major steps involved in mapping the integrated water vapour with GPS. The first step is to use precise measurements of atmosphere pressure at each GPS receiver so that the total delay due to the neutral atmosphere can be separated into hydrostatic and wet components. The second step is to transform the retrieved zenith wet delay into an estimate of precipitable water vapour. The success of this new technique relies on the fact that there will be a negligible contribution to GPS phase delay from ionosphere, cloud and rain particles.

7.1.3.1 Effect of Ionosphere on GPS Phase Delay Measurement

Both the ionosphere and the neutral atmosphere introduce refractive delays. Above about 80 km above the Earth's surface, solar ultra-violet radiation is absorbed by oxygen and nitrogen molecules, which (if all of the energy transferred to them cannot be absorbed) then decompose either into free atoms or ionised molecules. This results in the formation of the electrified region known as the ionosphere [5].

The free electrons of the ionosphere cause the phase velocities of carrier waves to increase and the group velocities of modulations to reduce. The magnitude of the group delays is, to a good approximation, proportional to the total electron content (TEC) along the path between satellite and receiver, and inversely proportional to the square of the carrier frequency. By making measurements at two sufficiently widely spaced frequencies, the ionospheric effect can be largely eliminated by scaling and subtracting the times of arrival for the two signals. Ionospheric errors sources contaminating GPS-derived estimates of the ZWD can be reduced by an order of magnitude to 1 mm or less, except under extraordinary circumstances such as a major magnetic storm [4] [9].

Ionospheric delays affecting observation recorded by a dual-frequency GPS receiver can thus be effectively eliminated without reference to observations recorded by other GPS receivers in the same network. The same technique cannot eliminate range errors introduced by the troposphere because the neutral atmosphere is essentially non-dispersive at GPS frequencies. This ranging error can be used, however, to provide information about the physics and/or chemistry of the lower atmosphere.

7.1.3.2 Effect of Hydrometeors on GPS Phase Delay Measurement

Besides the gaseous compounds in the atmosphere, there are also several forms of particles, mainly hydrometeors such as fog, rain, cloud and ice. (Although other particles such as dust and sand occasionally occur, their presence is only significant in certain geographical regions and/or for small periods of time.)

Hydrogen bonds between water molecules (in both liquid water and solid phases) greatly reduce the contribution of the dipole moment to e/m propagation delay. For non-scattering particles such as cloud and fog droplets, and for GPS frequencies, the Clausius-Mossotti equation can be applied as Equation (7.10), where M is the mass content of the particles per unit volume of air, ρ is the density of the particles and ε is the relative permittivity of the particles.

$$N = 1.5\times10^{6}\frac{M}{\rho}\left[\frac{\varepsilon-1}{\varepsilon+2}\right] \tag{7.10}$$

Equation (7.10) can be simplified as Equation (7.11), where M_l is the liquid water content per volume of air along the propagation path in g/m^3 and ε' is the permittivity of liquid water [10].

$$N_{cloud,fog} = \frac{3}{2}\frac{M_l}{\rho_1}\left[\frac{\varepsilon'-1}{\varepsilon'+2}\right] = 1.45M_l \tag{7.11}$$

Thus, for a path length of 1 km in cloud having liquid water content of 0.1 g/m^3, the induced path delay can be found to be 1.45 mm by using Equation (7.1) and (7.11). Consequently, the presence of cloud (water or ice) does not discernibly affect the accuracy of water vapour estimation from GPS measurements [11].

It can be shown from scattering theory that uniform slabs of water cloud and light rain (up to 12 mm/h) with representative drop-size distributions, introduce less than 1 mm/km of zenith delay at 1.5 GHz. In stratiform rain, sustained by a population of ice particles, the expected delay from ice and rain regions will be less than 5 mm/km [12]. The resulting phase delay effects produce negligible consequences on the recovery of the vector baseline component even under assumptions of excessively high ice volume concentrations combined with heavy snowfall rates [13].

In conclusion it can be stated that the accuracy of GPS-derived water vapour estimates is not significantly degraded by the ionosphere or by the occurrence of tropospheric hydrometeors. In the work reported here, the processing of GPS observations to obtain zenith total delay was performed by the GPS-Inferred Positioning System and Orbit Analysis Simulation (GIPSY-OASIS) II software, applying the precise point positioning method [14].

7.1.4 GIPSY-OASIS II Software

GIPSY-OASIS is a general satellite orbit analysis software package for GPS, developed by the Jet Propulsion Laboratory (JPL) Pasadena, NASA (USA). It is designed to produce position estimates of high accuracy, in the order of millimetres. The software can process all GPS phase and pseudo-range data input and produce a full covariance matrix and estimate vector, plots and tables of pre- and post-fit measurement residuals, baseline coordinates in various coordinate

systems (both local and global), satellite orbits, and the evolution of stochastic parameters.

RINEX (Receiver Independent EXchange) format data recorded at GPS receivers are needed as input into GIPSY. The programme can be run on either a graphical or a command line interface. Different strategies can be chosen for each run. These include basic estimates of orbits and stations, precise point positioning, fixed broadcast orbits, fixed precise orbits and clocks. For precise orbits strategies, the software requires information on precise satellite orbits and clocks, as well as polar motion effects during the time of observation. This information can be obtained from JPL. Corrections are included for long-term and periodic Earth movements including tidal pressures. On completion of the processing, the software outputs the precise point position for the period of observation and estimates zenith total delay (ZTD) at a time resolution of 5 minutes. This is a mean value estimate for the sampling interval.

The estimates of zenith phase delay can be further separated into hydrostatic and wet components. The line-of-sight delay for each component is determined by the product of the zenith delay and a mapping function (geometric factor), which accounts for the elevation angle dependence of the observation. The mapping function, $m(E)$, can be defined as the ratio of the electrical path length through the atmosphere at an elevation angle, E, to the electrical path length in the zenith direction. The total tropospheric delay from a station u to a satellite k is given [15] by:

$$T_u^k = T_d^z m_d(E) + T_w^z m_w(E) \qquad (7.12)$$

Where T_d^z is the dry (or hydrostatic) component of the zenith delay, T_w^z is the wet component of the zenith delay, $m_d(E)$ is the dry (or hydrostatic) mapping

function, and $m_w(E)$ is the wet mapping function. Neil's model [16] has been used in the above equation for the calculation of mapping functions.

In GIPSY, the nominal dry zenith delay at sea level is given by Equation (7.13), where h is the geodetic height (in meter); and the nominal wet zenith delay at sea level is given by Equation (7.14):

$$T_d^z = (1.01)\cdot 2.27e^{-0.1160E-3h} \tag{7.13}$$

$$T_w^z = 0.1m \tag{7.14}$$

In Neil's model, both mapping functions have the form of Equation (7.15).

$$m(E)=\frac{\left(1+\dfrac{a}{1+\dfrac{b}{1+c}}\right)}{\left(\sin(E)+\dfrac{a}{\sin(E)+\dfrac{b}{\sin(E)+c}}\right)} \tag{7.15}$$

The given dry mapping function is of seasonal and height dependence and the coefficient (a, b and c) are obtained in a similar manner, a for example, is obtained for a particular latitude λ and time t (measured from January 0.0 (in UT days) using:

$$a(\lambda_i,t)=a_{avg}(\lambda_i)+a_{amp}(\lambda_i)\cos\left(2\pi\frac{t-T_0}{365.25}\right) \tag{7.16}$$

where T_0 is an adopted phase, namely the 28th day of the year (DOY 28). For a given latitude λ, the value of $a(\lambda,t)$ can be interpolated from adjacent $a(\lambda_i,t)$. The values of a_{avg} and a_{amp} are provided in GIPSY.

In addition to the seasonal dependence of the dry mapping function, a dependence of the height above the point of observation exists. The height correction term $\Delta m(E)$ is given by:

$$\Delta m(E) = \frac{dm(E)}{dh} H \tag{7. 17}$$

Where H is the geoid height (in meter) and the function $\frac{dm(E)}{dh}$ is computed using:

$$\frac{dm(E)}{dh} = \frac{1}{\sin(E)} - \frac{\left(1 + \frac{a_{ht}}{1 + \frac{b_{ht}}{1 + c_{ht}}}\right)}{\left(\sin(E) + \frac{a_{ht}}{\sin(E) + \frac{b_{ht}}{\sin(E) + c_{ht}}}\right)} \tag{7. 18}$$

Where coefficients a_{ht}, b_{ht} and c_{ht} of both dry and wet mapping function are given in GIPSY-OASIS manual [15]. No temporal or height dependence exists in this model for the wet component.

Figure 7. 2 shows the variation of dry mapping function with elevation angle and latitude, when the altitude of the observation point assumed to be zero above the mean sea level, and latitude is 70 degrees. The result is also compared with cosecant function of the elevation angle. It can be seen that at low latitude positions, the dry mapping function factor increases faster than at high latitude positions when elevation angle decreases as indicated in the model.

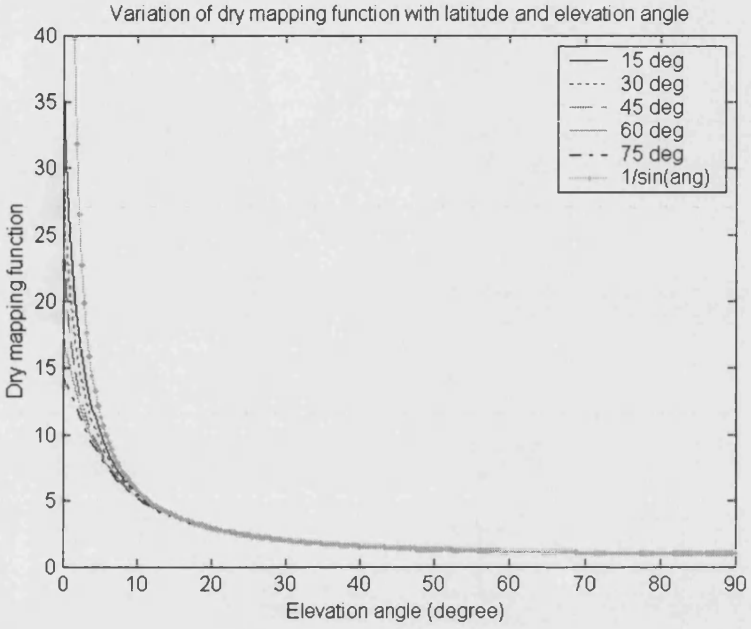

Figure 7. 2 Comparison of dry mapping function with latitude and elevation angle.

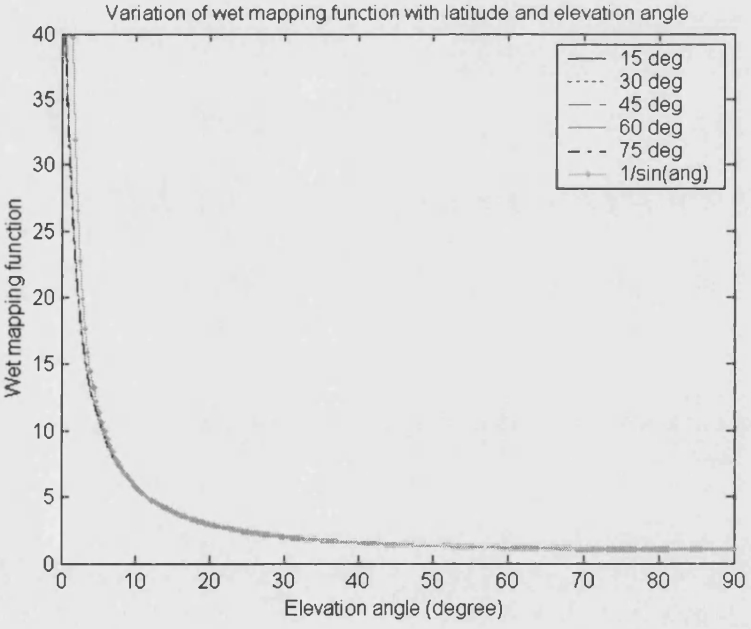

Figure 7. 3 Comparison of wet mapping function with latitude and elevation angle.

Figure 7. 3 shows the variation of wet mapping function with elevation angle and latitude compared with cosecant function of the elevation angle. There are only slight differences of mapping function at different latitude positions and as elevation angle varies. According to Neil, the biases of his model for the dry (hydrostatic) component at 5° elevation is less than 0.02 % (~4 mm) with RMS deviations of 0.1 % (~23 mm). For the wet component, the bias is less than 0.5 % (~5 mm for 100 mm of wet zenith delay) and the RMS deviation is approximately 0.6 % (~6 mm) for 5° elevation. The model should be valid for elevation angles equal to, or greater than, 3° [16].

7.1.5 Accuracy Of GPS Water Vapour Retrieval Measurements

Traditional water vapour observing systems include radiosonde, surface-based microwave radiometers (WVR), satellite-based microwave and infrared radiometers, and cloud and weather radars/lidars. Each of these systems has advantages and limitations.

Radiosonde profiles provide information of the vertical distribution of water vapour in the atmosphere, but are labour intensive and, typically, are launched only a few times per day. Releasing radiosondes can be an expensive operation because many of the instruments are never retrieved, and many of those that are retrieved are often in poor condition. Surface-based radiometers are capable of high temporal resolution, but are costly and do not function well in all-weathers, especially during intensive rain. Satellites provide global coverage, but have limited accuracy over land and cannot easily observe the lower atmosphere where most water vapour is concentrated. Infrared radiometers can only provide reliable data under clear sky conditions.

The newly developed GPS approach for water vapour estimation has significant advantages including global coverage, continuous operation, high temporal

resolution and near real-time data acquisition. GPS estimates are found to be sensitive to a number of constraints, however, including: the accuracy of GPS satellite orbits; the effect of atmospheric dynamics on the hydrostatic delay; the elevation angle of GPS receivers and the mapping function employed.

7.1.5.1 Accuracy of GPS Satellite Orbits

The discontinuities of the International GPS Service (IGS) orbits at the day boundaries led to discontinuities in the water vapour estimate time series of up to 2 mm. The improvement in orbit accuracy can be achieved by using a more accurate definition of the terrestrial reference frame [17].

7.1.5.2 Atmospheric Dynamics on the Hydrostatic Delay

The effect of atmospheric dynamic is likely to introduce errors of less than 1 % of the hydrostatic delay that, typically, would correspond to only a few millimetres. If the station barometers are calibrated to better than 0.3 hPa, the effects of this 'noise' source on hydrostatic delay can be minimized to less than 1 mm [18].

7.1.5.3 Elevation Angle of GPS Receivers

When low angle elevation data are included in the analysis, small changes in water vapour within the model can cause large variations in the delay along the low-elevation path. A loss of sensitivity to ZWD is expected to occur when only high-elevation ray paths are used in GPS analysis. At low elevation angles, however, multipath effect will become stronger, which will cause error in pseudorange and carrier phase measurements. Multipath is difficult to characterize in general way because its amplitude and phase depend on many parameters of the receiving antenna's local environment. Many of these parameters are sufficiently constant, however, for multipath to repeat day-to-day because of the periodic ground tracks of the GPS satellites. The most common sources of multipath are buildings, trees, and the ground itself, especially when the receiver is near, or on, a

smooth and flat surface that is a good reflector at L-band. Multipath signals occur, typically, on a time scale of less than a few minutes and, theoretically, can be averaged out through long-term measurement.

The significance of multipath on GPS phase measurements depends partly on the type of antenna employed. Choke ring antennas, for example, limit multipath effects, more information can be found at [19]. Multipath can also be reduced by site location and data processing. Quality checking software, which can be used to improve GPS data, also looks into multipath and can help to eliminate its effects. The error of estimated IPWV due to multipath is of the order of 1 mm.

7.1.5.4 Mapping Function

If the atmosphere comprises a plane-parallel refractive medium, a simple cosecant function of elevation angle will map the zenith path to the slant path. The curvature of the atmosphere, however, and ray bending produce a more complex mapping function, required especially at low elevation angles. The estimation of water vapour is sensitive to small changes in the mapping function. (This is particularly true for the wet mapping function.) For these reasons, the elevation angle cut-off of GPS receivers has to be carefully chosen to obtain the optimum balance between loss of sensitivity at high elevation angles, uncertainty of the mapping function and measurement distortion due to effect of multi-path at low elevation angles.

By using GPS processing algorithms and post-processing techniques, water vapour estimates can be achieved with an accuracy better than 1.5 mm [20]. IPWV measurements from GPS and ground-based microwave radiometer (WVR) tracked each other well [21], and nearly all features in the GPS time series agree well with the WVR data [22]. Frequently, the WVR data exhibit larger short-period variations than the GPS data, the difference being attributable at least partly due to errors in the WVR algorithm under the influence of liquid

water. (The mean atmospheric radiating temperature is assumed to be constant in the retrieval of WVR data but actually varies with water vapour content along the path [23].) Part of the difference may also be due to the filtering of short-period fluctuations in the GPS data extraction algorithm [24].

7.2 Estimated Integrated Water Vapour Content

The estimated integrated water vapour is a parameter that measures the path-integrated water vapour content contained in a vertical column above the GPS receiver. Under the correct conditions the water vapour may become condensed to form small liquid water falling as precipitation. The depth of liquid water if all the water vapour is condensed into a column container of 1 m^2 base area, is referred to as the 'precipitable' water vapour, or integrated precipitable water vapour (IPWV), as in Equation (7.8). In our experiment, good agreement between the measurement of IPWV by GPS and IPWV obtained from radiosonde profiles has been found [25].

7.2.1 Comparison of IPWV with Radiosonde Measurements

Balloon soundings of temperature, pressure and relative humidity provide an alternative approach to measure the integrated water vapour content. Based on the definition of IPWV using Equation (7.8), the calculation of IPWV from radiosonde profiles requires a straight-forward numerical integration. Since radiosonde measurements are not continuous, when real time comparison with IPWV estimates from the GPS is needed, a one-hour period centred on each radiosonde launch time is chosen to produce an averaged GPS measurement. The mean IPWV can then be compared with values calculated from the relevant sounding profile. Results of IPWV measured from 48 valid sounding profiles taken in January 2000 are compared with corresponding GPS measurements in Figure 7. 4.

The time-series of IPWV values obtained from both measurements demonstrates remarkable agreement on a profile-to-profile basis. Nearly 30 % of the values are almost identical, more than a further 60 % show differences between 1 and 2 mm and only a few points have differences larger than 5 mm. It is noted that IPWV measured from radiosonde profiles appear to be generally larger than that measured by GPS in this month (although this difference is small).

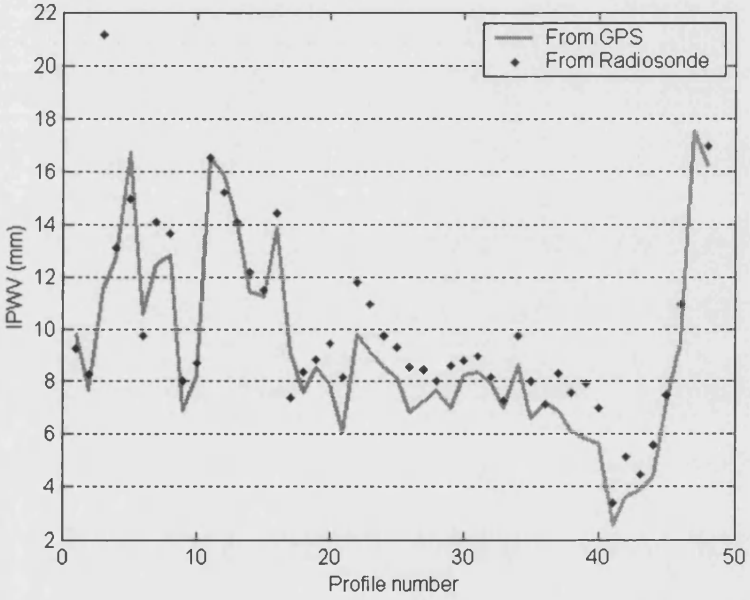

Figure 7. 4 GPS estimated IPWV compared with radiosonde measurement for each sounding profile in January 2000

Monthly mean values of IPWV are compared for the year of 2000 in Figure 7. 5. The correlation coefficient between the two curves is 0.9428. The maximum difference between the curves is 3.2 mm and occurs in August 2000.

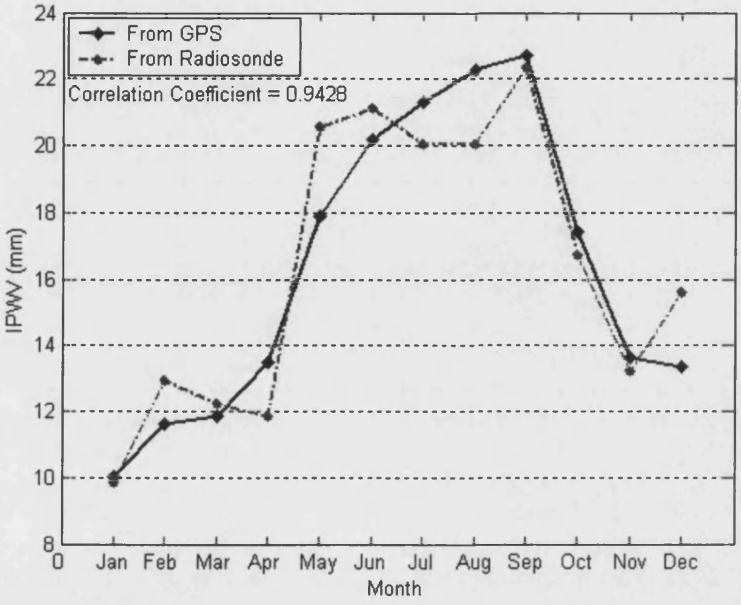

Figure 7. 5 Monthly averaged IPWV comparison from radiosonde and GPS measurements for year 2000

The disparity between the two IPWV measurements is not unexpected. These is a separation of 18 km between the two measurement sites and the passage of weather system across the two sites may, therefore, be expected to lead to differences in simultaneous measurements at the two sites [25]. In addition, the upward track of radiosonde balloons can deviate from vertical under the influence of wind, especially at high altitude, leading to errors between the measured IPWV for the actual trajectory compared with that for the assumed zenith trajectory (due to the highly variable distribution of water vapour in both the vertical and horizontal directions).

7.2.2 Diurnal and Seasonal Variation of IPWV

The annual cumulative distributions of the delay due to water vapour (ZWD) and IPWV for the year of 2000 are shown in Figure 7. 6.

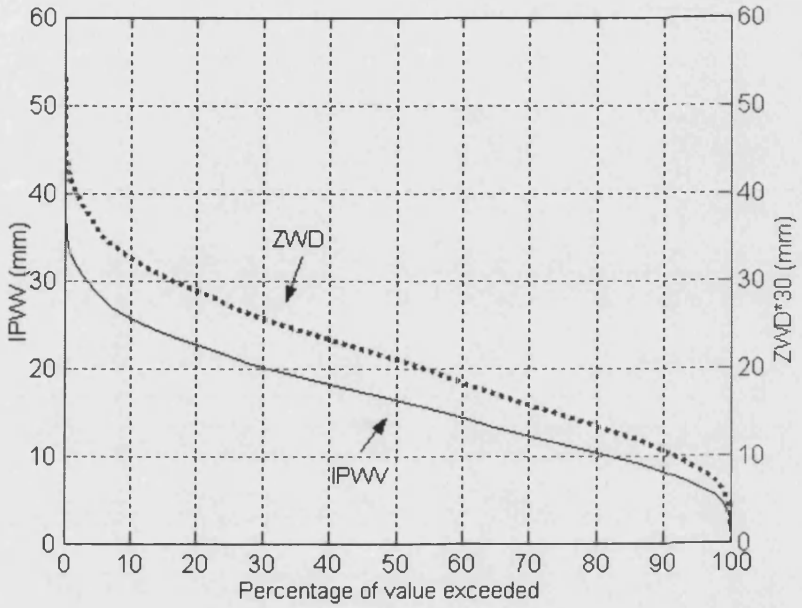

Figure 7. 6 Percentage of exceedance for IPWV and ZWD of the year 2000

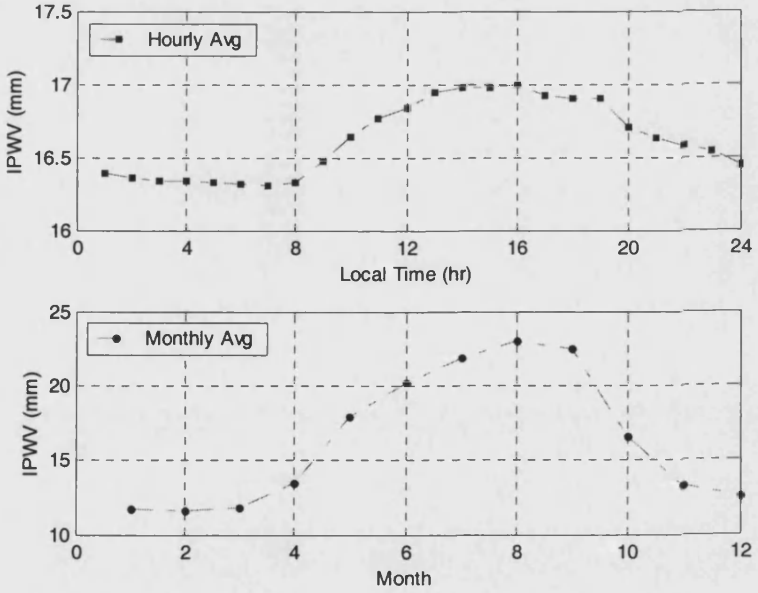

Figure 7. 7 Diurnal and seasonal variations of IPWV (mm)

The variables appear to have strong correlation on a equal-time basis. Values of IPWV are generally between zero and 40 mm, with the majority lying in the range between 10 and 20 mm. IPWV shows a significant diurnal and seasonal variation, Figure 7. 7. Hourly averaged IPWV throughout the whole 19 months measurement campaign shows: a peak between 14.00 and 16.00 hr. Monthly averaged IPWV peaks in August before starting to decrease during colder months. Both observations seem to reveal the indirect relation between IPWV and air temperature. As temperature rises, the capacity of air to hold water vapour increases and more water vapour can be expected along the path. Due to the existence of turbulent mixing and condensation, however, path-integrated water vapour may represent a better reflecting of weather conditions aloft, than point measurements at the surface.

7.3 Summary:

GPS water vapour estimation techniques have several advantages over conventional water vapour measurement systems, including the increasingly more widespread and dense distribution of GPS stations, low operational costs and 24-hour, near-real-time availability. Measurement of atmospheric water vapour by Earth-based GPS receivers has been demonstrated to be comparable with measurement using radiosondes.

GPS techniques provide continuous measurement of IPWV recorded in greater temporal resolution than radiosonde data. The measured variable (ZWD) contains information about the integrated water vapour along the path. This is believed to be closely involved in the scintillation processes. In the following chapter, the potentials of GPS estimated IPWV is further explored and a set of new prediction models for scintillation intensity based on the estimated IPWV are presented.

7.4 References:

[1] P. Enge and P. Misra, "Special issue on Global Positioning System," *Proceeding of The IEEE*, vol. 87, pp. 3-15, 1999.

[2] R. D. Fontana, W. Cheung, and T. Stansell, "The modernized L2 civil signal," *GPS world*, pp. 28-33, Sept 2001.

[3] L. L. Yuan, R. A. Anthes, R. H. Ware, C. Rocken, W. D. Bonner, M. G. Bevis, and S. Businger, "Sensing climate change using the global positioning system," *J. Geophys. Res*, vol. 98, pp. 14925-14937, 1993.

[4] M. Bevis, S. Businger, T. A. Herring, C. Rocken, R. A. Anthes, and R. H. Ware, "GPS meteorology: Remote sensing of atmospheric water vapour using the Global Positioning System.," *J. Geophys. Res*, vol. 97, pp. 15787-15801, 1992.

[5] MetOffice, *A course in elementary meteorology*. London: Her Majesty's Stationery Office, 1962.

[6] J. L. Davies, T. A. Herring, I. I. Shapiro, and G. Elgered, "Geodesy by radio interferometry: Effects of atmospheric modelling errors on estimates of baseline length," *Radio Sci*, vol. 20, pp. 1593-1607, 1985.

[7] M. Bevis, S. Businger, T. A. Herring, C. Rocken, R. A. Anthes, and R. H. Ware, "Remote sensing: atmospheric water vapour using the Global Positioning System.," *J. Geophys. Res*, vol. 97, pp. 15787-15801, 1992.

[8] J. Askne and H. Nordius, "Estimation of tropospheric delay for microwaves from surface weather data.," *Radio Sci*, vol. 22, pp. 379-386, 1987.

[9] J. Spilker, "GPS signal structure and performance characteristics," *J. Inst. Navi*, pp. 121-146, 1978.

[10] F. S. Solheim and J. Vivekanandan, "Propagation delays induced in GPS signals by dry air, water vapour, hydrometeors and other particulates.," *J. Geophys. Res*, vol. 104, pp. 9663-9670, 1999.

[11] S. Businger, S. R. Chiswell, M. Bevis, J. P. Duan, R. A. Antes, C. Rocken, R. H. Ware, M. Exner, T. Vanhove, and F. S. Solheim, "The promise of GPS in atmospheric monitoring," *Bulletin of the American Meteorological Society*, vol. 77, pp. 5-18, 1996.

[12] O. T. Davies and P. A. Watson, "GPS phase-delay measurement: Technique for calibration and analysis in millimetre-wave radio propagation studies.," *IEE Proc. Microwave Antenas and Propagation.*, vol. 146, pp. 369-373, 1999.

[13] J. M. Tranquilla and H. M. Al-Rizzo, "Range errors in Global Positioning System during ice cloud and snowfall periods," *IEEE Trans. Antennas Propagat.*, vol. 42, pp. 157-165, 1994.

[14] J. F. Zumberge, M. B. Heflin, D. C. Jefferson, M. M. Watkins, and F. H. Webb, "Precise point positioning for the efficient and robust analysis of GPS data from large network.," *J. Geophys. Res*, pp. 5005-5017, 1997.

[15] GIPSY-OASIS, "GIPSY-OASIS Handout," 1999, pp. 106-108.

[16] A. Neil, "Global mapping functions for the atmosphere delay at radio wavelengths," *Journal of Geophysical Research*, vol. 101, pp. 3227-3244, 1996.

[17] P. Tregoning, "Accuracy of absolute precipitable water vapour estimates from GPS observations," *J. Geophys. Res*, vol. 103, pp. 28701-28710, 1998.

[18] G. Elgered, J. L. Davies, T. A. Herring, and I. I. Shapiro, "Geodesy by radio interferometry: water vapour radiometry for estimation of the wet delay," *J. Geophys. Res*, vol. 96, pp. 6541-6555, 1991.

[19] http://www.ashtech.com.

[20] E. R. Westwater, H. Y, S. I. Gutman, and D. E. Wolfe, "Remote sensing of total precipitable water vapour by microwave radiometers and GPS during the 1997 water vapor intensive operating period.," presented at International Geoscience and Remote Sensing symposium, IGARSS'98, Seattle,USA, 1998.

[21] J. P. Duan and M. Bevis, "GPS meteorology: direct estimation of the absolute value of precipitable water.," *J. App. Meteor.*, vol. 35, pp. 830-838, 1996.

[22] G. Elgered, J. M. Johansson, and B. O. Ronnang, "Measuring regional atmospheric water vapour using the Swedish permanent GPS network.," *Geophysical Research Letters*, vol. 24, pp. 2663-2666, 1997.

[23] S. R. Chiswell, S. Businger, M. Bevis, F. Solheim, C. Rocken, and R. Ware, "Improved retrieval of integrated water vapour from water vapor radiometer measurements using numerical weather prediction models.," *J. Atmos. Oceanic Technol.*, vol. 11, pp. 1253-1261, 1994.

[24] P. Elosegui, J. L. Davies, J. M. Johansson, and I. I. Shapiro, "Detection of transient motions with the Global Positioning System: The effects of signal scattering on estimates of site position.," *J. Geophys. Res*, vol. 101, pp. 11249-11261, 1996.

[25] O. T. Davies and P. A. Watson, "Comparison of integrated precipitable water vapour obtained by GPS and radiosondes.," *Electron. Lett.*, vol. 34, pp. 645-646, 1998.

Chapter 8

GPS-INFORMED MODEL – PART II

GPS estimated IPWV has several advantages over the commonly used scintillation predictor – surface measured wet term of refractivity N_{wet}. Variation of IPWV has demonstrated better correlation with seasonal and diurnal variations of scintillation than N_{wet}. Three different approaches to incorporating a GPS-derived water vapour estimate into a model for scintillation prediction are explored. A comparison of the performance of existing and new models supports the assertion that the new models offer improved prediction.

8.1 Design of An Empirical Prediction Model for Scintillation Intensity

A desired prediction model for scintillation intensity needs to consider all the necessary characteristics of scintillation and their relationship to meteorological and system parameters. As discussed in Chapter 4 and 5, the received scintillation intensity is related to:

1) The effective diameter of receiving antenna (since the signal at the antenna output is a spatial average of the random fluctuations of the wave front across the antenna aperture)

2) The elevation angle of receiving antennas (since low elevation angles result in a longer path exposed to turbulence and the atmosphere generally)

3) The operating frequency of the beacon (since the fundamental mechanism of electronmagnetic scattering that results in scintillation is a sensitive function of the electrical size of the scatterers)

4) The degree of turbulence along the path (since this is the mechanism by which spatial and temporal variation in the refractive index field is generated)

In general, scintillation increases as antenna aperture decreases, elevation angle decreases, and frequency increases. For geostationary satellite beacons, the statistics of scintillation measured at a given location may be peculiar to that location for several reasons: i) the climate patterns vary from one place to another ii) aerographic micro-climates iii) the geometry of the path including elevation angle and azimuthal orientation with respect to the prevailing wind will vary from place to place.

In Chapter 6, it was seen that existing semi-empirical models for scintillation intensity prediction have taken some or all of these considerations into account. It can be concluded that most of the semi-empirical models for scintillation intensity prediction have taken each of these considerations as an individually inter-independent factor, they are: the antenna averaging factor, the elevation dependence factor, the frequency dependence factor and meteorological dependence factor. Based on our results of scintillation characterisation presented previously, in order to develop a new model of scintillation prediction for Sparsholt, the factors affecting scintillation intensity will be integrated in the following way:

8.1.1 Antenna Averaging Factor

For an antenna of finite effective diameter D (m), its low-pass filtering effect of incident fluctuation can be calculated by the Haddon-Vilar model [1]:

$$g(x)=\frac{\sigma_g^{\,2}(D)}{\sigma_g^{\,2}(0)}=3.8637\left(x^2+1\right)^{11/12}\cdot\sin\left[\frac{11}{6}\arctan\left(\frac{1}{x}\right)\right]-7.0835x^{5/6}$$
$$\approx 1-7.0835x^{5/6} \qquad (x<<1) \tag{8. 1}$$

where $x=1.22\eta\cdot D^2\cdot(f/L)$ is a measure of the ratio between the effective antenna diameter and the size of the first Fresnel-zone. L is the effective path length, which is a function of turbulent layer height h and elevation angle θ, according to:

$$L(h,\theta)=\frac{2h}{\sqrt{\sin^2\theta+2.35\times10^{-4}}+\sin\theta} \tag{8. 2}$$

The turbulence height h is assumed to be 1000 m as given by the ITU-R. The averaging factor for scintillation intensity received by a finite size antenna is denoted by $G(f,h,\theta)$.

8.1.2 Elevation Dependence Factor

The part of an Earth-satellite path that may be subject to atmospheric turbulence or high frequency component of rain scattering is dependent on the elevation angle of an antenna beam. For scintillation intensity calculations, the ITU-R provides an elevation dependence factor denoted by $F_1(\theta)$:

$$F_1(\theta)=\sin^{-1.2}\theta \tag{8. 3}$$

As elevation decreases the effective path length in a turbulent region becomes longer.

8.1.3 Frequency Dependence Factor

Based on Tatarskii's theory of clear-air turbulence (Chapter 4) the scinitllaiton intensity at the output of a point receiver depends on wavelength (and therefore carrier frequency) of the transmitted signal according to 7/12 power law [2]. The

frequency dependence factor of scintillation intensity, denoted by $F_2(f)$, as given the ITU-R is:

$$F_2(f) = f^{7/12} \tag{8. 4}$$

where f is the operating frequency in GHz.

8.1.4 Climate Dependence Factor

The normalized scintillation standard deviation, σ_{norm}, is related to the measured standard deviation, σ_{meas} by:

$$\sigma_{norm} = \frac{\sigma_{meas}}{G(f,h,\theta)\cdot F_1(\theta)\cdot F_2(f)} \tag{8. 5}$$

Variations in humidity, pressure, temperature and the magnitude and scale size of turbulence in the troposphere change the refractive index along the propagation path. For clear-air scintillation, by comparing Equation (8.5) with Equation (4.6), it is clear that the normalized intensity plays an equivalent role to the structure constant of refractive index, which is a measure of the intensity of refractive index variation. Considering scintillation will be caused, in general, by other sources, the ideal normalized intensity can be identified as a variable that describes the instability of the atmosphere and reflects the corresponding meteorology at the time of measurement. It therefore represents a climate dependence factor.

Due to the complexity of atmospheric processes, the climate dependence factor seeks meteorological variables or fix relationships of these variables that have a stable correlation with scintillation intensity and can be repeatedly observed in a large number of experiment databases. These candidate predictors should be conveniently accessed without the need for sophisticated or expensive

experiment. They are responsible for representing atmospheric instability and will therefore largely determine prediction accuracy in the resulting model.

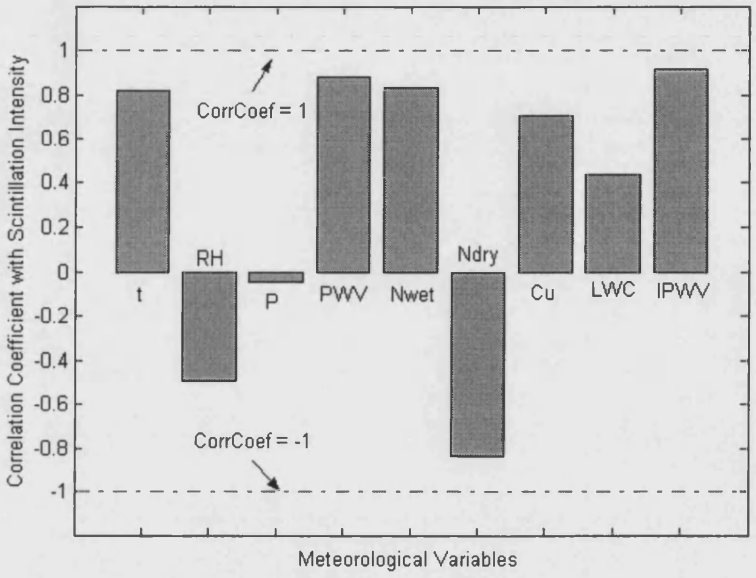

Figure 8. 1 Comparison of correlation coefficient with scintillation intensity by monthly averaged values of meteorological variables

(Key: t – temperature, RH – relative humidity, P – pressure, PWV – path water vapour (derived from radionsonde), N_{wet} – wet term of refractivity, N_{dry} - dry term of refractivity, Cu – percent Cumulus cover, LWC – cloud liquid water content, IPWV – integrated precipitable water vapour (derived from the GPS)).

A review of existing models (Chapter 6) has revealed that a number of meteorological variables have been proposed as candidate climate dependence factors including the surface-measured temperature (t), wet term of refractivity (N_{wet}), and relative humidity (RH), mean percentage of cumulus cloud coverage (Cu), liquid water content of heavy cloud (LWC) and integrated water vapour content from radiosonde measurement (PWV). Figure 8. 1 summarizes selected meteorological variables and the correlation coefficients of their monthly mean values with those of the observed scintillation intensity.

Among these variables, GPS-derived integrated precipitable water vapour measurements (IPWV) have the highest correlation. Conversely, the path-integrated liquid water content does not exhibit significant correlation with scintillation. Surface-measured temperature and N_{wet} appear to correlate positively with scintillation while relative humidity and N_{dry} have negative correlations. The measured surface pressure has virtually no correlation with the scintillation intensity.

8.2 Improving the Existing ITU-R Model

The results of comparing the performance of 15 existing models when tested against our beacon measurement database (Chapter 6) suggests, that the model recommended by ITU-R provides a relatively accurate prediction in terms of overall low RMS error and high correlation with the measurement. The basic form of this model has been obtained by applying the principles described above. The surface measured wet term of refractivity (N_{wet}) is used to represent the climate dependence factor. A highly correlated predictor will generally lead to small prediction errors especially for linear formulas, and optimal performance (least RMS errors) can be achieved by regression techniques. Figure 8. 1 therefore implies that the prediction of scintillation intensity can be further improved by employing IPWV as an alternative or additional predictor.

8.2.1 Importance Of Water Vapour

The high correlation between measured scintillation intensity and IPWV or N_{wet} is not peculiar to our database. Similar correlations had also been found by Karasawa [3], Vilar [4] and Marzano [5] using datasets measured at other locations. Furthermore, water vapour has long been believed to play an important role in the generation of scintillation.

The differential of Equation (4.1), can be used to relate fluctuations in refractive index at a given height with that of meteorological variables:

$$\delta n = \delta T \cdot \left[-\frac{77.6}{T^2}\left(p + 9620\frac{e}{T} \right) \right] + \delta p \cdot \left(\frac{77.6}{T} \right) + \delta e \cdot \left(\frac{373256}{T^2} \right) \tag{8. 6}$$

where T is the temperature in K, p is the pressure in hPa and e is the water vapour pressure in hPa. Refractive index variations can then be treated as principally dependent on temperature and humidity, as variations of pressure can be practically disregarded. Equation (8.6) supports the traditional notion that temperature and humidity are suitable predictors for scintillation.

Vapour as the most common phase that water present itself in the atmosphere has particularly large latent heat. The phase changes in water are accompanied by changes in latent heat. It follows that the water vapour content of the atmosphere represents a vast storehouse of heat in latent form. At a given temperature, humid air is lighter (less dense) than dry air because the molecular weight of water vapour is 18 whereas dry air has a weight of 28.9. This may have a significant effect on the buoyancy forces or vertical acceleration of air parcels and therefore the stability of the atmosphere. Furthermore, by comparing the visual experience when turbulence happens with the microwave properties, in the context of scintillation water vapour effectively can be regarded as a disclosure agent for turbulence.

8.2.2 Calculation of N_{wet} in the ITU-R Model

The meteorological dependence factor involved in the ITU-R model is through the wet term of refractivity (N_{wet}), which is computed from the surface point measurements of water vapour pressure e (in hPa) and temperature T (in K):

$$N_{wet} = 3.732 \times 10^5 \cdot \frac{e}{T^2} \tag{8. 7}$$

Both e and T are required to be averaged over a period of duration equal to, or longer than, a month. The coefficients in Equation (6.18) are obtained from linear regression and suggest an emphasised weight over the wet refractivity (N_{wet}) compared to the value in a natural environment is needed for the prediction model to achieve its optimal performance. The variations of the dry term of refractivity (N_{dry}) are assumed to be virtually zero and are not taken into considerations in the calculation of the reference intensity. This reflects the significance of water vapour for scintillations.

It is noted that the wet term of refractivity (N_{wet}) is the sole meteorological input to ITU-R model, calculated by using mean values of surface-measured parameters. A surface-measured variable can be used to characterise its integrated path values only when the two quantities are highly correlated. Inhomogeneity in the index of refraction is believed to concentrate at the top of the planetary boundary layer, which is a relatively moist layer of air ranging from the Earth's surface up to a height of 1-1.5 km. Results in Chapter 5 have further suggested that during different season, the height of boundary layer may extend a significant fraction along the tropospheric path. In general, these layers are expected to be higher in summer and lower in winter. The increased height of turbulence layers could affect surface N_{wet} in a way that it is not necessary always correlated with turbulence forces along the path.

Water vapour is particularly variable with height compared with pressure and temperature, with a smaller de-correlation distance vertically than horizontally. When influenced by condensation and turbulent mixing in the lower troposphere, it has a more complicated behaviour than temperature and pressure, and its distribution could get more inhomogeneous along the link path.

Chapter 5 shows that, unlike scintillation intensity, the surface-measured wet term of refractivity does not have significant diurnal variations, although its seasonal variation correlates well with that of scintillation. This limits how well N_{wet} can predict short-term mean values of scintillation intensity (for example on a time scale of hours). It follows that either there are factors causing the variation of scintillation intensity unrelated to variations of N_{wet} and these factors have significant effect on scintillation when monitoring for periods shorter than a day, or N_{wet} is insufficiently detailed or informed to describe these short-term changes of scintillation intensity.

Surface-measured N_{wet} when used alone does not seem to be a convincing predictor for scintillation, especially over short time scales. Due to the highly variable distribution of water vapour, it is reasonable to assume that a measurement based on the presence of water vapour throughout the troposphere (local to the propagation path) will provide richer information about conditions along the path and thus improves the prediction of scintillation. Any candidate variable that might replace, or compensate the weakness of N_{wet} should have a high and stable correlation with scintillation. Figure 8. 1 suggests ground-level measured temperature (t) and (GPS-derived) IPWV have either comparable or better correlation with the intensity than N_{wet}. Furthermore, both of these variables have significant diurnal variations.

Two directions are identified when incorporating t and IPWV in an improved model for the prediction of scintillation intensity. The objective of the first direction is to employ these measurements in the development of a path-informed new version of N_{wet} for the classical ITU-R model. In the second direction a linear relationship formula will be derived based on the direct correlation between these two variables and the recorded scintillation intensity.

8.3 Inference Of Proposed Models

Coefficients of the ITU-R model have been adjusted using experimental beacon data from the data banks collected from 13 countries mainly in Europe, North America and Japan. In order to obtain a path-informed version of N_{wet}, three methods of incorporating IPWV have been investigated. They are referred to as: i) the Reitan/Smith/Bolsenga approach, ii) the standard atmosphere approach and iii) the regression approach. The first is based on the relationship between total water vapour content and surface dew point temperature, the second uses an assumed water vapour profile and the third is based on a regression derived linear relationship of GPS-derived IPWV and surface dew point temperature.

8.3.1 Relation Between Total Water Vapour Content and Surface Dew Point

Total or integrated precipitable water vapour (IPWV) and surface dew point temperature have been studied for both meteorological and radio science purposes. Significant correlations have been found between these two quantities and several models have been proposed in the literature to relate them. Reitan and Smith models apply to monthly averaged values. The Bolsenga model applies to daily averaged values.

8.3.1.1 Reitan and Smith Model Approach

Reitan has found excellent correlation (0.96-0.99) between total precipitable water and surface dew point using mean monthly data from North America. A regression line relating the mean monthly surface dew point and mean monthly total precipitable water vapour obtained from a total of 540 observations has been found [6]. The formula for the regression line is given by Equation (8.8):

$$\ln U = A + B \cdot T_d \tag{8.8}$$

where U is the total precipitable water vapour in mm, T_d is the dew point temperature in K. The coefficients are $A = -14.353$ and $B = 0.0614$.

Smith proposed a relationship of similar form to Equation (8.8). A is not a constant, however, but is a variable dependent upon the actual moisture profile. The relationship is [7]:

$$\ln U = [-15.649 - \ln(\lambda + 1)] + 0.0707 T_d \quad (8.9)$$

λ is the power law coefficient of the mixing ratio profile obtained, for example, from balloon soundings, and depends on latitude and season. Smith illustrates λ values obtained using the mean Northern Hemisphere soundings tabulated by London [8], Table 8. 1. (Only the latitudinal zones that covers our measurement sites are quoted.)

Latitudinal Zone (deg N)	Winter	Spring	Summer	Fall	Annual Average
40-50	2.70	2.95	2.77	2.71	2.78
50-60	2.52	3.07	2.67	2.93	2.79
Northern Hemisphere Average	2.52	2.64	2.62	2.70	2.61

Table 8. 1 Seasonal and latitudinal mean values of λ for Smith model

In our calculation, the northern hemisphere averages are chosen for Sparsholt (51.083N, 1.383W). These are 2.52 for winter, 2.64 for spring, 2.62 for summer and 2.70 for autumn.

Figure 8. 2 shows that Reitan and Smith models generally give good prediction for surface dew point temperature and have comparable performance on our measured data. Both models have slightly greater prediction errors for small and large surface dew point temperatures.

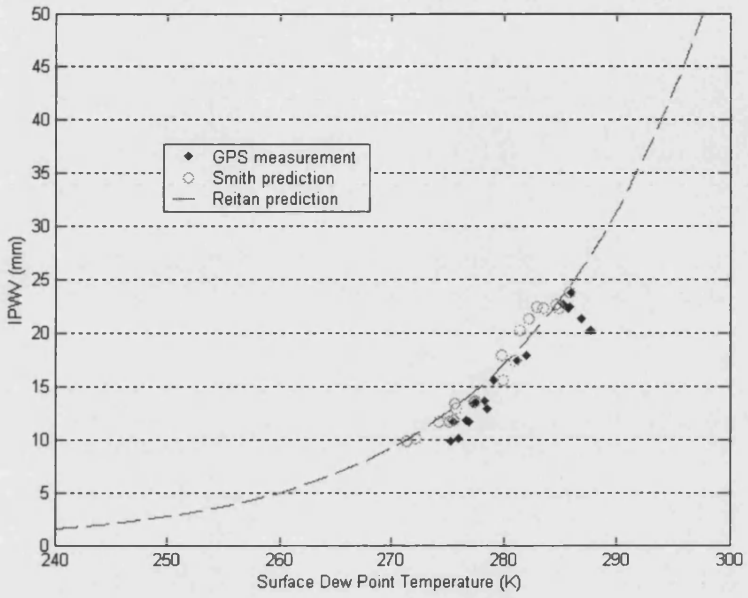

Figure 8. 2 Comparison of monthly averaged dew point temperature predicted by Retain /Smith models from the GPS measurement and those measured on the ground

8.3.1.2 Bolsenga Model Approach

Bolsenga has tracked the same procedure to determine the regression relations between mean daily and hourly observations of total water vapour content and surface dew point [9]. He found the coefficients of Equation (8.8) to be $A = -18.574$ and $B = 0.0769$ for the mean daily observations, and $A = -16.636$ and $B = 0.06912$ for the hourly observations.

The prediction is compared with data in Figure 8. 3 for the 19 months of measurement.

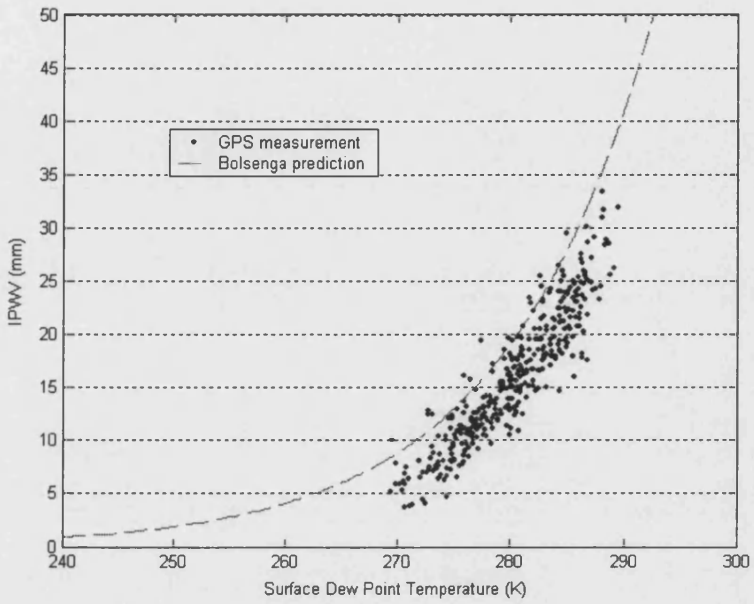

Figure 8. 3 Comparison of daily averaged dew point temperature predicted by Bolsenga model from the GPS measurement and those measured on the ground

The computed surface dew point temperature T_d (K), is related to the surface water vapour pressure, e (hPa) by:

$$e = 6.11\exp\left(2.5\times10^6 / 461.5\times\left(1/273.15 - 1/T_d\right)\right) \tag{8. 10}$$

A new version of N_{wet} can therefore be estimated from IPWV and then used to calculate the reference intensity using Equation (6.17), (6.18) and (6.19) in the classical ITU-R model. Results using the Reitain approach to correlate IPWV with T_d for the prediction of scintillation intensity is referred to here as the Reitain model prediction and that of using the Smith approach is referred as Smith model prediction.

8.3.2 Standard Atmosphere Approach

According to the reference standard atmosphere [10], which is based on the United States Standard Atmosphere (1976), the atmosphere is divided into seven

successive layers showing linear variation with temperature. The water vapour ρ_w can be modelled by an exponential relationship with altitude. If ρ_0 is taken as the scale height (typically $h_0 = 2000\,m$), then water vapour density ρ_w (in g/m^3) at a given altitude h (in m) can be approximated:

$$\rho_w(h) = \rho_0 \exp(-h/h_0) \tag{8. 11}$$

Recall the definition of IPWV from Equation (7.8):

$$IPWV = \frac{1}{\rho_l} \cdot \int_H^\infty \rho_w \cdot dz \tag{8. 12}$$

where H is the altitude of the ground-based GPS receiver above mean sea level, (about 90 m in our case). IPWV can be related to the water vapour density at ground level ρ_0 by:

$$\begin{aligned} IPWV &= \frac{1}{\rho_l} \cdot \int_H^\infty \rho_0 \cdot e^{-\frac{z}{h_0}} \cdot dz = \frac{1}{\rho_l} \cdot \rho_0 \cdot (-h_0) \cdot \int_{-\frac{H}{h_0}}^{-\infty} e^m \cdot dm \\ &= 0.956 \frac{\rho_0}{\rho_l} \cdot h_0 \end{aligned} \tag{8. 13}$$

where ρ_l is the liquid water density 1000 kg/m^3. It is noted the unit of GPS estimated IPWV is millimetre and the unit of humidity from different sources can be diverse. It is preferred here to express all quantities in SI units:

$$\begin{aligned} \rho_0 &= \frac{\rho_l}{0.956 h_0} \cdot IPWV = \frac{10^6}{2000} \cdot \left(\frac{g}{m^3}\right) \cdot \left(\frac{1}{m}\right) \cdot IPWV \cdot (mm) \\ &= \frac{10^6}{1911} \cdot IPWV \times 10^{-3} \left(\frac{g}{m^3}\right) \\ &= 0.523 \cdot IPWV \left(\frac{g}{m^3}\right) \end{aligned} \tag{8. 14}$$

The above expression can be incorporated into the relationship between IPWV and surface water vapour partial pressure e by applying the gaseous hydrostatic equation:

$$e = \frac{\rho \cdot T}{216.7} = \frac{1}{216.7} \cdot \rho_0 \cdot T_{surf} = \frac{0.523}{216.7} \cdot IPWV \cdot T_{surf} = \frac{1}{414.3} \cdot IPWV \cdot T_{surf} \quad (8.15)$$

where T_{surf} is the surface measured temperature (K). An IPWV-informed version of wet term of refractivity can therefore be calculated from Equation (8.16):

$$Nwet_n = 3.732 \times 10^5 \cdot \frac{e}{T_{surf}^{\ 2}} = 3.732 \times 10^5 \cdot \frac{1}{414.3} \cdot IPWV \cdot T_{surf} \cdot \frac{1}{T_{surf}^{\ 2}} = 3.732 \times 10^5 \times \frac{1}{414.3} \cdot \frac{IPWV}{T_{surf}} = 900.797 \cdot \frac{IPWV}{T_{surf}} \quad (8.16)$$

8.3.3 Linear Regression Approach

A straight-line relationship between IPWV and surface water vapour pressure is assumed, i.e.:

$$e = A_1 \cdot IPWV + B_1 \quad (8.17)$$

where coefficients $A_1 = 0.4012$ and $B_1 = 3.9485$ are constants obtained from linear regression techniques in a least square sense using Dataset 2.

Equation (8.17) essentially infers surface water vapour from the integrated path measurement for the calculation of wet refractivity that is then used in the classical ITU-R model. We refer to this as the Bath 1 model.

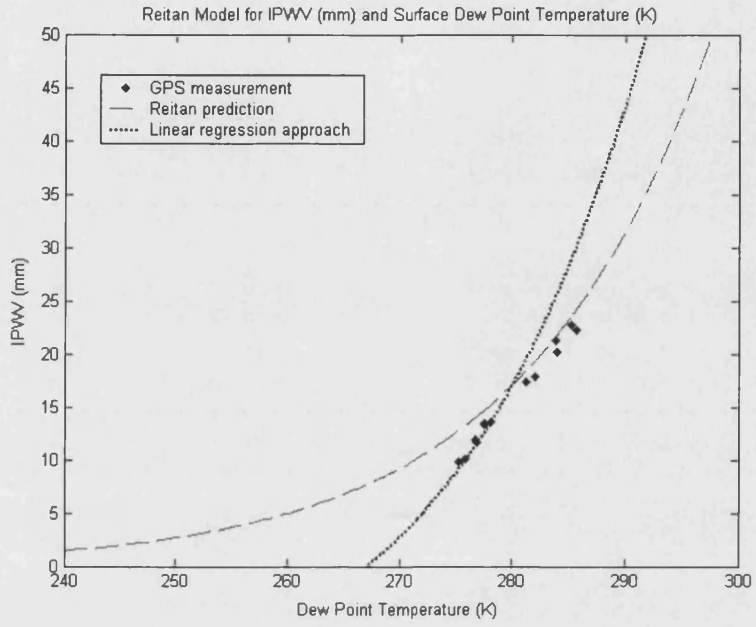

Figure 8. 4 Linear regression relationship between IPWV and surface dew point temperature compared with Reitan prediction and measurement

By converting Equation (8.17) into a relationship between surface dew point temperature and IPWV, direct comparisons of Bath 1 model prediction, the Reitan model prediction and the GPS and simultaneous meteorological measurements can be made, Figure 8. 4. The dotted curve relating IPWV and surface dew point temperature does not follow the measured values exactly, especially at higher values of IPWV. It has been found, however, that higher values of IPWV are likely to be associated with rain events, or strong cloud activity. It is possible that turbulence under these conditions may occur predominantly in one (or possibly more than one) thin turbulent layer(s) [11].

8.3.4 Direct Correlation Approach

IPWV and surface temperature have been shown to possess the two highest correlations with monthly mean scintillation intensity. It is reasonable, therefore, to assume the following relationship:

$$\sigma_{ref} = A_2 \cdot t + B_2 \cdot IPWV + C_2 \quad (8.18)$$

where t is the surface temperature measured in degree Celsius. The regression coefficients $A_2 = 3.198 \times 10^{-5}$, $B_2 = 2.0537 \times 10^{-4}$ and $C_2 = 0.006$ yield a minimum RMS error between monthly scintillation prediction and measurement in Dataset 2.

A normalized intensity predicted using Equation (8.18) and modified by applying the antenna aperture, frequency and elevation dependence corrections discussed earlier is referred to here as the Bath 2 model.

8.3.5 Prediction of the GPS-informed Models Compared with the ITU-R Model

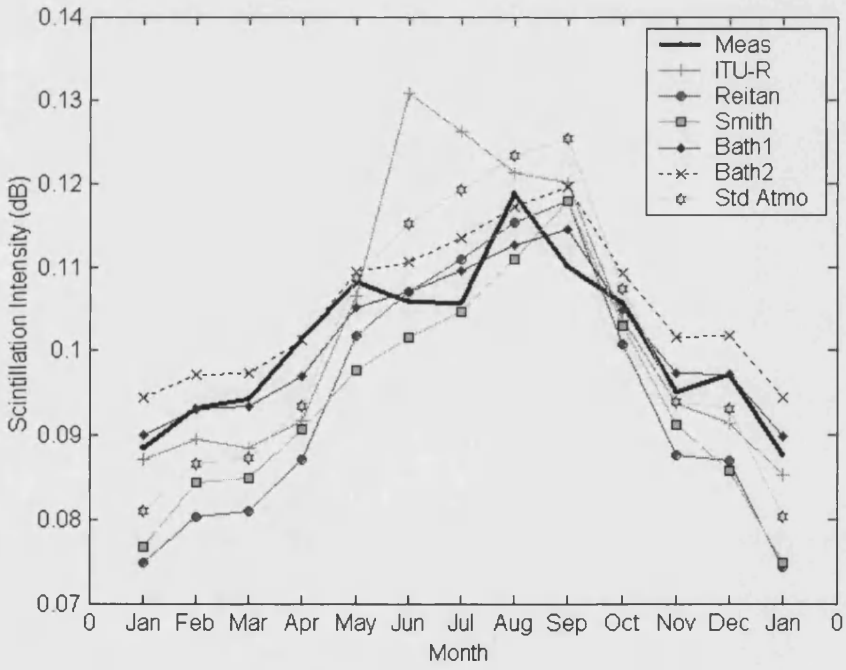

Figure 8. 5 Comparison of selected prediction methods with Dataset 2 measurement (20GHz)

Predictions of monthly scintillation intensity have been compared with the ITU-R model and beacon measurement for Dataset 2 (13 months) in Figure 8. 5. RMS errors between prediction and measurement are presented in Table 8. 2.

Prediction Method	RMS error	Correlation Coefficient
ITU-R	0.0102	0.8197
Reitan	0.0098	0.9374
Smith	0.0083	0.9527
Standard Atmosphere	0.0079	0.9344
Bath 1	0.0030	0.9402
Bath 2	0.0053	0.9383

Table 8. 2 Comparison of IPWV informed prediction and measurements of Dataset 2 (20 GHz)

It can be seen that in the comparison that all the models using IPWV as a predictor have higher correlation with the measured scintillation intensity and lower RMS errors than the classical ITU-R model. It is noted that these models have generally better prediction during the warmer months (May - September). The Smith model has better performance than the Reitan model, as the required coefficients have been adjusted to better describe the specific climate. Naturally, the two models derived through linear regression give the best predictions, the Bath1 model follows best of all.

Further test has been carried out on the remaining 6-month database (Dataset 1). Model predictions are compared with the beacon measurement in Figure 8. 6 and the RMS errors and correlation coefficients are shown in Table 8. 3.

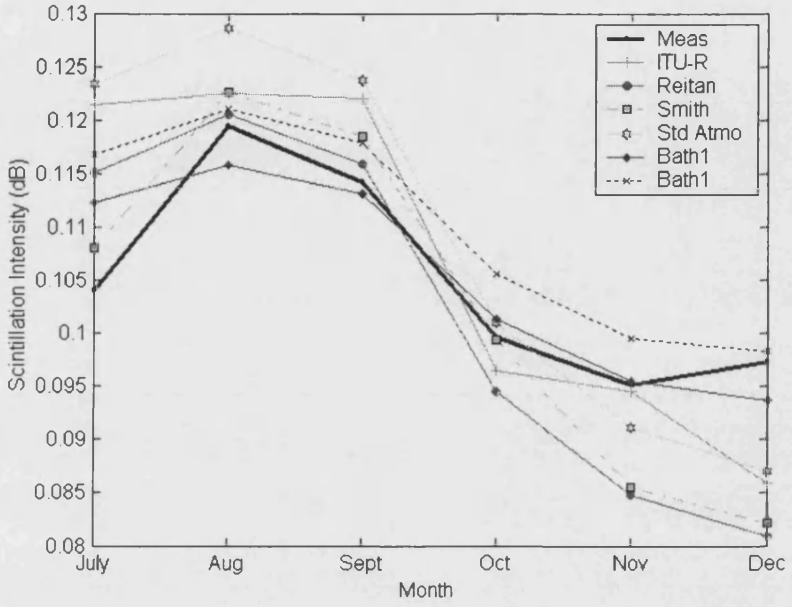

Figure 8. 6 Comparison of selected prediction methods with Dataset 1 measurements (20GHz)

Prediction Method	RMS error	Correlation Coefficient
ITU-R	0.0093	0.8459
Reitan	0.0094	0.8884
Smith	0.0088	0.9125
Standard Atmosphere	0.0106	0.8847
Bath 1	0.0040	0.8969
Bath 2	0.0063	0.9063

Table 8. 3 Comparison of IPWV-informed prediction and measurements of Dataset 1 (20 GHz)

In spite of the expected yearly variation between 1999 and 2000, Bath1 and Bath2 models have demonstrated reasonable consistency in terms of their performances. The performance of the new models and the ITU-R model are summarized in Figure 8.7.

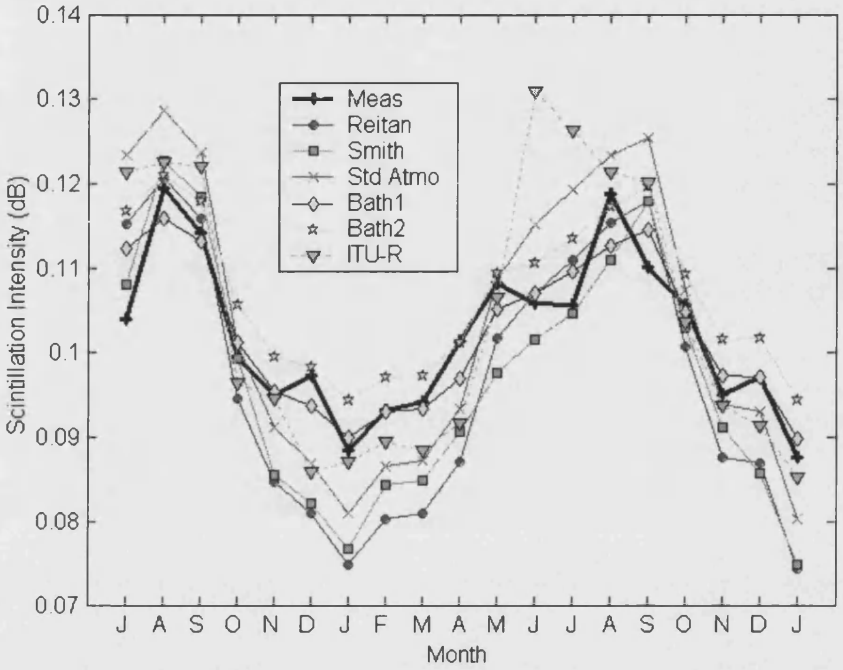

Figure 8. 7 Prediction models using IPWV compared with the ITU-R model

8.4 Results And Discussions

The new models are compared with the rest of 15 existing models in Figure 8.8. The RMS errors and percentage fractional errors are compared in Table 8. 4 and 8.5.

Model	RMS Error (dB)	Correlation Coefficients
Bath 1	0.0034	0.9286
Bath 2	0.0056	0.9298
Smith	0.0085	0.9291
Std Atmosphere	0.0089	0.9211
Reitan	0.0097	0.9243
ITU-R	0.0099	0.8294
Vasseur	0.0154	0.5669
Otung	0.0170	0.8294
Marzano-STN2	0.0178	0.8419
Kamp II	0.0180	0.7776
Karasawa	0.0209	0.8294
Kamp III	0.0221	0.8403
Marzano-DPSP	0.0276	0.7772
Marzano-STNV2	0.0328	0.7863
Marzano-MPSP	0.0345	0.7870
Kamp I	0.0354	0.6719
Marzano-STHV2	0.0394	0.7706
Marzano-STH2	0.0417	0.7830
Ortgies-N	0.0515	0.7990
Ortgies-T	0.0624	0.7904

Table 8. 4 RMS errors and correlation coefficients between estimated and measured scintillation intensity at 20 GHz on a monthly basis in rank order of RMS error

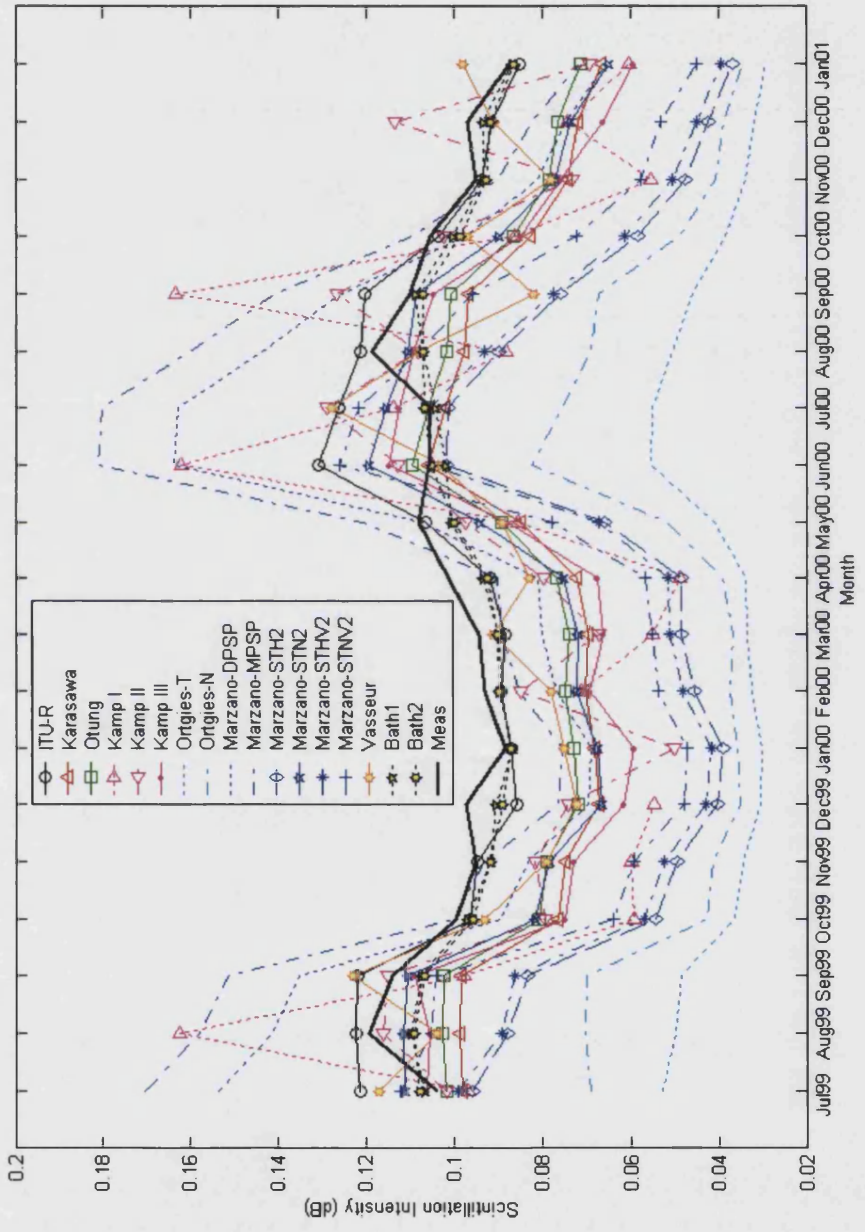

Figure 8. 8 Model prediction comparison for scintillation intensity

Model	Bias (F)	RMS error (F)	Skewness (F)
ITU-R	-1.5837	9.4806	-0.9821
Karasawa	19.25	21.0093	-0.9174
Otung	15.0808	17.0484	-0.9733
Kamp I	15.4205	34.5623	-1.1095
Kamp II	9.0708	18.7795	-0.0834
Kamp III	18.0493	22.8299	-0.4973
Ortgies-T	61.1017	61.4370	-0.9887
Ortgies-N	50.0741	51.5850	-0.7861
Marzano-DPSP	-1.4926	26.6830	-0.8516
Marzano-MPSP	-12.8679	32.2724	-0.7900
Marzano-STH2	38.6812	42.5867	-0.7747
Marzano-STN2	13.2356	18.4038	-0.6197
Marzano-STHV2	36.0036	40.2083	-0.8465
Marzano-STNV2	26.0489	33.9751	-0.7713
Vasseur	7.9117	15.0655	-0.7150
Reitan	5.8373	10.0498	-0.4020
Smith	5.5878	8.7068	-0.3103
Std Atmosphere	-0.9430	8.5626	-0.4612
Bath 1	-0.1838	3.1704	-0.3986
Bath 2	-4.5331	5.5920	-0.3370

Table 8. 5 Bias, RMS error, skewness of the percentage fractional error together with the correlation coefficient between estimated and measured scintillation intensity at 20 GHz on a monthly basis

8.4.1 Discussion

On the basis of our examination of the data available for this study, the classic ITU-R model provides good prediction of long-term scintillation intensity. Its performance is least good, however, in the warmer months in both years 1999 and 2000. This may be explained by a decrease in correlation between surface

weather conditions and conditions along the path during relatively hot and humid weather as revealed in Chapter 5. (The ITU-R model assumes this correlation is very high). New models utilizing path-integrated water vapour measurement (IPWV) have been proposed. These models provide improved performance during warmer months. The Bath 1 and Bath 2 models have the best agreement with the measurement. They have stable and lower errors when tested on a data subset unused in their derivation.

The Bath models are based on all valid scintillation measurements, which does not exclude scintillation occurring during cloud and/or rain events. Models that describe scintillation in 'all-weather' conditions may have wider application in practical system planning than those restricted to clear-air conditions.

Although the data used for evaluation so far is limited, the proposed new models presented appear to give good predictions. To further verify or improve the prediction procedure, data over a wide range of frequencies and elevation angles are needed, bearing in mind that the coefficients need to be adjusted to the local climate.

The results of proposed new prediction models are promising. The Bath1 model has demonstrated an ability to predict scintillation intensity with an RMS error I the monthly mean scintillation intensity of 0.003 dB. This represents an improvement over the ITU-R model, which has an RMS error of 0.008 dB (See page P147 for an explanation of these values' significance).

8.5 Summary:

All the proposed new models for scintillation intensity prediction in this chapter are semi-empirical models framed by the theory of clear-air turbulence induced fluctuation. Antenna averaging factor, frequency dependence, elevation angle dependence, and climate dependence are treated as independent considerations.

Although the structure function of the turbulence could not be obtained directly in our case, the climate dependence of the models have been expressed by surface measured temperature and IPWV estimated by the GPS. A justification of this approach has been given and the detailed methodology has been explained.

By comparison of performance between new models and existing models in terms of RMS error and correlation coefficient, it can be concluded that for prediction of scintillation intensity for locations closed to Sparsholt, the author recommends the newly developed using IPWV estimated from GPS measurements and particularly the Bath1 and Bath2 model.

8.6 References:

[1] J. Haddon and E. Vilar, "Scattering induced microwave scintillations from clear air and rain on earth space paths and the influence of antenna aperture.," *IEEE Trans. Antennas Propagat.*, vol. 34, pp. 646-657, 1986.

[2] V. I. Tatarskii, *Wave propagation in a turbulent medium.* New York: McGraw-hill, 1961.

[3] Y. Karasawa, K. Yasukawa, and M. Yamada, "Tropospheric scintillation in the 14/11 GHz bands on earth-space paths with low elevation angles," *IEEE Trans. Antennas Propagat.*, vol. 36, pp. 563-569, 1988.

[4] E. Vilar and J. Haddon, "Measurement and modelling of scintillation intensity to estimate turbulence parameters in an earth-space path," *IEEE Trans. Antennas Propagat.*, vol. AP-32, pp. 340-346, 1984.

[5] F. S. Marzano and G. d'Auria, "Model-based prediction of amplitude scintillation variance due to clear-air tropospheric turbulence on Earth-Satellite microwave links.," *IEEE Trans. Antennas Propagat.*, vol. 46, pp. 1506-1518, 1998.

[6] C. H. Reitan, "Surface dew point and water vapor aloft.," *Journal of applied meteorology*, vol. 2, pp. 776-779, 1963.

[7] W. L. Smith, "Notes on the relationship between total precipitabe water and surface dew point.," *Journal of applied meteorology*, vol. 5, pp. 726-727, 1966.

[8] J. London, "A study of the atmospheric heat balance. Final Report, Contract no. AF18(122)-165," New York University, College of Engineering, Research Div. University Heights., New York 1957.

[9] S. J. Bolsenga, "The relationship between total atmospheric water vapour and surface dew point on a mean daily and hourly basis.," *Journal of applied meteorology*, vol. 4, pp. 430-432, 1965.
[10] ITU-R, "Reference standard atmospheres," Rec. P835-3.
[11] E. Matricciani, M. Mauri, and C. Riva, "Relationship between scintillation and rain attenuation at 19.77 GHz," *Radio Sci*, vol. 31, pp. 273-279, 1996.

Chapter 9

CONCLUSIONS AND FUTURE WORK

9.1 Conclusions

Due to the congestion of the spectrum in the lower band frequency, millimetre wavelength will have to be considered in order to accommodate the increasing demand for broadcast and multi-media data channels. At these wavelengths, the challenge to devise a scintillation model that will improve the utilization of channel capacity and provide useful information for developing efficient mitigation techniques are being recognized. The work reported here represents a collaborative project between the Telecommunications, Space and Radio (TSaR) Research Group at the University of Bath and the Radio Communications Research Unit (RCRU) at the Rutherford Appleton Laboratory (RAL) to develop an improved tropospheric scintillation prediction model targeting at Ka bands.

The research was funded for three years and over 300 Matlab routines (see Appendix C) have been written. The invalid data due to satellite movements, receiver loss of lock and other forms of system failures are identified, corrected or removed by some of these routines. Sparsholt meteorological measurements were validated using comparative analysis with the data from Chilbolton and Middle-wallop. Special treatment was applied to problematic measurements periods.

A optimum high-pass filter with a cut-off frequency of 0.01 Hz has been identified and used to extract scintillation from fading signals. Selection of the

correct cut-off frequency was made by comparison of the processed signal power spectrum with that theoretically predicted based on the work of Ishimaru. A one-minute period was adopted as a standard unit of filtered data for the calculation of scintillation statistics and justified on the basis of stationarity considerations.

Under dry conditions, short-term scintillation log-amplitude PDFs fitted by a Gaussian or Rice-Nakagami distribution have been found indistinguishable for weak scintillation. Lognormal and Gamma distributions can both produce comparable fit to the measured long term scintillation log-amplitude distribution at 20 GHz, 40 GHz and 50 GHz by using a conditional probability approach. There is no strong evidence for the choice of one distribution being superior to the other on the evidence of our experimental data.

In contrast to the dry power spectrum, the wet power spectrum exhibits greater energy at the lower frequencies. Occasionally, small amount of spectral energy extend above 0.01 Hz. Such wet data displays large enough fluctuations to be treated as wet scintillation. Wet scintillation and rain attenuation are found to be statistically dependent.

Observations show that cumulus and cumulonimbus clouds have seasonal and diurnal varying distributions throughout the year. Scintillation occurring with high-density cloud appears to have higher intensity compared with scintillation occurring in the absence of dense cloud. Higher cloud liquid water density appears to have stronger effect on scintillation at higher frequencies. The direct correlation between cloud high-density liquid water and scintillation intensity is, however, modest.

A comprehensive review and evaluation of existing scintillation prediction models is presented including models to predict scintillation log-amplitude cumulative distribution and models to predict mean scintillation intensity. In the context of

the former the Karasawa model performs best when compared with the Moulsley-Vilar and Otung models for both signal enhancement and fade. In the context of the latter the ITU-R model gives best agreement with our measurements among the 15 existing models.

The choice of GPS informed measurements was motivated by previous work at the University of Bath. Earlier research in the Radio Science and Radio Systems research group demonstrated that water vapour estimation from GPS measurements is credible, accurate and can be readily available. Furthermore, GPS technique provides continuous measurement of IPWV recorded with fine temporal resolution. (A typical GPS receiver set-up consists of a robust choke-ring antenna feeding into an Ashtech CGRS (see Figure 3.2).)

Computations of IPWV from GPS measurements were verified by comparing them with PWV measurements obtained from radiosonde launches. The process includes the comparison of PWV estimates from individual profiles obtained from each launch with concurrent IPWV from the (processed) GPS measurements, and comparison of mean monthly IPWV and PWV. Results show that GPS IPWV provides good agreement with the measured PWV for both individual profiles and for monthly averages.

The new GPS informed models were designed using ground temperature recordings and IPWV calculated from the GPS measurements. The approach exploits the robustness of ITU-R model with the following modifications: i) a new version of IPWV-informed wet term of refractivity has been used as a substitution for surface measured wet term of refractivity (using three approaches), ii) a direct correlation method has been use to construct a meteorological dependence factor using IPWV and surface temperature. Results demonstrate the success of the proposed modifications.

9.2 Future Work

In the last two chapter of this thesis, the potential to use GPS measurements for scintillation studies has been demonstrated by incorporating path-integrated water vapour estimates into new models for scintillation prediction. The accuracy of GPS water vapour estimates is expected to improve with the development of more sophisticated hardware and data processing algorithms and the availability of larger meteorological database. For example, the improvement of the mapping function(s) will require incorporation of both the surface temperature and information about the upper troposphere. (The Neil mapping function used in GIPSY-OASIS II was originally derived from seasonal atmospheric data in North America).

Other useful information about the troposphere can be extracted from the GPS signals. GPS residuals have been found to have significant contributions arising from tropospheric fluctuations that occur over time scales shorter than the sampling time. It has been suggested that residuals can be used to estimate mean structure constant C_n^2 time series [2], which may also be used as a potential predictor for scintillation.

Scintillation intensity prediction could be further improved by incorporating climatic variation into the frequency and elevation correction factors.

Several years of propagation measurements must be made to obtain sufficient statistical reliability for an engineer to use the models derived from them with confidence. The proposed prediction models for scintillation intensity therefore need to be further validated using more experiment data, ideally gathered in other locations but with comparable elevation angle and operation frequency.

This thesis has been mainly concerned with the statistical and dynamic aspects of received signals suffering scintillation. Work is also needed to more fully

understand the impact of this scintillation on systems performance including the implications not only for variable E_b/N_0 but also the effect on receiver dynamics (PLL and other control loop operation, for example) and the implications for fade mitigation techniques. The implications for other system architecture elements such as modulation and multiple access schemes might also be considered – even if this is only to demonstrate conclusively that scintillation has no significant role.

9.3 References:

[1] C. Catalan, B. Gremont, E. Vilar, and C. L. Wrench, "Dynamical comparison of rainfall rate and rain attenuation; path averaging of rain attenuation," presented at AP2000 Milenium conference on Antenna and Propagation, Davos, Switzerland, 2000.

[2] C. J. Naudet, "Estimation of tropospheric fluctuations using GPS data.," *TDA Progress Report 42-126*, 1996.

Appendix A

USEFUL MATHEMACTICAL FORMULAS

1.1 Parameters to Describe Random Media

Time history of dielectric variations $\Delta\varepsilon(t)$ can be expressed as the sum of ambient value $[\varepsilon(t)-\varepsilon_0]$ and random fluctuations $\delta\varepsilon(t)$.

$$\Delta\varepsilon(t)=[\varepsilon(t)-\varepsilon_0]+\delta\varepsilon(t) \tag{A1. 1}$$

The autocorrelation function of dielectric constant is defined:

$$C(\tau)=\frac{\overline{\delta\varepsilon(t)\delta\varepsilon(t+\tau)}}{\delta\varepsilon(t)^2} \tag{A1. 2}$$

where the time average function defined as $\overline{\delta\varepsilon(t)}=\frac{1}{T}\int_0^T dt\delta\varepsilon(t)$.

The spatial covariance is to describe the similarity and spatial dependence between dielectric fluctuations of two points. It is defined as the ensemble-averaged product of the two fluctuations, given below:

$$B_\varepsilon(r_1,r_2)=\langle\delta\varepsilon(r_1,t)\delta\varepsilon(r_2,t)\rangle \tag{A1. 3}$$

for homogeneous medium the spatial covariance will only depend on the separation of the two vector r_1-r_2. For isotropic medium, the spatial covariance will only depend on the magnitude of the separation vector $\rho=|r_1-r_2|$.

Structure function is designed to evaluate the difference at a given measure point compared to nearly points in a positive scalar filed. The structure function of the refractive index of the medium is given as below:

$$D_n(r_1, r_2) = \left\langle [\delta n(r_1, t) - \delta n(r_2, t)]^2 \right\rangle \tag{A1. 4}$$

Experimental data suggests that the refractive-index structure function is well approximated by a $2/3$ scaling law over a wide range of separation:

$$D_n(\rho) = C_n^2 |\rho|^{2/3} \tag{A1. 5}$$

Three-dimensional Fourier transform for the spatial covariance, which has related the covariance to the power spectrum of the refractive index fluctuation $\Phi_n(\kappa)$:

$$\langle \delta n(r_1, t) \delta n(r_2, t) \rangle = \int d^3\kappa \Phi_n(\kappa) \exp[i\kappa \cdot (r_1 - r_2)] \tag{A1. 6}$$

1.1.1 Richardson Number

Richardson number is a dynamically significant stability indicator, denoted as Ri. It is a dimensionless parameter whose values determines convection is free or forced, as defined by

$$Ri = \frac{F_{bouyancy}}{F_{inertial}} = \frac{g\alpha \cdot \Delta TL}{U^2} \tag{A1. 7}$$

where g is the gravitational acceleration, α is the thermal expansion coefficient, ΔT is the temperature difference and U is the velocity scale. The equation can be written in the following form:

$$Ri = \frac{g/\theta \cdot d\theta/dz}{|dv/dz|^2} \tag{A1. 8}$$

where 6 is the potential temperature and dv/dz is the vertical wind shear.

When Ri is small, that is $F_{buoyancy} << F_{inertial}$, when convection occurs when the buoyancy force is negligible and temperature variations are not large enough to alter the flow significantly. This convection mode is referred as forced convection. Otherwise, convection flow is produced by buoyancy force, when the fluid would be at rest in the absence of temperature variations, referred as free convection.

1.1.2 Reynolds Number

The Reynolds number for a flow through a pipe is denoted as Re and defined as:

$$\mathrm{Re} = \frac{\rho \cdot \bar{u} d}{h} = \frac{\bar{u} d}{v} \tag{A1. 9}$$

where ρ is the density of the fluid, $\bar{u}$ is the velocity scale, d is the pipe diameter, and v is the kinematic viscosity of the fluid. When $\mathrm{Re} < 30$, laminar flow has been experimentally found, when $\mathrm{Re} >> 30$, flow becomes turbulent.

Turbulence is also known as "turbulent diffusion" or "eddy diffusion." In this process, small-scale random fluctuations accelerate diffusion. In 1926, L. F. Richardson proposed that the average distance between particles grows as $t^{3/2}$. In 1941, A. Kolmogorov proposed that the difference in velocity between two points grows as $d^{1/3}$ where d is the distance between the points, states as:

$$u(k) = \left(\frac{\varepsilon}{k}\right)^{1/3} \tag{A1. 10}$$

where $u(k)$ is the spatial fouier transform, ε is the energy current flowing from large-scale eddies to small-scale eddies and k is the wave number. In 1995, Majda and Elliott computationally confirmed the $t^{3/2}$ and $d^{1/3}$ hypotheses over ~12 orders of magnitude. Critical to Kolmogorov's 1941 theory were the assumption that ε is roughly constant (with weak fluctuations only) and depends only on

forcing on the inertial and integral scales. In his 1964 paper, he argued instead that because of fluctuations, ε should be a function of space and time capable of varying over many orders of magnitude, producing fluctuations called intermittency. Current theory is unable to decide in favour of either weak fluctuation of intermittency.

1.2 Equations Used in Vasseur Model

1.2.1 Calculation of Mean Structure Parameter Profile

The mean structure parameter at height z is calculated by Equation (A1.7), the expressions are given in terms of basic meteorological profiles [1] and [2]

$$\left\langle C_n^{\,2}(z)\right\rangle = 2.8M_0(z)^2\left\langle R(z)\right\rangle\int_0^{\infty} L_0^{\,4/3}P_{L_0}\int_0^{\infty} P_s\cdot\int_{-\infty}^{S^2R_{ic}}\left\langle N^2\right\rangle P_{N^2}\,dN^2\,dS\,dL_0 \tag{A1.11}$$

Where $C_n^{\,2}(z)$ is the vertical profile of the refractive index structure constant; $M_0(z)=M_0N^2R^{1/2}$, R represents the humidity contribution to M^2; L_0, S or N^2 represents the out scale of turbulence, wind shear and the buoyancy forces.

$$M_0(z)=-77.6\times10^{-6}\frac{p(z)}{gT(z)} \tag{A1.12}$$

$$\left\langle R(z)\right\rangle=\left[1+1.55\times10^4\frac{g(z)}{T(z)}-\frac{1.55\times10^4}{2}\frac{g\dfrac{\partial q}{\partial z}(z)}{\left\langle N^2(z)\right\rangle T(z)}\right]^2 \tag{A1.13}$$

$q(z)=0.6225\dfrac{e(z)}{p(z)}$ is the specific humidity; $\left\langle N^2(z)\right\rangle = g\dfrac{\partial \ln 6}{\partial z}(z)$ is the mean value of buoyancy forces (in s^{-2}); $\theta = T(z)\left(\dfrac{1000}{p(z)}\right)^{0.2858}$ is the potential temperature (in K); P_{L_0} is a uniform distribution between $L_{0\min}=3m$ and $L_{0\max}=100m$:

$$P_{L_0} = \frac{1}{L_{0\max} - L_{0\min}} \quad \text{if } L_{0\min} \le L_0 \le L_{0\max}$$
$$= 0 \quad \text{otherwise} \tag{A1. 14}$$

P_s follows a Rice distribution:

$$P_s = \frac{S}{\sigma_s{}^2(z)} \exp\left(-\frac{S^2 + \langle S(z) \rangle^2}{2\sigma_s{}^2(z)} \right) I_0\left(\frac{S\langle S(z) \rangle}{\sigma_s{}^2(z)} \right) \tag{A1. 15}$$

$$\langle S(z) \rangle = \sqrt{\left(\frac{\partial v \cos\varphi}{\partial z}(z) \right)^2 + \left(\frac{\partial v \sin\varphi}{\partial z}(z) \right)^2} \tag{A1. 16}$$

$\langle S(z) \rangle$ is the mean wind shear in s^{-2}; $\sigma_s = 0.18 L_0{}^{-0.3} \left| \langle N^2(z) \rangle \right|^{0.25} \rho(z)^{-0.15}$;

$\rho(z) = 0.348(p(z)/T(z))$ is the mean density of dry air in the slab, in kg^2/m^3.

P_{N^2} is a Gaussian distribution:

$$P_{N^2} = \frac{1}{\sqrt{2\pi}\sigma_N(z)} \exp\left[-\frac{\left(N^2 - \langle N^2(z) \rangle \right)^2}{2\sigma_N{}^2(z)} \right] \tag{A1. 17}$$

$$\sigma_N(z) = \sqrt{\frac{6}{5}} \sigma_S(z) \sqrt{\left| \langle N^2(z) \rangle \right|} \tag{A1. 18}$$

1.2.2 Calculation 2-D Cross-correlation Function of the Structure Parameter

Expressions developed by Ravard and Chevrier enables to relate the 2-D cross-correlation function of the structure parameter to the long-term characteristics of the mean-structure parameter [3] and [4].

$$\Gamma_{C_n^2}(z, z+\Delta z, \tau) = p50_{\langle C_n^2 \rangle}(z) p50_{\langle C_n^2 \rangle}(z+\Delta z) \cdot \exp\left(\frac{s^2 \langle C_n^2 \rangle(z) + s^2 \langle C_n^2 \rangle(z+\Delta z)}{2} \right) \cdot \exp[\Gamma_r(z, z+\Delta z, \tau)] \tag{A1. 19}$$

where $s^2\langle C_n^2\rangle(z)$ is a parameter of the $\langle C_n^2(z)\rangle$ log-normal distribution

$$s_{\langle C_n^2\rangle}(z)=\sqrt{\frac{1}{2}\ln\left(\frac{\langle\overline{C_n^2}\rangle+\sigma_{\langle C_n^2\rangle}(z)}{p^2 50_{\langle C_n^2\rangle}(z)}\right)} \tag{A1. 20}$$

$\Gamma_r(z,z+\Delta z,\tau)$ is given

$$\Gamma_r(z,z+\Delta z,\tau)=\frac{s_{\langle C_n^2\rangle}(z)s_{\langle C_n^2\rangle}(z+\Delta z)}{2}\cdot\left[A\left(\frac{\Delta z}{L_1}\right)\exp(-\tau/5)+A\left(\frac{\Delta z}{L_2}\right)\exp(-\tau/80)\right] \tag{A1. 21}$$

with $A(\Delta z/L)=1-|\Delta z/L|$ if $|\Delta z|<L$, otherwise zero. $L_1=100m$ and $L_2=2000m$.

1.3 References:

[1] J. M. Warnock, T. E. VanZandt, and J. L. Green, "A statistical model to estimate mean values of parameters of turbulence in the free atmosphere.," presented at 7th sym. of turbulence diffusion, 1985.

[2] J. M. Warnock and T. E. VanZandt, "A statistical model to estimate the refractivity turbulence structure constant Cn2 in the free atmosphere," NOAA Tech. Memo ERL AL-10, NOAA, Aeronom. Lab.Boulder, CO, Nov 1985.

[3] O. Ravard, "Study and modeling of intermittent VHF transmission channels." Rennes, France: Univ. Rennes I, 1994.

[4] O. Ravard and F. Chevrier, "Volume scattering by tropospheric turbulence at midlatitudes: Frequency validity range," *Radio Sci*, vol. 31, pp. 821-831, 1996.

Appendix B

USEFUL METEOROLOGICAL BACKGROUND

2.1 Cloud Identification

The current used cloud classification system has a historical origin, ten principle cloud forms are grouped into four primary cloud divisions, namely high clouds, middle clouds, low clouds and clouds with vertical development. Clouds height cannot be strictly identified, and the absolute heights are relative to different regions, normally they are higher in the tropical regions and lower towards the polar regions. Therefore, justifications are always made by visual clues [1] [2] [3] [4] and [5].

2.1.1 High Cloud

For middle and low altitudes, high clouds generally form above 6000m. They usually appear thin and white because the air at these elevations is quite cold composed of ice crystals. The most common high clouds are cirrus, cirrostratus and cirrocumulus.

2.1.1.1 Cirrus (Ci)

Cirrus always in line or bands form, nearly always have a component of motion from the west to east, indicting the prevailing winds at their elevation. Where they occur in a marked line across the sky they usually coincide with a jet stream at that level.

2.1.1.2 Cirrostratus (Cs)

Cirrostratus is a thin layer of ice crystals, which spreads across the sky from the west in advance of an approaching war front. Hence they are usually to predict rain or snow within 12 or 24 hours.

2.1.1.3 Cirrocumulus (Cc)

Cirrocumulus appears as small, rounded, white puffs that may occur individually or in long rows. It seldom covers more than a small portion of the sky and is the least common of the high clouds.

2.1.2 Middle Clouds

The middle clouds have bases between 2000 m and 7000 m in the middle latitudes. They are composed of water droplets as well as ice crystals. Some common middle clouds are altostratus and altocumulus.

2.1.2.1 Altostratus (As)

The altostratus is a darker-coloured cloud that contains ice crystals and water droplets. Altostratus clouds often form ahead of storms having widespread and relatively continuous precipitation.

2.1.2.2 Altocumulus (Ac)

They are white to grey clouds that are common composed mostly of water droplets ad rarely more than 1 km thick. The appearance of these clouds on a warm, humid summer morning often portends thunderstorms by late afternoon.

2.1.3 Low Clouds

Low clouds with their bases lying below 2000 m and are always composed of water droplets except in cold weather, they may contain ice particles and snow. Three common low clouds are identified: stratus, stratocumulus and nimbostratus.

2.1.3.1 Stratus (St)

Stratus is a uniform greyish cloud that often covers the entire sky, formed by orographic ascent or by turbulent mixing at low levels. It resembles a fog that does not reach the ground. The development of cellular up-and-down motion within the cloud may change it into a stratocumulus layer, when it is made unstable by radiative cooling at the top.

2.1.3.2 Stratocumulus (Sc)

Stratocumulus is a low cloud that appears in patches that often appears near sunset. Precipitation rarely falls from stratocumulus, although in winter precipitation in the form of shower may occur if the cloud elements develop vertically into much larger clouds and their tops grow colder.

2.1.3.3 Nimbostratus (Ns)

This type of cloud often associated with more or less continuously falling rain or snow. The intensity of this precipitation is usually light or moderate. If air becomes saturated, a lower layer of clouds or fog may form beneath the original cloud base.

2.1.4 Clouds with Vertical Development

Clouds that do not fit into any of the above three categories often extend upward into the middle or high altitudes, such as cumulus and cumulonimbus. They are related to one another and are strongly associated with unstable air.

2.1.4.1 Cumulus (Cu)

Cumulus cloud often develops on warm summer morning and by afternoon, become much larger and more vertical developed. If a cumulus congestus continues to grow vertically, it develops into a giant cumulonimbus.

2.1.4.2 Cumuluonimbus (Cb)

Cumulonimbus often called 'thunderstorm' cloud. Tremendous amounts of energy are released by the condensation of water vapour within a cumulonimbus and results in the development of violent up- and downdrafts, which may exceed 50 knots.

2.2 Wind

Wind shear in the vertical direction is a common cause of cloud formation. If a layer of air is moving faster than the layer underneath they interact at their boundary so as to reduce the difference in their speeds. Turbulent mixing occurs through a limited depth and if the air is moist enough cloud is formed. Jet stream cirrus is an example, which is sometimes very restricted laterally.

[1] C. D. Ahrens, *Meteorology today - an introduction to weather, climate, and the environment*: West publishing company, 1994.
[2] D. H. McIntosh and A. S. Thom, *Essentials of meteorology*: Wykeham publications (London) Ltd, 1969.
[3] F. K. Lutgens and E. J. Tarbuck, *The Atmosphere -- An Introduction to Meteorology*. New Jersery: Prentice-Hall Inc. Englewood Cliffs, N. J. 07632, 1982.
[4] J. T. Houghton, *The physics of atmospheres*: Cambridge University Press 1997, 1986, 1997.
[5] BADC Help File, "Hourly Weather Observation Data.."

Appendix C

MAJOR MATLAB ROUTINES

3.1 Major Routines For The Processing of ITALSAT Data

[ItalData,error_status] = LoadITAL(Day) reads ITALSAT raw data measured on Day from '.gz' files by specified path, and stores each measurement variable as a field of the structure ItalData. Day must be a string e.g '990129'. If there is any error in reading or loading the raw data, error flag recorded in error_status.

[SubData,findmeas_error] = FindMeas(data,error_status) searches and return the valid measurement. Invalid data are marked with zeros in the field of year(yr), month(mh), day(dy) and hour(hr) until the measurement began. If there is error in the processing or there is no valid measurement, error flag recorded in findmeas_error. Valid data saved as a new structure SubData.

[Y] = B_DIST(X) performs detection and correction for Type I of invalid beacon data. Invalid data samples are saved as nan in the returned Y.

[Y] = T_DIST(X) performs detection and correction for Type II of invalid beacon data. Invalid data samples are saved as nan in the returned Y.

[Y] = S_DIST(X) performs detection and correction for Type III of invalid beacon data. Invalid data samples are saved as nan in the returned Y.

[res] = MovAvg(data,winsize) performs the moving average filtering of one dimensional input data, of winsize length and results are output as res.

[Output] = HPF(Input,Fc) performs the high-pass filtering of Input with cut-off frequency Fc (in Hz), using 4^{th} order Butterworth digital filter.

[Output] = LPF(Input,Fc) performs the low-pass filtering of Input with cut-off frequency Fc (in Hz), using 4^{th} order Butterworth digital filter.

[gR] = AntenAvg_CCIR1986(freq,D,ang_d) applies the Crane-Blood model, for antenna of diameter D (in meter) operating at freq and elevation angle of ang_d (in degree). Antenna averaging factors output as gR.

[gx] = AntenAvg_Haddon(freq,D,aeff,ang_d) applies the Haddon-Vilar model, for antenna of diameter D (in meter) operating at freq and elevation angle of ang_d (in degree). Antenna averaging factors output as gR.

[AvgI,L_error,F_error] = AvgITAL(StarDate,FinDate,WinSize,Fc) returns mean scintillation intensity for specified period between StarDate and FinDate. Scintillation time-series are obtained by using high pass filter of cut-off frequency of Fc (in Hz). WinSize is the length of stationary period (in sec). StartDate and FinDate are in Matlab date number format. Error flag when loading raw data will be saved in L-error, error flag when searching for valid measurement will be saved in F_error.

[Dv,findmeas_error] = DiurITAL(StartDate,FinDate,WinSize,Fc) returns hourly averaged scintillation intensity and meteorological measurement by applying High Pass Filter of transient freq is Fc, for data time-series between StartData and FinData, which need to be date string in the format of 'yyyy/mm/dd'. Results are saved in structure Dv, which field are scint20, scint40, scint50, t, p, rh and rg.

[per] = PercentJBTest(data) performs the Bera-Jarque parametric hypothesis test to the one dimension input data and return the averaged ratio in percentage of number of samples passing the test to number of samples fail the test for all the divided blocks. The width of the blocks are corresponding to the tested stationary period range from 1 min to 60 min.

[per] = PercentLillieTest(data) performs the Lilliefors hypothesis test to the one dimension input data and return the averaged ratio in percentage of number of samples passing the test to number of samples fail the test for all the divided blocks. The width of the blocks are corresponding to the tested stationary period range from 1 min to 60 min.

[n1_20,n1_40,n1_50,n2_20,n2_40,n2_50,range_n1,range_n2,mean_value,rms_value] = LongTermPDF(winsize,array) calculates long-term PDF of scintillation log-amplitude for period specified in datenum array. winsize is the length of stationary period in sec, default cut-off frequency is 0.01Hz. Routine return the PDF according to pre-defined data ranges for three frequencies beacons and return the mean scintillation intensity saved in rms_value.

[Xrange,px] = Moulsley_Vilar(a,b) performs Moulsley_Vilar model (conditional probability) for long-term scintillation log-amplitude statistics. The method is assuming scintillation symmetrical. a is the mean of log scintillation variance, b is the variance of log scintillation variance, p1 is the distribution of scint variance, and is a function of (sigma_m, sigma_sigma, sigma), p2 is the

distribution of scintillation log-amplitude, and is a function of (X,sigma). Results x is the PDF corresponding to data range Xrange.

[muhat,sigmahat] = lognfit(x) performs best-fit lognormal parameters for input one-dimensional x, estimates muhat and sigmahat are the mean and std of log(X).

[muhat,sigmahat] = GausFit(x) calculates Gaussian fit for a distribution in a least-square sense.

[new_range,exceed] = PDFToExceed(data_range,pdf) converts data pdf (in percent) according to data_range to its exceedence statistics exceed (in percent) for a specified range.

[nwet, ndry] = NwetNdry(t,p,rh) calculates the wet and dry term of refractivity: nwet and ndry from input data t (in degree Calcium), p (in hPa) and rh (in %)

[p,mu_enh,mu_fad] = Karasawa_annual(sigma) applies Karasawa annual (at least monthly) statistics model for fade and enhancement, sigma is the averaged standard deviation of log-amplitude, p is the default range, mu_enh is the signal enhancement exceedence level and mu_fad is the signal fading exceedence level.

[p,mu_enh_a,mu_fad_a,mu_sigma_a,mu_enh_w,mu_fad_w,mu_sigma_w] = Otung_annual(sigma) applies the Otung annual and worst-month statistics for fade and enhancement. sigma is the averaged standard deviation of log-amplitude, p is the default range, mu_enh is the signal enhancement exceedence level, mu_fad is the signal fading exceedence level, mu_enh_w is the worst month signal enhancement exceedence level and mu_fad_w is the worst month signal fading exceedence level.

[sgm] = Pred_Reitan(t,ipwv,freq,D,aeff,ang_d) applies the Reitan method to predict scintillation intensity given system parameter. t is the surface temperature (in degree Calcium), ipwv in the integrated water vapour (in mm), freq is the operating frequency (in GHz), D is the antenna diameter (in meter), aeff is the antenna's efficiency and ang_d is the elevation angle (in degree).

[sgm] = Pred_AT(t,ipwv,freq,D,aeff,ang_d) applies the standard atmosphere method to predict scintillation intensity given system parameter. t is the surface temperature (in degree Calcium), ipwv in the integrated water vapour (in mm), freq is the operating frequency (in GHz), D is the antenna diameter (in meter), aeff is the antenna's efficiency and ang_d is the elevation angle (in degree).

[sgm] = Pred_Bath1(t,ipwv,freq,D,aeff,ang_d) applies the Bath1 method to predict scintillation intensity given system parameter. t is the surface temperature (in degree Calcium), ipwv in the integrated water vapour (in mm), freq is the operating frequency (in GHz), D is the antenna diameter (in meter), aeff is the antenna's efficiency and ang_d is the elevation angle (in degree).

[sgm] = Pred_Bath2(t,ipwv,freq,D,aeff,ang_d) applies the Bath2 method to predict scintillation intensity given system parameter. t is the surface temperature (in degree Calcium), ipwv in the integrated water vapour (in mm), freq is the operating frequency (in GHz), D is the antenna diameter (in meter), aeff is the antenna's efficiency and ang_d is the elevation angle (in degree).

[sgm] = Pred_Bolsenga_daily(t,ipwv,freq,D,aeff,ang_d) applies the Bolsenga method to predict scintillation intensity given system parameter as above.

[sgm] = Pred_Smith(t,ipwv,freq,D,aeff,ang_d)] applies the Smith method to predict scintillation intensity given system parameter as above.

[sgm_itu,ratio_ref] = Pred_ITU(Nwet,freq,D,aeff,ang_d) applies the ITU-R model to predict scintillation intensity given system parameter. Nwet is the surface wet term of refractivity, freq is the operating frequency (in GHz), D is the antenna diameter (in meter), aeff is the antenna's efficiency and ang_d is the elevation angle (in degree).

[sgm_itu, ratio_ref] = Pred_Otung(Nwet, freq, D, aeff, ang_d) applies the Otung model to predict scintillation intensity given system parameter as above.

[sgm_itu, ratio_ref] = Pred_Karasawa(Nwet, freq, D, aeff, ang_d) applies the Karasawa model to predict scintillation intensity given system parameter as above.

[sgm_kamp1, sgm_kamp2, sgm_kamp3] = Pred_Kamp (Nwet, Phc, Cu, Whc, freq, D, aeff, ang_d) applies the Kamp I, II and III models to predict scintillation intensity given system parameter as above. Whc is heavy cloud water content (liquid water density > 0.7 kg/m^2, in %), Cu is Cumulus cloud occurrence (in %) and Phc is the probability of heavy cloud presence (in %).

[sgm_t, sgm_n] = Pred_Ortgies(T, Nwet, freq, D, aeff, ang_d) applies the Ortgies N and T models to predict scintillation intensity.

[sgm_dpsp, sgm_masp, sgm_sth2, sgm_stn2, sgm_sthv2, sgm_stnv2] = Pred_Marzano (T,H,Nwet, pwv, freq, D, aeff, ang_d) applies the Marzano MPSP, NPSP, STH2, STN2, STHV2 and STNV2 models to predict

scintillation intensity. H is the surface relative humidity (in %), pwv is the water vapour path integrated measured from radiosonde.

[result] = skew_interval(daylist_array) calculates the skewness for each specified time interval for specified days given in daylist_array.

[result] = skew_sigma(daylist_array) calculates the skewness for each specified intensity bin group for specified days given in daylist_array.

[Output] = ModSkewness(Input,WinSize) calculates the skewness with specified window width WinSize

[Output] = ModAvg(Input,WinSize) calculates the mean with specified window width WinSize

[Output] = ModStd(Input,WinSize) calculates the standard deviation with specified window width WinSize

3.2 Major Routines For The Processing of Radiosonde Data

[X] = LoadSonde(filename) reads standard radiosonde profiles from concatenated profiles from filename, and stores each meteorological measurement of n-th profile as a field of the n-th element of the structure X.

[p, z, t, e, v, Phi, rh, error] = DataPrep(profile,n) performs the data preparation by finding valid measurement in profile n and interpolating onto basic altitude levels, where e is water vapour pressure (in hpa), rh is relative humidity (in %), p is pressure (in hpa) and phi is wind direction (in radian).

[data_new,error_est] = est_2(ht,data) applies linear interpolate to the original radionsonde profile data for altitude specified by ht (in m). Output data is saved in to variable data_new, error flag in the processing of linear interpolate will saved in error_est.

[Td] = RH2DewTemp(TT,RH) calculates the dew point temperatures Td (in K) from relative humidity RH (in %) and dry bulb temperature TT (in K). Input variables should be one-dimensional data, further reference can be found at http://www.agsci.kvl.dk/~bek/relhum.htm.

[RH,eTD] = DewTemp2RH(TT,TD) calculates relative humidity RH (in %) from dry bulb temperature TT (in K) and dew point temperature TD (in K). eTD is the water vapour partial pressure (in hPa). Input variables should be one-dimensional data, further reference can be found at "Essentials of Meteorology", D.H.McIntosh & A.S.Thom, page 19.

svp = svp(t) calculates the saturation vapour pressure of water vapour over a) t > -30 degC : water, b) t < -50 degC : ice c) -50 degC < t < -30 degC : a linear interpolation between the two from temperature t (in degree Calcium) should be one-dimensional array.

[cloud,array,error_ct] = CloudThick(pressure,altitude,rel_hum) calculates the cloud occurrence using the Salonen model from the given pressure, altitude, relative humidity (rel_hum) profile. Each layer of cloud thickness, base and top altitude are saved in array cloud. The corresponding indexes of samples in cloud are saved in array. If there is no cloud, error_ct = 1,otherwise error_ct = 0.

[lwc, Total_ct, Total_clwc, cloud, error_lwc] = ColumnLW (cloud, array, error_ct, temp, altitude) calculates the columnar liquid water content of each layer of cloud using the Salonen model and processing result from CloudThick. Lwc is a structure contained temp profile, height of samples, liquid water content and columnar liquid water content of each layer. Total_ct is the total cloud thickness (in meter). If error makes no calculation of liquid water content, error_lwc = 1, otherwise error_lwc = 0.

[result] = LongTerm_Cn2 (Start_month, Fin_month) derives structure constant vertical profile of refractive index from radiosonde measurements recorded between Start_month and Fin_month using method described in Appendix A. Both input variable should be a date string specified by Matlab. The model is proposed to only work for long-term data.

[pdfshear] = Ps(L0,s,t,p,z,v,Phi) calculates the PDF of wind shear s, t is temperature (in K), p is pressure (in mb/hp), z is altitude (in m), Phi is wind direction (in degree), L0 is outer scale of turbulence, theta is the potential temperature (in K), g = 9.81 (in m/s^2) the acceleration of gravity, estS is the mean wind shear (in S^(-2)) and s is the wind shear (in S^(-2)). Formulas are referred to Appendix A.

[pnsqr] = PNsqr(Nsqr,L0,p,t,z) calculates the PDF of Nsqr, t is temperature (in K), p is pressure (in mb/hp), z is altitude (in m), L0 is outer scale of turbulence, theta is the potential temperature (in K), g = 9.81 (in m/s^2) the acceleration of gravity, estNsqr is the mean value of buoyancy forces (in S^(-2)), Rho is mean density of dry air in the slab (in kg/m^3), PN2 is a Gaussian distribution. Formulas are referred to Appendix A.

[pnsqr] = GausPNsqr(L0,p,t,z) calculates the PDF of PN2, formulas are referred to Appendix A.

[sumPN2] = IntPNsqr(L0,s,t,p,z) performs integration of the PNsqr, low and up limit of the integration and formulas are given by Vasseur in Appendix A.

[sumps] = IntPs(L0,p,t,z,v,Phi) performs integration of the Ps, low and up limit of the integration and formulas are given by Vasseur in Appendix A.

[result] = CrossCorr_2d_cn2(cn2,z,z1,z2,tau) calculates 2-D cross correlation of Cn2 profile, formulas are referred to Appendix A.

[result] = CrossCorr_2d_r(cn2,z,z1,z2,tau) calculates 2-D cross correlation of Cn2 profile, formulas are referred to Appendix A.

[result] = SigmaSigmaChiSqr(cn2_meas,z,f,theta,mean_sigma_chi_sqr) calculates the standard deviation of scintillation variance. n2_meas is an accumulated matrix of cn2 profile, z is altitude above sea level, f is carrier frequency (in GHz), k is wave number, theta is elevation angle (in degree). Formulas are referred to Appendix A.

[y] = ZeroIsotherm(t,ht) detects 0°C-isotherm height from each temperature profile., t is temperature profile and ht is height profile.

[sigma_sqr,p_sigma_sqr,m,s] = Vasseur_m_s (mean_sigma_chi_sqr, sigma_sigma_result) calculates the parameter m and s for Vasseur model of scintillation log-amplitude distribution. Formulas are referred to Appendix A.

[ipwv] = ProfileIPWV(sondename) calculates the IPWV for each radiosonde profile, filename saved as sondename.

3.3 Major Routines For The Processing of Synoptic Data

[datafile,data] = LoadSynop(filename) loads the SYNOP data from UK hour weather measurement recorded before the year 2000, data file are saved as '.hwx' file. Details of each field of datafile can be found in Met Office User Guide.
[datafile,data] = LoadWeather(filename) loads the SYNOP data from UK hour weather measurement for year 2000 and after 2000. Details of each field of datafile can be found in Met Office User Guide.

[ca,cato,ca_mon,error] = CloudOccur(data,monnum) calculates the cloud occurrence of different type. Each column of array ca is the occurrence of that type of cloud, the same order as the BADC instruction. Cato returns the total cloud occurrence of the day.

[p_speed,mon_p] = D3PSpeed(data) calculates the wind speed parallel to the direction of path link. Path geometries are pre-defined in the routine.

[p_speed,mon_p] = D3TSpeed(data) calculates the wind speed transverse to the direction of path link. Path geometries are pre-defined in the routine.

[cloud_amount,cloud_base] = Diural_Cloud_Var_hwx(datafile) returns the cloud amount of all types of cloud averaged on each hour from SYNOP data recorded before the year of 2000. datafile is the structure read from LoadSynop routine. Cloud types are in the order 1:CI 2:CC 3:CS 4:AC 5:AS 6:NS 7:SC 8:ST 9:CU 10:CB. Both cloud_amount and cloud_base are array of size (10,24,5) – (10 types of cloud, 12 months, spring, summer, autumn, annual).

[cloud_amount,cloud_base] = Diural_Cloud_Var_weather(datafile) returns the cloud amount of all types of cloud averaged on each hour from SYNOP data recorded in or after the year 2000. datafile is the structure read from LoadWeather routine. Cloud types are in the order 1:CI 2:CC 3:CS 4:AC 5:AS 6:NS 7:SC 8:ST 9:CU 10:CB. Both cloud_amount and cloud_base are array of size(10,24,5) – (10 types of cloud, 12 months, spring, summer, autumn, annual).

[Hr,t_hr] = Diural_Met_Var_hwx(datafile) returns the meteorological measurements averaged on each hour from SYNOP data recorded before the year of 2000. datafile is the structure read from LoadSynop routine. Hr is a structure containing field of temperature temp (in 0.1 degree Calcium), surface pressure mslp (in 0.1hPa), total cloud amount tca (in okta) and dew point temperature dpt (in 0.1 degree Calcium).

[Hr,t_hr] = Diural_Met_Var_weather(datafile) returns the meteorological measurements averaged on each hour from SYNOP data recorded in or after the year 2000. datafile is the structure read from LoadWeather routine. Hr is a structure containing field of temperature temp (in degree Calcium), surface pressure mslp (in hPa), total cloud amount tca (in okta) and dew point temperature dpt (in degree Calcium).

[cloud_amount,cloud_base] = Monthly_Cloud_Var_hwx(datafile) returns the cloud amount of all types of cloud averaged on each month from SYNOP data recorded before the year of 2000. datafile is the structure read from LoadSynop routine. Cloud types are in the order 1:CI 2:CC 3:CS 4:AC 5:AS 6:NS 7:SC 8:ST 9:CU 10:CB. Both cloud_amount and cloud_base are array of size (10,12) – (10 types of cloud, 12 months).

[cloud_amount,cloud_base] = Monthly_Cloud_Var_weather(datafile) returns the cloud amount of all types of cloud averaged on each month from SYNOP

data recorded in or after the year 2000. datafile is the structure read from LoadWeather routine. Cloud types are in the order 1:CI 2:CC 3:CS 4:AC 5:AS 6:NS 7:SC 8:ST 9:CU 10:CB. Both cloud_amount and cloud_base are array of size (10,12) – (10 types of cloud, 12 months).

[mn] = Monthly_Met_Var_hwx(datafile) returns the meteorological measurements averaged on each month from SYNOP data recorded before the year of 2000. datafile is the structure read from LoadSynop routine. mn is a structure containing field of temperature temp (in 0.1 degree Calcium), surface pressure mslp (in 0.1hPa), total cloud amount tca (in okta) and dew point temperature dpt (in 0.1 degree Calcium).

[mn] = Monthly_Met_Var_weather(datafile) returns the meteorological measurements averaged on each month from SYNOP data recorded in or after the year 2000. datafile is the structure read from LoadWeather routine. mn is a structure containing field of temperature temp (in degree Calcium), surface pressure mslp (in hPa), total cloud amount tca (in okta) and dew point temperature dpt (in degree Calcium).

3.4 Major Routines For The Processing of GPS Data

[GPSData] = LoadGPS(filename) loads in GPS data and saved data into structure GPSData, whose fields are measurement time, ts, yr, mh, dy, sec (in sec), ztd (in m), zhd (in m), zwd (in m), ipwv (in mm), p (in hPa), t (in degree Calcium) and rh (in %).

[res] = MapFun_Dry(t,t0) calculates the Neil dry mapping function with latitude and elevation angle. Coefficient matrix has been given in GYPSIS handout.

[res] = MapFun_Wet calculates the Neil dry mapping function with latitude and elevation angle. Coefficient matrix has been given in GYPSIS handout.

[td_k] = ipwv_Bolsenga_daily(ipwv) applies the Bolsenga model given IPWV (in mm) to estimate the surface dew point temperature td_k (in K) on a daily basis.

[td_k] = ipwv_Reitan(ipwv) applies the Reitan model given IPWV (in mm) to estimate the surface dew point temperature td_k (in K) on a monthly basis.

[td_k] = ipwv_Smith(ipwv) applies the Smith model given IPWV (in mm) to estimate the surface dew point temperature td_k (in K) on a monthly basis. Coefficients of Smith model lamda are quoted in Chapter 8.

[rms] = rms_error(meas,pred) returns the RMS error between measurement (meas) and prediction (pred).

[pf_error] = fractional_error(meas,pred) returns the fractional percentage error between measurement (meas) and prediction (pred) introduced in Chapter 6.

3.5 Major Routines For The Processing of Rain Gauge Data

[result] = RainAmount_diurnal calculates total rain amount averaged for each hour from all the rain gauge measurement.

[result] = RainAmount_Season calculates total rain amount averaged for calendar month from all the rain gauge measurement.

[range,exce] = RainExceed(array) calculates rain rate exceedence statistics for datenum stored in array according to a default range (0:0.1:50) mm/s

[result] = RainInteg(data,time_period) returns the integrated rain amount (defined as rain rate times measurement duration) in mm.

[day] = FindNonRainDay returns datenum that has no rain being observed.

[rain_month_per,dry_month_per] = MonthlyRainPercent returns percentage of wet time (with rain) and dry time (without rain) for each month of the whole rain gauge database.

Notes: All the listed routines are '.mat' files that have been written to realize each individual function or processing. They are saved as a library. Main routines using combination of the above routines are not listed.

Appendix D

MAJOR PUBLICATIONS

P. Yu, I. A. Glover, O. T. Davies, P. A. Watson, S. Ventouras, C. Wrench, "Scintillation Intensity Prediction Using GPS Measurements," *12th Inter. Conf. On Anten & Prop* Exeter, UK, April 2003.

P. Yu, I. A. Glover, O. T. Davies, P. A. Watson, S. Ventouras, C. Wrench, "Scintillation Intensity Prediction Using Path-Integrated Measurements," *Open Sym. On Prop. & Remote Sensing, URSI Commission F*, Garmish-Partenskirchen, Feb 2002.

P. Yu, O. T. Davies, I. A. Glover, P. A. Watson, S. Ventouras, C. Wrench, "Slant Path Scintillation Intensity Prediction Using GPS Data," *11th Inter. Conf. On Anten & Prop* Manchester, UK, April 2001.

Scintillation Intensity Prediction Using GPS Measurements

P Yu[1], I A Glover[2], P A Watson[3], O T Davies[4], S Ventouras[5], C Wrench[6]

[1, 2, 3] University of Bath, UK

[4, 5, 6] Radio Communications Research Unit, CLRC - Rutherford Appleton Laboratory, UK

ABSTRACT

This paper presents two new empirical methods for Ka-band tropospheric scintillation prediction using Global Positioning System (GPS) measurements. The predictions have been compared with 19 months of ITALSAT beacon measurements at 20 GHz. The proposed models achieve significant improvement compared with the classical ITU-R model. The potential of GPS measurements to further improve scintillation prediction methods are also discussed.

INTRODUCTION

Tropospheric scintillations are small-scale random fluctuations in the amplitude, phase and angle-of-arrival of a received signal. They occur on a time scale of a few seconds to several tens of seconds and occur because the troposphere has a spatial and temporal random component in its refractive index produced by turbulence. The magnitude of tropospheric scintillation depends on the magnitude and structure of the refractive index variation. It increases with frequency and with the path length through the medium, and decreases as the antenna beam-width decreases due to aperture averaging [1]. This effect becomes important at Ku- and Ka-band wavelengths, and must be accounted for accurately to complete a satisfactory link budget for low-fade margin communication systems, especially when operating at low elevation angles.

For microwave propagation (at least up to 30 GHz), radio refractive index is independent of frequency and can be expressed by [**ref**]:

$$n = 1 + (N_{dry} + N_{wet}) \times 10^{-6} \quad (1)$$

$$N_{dry} = 77.6 \frac{P}{T} \quad (2)$$

$$N_{wet} = 3.732 \times 10^{6} \frac{e}{T^2} \quad (3)$$

where T is temperature in K, e is water vapour pressure in hPa, and P is atmospheric pressure in hPa. The differential of expression (1) is related to variations of T, P and e by:

$$\partial n \times 10^{6} = \partial T\left[-\frac{77.6}{T^2}\left(P + 9620\frac{e}{T}\right)\right] + \partial P\left(\frac{77.6}{T}\right) + \partial e\left(\frac{373200}{T^2}\right) \quad (4)$$

In practical situations, pressure variations are small and can be disregarded. Temperature and humidity therefore play the key the role in refractivity fluctuation. Equation (4) underlines the importance of water vapour to refractive index fluctuation and implies that temperature and humidity could be used as the principal variables for prediction of scintillation. A typical example is the current ITU-R model.

ITU-R MODEL

Karasawa and Yamada [2] found that the long term monthly averaged rms fluctuations are well-correlated with the wet term of the radio refractivity given in (3), and developed a semi-empirical model for scintillation prediction. This model was later adopted by ITU-R in their recommended method for predicting scintillation statistics, i.e.:

$$\langle \sigma \rangle_m = \sigma_{ref} \cdot f^{\frac{7}{12}} \cdot \frac{g(x)}{(\sin\theta)^{1.2}} \quad (5)$$

$$\sigma_{ref} = 3.6 \times 10^{-3} + 10^{-4} \times N_{wet} \quad (6)$$

$\langle \sigma \rangle_m$ is monthly averaged scintillation intensity, $g(x)$ is the antenna aperture averaging factor proposed by Haddon and Vilar [3], θ is the elevation angle and f is frequency in GHz.

Ground-based measurements of local surface temperature and water vapour pressure (humidity) are used to calculate N_{wet} which is then used as an input for the reference intensity σ_{ref}. This parameter is designed to reflect seasonal and regional variation of weather conditions at the receiver location and is assumed to be equivalent to a measure of the path-averaged structure constant profile. However, using only a single point measurement of humidity at the surface to indicate the effect of turbulence (which occurs aloft and may extend along a significant fraction of the tropospheric path) on refractive index fluctuation seems intuitively inadequate, especially since water

vapour is known for to have more complicated behaviour than pressure and temperature, the effects of condensation and turbulent mixing in the lower troposphere making its distribution inhomogeneous and highly variable along the link path.

It might be expected that a measurement based on the presence of water vapour throughout the local troposphere and thus providing richer information about conditions along the path would provide improved scintillation prediction. GPS provides an opportunity for such a measurement, providing an accurate estimate of water vapour contained in a vertical column above the GPS receiver. This quantity is referred to as the integrated precipitable water vapour (IPWV).

Mindful that the parameters in equation (6) have been empirically adjusted using existing experimental evidence from the ITU-R databank, the following method of incorporating IPWV into a scintillation prediction model has been tried. The time-averaged value of IPWV has been substituted for the time averaged surface water vapour pressure in Equation (3). The resulting new estimate of N_{wet} is then used in the conventional ITU-R model (Equations (5) and (6)).

Three ways of incorporating IPWV have been investigated referred to here as the Reitan/Bolsenga, Bath 1 and Bath 2 models. These are described briefly below.

Reitan/Bolsenga

An empirical relationship between monthly averaged IPWV and surface dew point proposed by Reitan [4] is given in Equation (7).

$$\ln U = A + B \cdot t_d \qquad (7)$$

U is integrated precipitable water (cm), t_d is the dew point temperature (°C), $A = -0.981$ and $B = 0.0341$. Given temperature, partial pressure is calculated from the monthly averaged IPWV. Monthly scintillation intensities $\langle\sigma\rangle_{m\,Reitan}$ are then estimated from Equation (5) and (6).

Bolerga proposed a similar model to Equation (7) for daily averaged values with $A = -1.288$ and $B = 0.0384$ [5].

Bath 1

A straight line relationship between IPWV and e is assumed, i.e.:

$$e = A_1 \cdot IPWV + B_1 \qquad (8)$$

We refer to this as the Bath 1 model.

Bath 2

IPWV and surface temperature have the two best correlations with scintillation intensity, $\langle\sigma\rangle_m$ (see Table 1). The following relationship is therefore assumed.

$$\sigma_{ref} = A_2 \cdot t + B_2 \cdot IPWV + C_2 \qquad (9)$$

t is surface temperature (°C). This model is referred to as Bath 2.

The regression coefficients A_1, A_2, B_1, B_2 and C_2 in Bath 1 and Bath 2 have been calculated to achieve minimum mean square error between monthly scintillation prediction and measurement.

DESCRIPTION OF MEASUREMENTS AND DATA PROCESSING

BEACON MEASUREMENTS

Satellite beacons measurements are obtained from ITALSAT. The Earth station is Sparsholt (Hampshire, UK), the frequency is 18.9 GHz, the elevation angle is 30°, the antenna diameter is 1.2 m and the sampling interval is 1 s. 580 days of measurements between July 1999 and January 2001 (19 months) are available and have been divided into two data subsets; Data Set 1 from July 1999 to December 1999 (6 months) and Data Set 2 from Jan 2000 to Jan 2001 (13 months).

The scintillation signal χ dB, is extracted from the overall signal using a 6th order Butterworth high-pass filter to exclude low frequency components caused by other effects such as rain, gaseous attenuation and system drifts. The cut-off frequency of the filter is 0.02 Hz, which was chosen by comparing the averaged signal power spectrum in clear air with the theoretical temporal frequency spectra of wave fluctuation in turbulence derived by Ishimaru [6]. Scintillation intensity, σ, is calculated for each 600 sample (10 minute) block, during which meteorological parameters are believed to be essentially constant, and the random fluctuations are believed to be essentially stationary. Finally, the monthly and daily mean scintillation intensities, $\langle\sigma\rangle_m$ and $\langle\sigma\rangle_d$, are calculated.

GPS MEASUREMENTS

The dual-frequency GPS receiver and co-located meteorological sensor are stationed at Chilbolton, an RAL observatory 8 km from Sparsholt. The GPS measurements are processed by the JPL GIPSY-OASIS II software and IPWV is estimated with a time resolution of 5 minutes using the methods described in [7] and [8].

RESULTS

Correlation coefficients between monthly time-averaged scintillation intensity and meteorological variables (temperature in °C, pressure in hPa, relative humidity in % and IPWV in mm) for both Data Set 1 and Data Set 2 are compared in Table 1.

The Reitan monthly model and IPWV estimates for the measurements in Data Set 2 are compared in Figure 1. The Bolsenga daily model and the IPWV estimates are compared in Figure 2, the dotted line represents Equation (8) with coefficients $A_1 = 0.359$ and $B_1 = 3.857$ as derived using Data Set 2.

Scintillation intensity predictions using these values have been compared with measurements from Data Set 1. The results are presented in Figure 3 and Figure 4. Errors between predicted and measured intensities are summarised in Table 2 and Table 3.

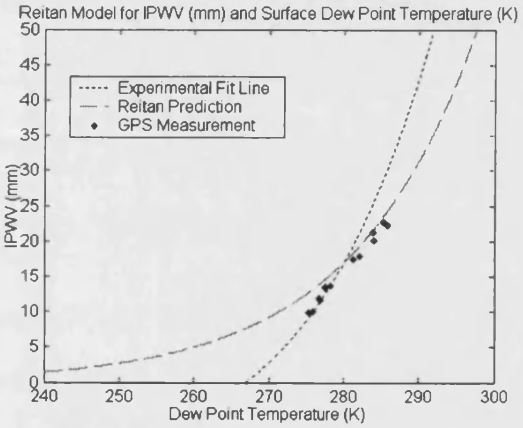

Figure 1 Comparison of monthly Retain IPWV prediction and GPS measurement (Data Set 2)

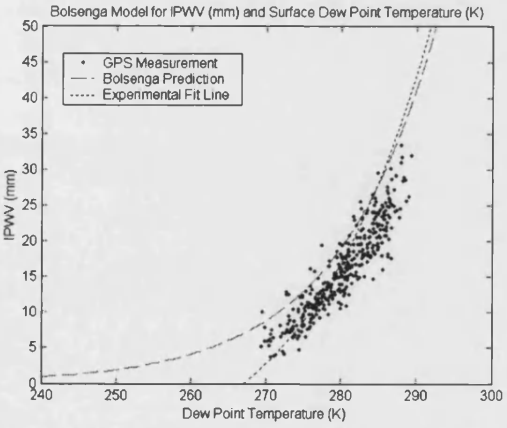

Figure 2 Comparison of daily Bolsenga IPWV prediction and GPS measurement (Data Set 2)

Subset	<t>	<p>	<rh>	<IPWV>
$\langle\sigma\rangle_{m1}$	0.4655	-0.3174	0.0313	0.5797
$\langle\sigma\rangle_{m2}$	0.6861	-0.1345	-0.0871	0.6166

Table 1 Correlation coefficient between variables and scintillation intensity averaged monthly

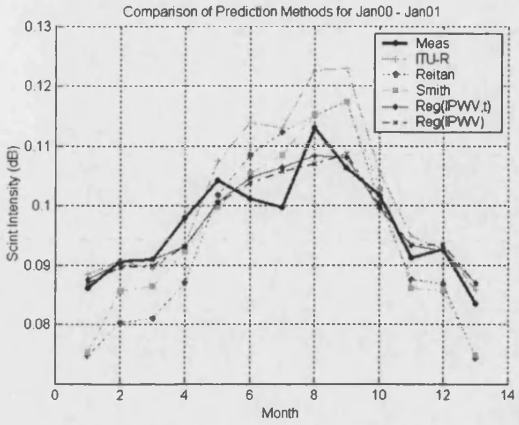

Figure 3 Comparison of selected prediction methods with Data Set 2measurements (20 GHz)

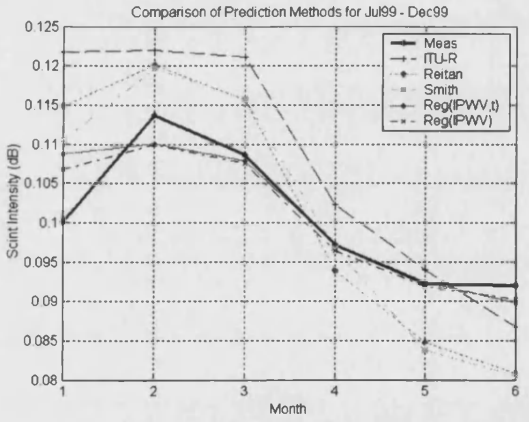

Figure 4 Comparison of selected prediction methods with Data Set 1 measurements (20 GHz)

Prediction Method	rms Error (dB)	Correlation with Measurements
ITU-R	0.0078	0.9184
Reitan	0.0085	0.9149
Bath 2	0.0033	0.9143
Bath 1	0.0033	0.9135

Table 2 Comparison of IPWV informed prediction and measurements from Data Set 2 (20 GHz)

Prediction Method	rms Error (dB)	Correlation with Measurements
ITU-R	0.0112	0.8624
Reitan	0.0091	0.9086
Bath 2	0.0039	0.8836
Bath 1	0.0033	0.9164

Table 3 Comparison of IPWV informed prediction and measurements from Data Set 1 (20 GHz)

CONCLUSIONS

On the basis of the data used in this study the classic ITU-R model provides generally good prediction of long-term scintillation. Its performance is least good, however, in the summer months. This may be explained by a decrease in correlation between surface conditions and conditions along the path during hot and humid weather.

Both Bath 1 and Bath 2 models have stable and lower errors than the ITU-R model when tested on an independent data subset.

The Bath models are based on all valid scintillation measurements, which does not exclude scintillation occurring during cloud and/or rain. (Effects other than scintillation during these cloudy or rainy conditions are removed by the de-raining process.) Models that describe scintillation in 'all-weather' conditions may have wider application in practical system planning than those restricted to clear-air conditions.

The dotted curve relating IPWV and surface dew point temperature in Figure 1 and Figure 2, does not follow the measured values exactly, especially at higher values of IPWV. Higher values of IPWV are likely to be associated with rain events, or heavy cloud. It is possible, however, that turbulence under these conditions may occur predominantly in one (or possibly more than one) thin turbulent layer(s) [9].

Although the data used for evaluation so far is limited, the new models presented are proved to have quite good prediction accuracy. To further verify or improve the prediction procedure, data over a wide range of frequencies and elevation angles are needed, bearing in mind that the coefficients need to be adjusted to the local climate.

Analysis not presented here shows, not unexpectedly, that the Bath models do not work well in the context of daily averages of scintillation.

GPS measurements have several advantages for water vapour estimation over conventional methods such as radiosonde and radiometer measurements. Accuracy continues to improve with the development of more sophisticated hardware and data processing algorithms. GPS residuals are believed to have significant contributions from the tropospheric fluctuations that occur over time scales shorter than the sampling time (5 minutes in our case corresponding to a frequency higher than 0.003 Hz). It has been suggested that residuals can be used to estimate mean structure constant C_n^2 time series [10]. This might also be used as a potential predictor for scintillation.

ACKNOWLEDGEMENT

We would like to thank the Radio Communications Research Unit (RCRU) at Rutherford Appleton Laboratory for kindly providing the ITALSAT beacon measurements.

REFERENCE:

[1] ITU-R, "Propagation data and prediction methods required for the design of Earth-space telecommunications systems," Rec. P 618-7.

[2] Y. Karasawa, M. Yamada, and J. Allnutt, "A new prediction method for tropospheric scintillation on earth-space paths.," *IEEE Trans. Antennas Propagat.*, vol. 36, pp. 1608-1614, 1988.

[3] J. Haddon and E. Vilar, "Scattering induced microwave scintillations from clear air and rain on earth space paths and the influence of antenna aperture.," *IEEE Trans. Antennas Propagat.*, vol. 34, pp. 646-657, 1986.

[4] C. H. Reitan, "Surface dew point and water vapor aloft.," *Journal of applied meteorology*, vol. 2, pp. 776-779, 1963.

[5] S. J. Bolsenga, "The relationship between total atmospheric water vapour and surface dew point on a mean daily and hourly basis.," *Journal of applied meteorology*, vol. 4, pp. 430-432, 1965.

[6] A. Ishimaru, *Wave propagation and scattering in random media.* New York: Academic, 1978.

[7] J. L. Davies, T. A. Herring, I. I. Shapiro, and G. Elgered, "Geodesy by radio interferometry: Effects of atmospheric modelling errors on estimates of baseline length," *Radio Sci*, vol. 20, pp. 1593-1607, 1985.

[8] J. Askne and H. Nordius, "Estimation of tropospheric delay for microwaves from surface weather data.," *Radio Sci*, vol. 22, pp. 379-386, 1987.

[9] E. Matricciani, M. Mauri, and C. Riva, "Relationship between scintillation and rain attenuation at 19.77 GHz," *Radio Sci*, vol. 31, pp. 273-279, 1996.

[10] C. J. Naudet, "Estimation of tropospheric fluctuations using GPS data.," *TDA Progress Report 42-126*, 1996.

Open Sym. on Prop. & Remote Sensing, URSI Commission F, Feb 2002

Scintillation Intensity Prediction Using Path-integrated Measurements

P Yu[1], I A Glover[1], O T Davies[1], P A Watson[1], S Ventouras[2], C Wrench[2]

[1]Department of Electronic and Electrical Engineering, University of Bath, Claverton Down, Bath, BA2 7AY, UK

[2]Radio Communications Research Unit, CLRC - Rutherford Appleton Laboratory, Chilton, Didcot, OX11 0QX, UK

Tel: + 44 1225 826061, Fax: + 44 1225 826305, E-mail: p.yu@bath.ac.uk
Tel: + 44 1225 826330, Fax: + 44 1225 826305, E-mail: p.a.watson@bath.ac.uk
Tel: + 44 1225 826309, Fax: + 44 1225 826305, E-mail: i.a.glover@bath.ac.uk
Tel: + 44 1235 446427, Fax: + 44 1235 446140, E-mail: o.t.davies@rl.ac.uk
Tel: + 44 1235 446427, Fax: + 44 1235 446140, E-mail: c.l.wrench@rl.ac.uk

Abstract – A recently developed method of inferring integrated water vapour (IPWV) along a zenith path from Global Position System (GPS) measurements, referred as the GPS-informed ITU-R model, is applied to scintillation intensity prediction. Vertical profile radiosonde data from an essentially co-located site has been used to infer the occurrence of cloud and the integrated liquid water content (ILWC) of this cloud has been estimated. ILWC has been correlated with the error between observed scintillation and the scintillation predicted by the ITU-R model in both its conventional and GPS informed varieties.

I. INTRODUCTION

Small-scale variations in humidity, pressure and temperature in a turbulent troposphere can change refractive index along a radio propagation path. These small-scale and time varying perturbations cause fluctuations in signal amplitude, phase, and angle of arrival, known as scintillations.

Current models for the prediction of scintillation intensity are principally based on monthly average values of the wet component of tropospheric refractivity, N_{wet}, estimated from ground based meteorological measurements. The resulting (monthly average) predictions have been found useful in the context of systems planning and design. As pressure on spectrum increases and higher frequency bands are pressed into service the scintillation problem becomes more severe. Furthermore, as lower availability systems become more important the impact of scintillation on system performance becomes more severe and the estimation of realistic link margins becomes more critical. A prediction method for scintillation intensity at the higher frequencies on a time-scale shorter than a month would therefore be of considerable value.

II. NEW PREDICTON METHOD BASED ON GPS MEASUREMENTS

A. *Current Practice*

Monthly averaged scintillation intensity is currently predicted by scaling a reference intensity, σ_{ref}, with frequency, f (GHz), elevation angle, ε, and antenna aperture averaging factor, g according to [1]:

$$\sigma = \frac{\sigma_{ref} f^{7/12} g}{\sin^{1.2}\varepsilon} \tag{1}$$

where g is the Haddon and Villar aperture-averaging factor [2], a function of effective diameter (or physical diameter and aperture efficiency), frequency, and height to the turbulent layer (which is assumed to be thin). g has the following form:

$$g(x) = \left(\begin{array}{l} 3.86 \cdot \left(x^2+1\right)^{11/12} \\ \cdot \sin\left[\frac{11}{16}\arctan\frac{1}{x}\right] - 7.08 \cdot x^{5/6} \end{array} \right)^{1/2} \tag{2}$$

Regression analysis has been used to relate the reference intensity to the wet component of refractivity, N_{wet}, resulting in the empirical model:

$$\sigma_{ref} = 3.6\times10^{-3} + 10^{-4} N_{wet} \tag{3}$$

N_{wet} is found from ground-based measurements of monthly mean absolute temperature, T (K), and water vapour partial pressure, e (hPa), using:

$$N_{wet} = 3.732 \times 10^5 \cdot \frac{e}{T^2} \quad (4)$$

Partial pressure, e, is given in terms of the saturated partial pressure, e_s (hPa), and relative humidity, H (%), by:

$$e = \frac{He_s}{100} \quad (5)$$

Between -20°C and 50°C the saturated vapour pressure over (liquid) water is given, to within 0.2%, by:

$$e_s = 6.1121 \exp\left(\frac{17.502t}{t+240.97}\right) \quad (6)$$

where t is temperature in degrees Celsius.

The range of validity claimed for the model is 30 GHz ≥ f ≥ 4 GHz and ε ≥ 4 degrees.

B. Methodology Using GPS Measurements

Scintillation is caused by turbulent mixing of air masses with different values of refractivity. The only meteorological input parameter for the ITU-R Model is through the monthly mean value of wet-term refractivity N_{wet} at ground level, which is not actually directly associated with turbulence.

In the context of scintillation, we believe water vapour effectively acts as a disclosure agent for turbulence. The variation in tropospheric refractivity at a particular height (and therefore pressure) is dominated by water vapour content and it seems reasonable, therefore, that a height-integrated measurement of water vapour should be useful as an input to a scintillation prediction. Such a model might be expected to yield improved (and shorter time-scale) predictions over a model using ground-based measurements of humidity due to the measurement of the presence of the disclosure agent closer to turbulent region of importance.

GPS has been used to measure the amount of water vapour contained within a continuous vertical column above the GPS antenna. As a GPS signal passes through the troposphere the velocity of the signal is reduced due to water vapour and oxygen in the troposphere.

The delays due to the individual satellites are combined into zenith total delay (ZTD), using a mapping function. The ZTD is usually written, when neglecting delay effects due to clouds or precipitation, in terms of the zenith hydrostatic delay (ZHD), due to all gases; and zenith wet delay (ZWD), due to water vapour [3], i.e.:

$$ZTD = ZHD + ZWD \quad (7)$$

ZHD is typically around 2.3 m, and can be modelled quite accurately from an atmospheric pressure measurement at the GPS antenna, p_S (hPa), using:

$$ZHD = \frac{0.0022768 p_S}{f(\phi, h)} \quad (8)$$

Where $f(\phi, h)$ allows for the variation of the acceleration due to gravity with location on the Earth. Where ϕ is latitude (degrees) and h is height (km) of the GPS antenna.

ZWD is much more variable than ZHD, and ranges from a few centimetres up to 40 cm. Subtraction of ZHD from ZTD yields ZWD.

Integrated precipitable water vapour (IPWV) is defined [4] by:

$$IPWV = \frac{1}{\rho_l}\int_H^\infty \rho_v dz = \frac{1}{\rho_l R_v}\int_H^\infty \frac{e}{T} dz \quad (9)$$

where $R_w = r/M_w$ and ρ_l (the liquid water density) is 1000 kg/m^3. In the literature [5], ZWD is mapped onto IPWV using:

$$IPWV = ZWD\left[\frac{10^6}{\rho(R/M_w)\left[(k_3/T_m)+k_2'\right]}\right] \quad (10)$$

A path-integrated version of relative humidity (H), calculated from IPWV, has been substituted for the ground-measured humidity in equation (5). After applying the ITU-R model summarized by equations (2), (3) and (4), we obtain a new scintillation intensity prediction. A flow-diagram of the technique is shown in Figure 1.

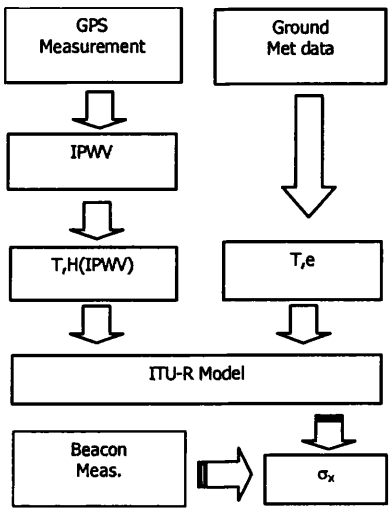

Figure 1. Program Flow-chart

C. *ITALSAT Beacon Measurement*

The Radio Communications Research Unit (RCRU) of the CLRC Rutherford Appleton Laboratory operates a receiving ground station to monitor and record ITALSAT F1 beacon signals at Sparsholt in Hampshire (latitude 51. 084° N, longitude 1.392° W).

The ITALSAT F1 beacon frequencies received are 18.7, 39.6 and 49.5 GHz. The following results are based mainly on the analysis work of the measurements at 18.7 GHz, with the elevation angle at 29.9 degree. Further details of the receiver design and operation can be found in [6] and [7]. Concurrent and co-located ground-based measurements of ancillary meteorological variables including temperature and relative humidity are available.

An analysis of 580 days of data recorded between July 1999 and Jan 2001 has been undertaken. The 1 Hz time series data was de-rained prior to the calculation of scintillation intensity using a high-pass filter. The cut-off frequency of the filter was 0.004 Hz. Low frequency variations such as diurnal amplitude variations due to the satellite station keeping, are unimportant in the context of scintillation studies since they are removed by the low-pass filtering.

The standard deviation of signal fluctuations has been calculated over every 10 minutes period and the monthly mean value of scintillation intensity has been found.

D. *GPS Data*

The concurrent GPS measurements have been taken at Chilbolton, a distance of 8 km from Sparsholt.

The measurements are processed by the JPL GIPSY-OASIS II software, using the precise point positioning method. Corrections are included for long-term and periodic Earth movements including tidal pressures. Phase variations caused by the ionosphere are removed by making use of the observations on two frequencies. The software outputs ZTD estimates with a time resolution of 5 minutes.

E. *Results*

At 18.7 GHz, the results show reasonable agreement between the GPS-informed prediction and measurements, especially during winter months, Figure 2.

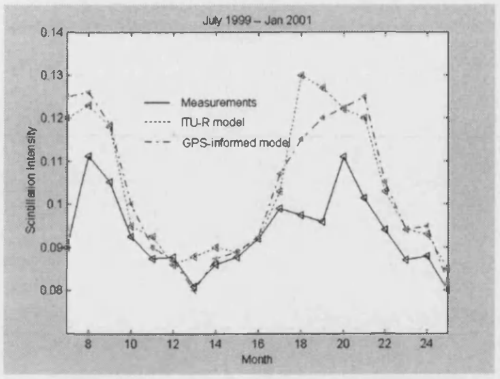

Figure 2. Monthly average scintillation intensity prediction and measurements

During the summer months both the GPS-informed model and the classical ITU-R model significantly over-estimate scintillation intensity. The improvement in prediction when using path-integrated estimates in place of the ground-based point estimates is not significant. The error between the GPS-informed model and the measurement is shown in Figure 3.

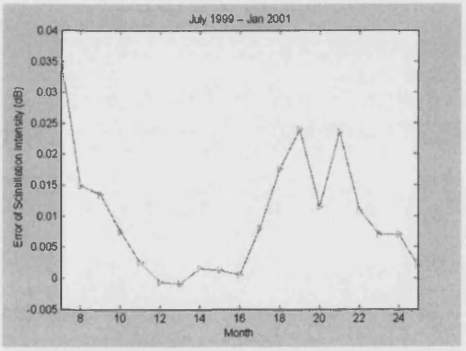

Figure 3. Scintillation Prediction Error

Significant differences in averaged scintillation intensity have been observed, in turbulent mixing of air masses with different water contents, in and around clouds and precipitation [8]. The diurnal correlation between scintillation and parameters, which indicate the occurrence of clouds with large water content, has also been observed [9]. To date, the effects due to liquid water within cloud have not been included in the GPS-informed model, IPWV only indicating water vapour along the path. The hypothesis is that scintillation originating in cloud is, at least partly, responsible for the disappointing level of improvement of the GPS informed prediction model over the traditional ITU-R model.

III. FURTHER INVESTIGATION USING RADIOSONDE DATA

A. *Salonen Model and Liquid Water Content*

The hypothesis referred to above is being investigated using vertical-profile radiosonde data in association with Salonen's cloud model [10]. The critical humidity function in the Salonen model is:

$$U_c = 1 - \alpha \cdot \sigma(1-\sigma)\cdot[1+\beta(\sigma-0.5)] \qquad (11)$$

where α = 1.0 and $\beta = 3^{0.5}$, σ is the ratio of pressure at the height in question and the surface. If the measured humidity is higher than the value of U_c at the same height, then cloud is assumed to be present at that height.

The liquid water content, w (g/m^3), as a function of temperature, t (°C), and height from cloud base, h_c (m), is calculated using:

$$w = w_0(1 + c \cdot t)\left(\frac{h_c}{h_r}\right)^a p_w(t) \qquad (12)$$

where a = 1.4, c = 0.041 /°C, w_0 = 0.14 g/m^3, is the liquid water content, if $h_c = h_r$ = 1500 m at 0°C. $P_w(t)$ is approximated by the function:

$$p_w = \begin{cases} 1 & 0°C < t \\ 1 + \dfrac{1}{20} & -20°C < t < 0°C \\ 0 & t < -20°C \end{cases} \qquad (13)$$

B. *Radiosonde Measurements*

The RS80 radiosonde, manufactured by the Finnish company Vaisala, has been used by the UK Met Office to take the measurement used in this work. The data comprise vertical profiles of temperature, dew-point temperature, wind speed and wind direction at standard and significant pressure levels. The standard pressure levels are 1000, 925, 850, 700, 500, 400, 300, 250, 200, 150, 100, 70, 50, 30, 20 and 10 mb. Significant pressure levels are calculated according to the Met Office criteria and constitute levels at which significant events occur in the profile for example turning points. Stations conduct ascents up to four times daily at the synoptic hours of 00, 06, 12, 18 GMT. The instrument takes measurements at heights of up to 20 to 30 km, at approximately 1.3 seconds intervals during the ascent, and the apparatus rises through the atmosphere at approximately 5m/s.

Data measured at Herstmonceux has been chosen because this is the closest operational site to Sparsholt, the location of ITALSAT receiver.

C. *Data Analysis*

The radiosonde data has been pre-processed in order to adjust the format and convert dew-point temperature into relative humidity. The Cloud base and top are calculated using linear interpolation of the in-cloud samples suggested from the critical humidity theory. An example of cloud inference is shown in Figure 4.

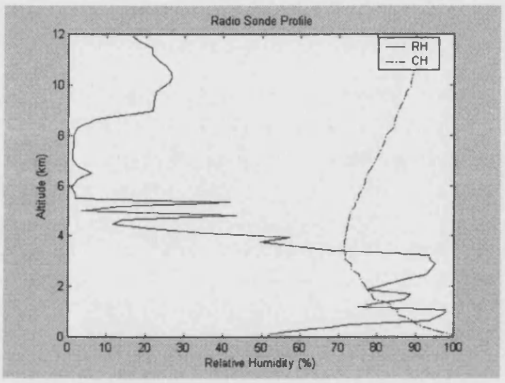

Figure 4. Relative humidity and critical humidity

The integrated liquid water content (ILWC) is calculated by integrating the cloud liquid water content w with respect to height within each layer of cloud up to the tropopause. (An average value of the tropopause height has been chosen as 12 km at mid-latitude locations.)

Long-term monthly mean values of total cloud thickness (T_{ct}) and ILWC have been calculated for the 19-month period that coincides with the ITALSAT and GPS measurements, Figure 5 and Figure 6.

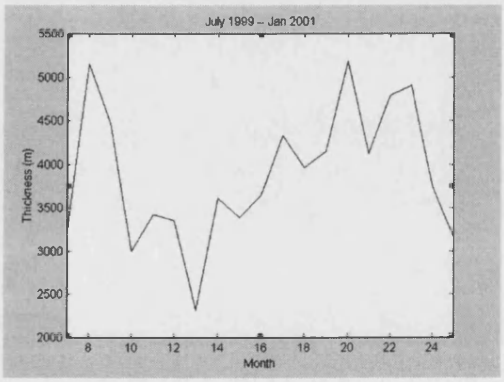

Figure 5. Monthly average T_{ct} (m)

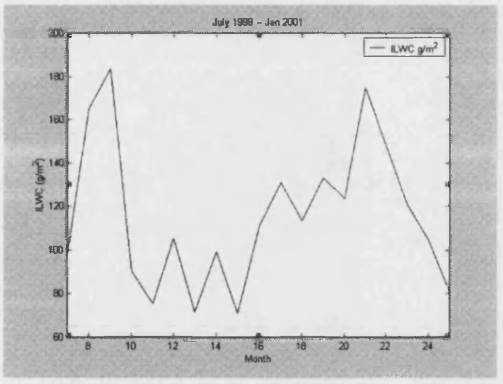

Figure 6. Monthly average ILWC (g/m^2)

The statistics of heavy clouds during the year 2000, which T_{ct} >1000 m, has been calculated, in Figure 7.

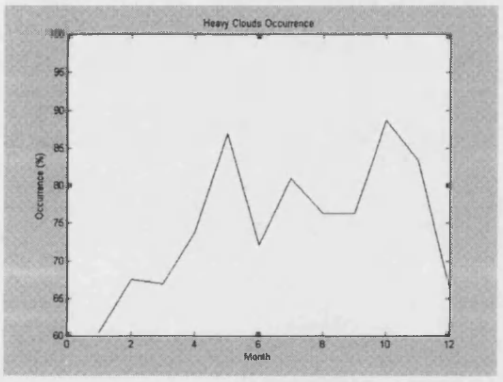

Figure 7. Heavy clouds occurrence (%)

Heavy clouds tend to appear mostly during the summer time, where the error between the GPS-informed model and the measurement is biggest.

IV. CONCLUSION

There is remarkably close agreement between the correlations for GPS derived path-integrated parameter and the point (ground-based) parameter. This suggests that the IPWV is a reasonable candidate parameter for prediction of scintillation intensity but has not (in this limited analysis) been shown to be superior to ground based measurements of temperature and humidity.

Significant correlation exists between ILWC and the GPS-informed model prediction error. This suggests that ILWC may be a useful quantity in refining ITU-type scintillation prediction models such as the one we have proposed. The ITALSAT database used for this analysis is currently being separated into cloudless and cloudy subsets in order to investigate this further.

V. ACKNOWLEDGEMENT

The authors wish to thank the CLRC-Rutherford Appleton Laboratory for providing the ITALSAT beacon measurements. And also wish to thank the United Kingdom Meteorological Office for access to radiosonde measurements (supplied through the British Atmospheric Data Centre).

VI. REFERENCES

[1] ITU-R: 'Propagation data and prediction methods required for the design of Earth-space telecommunications systems', Recommendations of the ITU-R, Rec. P.618-6, 1999.

[2] Haddon, J. and Villar, E.: 'Scattering induced microwave scintillations from clear air and rain on Earth space paths and the influence of antenna aperture', *IEEE Trans. Antennas and Propag.*, 1986, Vol. 34, No. 5, pp. 646 - 657.

[3] Davis, J. L., Herring, T. A., Shapiro, I. I., Rodgers, and A. E. E., Elgered, G.: 'Geodesy by radio interferometry: Effects of atmospheric modeling errors on estimates of baseline length', *Radio Sci.*, 1985, vol. 20, No. 6, pp.1593 - 1607.

[4] Askne, J., Nordius, H.: 'Estimation of tropospheric delay for microwaves from surface weather data.', *Radio Science,* Vol 22, No.3, PP.379-386, May-June 1987

[5] Davies, O. T. and Watson, P. A.: 'Comparisons of 93 GHz radiometer predicted attenuation with integrated precipitable water vapour measured using GPS', *Electron. Lett.*, Vol. 33, No.25, pp. 2114-2116, 1997.

[6] Woodroffe, J. M., Davies, P. G. and Norbury, J. R.: 'Combined Olympus and ITALSAT propagation experiment in the UK', *WPP - 60. Proc. Olympus Utilisation Conference*, Seville, Spain, 1993.

[7]. Ventouras. S., Wrench, C. L., and Davies, P. G.: 'Propagation measurements using ITALSAT beacons together with associated measurements of radar reflectivity from rain and clouds at 3 GHz and 35 GHz',. *Proc. 10th Int. Conf. on Antennas. and Propag. (vol. 1)*, Edinburgh, 1997.

[8]. Mohd Yusoff, M. M. B., Sengupta, N., Alder, C., Glover, I. A., Watson, P. A., Howell, R. G. and Bryant, D. L.: ' Evidence for the presence of turbulent attenuation on low-elevation angle earth-space paths – Part I: Comparison of CCIR recommendation and scintillation observations on a 3.3 ° path,' *IEEE Trans. Antennas Propagat.,* Vol. 45, pp. 73-84, Jan. 1997.

[9]. Tervonen, J. K., van de Kamp, M. M. J. L., and Salonen, E. T.: ' Prediction model for the diurnal behaviour of the tropospheric scintillation variance', *IEEE Trans. Antennas Propagat.*, Vol. 46, pp. 1372-1378, Sept. 1998.

[10]. Salonen, E. and Uppala, S.: ' New Prediction Method of cloud Attenuation.', *Electronic Letters*, Vol. 27, No. 12, 6th June, 1991.

11th ICAP Manchester, U. K. April 2001

SLANT PATH SCINTILLATION INTENSITY PREDICTION USING GPS DATA

P Yu[1], O T Davies[1], P A Watson[1], I A Glover[1], S Ventouras[2], C Wrench[2]

[1]Department of Electronic and Electrical Engineering, University of Bath, Claverton Down, Bath, BA2 7AY, UK

[2]Radio Communications Research Unit, CLRC - Rutherford Appleton Laboratory, Chilton, Didcot, OX11 0QX, UK

Tel: + 44 1225 82xxxx, Fax: + 44 1225 826305, E-mail: eeppy@bath.ac.uk
Tel: + 44 1225 323316, Fax: + 44 1225 826305, E-mail: eesod@bath.ac.uk
Tel: + 44 1225 826330, Fax: + 44 1225 826305, E-mail: eespaw@bath.ac.uk
Tel: + 44 1225 826309, Fax: + 44 1225 826305, E-mail: eesiag@bath.ac.uk
Tel: + 44 1235 446528, Fax: + 44 1235 446140, E-mail: s.ventouras@rl.ac.uk
Tel: + 44 1235 446427, Fax: + 44 1235 446140, E-mail: c.l.wrench@rl.ac.uk

ABSTRACT

A recently developed method of inferring integrated water vapour along a zenith path using GPS measurements is applied to scintillation intensity prediction. The hypothesis is that the values of N_{wet}, obtained from such measurements will be both more accurate and shorter-term predictors than those based on monthly averaged temperatures and relative humidities. This is because the important tropospheric turbulence that is the cause of scintillation occurs most frequently aloft rather than at ground level.

INTRODUCTION

Current models for the prediction of scintillation intensity are principally based on monthly average values of the wet component of tropospheric refractivity, N_{wet}, as estimated from ground based meteorological measurements (e.g. temperature and humidity). The resulting (monthly average) predictions have been found useful in the context of systems planning and design. As pressure on spectrum increases and higher frequency bands are pressed into service the scintillation problem becomes more severe, the estimation of realistic link margins becomes more critical, and the monthly averaging of current models becomes increasing disadvantageous. A prediction method for scintillation intensity at these higher frequencies with averaging on a time-scale shorter than a month would therefore be of considerable value.

CURRENT PRACTICE

Monthly averaged scintillation intensity is currently predicted [1] by scaling a reference intensity, σ_{ref}, with frequency, f (GHz), elevation angle, ε, and antenna aperture averaging factor, g according to:

$$\sigma = \frac{\sigma_{ref} f^{7/12} g}{\sin^{1.2} \varepsilon}$$

where g is the Haddon and Villar aperture averaging factor [2], a function of effective diameter (or physical diameter and aperture efficiency), frequency, and height to the turbulent layer (which is assumed to be thin). Regression analysis has been used to relate the reference intensity to the wet component of refractivity, N_{wet}, resulting in the formula:

$$\sigma_{ref} = 3.6 \times 10^{-3} + 10^{-4} N_{wet}$$

N_{wet} is found from ground-based measurements of monthly mean absolute temperature, T (K), and water vapour partial pressure, e (hPa), using:

$$N_{wet} = 3.732 \times 10^{5} \frac{e}{T^2}$$

and partial pressure, e, is given in terms of the saturated partial pressur, e_s (hPa), and relative humidity, H (%), by:

$$e = \frac{He_s}{100}$$

Between -20°C and 50°C the saturated vapour pressure over (liquid) water is given, to within 0.2%, by:

$$e_s = 6.1121 \exp\left(\frac{17.502t}{t + 240.97}\right)$$

where t is temperature in degrees celsius.

The above model, which is typical of several similar models in form, is based on a collection of measurements that include the parameter ranges given in Table 1.

Parameter	Range
Frequency	7 - 14 GHz
Antenna diameter	4 - 32 degrees
Elevation angle	3 - 36 m

Table 1 Parameter ranges of experiments contributing to ITU-R model

The range of validity claimed for the model, however, is 20 GHz $\geq$ f $\geq$ 4 GHz and $\varepsilon \geq 4$ degrees.

RATIONALE

The rationale for undertaking this work is based on the following premises.

1. Scintillation is caused by turbulent mixing of air masses with different values of refractivity
2. The variation in tropospheric refractivity of air at the same height (and therefore pressure) is dominated by water vapour content
3. In the context of scintillation water vapour effectively acts as a disclosure agent for turbulence
4. A height-integrated measurement of water vapour will be better correlated, on a shorter time-scale, with water vapour in the turbulent region than water vapour at the ground
5. GPS derived measurements of tropospheric excess delay provide a direct, convenient and almost universally available method of deriving height-integrated tropospheric water vapour content

The essence of this paper lies in testing the hypothesis expressed by premise 4.

METHODOLOGY

A database of concurrent GPS and satellite beacon measurements has been recorded. The beacon data is available at frequencies of approximately 20, 40 and 50 GHz although only (a limited amount of) 50 GHz transmissions have been analysed to date. In order to test whether GPS derived measurement of height-integrated water vapour is likely to be an improved short-term predictor of scintillation intensity the time-series standard deviations are correlated with the wet component of excess tropospheric delay. Correlation of signal standard deviation with the wet component of refractivity, derived from the ground based temperature and humidity measurements, is also found for comparison purposes. The correlation analysis is done using averaging times of 1 day, 6 hours, 1 hour and 5 minutes in both cases.

A correlation of scintillation intensity with wet delay that is higher than the correlation with wet refractivity would suggest that the GPS measurements provide a better predictor of scintillation than the ground based measurements.

BEACON MEASUREMENTS

The Radio Communications Research Unit (RCRU) of the CLRC Rutherford Appleton Laboratory operates a receiving ground station to monitor and record ITALSAT F1 beacon signals at Sparsholt in Hampshire (latitude 51° 04' N; longitude 01° 26' W). Sparsholt was selected so that the atmospheric path between the Earth-station and satellite can be scanned by meteorological radars that RCRU operates from Chilbolton.

ITALSAT F1 beacon frequencies are 18.685, 39.087, 39.592, 40.097, and 49.490 GHz. The 18 GHz signal is vertically polarised; the three signals close to 40 GHz are right hand circularly polarised; and the signal close to 50 GHz is switched between horizontal and vertical polarisations at a rate of 933 Hz. Preliminary results in this study are currently available for the 50 GHz signal only but analysis of other signal frequencies is also being undertaken.

The millimetre wavelength receivers at Sparsholt are situated inside a specially adapted cabin from where ITALSAT F1 is observed at an elevation of approximately 30 degrees. The 18.7 GHz antenna is externally mounted on the roof of the cabin, and the millimetre-wave units view the satellite through radomes of woven PTFE acquired from Gore Associates.

The 50 GHz receiver, and the 40 GHz triple channel receiver, designed and built by RCRU, have been operating at Sparsholt since April 1997. Table 2 shows the receiver antenna sizes and beamwidths. Further details of the receiver design and operation can be found in [3] and [4]. Operating alongside the beacon receivers is a 51 GHz radiometer that measures sky

brightness temperature in the direction of the ITALSAT satellite. These measurements can be used during data analysis to distinguish genuine fades from spurious outages, and to help provide a baseline against which to estimate fade depth. All receivers are sampled at a frequency of 1 Hz.

Receiver Frequency (GHz)	Antenna Diameter (cm)	Receiver Beamwidth (deg.)	
		E-plane	H-plane
18.7	122	0.9	0.9
39.6	61	1.1	0.86
49.5	61	0.7	0.7
51.0	30.5	1.2	1.1

Table 2 Principal antenna characteristics for Sparsholt ITALSAT receivers

Concurrent and co-located ground-based measurements of ancillary meteorological variables including temperature and relative humidity are available.

The most recently acquired data is subject to diurnal amplitude variations due to the abandonment of North-South ITALSAT station keeping and the consequent variations in antenna gain with satellite position. (Satellite tracking has not been employed.) These low frequency variations are unimportant in the context of scintillation studies, however, since they are easily removed by low-pass filtering.

GPS MEASUREMENTS

The GPS measurement employs multiple satellite observations using an Ashtech CGRS duel-frequency GPS receiver. Four to eight GPS satellites with elevation angles greater than 10 degrees are typically visible from the site of the measurements at any one time. A choke-ring receiving antenna is employed which is mounted on top of a 10 m mast to reduce the impact of multipath propagation arising from surface reflections.

Previous GPS based studies have processed observations using the double-differencing technique [5]. This requires observations from two GPS receivers and knowledge of the precise satellite orbits prior to processing. The effect of the receiver and satellite clock drifts is removed during processing. This study adopts the precise point positioning strategy [6], as implemented in the Jet Propulsion Laboratory (JPL) GIPSY-OASIS software. This strategy requires satellite clock drifts as well as precise satellite positions beforehand. The receiver clock drift is estimated during processing, thus avoiding the need for a second GPS receiver. Descriptions of the precise satellite orbits and clocks as well as polar motion effects are available at a JPL ftp site, approximately two weeks after the observation date. Phase variations of the GPS signal due to the ionosphere are removed by making use of simultaneous observations at the two frequencies. A stochastic estimator is employed for the determination of the receiver clock and the signal delay introduced by the Earth's atmosphere. A mapping function produces the zenith total delay (ZTD) from the individual delays along each satellite slant path. At completion of processing, the software outputs the precise point position for the period of the observation and estimates, at a time resolution of 5 minutes, for the ZTD and receiver clock drifts.

The ZTD is usually written, when neglecting delay effects due to clouds or precipitation, in terms of the zenith hydrostatic delay (ZHD) and zenith wet delay (ZWD) [7], i.e.:

$$ZTD = ZHD + ZWD$$

ZHD is typically around 2.3 m, and can be modelled quite accurately [7] from an atmospheric pressure measurement at the GPS antenna, p_S (hPa), using:

$$ZHD = \frac{0.0022768 p_S}{f(\phi, h)}$$

where $f(\phi, h)$ allows for the variation of the acceleration due to gravity with location on the Earth. The following simple expression has been developed for $f(\phi, h)$ [8]:

$$f(\phi, h) = 1 - 0.00266 \cos 2\phi - 0.00028h$$

where ϕ is latitude (degrees) and h is height (km) of the GPS antenna. With a high-accuracy pressure sensor (~0.2 hPa) the ZHD can be deduced within a millimetre.

ZWD is much more variable than ZHD, and ranges from a few centimetres up to 40 cm. Subtraction of ZHD from ZTD yields ZWD.

DATA DE-RAINING

The 1 Hz time series data was de-rained prior to the calculation of scintillation intensity using a multipole high-pass filter. The

amplitude response of this filter is shown in Figure 1. The cut-off frequency of the filter was 0.04 Hz, a value was adopted in line with recommendations arising from a detailed study of the effect of filter cut-off frequency on scintillation statistics [9].

RESULTS

A preliminary analysis of 80 days of data recorded between April and August 1999 has been undertaken. These days were chosen on the basis of their being free from hardware effects that might contaminate the scintillation intensity measurements such as receiver drop-outs etc. Scattergrams of time-series standard deviation against GPS derived zenith wet delay are shown in Figures 2 - 4 for averaging times of 1 day, 6 hours and 1 hour respectively. The corresponding scattergrams for standard deviation against wet refractivity are shown in Figure 5 - 7. The correlation coefficients corresponding to each scattergram are given in Table 3.

Averaging time	Correlation coefficient	
	τ_{wet}	N_{wet}
1 day	0.39	0.37
6 hours	0.20	0.25
1 hour	0.21	0.20

Table 3 Correlation coefficients

COMMENTS

Comments rather than conclusions are presented here since the small amount of data analysed so far makes firm conclusions inappropriate.

The correlation coefficients presented in Table 3 are low (even considering the short averaging periods). This may be due to the high frequency of the measurement (at least an octave above the range normally considered valid for models of the type being investigated) or contamination of the analysed data with scintillation arising from a mechanism un- (or weakly) correlated with water vapour concentration.

There is remarkably close agreement between the correlations for GPS derived path-integrated parameter and the point (ground-based) parameter. This suggests that the zenith wet delay is a reasonable candidate parameter for prediction of scintillation intensity but has not (in this limited analysis) been shown to be superior to ground based measurements of temperature and humidity.

REFERENCES

[1].ITU-R: 'Propagation data and prediction methods required for the design of Earth-space telecommunications systems', Recommendations of the ITU-R, Rec. P.618-6, 1999.

[2].Haddon, J. and Villar, E.: 'Scattering induced microwave scintillations from clear air and rain on Earth space paths and the influence of antenna aperture', *IEEE Trans. Antennas and Propag.*, 1986, **34**, (5), pp. 646 - 657.

[3].Woodroffe, J. M., Davies, P. G. and Norbury, J. R.: 'Combined Olympus and ITALSAT propagation experiment in the UK', *WPP - 60. Proc. Olympus Utilisation Conference*, Seville, Spain, 1993.

[4].Ventouras. S., Wrench, C. L., and Davies, P. G.: 'Propagation measurements using ITALSAT beacons together with associated measurements of radar reflectivity from rain and clouds at 3 GHz and 35 GHz',. *Proc. 10th Int. Conf. on Antennas. and Propag. (vol. 1)*, Edinburgh, 1997.

[5].Rocken, C., Vam Hove, T., Johnson, J., Solheim, F., Ware, R., Bevise, M., Chiswell, S., and Businger, S.: 'PS/STORM - GPS sensing of atmospheric water vapour for meteorology', *J. Atmos. Ocean. Technol.*, 1995, **12**, (3), pp. 468 - 478.

[6].Zumberge, J. F., Heflin, M. B., Jefferson, D. C., Watkins, M. M., and Webb, F. H.: 'Precise point positioning for efficient and robust analysis of GPS data from large networks', *J. Geophys. Res.*, 1997, **102**, (B3), pp. 5005 - 5017.

[7].Davis, J. L., Herring, T. A., Shapiro, I. I., Rodgers, and A. E. E., Elgered, G.: 'Geodesy by radio interferometry: Effects of atmospheric modeling errors on estimates of baseline length', *Radio Sci.*, 1985, **20**, (6), pp.1593 - 1607.

[8].Saastamoinen, J.: 'Atmospheric correction for the troposphere and stratosphere in radio ranging of satellites', *The use of artificial satellites for geodesy, Geophys. Monogr. Ser.*, 1972, **15**, pp.247 - 251.

[9].Otung, I. E., Al-Nuaimi, M. O., and Evans, B. G.: 'Extracting scintillations from satellite beacon propagation data', *IEEE Trans. on Antennas and Propag.*, **46**, (10), 1998, pp. 1580 - 1581.

amplitude response of this filter is shown in Figure 1. The cut-off frequency of the filter was 0.04 Hz, a value was adopted in line with recommendations arising from a detailed study of the effect of filter cut-off frequency on scintillation statistics [9].

RESULTS

A preliminary analysis of 80 days of data recorded between April and August 1999 has been undertaken. These days were chosen on the basis of their being free from hardware effects that might contaminate the scintillation intensity measurements such as receiver drop-outs etc. Scattergrams of time-series standard deviation against GPS derived zenith wet delay are shown in Figures 2 - 4 for averaging times of 1 day, 6 hours and 1 hour respectively. The corresponding scattergrams for standard deviation against wet refractivity are shown in Figure 5 - 7. The correlation coefficients corresponding to each scattergram are given in Table 3.

Averaging time	Correlation coefficient	
	τ_{wet}	N_{wet}
1 day	0.39	0.37
6 hours	0.20	0.25
1 hour	0.21	0.20

Table 3 Correlation coefficients

COMMENTS

Comments rather than conclusions are presented here since the small amount of data analysed so far makes firm conclusions inappropriate.

The correlation coefficients presented in Table 3 are low (even considering the short averaging periods). This may be due to the high frequency of the measurement (at least an octave above the range normally considered valid for models of the type being investigated) or contamination of the analysed data with scintillation arising from a mechanism un- (or weakly) correlated with water vapour concentration.

There is remarkably close agreement between the correlations for GPS derived path-integrated parameter and the point (ground-based) parameter. This suggests that the zenith wet delay is a reasonable candidate parameter for prediction of scintillation intensity but has not (in this limited analysis) been shown to be superior to ground based measurements of temperature and humidity.

REFERENCES

[1].ITU-R: 'Propagation data and prediction methods required for the design of Earth-space telecommunications systems', Recommendations of the ITU-R, Rec. P.618-6, 1999.

[2].Haddon, J. and Villar, E.: 'Scattering induced microwave scintillations from clear air and rain on Earth space paths and the influence of antenna aperture', *IEEE Trans. Antennas and Propag.*, 1986, **34**, (5), pp. 646 - 657.

[3].Woodroffe, J. M., Davies, P. G. and Norbury, J. R.: 'Combined Olympus and ITALSAT propagation experiment in the UK', *WPP - 60. Proc. Olympus Utilisation Conference*, Seville, Spain, 1993.

[4].Ventouras. S., Wrench, C. L., and Davies, P. G.: 'Propagation measurements using ITALSAT beacons together with associated measurements of radar reflectivity from rain and clouds at 3 GHz and 35 GHz',. *Proc. 10th Int. Conf. on Antennas. and Propag. (vol. 1)*, Edinburgh, 1997.

[5].Rocken, C., Vam Hove, T., Johnson, J., Solheim, F., Ware, R., Bevise, M., Chiswell, S., and Businger, S.: 'PS/STORM - GPS sensing of atmospheric water vapour for meteorology', *J. Atmos. Ocean. Technol.*, 1995, **12**, (3), pp. 468 - 478.

[6].Zumberge, J. F., Heflin, M. B., Jefferson, D. C., Watkins, M. M., and Webb, F. H.: 'Precise point positioning for efficient and robust analysis of GPS data from large networks', *J. Geophys. Res.*, 1997, **102**, (B3), pp. 5005 - 5017.

[7].Davis, J. L., Herring, T. A., Shapiro, I. I., Rodgers, and A. E. E., Elgered, G.: 'Geodesy by radio interferometry: Effects of atmospheric modeling errors on estimates of baseline length', *Radio Sci.*, 1985, **20**, (6), pp.1593 - 1607.

[8].Saastamoinen, J.: 'Atmospheric correction for the troposphere and stratosphere in radio ranging of satellites', *The use of artificial satellites for geodesy, Geophys. Monogr. Ser.*, 1972, **15**, pp.247 - 251.

[9].Otung, I. E., Al-Nuaimi, M. O., and Evans, B. G.: 'Extracting scintillations from satellite beacon propagation data', *IEEE Trans. on Antennas and Propag.*, **46**, (10), 1998, pp. 1580 - 1581.